Mathematical modelling of turbidity currents

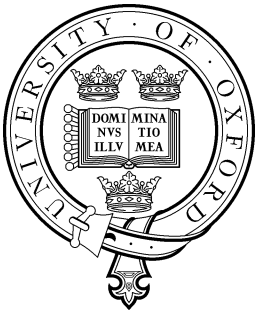

Gemma Louise Fay

University College

University of Oxford

Thesis submitted for the degree of

Doctor of Philosophy

Trinity 2012

‘Good luck with the work Bob! It’s only maths’
– Ceri Roberts.

Acknowledgements

I gratefully acknowledge the financial support of the EPSRC which allowed me to complete this thesis.

I would like to thank my supervisors Dr Andrew Fowler and Dr Peter Howell for their support and encouragement during the course of this DPhil. Andrew, for his advice from the start and many trips to the Lamb and Flag, and Pete, for joining the DPhil team part way through, for which I am incredibly grateful. I have very much enjoyed the many hours spent we have spent working on the mathematical problems that have arisen in this thesis!

The DPhil experience was aided by a great many people, not least the friends I have made whilst studying at OCIAM, including Cara, Dave, Anthony, Martin, Michi, my officemates Andy and Emma and the wider circle at Coffee Time, the Royal Oak and on GeoCorridor. Thanks to all of you for making my time here so much fun!

Outside of OCIAM, I have been lucky enough to meet some incredible friends at University College and through the extended Univ network. Ceri, George, Eoin, Heather, Dan, John, Sarah, Tristen, Geraint, Tisch, Katri, JB, Nicole, Stu, Nick, Jon and Danielle; you are all fantastic friends. Thank you for the plentiful pub trips, Said Lunches, dinners, shoulders to cry on and words of encouragement along the way – you have made my time in Oxford truly wonderful!

Thanks also to the friends and family from Newcastle, York and beyond who have provided further support, encouragement and slightly confused questions about turbidity currents. I hope you enjoy reading my thesis and/or having a pint with me now that I'm finished! Particular thanks to Silvana who was always ready to provide PhD counsel, to Rich, who spent several evenings and weekends proofreading my whole thesis and to Tony and Patricia, whose unwavering belief that I could do it helped keep me going!

Thanks to Dad, Suz and Fran who were a source of never ending

support during my time in Oxford, for which I am very grateful. The breaks back in Newcastle, visits to Oxford and phonecalls in times of need were all much appreciated! Particular thanks to Dad, for the reminder that I could go and sit by the front door if I wanted to 'eat in hall' whilst in Newcastle. You were all super and I couldn't have done it without you!

And, of course; Mike, who managed to be here for me every day, even when thousands of miles across the globe. I am so grateful for everything you did to help me get through this; the 48 hour visits, the questions about asymptotics I would email you about, the many hours you spent proofreading and the millions of reminders that I could really do it! You were here for every doubt, every panic and every celebration along the way and I could not have completed this thesis without your love, support and understanding. Thank you.

Finally, for my Mum, who could not be here to see this thesis; I am sure you would be proud.

Mathematical modelling of turbidity currents

Gemma Louise Fay

University College
University of Oxford

Thesis submitted for the degree of
Doctor of Philosophy

Trinity 2012

Turbidity currents are one of the primary means of transport of sediment in the ocean. They are fast-moving, destructive fluid flows which are able to entrain sediment from the seabed and accelerate downslope in a process known as 'ignition'. In this thesis, we investigate one particular model for turbidity currents; the 'Parker model' of Parker, Fukushima, and Pantin (1986), which models the current as a continuous sediment stream and consists of four equations for the depth, velocity, sediment concentration and turbulent kinetic energy of the flow.

We propose two reduced forms of the model; a one-equation velocity model and a two-equation shallow-water model. Both these models give an insight into the dynamics of a turbidity current propagating downstream and we find the slope profile to be particularly influential. Regions of supercritical and subcritical flow are identified and the model is solved through a combination of asymptotic approximations and numerical solutions.

We next consider the dynamics of the four-equation model, which provides a particular focus on Parker's turbulent kinetic energy equation. This equation is found to fail catastrophically and predict complex-valued solutions when the sediment-induced stratification of the current becomes large. We propose a new 'transition' model for turbulent kinetic energy which features a switch from an erosional, turbulent regime to a depositional, stably stratified regime. Finally, the transition model is solved for a series of case studies and a numerical parameter study is conducted in an attempt to answer the question 'when does a turbidity current become extinct?'.

Contents

Chapter 1

Introduction

1.1 Motivation: modelling density currents

A density current, or gravity current, is a primarily horizontal flow of a fluid of one density through a fluid of another density (Kuenen, 1951; Middleton, 1966a; Benjamin, 1968; Simpson, 1999; Peakall et al., 2001; Parsons et al., 2007). The difference in density can be caused by a difference in salinity, temperature or concentration of a suspended sediment, for example, and typically is relatively small, perhaps only a few percent. A density current is kept in motion by the pressure gradient between the two fluids, and when the current is present on a slope, the current will flow downstream because gravity acts on the excess

The figure originally located here has been removed from this version of the thesis for copyright reasons.

(a) Pyroclastic flow at Merapi Volcano

(b) Powder snow avalanche

Figure 1.1: Pyroclastic flows and powder snow avalanches are two examples of gravity currents in nature. Images (a) http://mail.colonial.net/~hkaiter/volcanoes.html, (b) http://www.uvm.edu/~inquiryb/webquest/sp08/pmontgom/avalanchesandmudslies.html. Canadian Avalanche Association.

density of the suspension to provide a driving force.

In nature we observe many types of density current, including pyroclastic ash flows from volcanoes (*e.g.* Huppert and Dade (1998); Trofimovs et al. (2008)) and airborne powder snow avalanches (*e.g.* Hopfinger (1983); Ancey (2001)), which are pictured in Figure 1.1. In this work we will focus on one specific type of gravity current; 'turbidity currents', which are powerful, fast-moving streams of sediment which propagate through the ocean on the seabed (*e.g.* Kuenen and Migliorini (1950); Bagnold (1962); Komar (1969)). Turbidity currents can travel hundreds of kilometers over a gentle slope at high speed, the sediment being kept in suspension by fluid turbulence (Bagnold, 1962; Middleton, 1966a; Komar, 1969; Parker et al., 1986). Our aim is to provide a thorough mathematical understanding of the turbidity current model of Parker, Fukushima, and Pantin (1986), and to make a first step towards answering the question; 'how far can a turbidity current travel downstream?'.

In the remainder of this chapter we introduce the reader to turbidity currents by providing a review of the literature in Section 1.2, and an overview of existing modelling techniques in Section 1.3. We will conclude by introducing the model we will use in this thesis in Section 1.4, and providing an outline of the following chapters in Section 1.5.

1.2 Background: submarine turbidity currents

Submarine turbidity currents are avalanches of littoral[1] sediment from the continental shelf to the deep ocean (Parker et al., 1986). Typically these currents travel great distances at high speeds, entraining material from the sea bed and sometimes resulting in damage to man-made structures on the seafloor (Heezen and Ewing, 1952; Ryan and Heezen, 1965; Krause et al., 1970; Mulder et al., 1997). Turbidity currents can occur on a small scale in lakes and reservoirs (Gould, 1951) but large events are most common in the ocean. Sediment, transported to the sea by rivers, accumulates on the continental shelf until a turbidity current into the deep ocean is triggered (*e.g.* Meiburg and Kneller (2010)). The typical geometry of an offshore environment where a turbidity current might take place is shown in Figure 1.2.

A turbidity current can be initiated when the build-up of sediment at the top

[1]The littoral zone is the area of the ocean close to the shore. It begins at the high water mark and extends into the sea, often beyond the intertidal region.

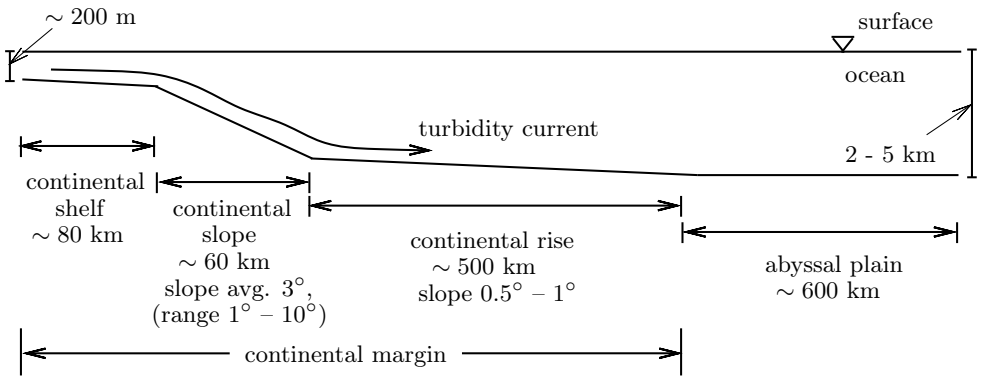

Figure 1.2: The path of a turbidity current. Upon initiation, a turbidity current moves down the continental slope under the force of gravity and continues down the continental rise until it reaches the abyssal plain. Here it spreads out on the seafloor as a deep sea fan, the current finally becoming extinct when it has lost all of its energy.

of the continental slope is large and further sediment deposition or an external forcing causes the material to flow (Huppert and Simpson, 1980; Meiburg and Kneller, 2010). This is similar to the way in which a snow avalanche might be triggered by the weight of the material exceeding its cohesive properties when the build up of snow is great (Hopfinger, 1983; Ancey, 2001). External factors causing turbidity currents include periodic fluctuations in the sediment budget (Bornhold et al., 1994; Khripounoff et al., 2003; Mulder et al., 2003) or an earthquake on- or offshore (Heezen and Ewing, 1952; Ryan and Heezen, 1965). Turbidity currents can also be triggered by a pyroclastic flow or avalanche intruding into the sea (Freundt, 2003). In July 2003, Soufrière Hills volcano in Montserrat in the West Indies experienced a massive lava dome collapse (Trofimovs et al., 2008, 2012). The resulting pyroclastic flow avalanched down the valley, carrying ash and volcanic material into the ocean, as is shown in Figure 1.3. The large volume of sediment that entered the ocean caused a tsunami wave to be generated and a turbidity current on the sea bed was induced.

The typical lengths of the offshore environment are shown in Figure 1.2. The runout distance of a turbidity current can be on the order of 1000 km (Eidsvik and Brørs, 1989). Currents occur on various scales with velocities ranging from tens of centimetres per second to tens of metres per second and current depths from a few metres to hundreds of metres (Kneller and Buckee, 2000). The sediment comprising a turbidity current is typically particles of silt and sand which can range from 4-62 μm and 0.062-2 mm in diameter, respectively (Bagnold, 1962).

(a) Montserrat Island (b) Deposits from the Soufriére Hills eruption

Figure 1.3: The eruption of Soufrière Hills volcano and emplacement of material into the ocean. Images (a) http://earthobservatory.nasa.gov/IOTD/view.php?id=40803, (b) http://www.noc.soton.ac.uk/gg/people/Talling/.

The interstitial fluid in a turbidity current is ocean water. As the current travels along the seabed it is able to entrain and deposit sediment at its base and entrain fluid at its upper interface (Parker, 1978, 1982). Unlike a granular flow where the sediment is kept in suspension due to grain-grain interactions (Hutter, 2005), the sediment in a turbidity current is kept suspended in the current by fluid turbulence (Middleton, 1966a). A particular feature of turbidity currents is their ability to continuously entrain sediment and accelerate in a condition known as 'ignition' (Bagnold, 1962; Parker, 1982; Parker et al., 1986) which we describe in detail in Section 1.2.2.

1.2.1 Observations of turbidity currents

Little is known about large-scale turbidity currents in the deep ocean as they are hard to predict and even harder to measure. One of the most famous turbidity currents occurred in 1929 off the coast of Newfoundland in Canada (Heezen and Ewing, 1952; Kullenberg, 1954). The current was triggered by an earthquake and sediment ran out into the Atlantic Ocean for several hours. Sequential snapping of transatlantic telephone cables occurred as a result of the current, see Figure 1.4, allowing the runout distance and speed of the current to be estimated at 600 km and 28 m s^{-1} respectively. The current is thought to have spread out on the abyssal plain in a deposit 0.1m high, covering over 280 000 km^2 of the sea floor.

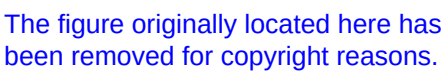

(a) Buildings in Lord's Cove destroyed by the tsunami.

(b) Submarine cable breaks

Figure 1.4: The aftermath of the 1929 Grand Banks earthquake which resulted in a tsunami and turbidity current. Images (a) the tsunami destroyed buildings and homes at the southern end of the Burin Peninsula in Newfoundland (Mosdell, 1929), (b) the submarine slump on the Laurentian slope produced a turbidity current which snapped transatlantic cables laid on the sea floor (Doxsee, 1948).

We infer information about turbidity currents from events such as these; often damaged infrastructure or marine equipment is the only knowledge we have that a turbidity current has occurred. However, in the last 40 years techniques for measurement have improved and more information has been obtained. Normark and Dickson (1976) observed periodic turbidity currents in Lake Superior over a two-year period and were able to measure current speed, direction and water temperature over 30 weeks of two summers. They used a series of current meters, anchored at 3 depths (5 m, 15.3 m and 45.8 m above the sea floor, in water depths of 205-215 m), in two locations in a valley on the lake bed. Their equipment was able to record speeds with an accuracy of $\pm$1.5cm s^{-1} and recordings were made continuously, except for breaks to charge the batteries of the equipment. In the 1972 experiments, average speeds of 3.3 cm s^{-1} and durations of 14 hours were recorded, whilst in 1973, average speeds of 10.8 cm s^{-1} and durations of 100 hours were recorded. The discrepancy is explained by the location of the two experiments; in 1973, the current meters were anchored much closer to the thalweg of the current.

More recently, Khripounoff et al. (2003) measured a large turbidity current in the Zaire submarine valley using current meters, turbidimeters and sediment traps. Khripounoff et al. (2003) found that at a depth of 150 m above the channel valley, speeds of 1.21 m s^{-1} were recorded and the authors postulated that the speed of the current closer to the channel bed would have been far higher. This was supported by evidence in sediment traps of coarse sand and plant debris at

40m above the sea floor, some 13 km south of the channel. Finally, attempts have been made by Xu et al. (2004) to record measurements of turbidity currents at the axis of the channel of the Monterey Submarine Canyon. Here, despite damage to equipment, current meters were able to record speeds at varying depths in the canyon and so the first ever turbidity current velocity profiles were produced.

With limited field data available on the dynamics of large turbidity current events, the need to model these dramatic and damaging flows becomes apparent. In Section 1.3 we will describe some of the current modelling techniques used to understand turbidity currents, with reference both to experimental work and theoretical studies.

1.2.2 Ignition of turbidity currents

The high speeds recorded by Khripounoff et al. (2003) and inferred by Heezen and Ewing (1952) suggest that turbidity currents have some mechanism which allows them to move rapidly over very gentle slopes. This phenomenon was first described by Bagnold (1962), who hypothesised that a condition exists where the input of gravitational energy into a turbidity current is just enough to maintain the turbulence required to keep sediment in suspension and to overcome friction at the base and the upper interface. Bagnold described this condition as 'autosuspension' as it is the suspended sediment that supplies the gravitational energy required to drive the flow and create the turbulence; that is, the sediment is suspending itself as it propagates downslope.

Parker (1982) introduced the term 'ignition' to describe this phenomenon in his study of highly erosive turbidity currents. He suggested that for a current to ignite, there must be enough loose sediment on the bed initially to be entrained by the flow. He speculated that this loose material would come from deposits of smaller turbidity currents that did not ignite but instead only deposited their material as they moved into the deep ocean, becoming extinct on the continental rise. Material that collected on the continental shelf would become part of much larger events ignited at the change of slope (see Figure 1.5) moving downslope and entraining loose material from the bed resulting in an ignitive current. Parker (1982) also suggested that these highly erosive currents would eventually be constrained by factors such as damping of turbulence at high concentrations or a limit on the entrainment rate of the current which would, in turn, limit the driving force downslope.

Further work by Fukushima et al. (1985) and Parker et al. (1986) looked at highly erosive turbidity currents in submarine canyons. Here, turbidity currents were found to reach velocities of 8 - 14 m s^{-1} and travel swiftly over a very shallow slope. In this case, it was speculated that the energy must come from the sediment in suspension. The process has been observed in Scripps Submarine Canyon where sediment entrainment caused acceleration of the current, resulting in further entrainment of sediment a self-reinforcing cycle was established (Fukushima et al., 1985). In a submarine canyon there is much loose sediment to be entrained into the flow making the ignition of a current much more likely here.

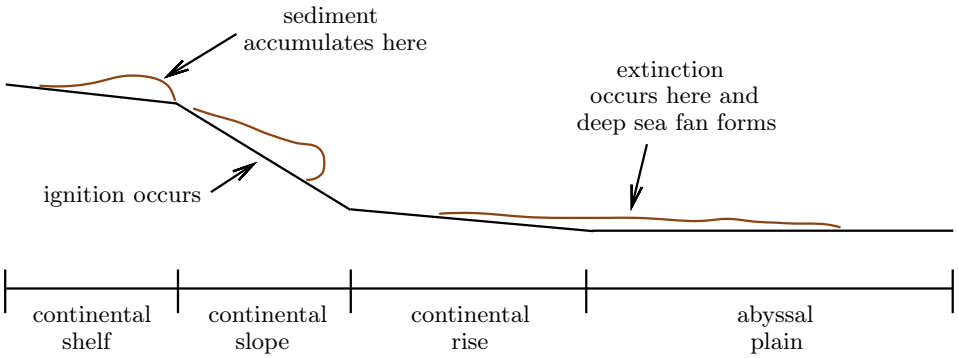

Figure 1.5: Build up, ignition and extinction of turbidity currents in relation to the geometry of the seafloor.

Finally, work by Pantin (1979) focused on conditions for triggering ignition on the continental slope versus ignition on the continental shelf. Ignition of currents on the continental shelf can be caused by events such as storm surges, outflow of large rivers and wave tides. Here, ignitive events occur on a small scale, with a velocity of approximately 1 m s^{-1} moving over a gradient of about 0.5°. On the continental slope the events are much larger; triggers of ignitive currents include submarine slumps, fault movements, giant eddies or tsunami surges and ignited currents move downslope with velocities greatly in excess of 1 m s^{-1} on a slope of about 3°.

1.3 Background: modelling turbidity currents

Comprehensive reviews of the literature on turbidity currents have been conducted recently by several authors including Kneller and Buckee (2000), Parsons et al. (2007) and Meiburg and Kneller (2010). A wider review on gravity cur-

rents can be found in Huppert (2006). We summarise these findings here, and refer the reader to these articles and references therein for further information.

1.3.1 Experimental models

Initial experiments on gravity currents focused on studying the behaviour of the front or the 'head' of the current (Middleton, 1966b; Britter and Simpson, 1978; Simpson and Britter, 1979). Subsequent technological advances allowed these studies to be expanded to consider the wider dynamics of the current, with the main body of the current providing a focus for some time (Parker et al., 1987; Garcia, 1994). Steady currents produced in the lab allowed measurements of the body of the flow to be taken, though for some time this process was limited due to the intrusive nature of the equipment used (Garcia, 1994). With further advances in profiling technology, such as laser Doppler Anemometry and ultrasonic Doppler velocity profiling, more and more information could be gleaned from experiments without disrupting the flow of a current downstream (Kneller et al., 1997; Best et al., 2001).

Despite the many advances in experimental technology used to examine turbidity currents, several limiting factors still remain. In particular, the type of sediment used to create the density difference in the current can be problematic. Very fine sediments can be affected by capillary forces or electrostatic forces which ultimately distort the behaviour of the sediment making it hard to directly relate experimental results to field data (Kneller and Buckee, 2000), whilst larger grain sizes may not scale correctly with the whole current behaviour (Middleton, 1966a). This problem is frequently overcome by making use of a brine solution (Pratson et al., 2001); however erosion and deposition are neglected as a result, and comparisons can only be made with very fine-grained turbidity currents.

Recently, the first results regarding ignition of a current in an experiment have been recorded. Work by Naruse et al. (2007), Sequeiros et al. (2009) and Pantin and Franklin (2011) has provided experimental justification of the self-acceleration phenomenon thought to be a distinguishing characteristic of turbidity currents (see Figure 1.6). This has allowed authors to confirm more readily the idea that ignition is connected to features in the submarine landscape, such as submarine canyons.

There is no doubt that experiments provide a vital understanding of turbidity current morphology; however it is often the case that the advantages of experi-

Figure a) is reproduced with permission. Source: Jerome Neufeld and Stephen W Morris, Nonlinear Physics, University of Toronto. http://www.flickr.com/photos/nonlin/3566826149/

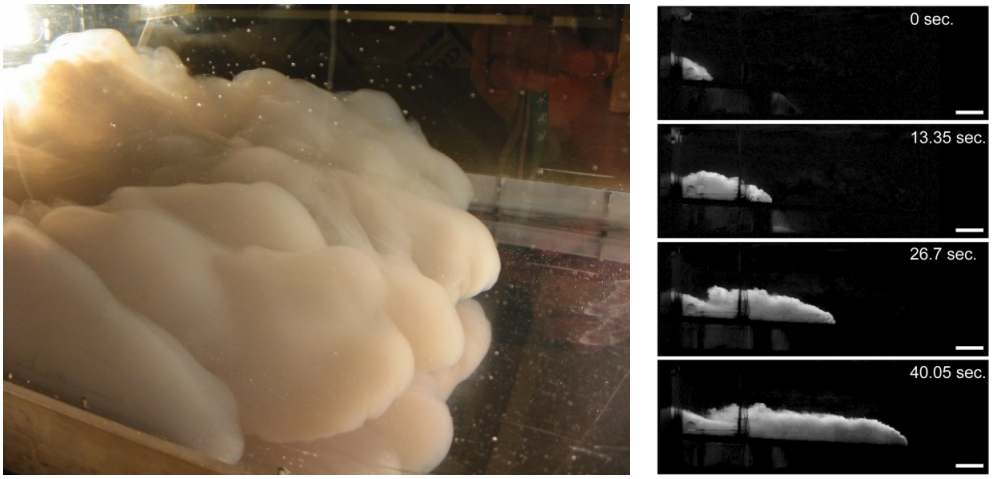

(a) Experimental turbidity current

(b) Ignition of an experimental turbidity current

Figure 1.6: Two experiments showing a turbidity current moving from left to right. Images (a) http://www.physics.utoronto.ca/~nonlin/turbidity/turbidity.html. (b) Naruse et al. (2007).

mental results are counteracted by the difficulties presented by scaling (Kneller and Buckee, 2000; Meiburg and Kneller, 2010). In addition, it is often necessary to consider only a few aspects of the flow, rather than the entire behaviour of the current, due to limitations placed on the experimental setup.

1.3.2 Theoretical models

Theoretical models for turbidity currents encompass a wide range of mathematical techniques and levels of sophistication. The most basic models are derived from dimensional analysis, and the complexity increases for 'box models', 2-dimensional depth averaged models and full 3-dimensional turbulence models.

Dimensional analysis The most basic theory for turbidity currents came about from dimensional analysis of the current and use of a result which has been much celebrated in the context of open-channel flows (Menard, 1950; Bonnecaze et al., 1993). By balancing the inertial and buoyancy forces of the flow it can be seen that the velocity of the advancing front of the current follows

$$u_f \propto \sqrt{g' h_f}, \tag{1.1}$$

where h_f is depth of the advancing front and g' is the reduced gravity

$$g' = \frac{\rho_s - \rho_l}{\rho_l} g. \tag{1.2}$$

Above, g is the gravitational acceleration, ρ_s is the density of the suspended material and ρ_l is the density of the ambient fluid. In equation (1.1) the proportionality factor is the Froude number for the flow, F, which takes a constant value of 0.7-0.8 for currents on an incline for a saline flow moving in fresh water. It has been shown by several authors (Benjamin, 1968; Middleton, 1993) that this factor varies only very slightly from this value if the slope is adjusted.

When using a basic model to consider the bulk of the flow, a Chézy-type equation is often used to model the velocity (Kuenen, 1951; Komar, 1969). This is suitable for a steady, uniform flow and takes into account the slope of the bed.

We will make use of dimensional analysis in later chapters, illustrating how a first approximation to the current behaviour can provide a great deal of information about the dynamics of the flow.

Box models Box models, or integral models, are not derived from the Navier-Stokes equations, but instead assume that a current evolves over a series of constant-area rectangles (Kneller and Buckee, 2000). This means that factors such as entrainment of the ambient fluid are ignored and the model does not account explicitly for turbulence. Box models are best suited to the study of low concentration, surge-type turbidity currents.

Box models have had relative success in comparing results to those from lock-exchange or 'dam-break' style experiments. Scaling laws that are admitted by box models have shown good comparison with experiments, particularly for currents which are governed by a balance between gravitational and inertial forces (Huppert and Simpson, 1980; Dade and Huppert, 1995). In addition, simplified box-models admit analytical solutions which can be compared with more complex shallow-water models and provide significant insight into the dynamics of the flow (Hogg et al., 2000; Harris et al., 2001).

Depth-averaged models Depth-averaged models are derived from the Navier-Stokes equations for a dilute suspension and consider vertically-averaged properties of a turbidity current (Rottman and Simpson, 1983; Parker et al., 1986; Bonnecaze et al., 1993; Huppert, 2006; Parsons et al., 2007). They typically neglect viscous forces and take the pressure to be hydrostatic, as well as pre-

suming that the current is well-mixed. This assumption is certainly suitable for fine sediment and the bulk of the flow, but is likely to be a large simplification in the later stages of the flow (Meiburg and Kneller, 2010).

Since turbidity currents are known to vary dramatically with depth, many models impose vertical profiles (or shape-factors) for the sediment concentration and velocity when deriving the model (Pantin, 1979; Parker et al., 1986; Garcia, 1994; Kneller and Buckee, 2000). Depth-averaged models are thus quasi-two-dimensional, since they account for some sort of vertical variation, but do not fully model the spatial or temporal vertical changes in the current.

Whilst depth-averaged models are not thought to precisely capture the internal dynamics of the current, they do produce relatively accurate results for the current evolution and depositional characteristics of the flow when compared to experimental data. In Section 1.4 we will outline the model of Parker et al. (1986), a depth-averaged model considering the variation of the height, velocity, sediment concentration and turbulent kinetic energy of the current. It is this particular depth-averaged model which we will proceed to study in this thesis.

Three-dimensional models In recent years the advance of large-scale computing has allowed 3-dimensional models incorporating vertical turbulence variations to be solved. Techniques such as direct numerical simulation (DNS) have allowed for in-depth studies of the interaction between a turbidity current and an erodible bed (Parsons et al., 2007; Meiburg and Kneller, 2010). DNS has also been used to look at how a turbidity current will impact upon man-made structures, a pressing question which many industrial companies wish to understand.

The disadvantages with this type of modelling lie in the high cost of the approach; these computations typically require a lot of computing power and computing time to resolve the turbulence. With several turbulence scales often involved, the resolution of the model must be very high, requiring high-speed supercomputers for optimum results. In addition to computing costs, there is still much debate regarding the proper formulation of initial and boundary conditions in numerical models for turbidity currents (Kneller and Buckee, 2000). Until these conditions can be appropriately formulated, the results of many computations, particularly near the boundary, have the potential to be unreliable.

1.4 The Parker model

The turbidity current model of Parker, Fukushima and Pantin was first introduced in the Journal of Fluid Mechanics in their 1986 paper *Self-accelerating turbidity currents*. The model describes conservation of mass, momentum, sediment concentration and turbulent kinetic energy in terms of the current height, and the depth-averaged quantities of velocity, sediment concentration and turbulent kinetic energy. The model is an improvement upon an earlier 3-equation model which did not have a description of conservation of turbulent kinetic energy. For details of the 3-equation model, the reader is referred to Parker (1982) and analysis by Zammett (2008). We refer to the Parker, Fukushima and Pantin 4-equation model as 'the Parker model' herein.

We present the geometry of a turbidity current in Figure 1.7. The current has a depth h, volumetric sediment concentration c, velocity u and turbulent kinetic energy k. It flows down a slope of angle θ and we suppose that the flow is approximately uni-directional; x marks the distance downslope. The derivation of the model from the equations of motion for a dilute suspension is outlined in full detail in Appendix A.1. of Parker et al. (1986).

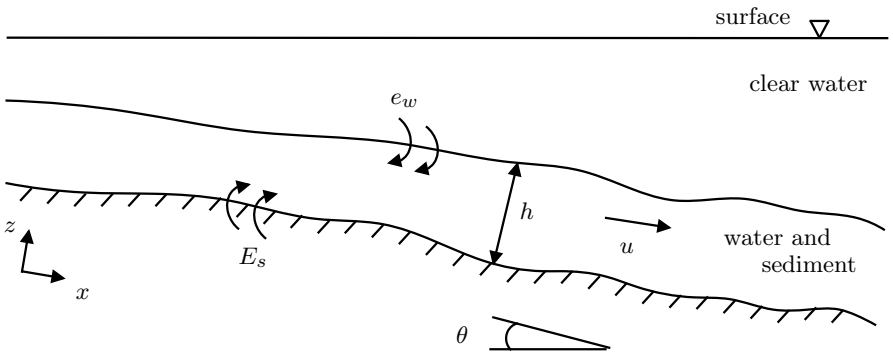

Figure 1.7: Downstream geometry of a turbidity current

The Parker model begins with an equation for the conservation of fluid mass

$$\frac{\partial h}{\partial t} + \frac{\partial (hu)}{\partial x} = e_w u, \tag{1.3}$$

where e_w is an empirical function derived by Parker et al. (1986) which describes the entrainment of clear ocean water into the turbidity current.

The second equation in the model describes the conservation of momentum in

the downstream direction:

$$\frac{\partial(hu)}{\partial t} + \frac{\partial(hu^2)}{\partial x} = -\frac{1}{2}Rg\frac{\partial(h^2c)}{\partial x} + RgShc - u_s^2. \quad (\mathbf{1.4})$$

Here, $S = \sin\theta$ is the underlying slope. The excess density, R, is defined by

$$R = \frac{\rho_s - \rho_l}{\rho_s}, \quad (\mathbf{1.5})$$

where ρ_s and ρ_l are the density of the sediment and the fluid respectively. The acceleration due to gravity is denoted by g and u_s is the friction velocity which is given by

$$u_s^2 = \frac{\tau}{\rho_l}, \quad (\mathbf{1.6})$$

where τ is the boundary shear stress. The first term on the right hand side of (1.4) is the pressure gradient term, the second term is the downslope component of the buoyancy and the third term represents the loss of momentum due to friction at the base of the turbidity current.

The third equation in the Parker model describes the conservation of sediment in the current:

$$\frac{\partial(hc)}{\partial t} + \frac{\partial(huc)}{\partial x} = v_s(E_s - r_0c). \quad (\mathbf{1.7})$$

Here, v_s is the sediment settling velocity, E_s is a dimensionless erosion rate coefficient and r_0 is a dimensionless coefficient representing the ratio of near bed sediment concentration to the average current sediment concentration. The amount of sediment in the turbidity current is increased or decreased depending on whether the current is eroding or depositing sediment at its base. The erosion rate of particles from the bed is the product v_sE_s.

The fourth equation describes the evolution of the turbulent kinetic energy of the flow, where k is the turbulent kinetic energy per unit mass:

$$\frac{\partial(kh)}{\partial t}+\frac{\partial(khu)}{\partial x} = u_s^2u-\varepsilon_0h+\frac{1}{2}u^3e_w-\frac{Rgh}{2}\left(2v_sc+cue_w+v_s(E_s-r_0c)\right). \quad (\mathbf{1.8})$$

Here, ε_0 is the layer-averaged mean rate of dissipation of turbulent kintic energy due to viscosity. A widely used means of describing ε_0, which is adopted by Parker et al. (1986), is

$$\varepsilon_0 = \beta\frac{k^{3/2}}{h}, \quad (\mathbf{1.9})$$

where β is a dimensionless dissipation rate coefficient. In equation (1.8), the first and third terms on the right hand side represent the rate at which kinetic

energy is produced, and the final terms are the work done against the density gradient, quantifying the effect of sediment-induced stratification.

1.4.1 Drag at the base of the current

In equation (1.4) we introduced the friction velocity, u_s. In the 3-equation model of Parker (1982) the friction velocity is simply parameterised by

$$u_s^2 = c_D u^2, \tag{1.10}$$

where c_D is a constant turbulent drag coefficient. However, following the inclusion of the equation for turbulent kinetic energy (1.8) the turbulent drag coefficient no longer need be a constant in time or space and it becomes a function of u and k, given by (Parker et al., 1986)

$$c_D = \frac{\alpha k}{u^2}. \tag{1.11}$$

Using this form of the turbulent drag in equation (1.10), the friction velocity becomes a function of turbulent kinetic energy,

$$u_s^2 = \alpha k, \tag{1.12}$$

where α is a dimensionless coefficient determined empirically (Parker et al., 1986). The parameterization of u_s in terms of k couples the turbulent kinetic energy equation (1.8) to the three other equations in the model, (1.3), (1.4), (1.7).

1.4.2 Erosion of sediment at the base of the current

In the Parker model the turbidity current is free to pick up loose sediment from the bed and incorporate it into the current. We refer to this process as 'erosion', and it is parameterised by the erosion rate coefficient, E_s, which is a function of the friction velocity. Whilst we call this process 'erosion', we in fact mean entrainment of loose material on the bed, rather than the active process of eroding the bed rock. The term erosion will be used throughout this thesis to differentiate it clearly from the process of entrainment of clear water at the top of the current.

Parker uses the friction velocity to parameterise the erosion rate coefficient, but

from equation (1.12) we can write it as a function of the turbulent kinetic energy,

$$E_s = E_s(k), \tag{1.13}$$

where

$$E_s(k) = \begin{cases} 0.3 & \text{if } Z \geq Z_m \\ 0 & \text{if } Z < Z_m, \end{cases} \tag{1.14}$$

and

$$Z = \sqrt{R_p}\frac{(\alpha k)^{1/2}}{v_s}. \tag{1.15}$$

Hence, Z is a measure of how easily particles are eroded from the bed compared to how quickly they settle out of suspension. The erosion rate coefficient of Parker is adapted from the empirical relation of Akiyama and Fukushima[2] used in the study of open-channel suspensions in flumes and rivers. The parameter Z_m is experimentally determined to take the value $Z_m = 13.2$ (Parker et al., 1986). When $Z > Z_m$ erosion is dominant in the model and when $Z < Z_m$ the settling out of particles from the current is the dominant process.

The settling velocity, v_s is given by the Stokes settling velocity,

$$v_s = \frac{(\rho_s - \rho_l)gD_s^2}{18\eta}, \tag{1.16}$$

where η is the dynamic viscosity of clear water (*e.g.* Batchelor (1967)). The particle Reynolds number is given by R_p and defined as

$$R_p = \frac{(Rg)^{1/2}D_s^{3/2}}{\nu_w}, \tag{1.17}$$

where D_s is a typical particle diameter and $\nu_w = \eta/\rho_l$ is the kinematic viscosity of clear water (*e.g.* Fowler (2011)).

1.4.3 Entrainment of ocean water

In equation (1.3) we introduce the entrainment rate e_w. This relation is derived empirically by Parker et al. (1986) and given by

$$e_w = \frac{p}{m + Ri}, \tag{1.18}$$

[2]Reference of Parker et al. (1986): 'Akiyama and Fukushima (1985). Entrainment of noncohesive bed sediment into suspension. *External memo*'. Not publically available.

where $p = 0.0015$ and $m = 0.02$ are empirically determined constants and Ri is the Richardson number defined by

$$Ri = \frac{Rgch}{u^2}. \tag{1.19}$$

The Richardson number is the ratio of potential to kinetic energy in the flow. If $Ri \ll 1$ then the kinetic energy is dominant and buoyancy is negligible. If $Ri \gg 1$, buoyancy is important as there is not enough kinetic energy available to homogenise the flow.

1.4.4 Ignition and the Parker model

The equations above for mass conservation (1.3), momentum conservation (1.4) and sediment conservation (1.7) form Parker's three equation model (Parker, 1982) and were originally used as a model for turbidity currents. However, analysis showed that the system predicted that erosive turbidity currents would 'ignite' unboundedly, that is, the velocity of the current would become unbounded as it moves downstream. Ignition occurs because of the positive feedback between erosion at the base of a turbidity current and the current velocity. As the current erodes more sediment, the bulk sediment concentration increases which causes the velocity to increase as the extra mass in the current drives the current downstream. It has been shown experimentally that this increase in velocity causes the erosion rate to increase, resulting in a positive feedback. In reality, ignition will not occur indefinitely and a turbidity current eventually becomes extinct, thus a fourth equation was introduced to the Parker model in an attempt to control ignition.

By introducing an equation for turbulent energy it is expected that eventually the amount of turbulent energy produced by the current would be exceeded by the amount expended working against buoyancy forces. In this case the turbulent energy would die out and the turbidity current would become extinct.

In this thesis we will define the current to be in an 'ignitive' state when erosion is occurring, u and c are increasing and k is positive. We define 'ignition' to be the point at which the ignitive state begins. The current will be defined as 'extinct' when the current has stopped eroding and c and u are decreasing to zero.

1.5 Thesis overview

The structure of this thesis is as follows. In Chapter 2 we nondimensionalise the model and examine the steady state. We use phase plane analysis to consider the conditions under which a current will ignite or become extinct. We then reduce the model to a one-equation velocity model to examine erosive and depositional currents, and look at how the velocity interacts with the slope, S.

In Chapter 3 we examine another nondimensionalisation for the model, which accounts for a large downstream length scale. We reduce the model to a system of two equations by parameterising k with respect to u and assuming c to be constant. The two-equation model is similar to the St. Venant or 'shallow-water' water equations for thin fluid flows (*e.g.* Whitham (1974)). We make use of the method of characteristics to solve the model and to understand how the current evolves in time and space over a constant, and a varying, downstream slope, identifying supercritical and subcritical flow regimes. We conclude by providing a discussion of the simplifying assumptions used in this chapter.

In Chapter 4 we return to the full model by reintroducing k and c into our analysis. These two variables are simply parameterised in Chapters 2 and 3, but they are key to a true understanding of ignition and extinction. By making use of small parameters in the model consider an equilibrium model of turbulent kinetic energy, though we find that this model breaks down as $k \to 0$. We examine the full turbulent kinetic energy equation, addressing modelling questions not considered by Parker et al. (1986) and find that the equation breaks down catastrophically, predicting complex-valued solutions for k when the density term in equation (1.8) becomes large. In order to overcome this failure, we provide a model which considers two regimes: one turbulent and one stably stratified. We perform some simple calculations with this model and consider further modelling questions surrounding the understanding of turbulent kinetic energy and erosion.

In Chapter 5, we numerically solve some simple case studies using the model of Chapter 4. This includes examining a 'slumping' avalanche problem and a fluvial 'steady inflow problem' for different slope profiles and realistic initial and boundary conditions.

We conclude with a discussion chapter, which provides a thorough review of the work covered in this thesis as considering possible extensions to the model proposed in Chapters 4 and 5.

1.5.1 Statement of originality

Chapter 2 reconsiders work of Zammett (2008), though unlike Zammett we begin by looking at a very large downstream length scale in our analysis of the steady state model. Chapter 3 provides an original discussion of a shallow-water model for turbidity currents, with the analytical consideration of shocks, boundary layers and current-slope interactions being new. Chapter 4 addresses, in-depth, modelling questions regarding the complete 4-equation model, which have not been considered by Parker et al. (1986) or other authors before. This chapter identifies that the Parker model fails to provide a real-valued solution for all possible values of the variables. A new 'transition' model is proposed, which is an adaptation of the Parker model, and provides a switch between a turbulent and stably stratified regime. Finally, the work of Chapter 5 is an extension of Chapter 4, testing the model for various basic case studies as well as considering how the model presented in this thesis helps to provide an understanding of the extinctive and ignitive behaviour of turbidity currents.

Chapter 2

The one-equation velocity model

In this chapter we explore the phenomenon of self-acceleration or 'ignition' using a simple velocity model. The mathematics of ignition was looked at in detail by Zammett (2008). Following Zammett, we begin by considering the conditions for ignition in the steady state. This will provide some insight into the interaction of the velocity with the gradient of the bed. Unlike Zammett, however, we will look at the effect of a very large downstream length scale in our analysis of the steady state model.

Following the steady state analysis we move on to consider the time-dependent equations. We reduce the model to only one equation by making assumptions about the variables h, c and k in order to focus on the behaviour of the velocity. This one-equation velocity model can be separated into erosional and depositional models which we look at independently. Both models are solved using the method of characteristics, which allows us to examine shock formation and propagation. We conclude by considering a simple varying slope profile, to demonstrate the interaction between the velocity and the slope.

2.1 Nondimensionalisation

We will start by deriving a nondimensional form of the Parker model. We assume that v_s, r_0, R and g are constant (typical values are given in Table 2.2) and we allow S to vary slowly downstream. The erosion rate, E_s, friction velocity, u_s, and turbulent kinetic energy, k are nondimensionalised as follows

$$E_s = E_0 E^\star, \quad u_s = u_s^0 u_s^\star, \quad k = k_0 k^\star. \tag{2.1}$$

In this notation, the letter with the zero subscript represents the scale and the starred letter represents the dimensionless value. We will specify that erosion 'switches on' at $k^\star = 1$, at which point $E^\star = 1$. Hence, we choose $E_0 = 0.3$ and from equation (1.14) we find

$$k_0 = \frac{(Z_m v_s)^2}{R_p \alpha}. \tag{2.2}$$

From equations (1.12) and (2.2), the scale for the friction velocity is found to be

$$u_s^0 = \frac{Z_m v_s}{\sqrt{R_p}}. \tag{2.3}$$

We now consider equations (1.3), (1.4), (1.7) and (1.8). We assume a balance between (*i*) the left- and right-hand sides of equation (1.3); (*ii*) the forcing term and the friction term in equation (1.4); (*iii*) the erosion and deposition terms in equation (1.7) and (*iv*) the first two terms on the right-hand side of equation (1.8). The slope is nondimensionalised as $S = S_0 S^\star$, where the slope scale is given as

$$S_0 = 0.05, \tag{2.4}$$

and corresponds to the typical gradient of the continental slope; $\theta = 3^\circ$. The remaining variables are nondimensionalised in the following way

$$h = h_0 h^\star, \quad u = u_0 u^\star, \quad c = c_0 c^\star, \quad x = x_0 x^\star, \quad t = t_0 t^\star, \quad e_w = e_0 e^\star. \tag{2.5}$$

The balances outlined above determine the following scales:

$$x_0 = \frac{Z_m^2 v_s^2 r_0 c_{D0}}{R_p R g S_0^2 E_0 p}, \qquad u_0 = \frac{Z_m v_s}{\sqrt{R_p c_{D0}}}, \qquad c_0 = \frac{E_0}{r_0}, \tag{2.6a}$$

$$t_0 = \frac{x_0}{u_0} = \frac{r_0 c_{D0}^{3/2}}{\sqrt{R_p} R g S_0^2 E_0 p}, \qquad h_0 = x_0 e_0 = \frac{Z_m^2 v_s^2 r_0}{R_p R g S_0 E_0}. \tag{2.6b}$$

After dropping the stars from $h^\star$, $u^\star$ $c^\star$ and $k^\star$, we find that the dimensionless

Parker model is given by

$$\frac{\partial h}{\partial t} + \frac{\partial (hu)}{\partial x} = e^\star u, \tag{2.7a}$$

$$\Lambda \left[\frac{\partial (hu)}{\partial t} + \frac{\partial (hu^2)}{\partial x} \right] = -\frac{1}{2}\delta \frac{\partial (h^2 c)}{\partial x} + Shc - k, \tag{2.7b}$$

$$\gamma \left[\frac{\partial (hc)}{\partial t} + \frac{\partial (huc)}{\partial x} \right] = E^\star - c, \tag{2.7c}$$

$$\Gamma \left[\frac{\partial (kh)}{\partial t} + \frac{\partial (khu)}{\partial x} \right] = ku - k^{3/2} + \frac{\Lambda}{2} u^3 e^\star - \frac{\delta h}{2} \left(\frac{2c}{\gamma r_0} + cue^\star + \frac{E^\star - c}{\gamma} \right), \tag{2.7d}$$

with parameters

$$\Lambda = \frac{pS_0}{c_{D0}^2}, \qquad \delta = \frac{p}{c_{D0}}, \qquad \gamma = \frac{Z_m p S_0}{r_0 c_{D0}^{3/2} \sqrt{R_p}}, \qquad \Gamma = \frac{pS_0}{c_{D0}\alpha}. \tag{2.8}$$

The typical values of the scales and parameters are shown in Table 2.1.

Scale or parameter	Value
x_0	1.2 m
t_0	11 s
h_0	0.023 m
u_0	0.94 m s^{-1}
c_0	0.19
k_0	0.035 m^2 s^{-2}
u_s^0	0.059 m s^{-1}
E_0	0.3
S_0	0.05
e_0	0.019
Ri_0	0.08
ν	0.25
γ	1.2
δ	0.4
Λ	4.7
Γ	0.2

Table 2.1: Values of scales and dimensionless parameters of the model.

The turbulent drag relation is given in equation (1.11). It is nondimensionalised as $c_D = c_{D0} c_D^\star$ where the scale is chosen to be $c_{D0} = 0.004$, after Parker et al.

(1986). This defines the dissipation rate β,

$$\beta = \frac{\alpha^{3/2}}{c_{D0}^{1/2}} = 0.5. \tag{2.9}$$

and with the star dropped from $c_D^\star$, the nondimensional turbulent drag rate is given by

$$c_D = \frac{k}{u^2}. \tag{2.10}$$

The dimensionless friction velocity is given as

$$u_\star^2 = k, \tag{2.11}$$

the dimensionless erosion rate is

$$E^\star = \begin{cases} 1 & \text{if } k \geq 1, \\ 0 & \text{if } k < 1, \end{cases} \tag{2.12}$$

and the nondimensional entrainment rate is given by

$$e^\star = \frac{u^2}{ch + \nu u^2}. \tag{2.13}$$

The dimensionless parameter ν is defined as

$$\nu = \frac{mS_0}{c_{D0}}, \tag{2.14}$$

the entrainment rate coefficient scale is

$$e_0 = \frac{pS_0}{c_{D0}},$$

and Ri_0 is the scale of the Richardson number, given by

$$Ri_0 = \frac{Rgc_0h_0}{u_0^2} = \frac{c_{D0}}{S_0}. \tag{2.15}$$

2.1.1 Comment on the nondimensionalisation

This nondimensionalisation was chosen to balance erosion and deposition in equation (1.2) and to set the erosion rate at $E^\star = 1$ when $k = 1$. As a result, the intrinsic length scale, x_0, which comes from the nondimensionalisation, is very small and bears minimal relation to reality; a turbidity current has a typ-

Symbol	Description	Typical Value
ρ_s	density of sediment	2.7×10^3 kg m^{-3} ‡
ρ_l	density of interstitial fluid	1×10^3 kg m^{-3}
R	excess density	1.7
r_0	basal concentration ratio	1.6 †
c_{D0}	dimensionless drag coefficient	0.004 †
α	empirical friction parameter	0.1 †
g	gravitational acceleration	9.8 m s^{-2}
ν_w	kinematic viscosity of water	1×10^{-6} m^2 s^{-1}
η	dynamic viscosity of water	1×10^{-3} Pa s
D_s	particle diameter	1×10^{-4} m ‡
R_p	particle Reynolds number	4
v_s	settling velocity	9×10^{-3} m s^{-1}
p	numerically determined constant	0.0015 †
m	numerically determined constant	0.02 †

Table 2.2: Values of constants and parameters. Constants labelled by † are taken from Parker et al. (1986), and those labelled by ‡ from Zammett (2008).

ical runout length in the order of 100s of kilometres. In addition, the sediment concentration scale, c_0, is much too high for the length scales that we are considering whilst t_0 and u_0 are unrealistically small for a large ignitive turbidity current.

In the next section we perform a rescaling to derive a more realistic length scale and velocity scale for the model and we consider what effect this has upon the analysis considered by Zammett (2008).

2.2 Steady state solutions

We consider the steady state version of equations (2.7). The flux of sediment is defined as $q = hu$. From equation (2.7a) we see that q is an increasing function of x, and so we use q as a surrogate space variable. This gives us three equations:

$$\Lambda q\frac{du}{dq} = -\Lambda u - \frac{1}{2}\delta\frac{d}{dq}\left(\frac{q^2c}{u^2}\right) + \left(\frac{cq+\nu u^3}{u^4}\right)\left(\frac{Sqc}{u} - k\right), \tag{2.16a}$$

$$q\frac{dc}{dq} = \frac{(cq+\nu u^3)(E^\star - c)}{\gamma u^4} - c, \tag{2.16b}$$

$$\Gamma q\frac{dk}{dq} = -\Gamma k + \frac{\Lambda}{2}u^2 - \frac{\delta qc}{2u} + \left(ku - k^{3/2} - \frac{\delta q}{\gamma u}\left(\frac{c}{r_0} + \frac{E^\star - c}{2}\right)\right)\left(\frac{cq+\nu u^3}{u^4}\right). \tag{2.16c}$$

For erosive currents we can assume that the initial concentration of sediment in the current will be high and under the assumption of a long length scale and high turbidity flux, we take $c = 1$. If a turbidity current is triggered by a submarine avalanche we can expect the initial flux of sediment to be very large. Typically, for a length scale of order 100 km we would expect a (dimensionless) turbidity flux of order $q \sim \mathcal{O}(10^5)$. Equation (2.13) tells us that $u \sim q^{1/3}$ and equation (2.10) that $k \sim u^2$ so we make a change of variables

$$U = q^{-1/3}u, \qquad \text{and} \qquad K = q^{-2/3}k. \tag{2.17}$$

If $U \sim \mathcal{O}(1)$, then this corresponds to a dimensional current velocity of 43 m s^{-1}, and $x \sim \mathcal{O}(1)$ corresponds to a dimensional downstream length scale of 120 km, which are physically realistic values for a large, erosive current. In addition, the change of variables above suggests that $h \sim O(q^{2/3}) \approx 50$ m, again, a physically realistic scale. Hence, these rescalings are suitable for the type of ocean turbidity current we wish to consider. This modifies equations (2.16) to

$$q\frac{d(Uq^{1/3})}{dq}\left(\Lambda - \frac{\delta}{U^3}\right) = -\Lambda U q^{1/3} - \frac{\delta q^{1/3}}{U^2} + \left(\frac{1+\nu U^3}{U^4}\right)\left(\frac{S}{U} - K\right)q^{1/3}, \tag{2.18a}$$

$$\Gamma q\frac{d(Kq^{2/3})}{dq} = -\Gamma K q^{2/3} + \frac{\Lambda}{2}U^2 q^{2/3} - \frac{\delta}{2U}q^{2/3} + (KU - K^{3/2})\left(\frac{1+\nu U^3}{U^4}\right)q^{2/3} - \frac{\delta}{\gamma}q^{1/3}\left(\frac{1}{r_0} + \frac{E^\star - 1}{2}\right)\left(\frac{1+\nu U^3}{U^4}\right). \tag{2.18b}$$

Looking at the relative size of terms on the right hand side of equation (2.18b) we discard terms of order $q^{1/3}$, which are small when compared to the terms of order $q^{2/3}$.

We now make a further change of variables, introducing a new independent variable s, defined by $s = \ln q$. Since $q \sim \mathcal{O}(10^5)$ we will have $s \sim \mathcal{O}(10)$.

Equations (2.18) now become two autonomous equations for U and K, namely

$$\frac{dU}{ds}\left(\Lambda - \frac{\delta}{U^3}\right) = -\frac{\delta}{U^2} + \left(\frac{1+\nu U^3}{U^4}\right)\left(\frac{S}{U} - K\right) - \frac{U}{3}\left(4\Lambda - \frac{\delta}{U^3}\right), \quad \textbf{(2.19a)}$$

$$\Gamma\frac{dK}{ds} = -\frac{5}{3}\Gamma K + \frac{\Lambda}{2}U^2 - \frac{\delta}{2U} + (KU - K^{3/2})\left(\frac{1+\nu U^3}{U^4}\right). \quad \textbf{(2.19b)}$$

Equations (2.19) are now examined using phase plane analysis.

2.2.1 Phase plane analysis

Figure 2.1 shows a phase portrait of the system. A pseudo saddle point[1] is marked by a black dot at $\psi = (0.42, 2.2)$, and another black dot marks the spiral sink at $\mathbf{\Sigma} = (0.66, 0.65)$, (for these parameter values). The vertical red dashed line in the centre of the phase plane marks the 'ignition line'. The nullclines are shown as red dashed curves.

We mark the extinctive and ignitive regions of the phase plane at the top of Figure 2.1. In the extinctive region, trajectories terminate at $(U, K) = (0, 0)$. In the ignitive region, trajectories terminate at the spiral sink, $\mathbf{\Sigma}$. There is a third region which we call the 'ignition line' region where trajectories terminate on the vertical red dashed line above ψ or emanate from the ignition line below ψ. The ignition line is the region where the wave speed is equal to zero, when $U = U_c$, where we define

$$U_c = \left(\frac{\delta}{\Lambda}\right)^{1/3}. \quad \textbf{(2.20)}$$

In the following subsections three types of behaviour are examined; extinction, ignition and 'ignition line behaviour'.

2.2.1.1 Extinction

Trajectories that begin in the extinctive region of the phase plane (to the left of the upper separatrix of the pseudo-saddle point and the ignition line below the pseudo-saddle point) reach $k = 1$, or $K \sim 10^{-4}$, in finite distance. From the definition of $E^\star$, (2.12), it is evident that at $k = 1$ erosion will switch off.

[1] A pseudo saddle point acts as both a source and a sink, but exhibits the dynamic properties of a saddle. We can see this in Figure 2.1; the upper separatrices of the pseudo saddle point terminate at ψ. The lower separatrices of the pseudo saddle point emanate from ψ. Trajectories nearby ψ behave like near the saddle point of a smooth system (Venkatasubramanian et al., 1995).

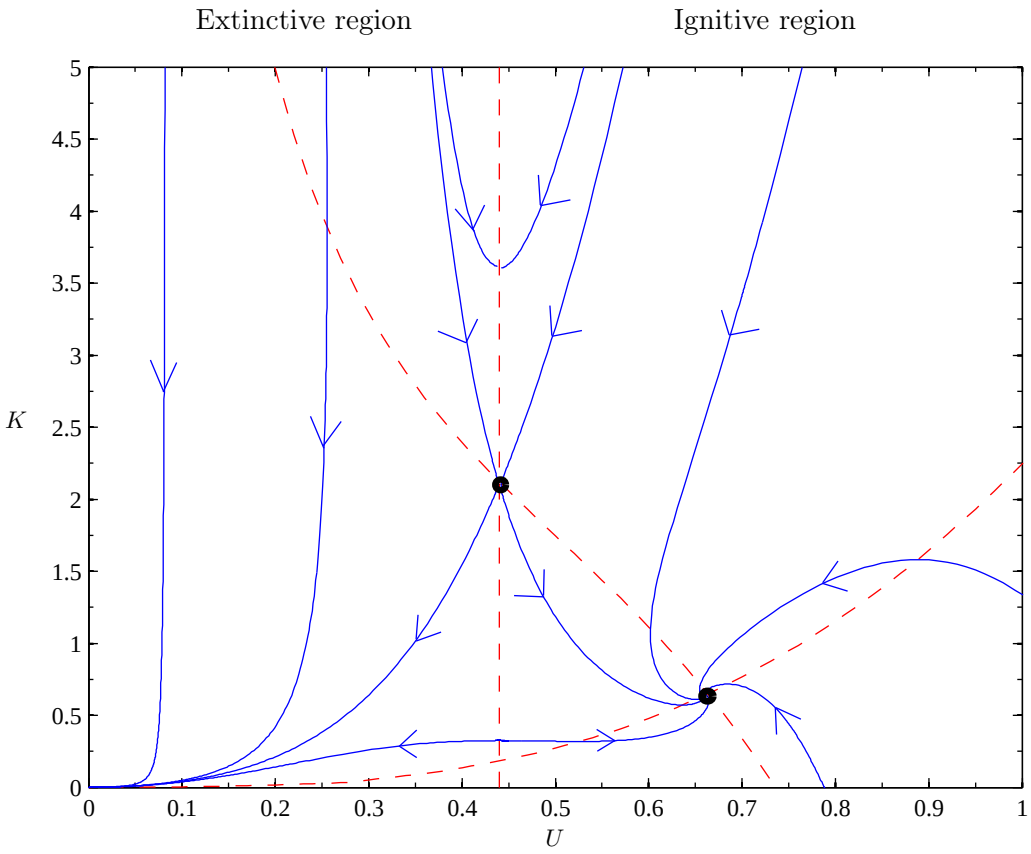

Figure 2.1: The (U, K) phase plane for equations (2.19). The vertical dashed line is the 'ignition line' at $U_c = \left(\frac{\delta}{\Lambda}\right)^{1/3}$; the curved dashed lines show the nullclines. The black circle at $\psi = (0.44, 2.2)$ marks the pseudo-saddle point and the black circle at $\mathbf{\Sigma} = (0.66, 0.65)$ marks the spiral sink. Parameter values are $\Lambda = 4.7$, $\delta = 0.4$, $\Gamma = 0.2$, $\nu = 0.25$, $S = 1$. The arrows indicate trajectory direction.

In order to consider the depositional regime where c is decreasing, we return to equations (2.16) where the sediment concentration, c, is a variable, and set $E^\star = 0$. Equation (2.16b) becomes

$$q\frac{dc}{dq} = -c\left(\frac{cq + \nu u^3}{\gamma u^4} + 1\right), \tag{2.21}$$

or, after the change of variables (2.17),

$$\frac{dc}{ds} = -c\left(\frac{c + \nu U^3}{\gamma U^4 e^{s/3}} + 1\right), \tag{2.22}$$

and equations (2.19) for variable c are given by

$$\frac{dU}{ds}\left(\Lambda - \frac{c\delta}{U^3}\right) = -\frac{c\delta}{U^2} + \left(\frac{c + \nu U^3}{U^4}\right)\left(\frac{Sc}{U} - K\right) - \frac{U}{3}\left(4\Lambda - \frac{c\delta}{U^3}\right), \tag{2.23a}$$

$$\Gamma\frac{dK}{ds} = -\frac{5}{3}\Gamma K + \frac{\Lambda}{2}U^2 - \frac{c\delta}{2U} + (KU - K^{3/2})\left(\frac{c + \nu U^3}{U^4}\right). \tag{2.23b}$$

The only non-negative equilibrium solution to equation (2.22) occurs at $c = 0$ and so we conclude that the sediment concentration of the current will rapidly approach zero once $E^\star = 0$. Once $c = 0$, the current has become extinct. We show an example of one such extinction in Figure 2.2.

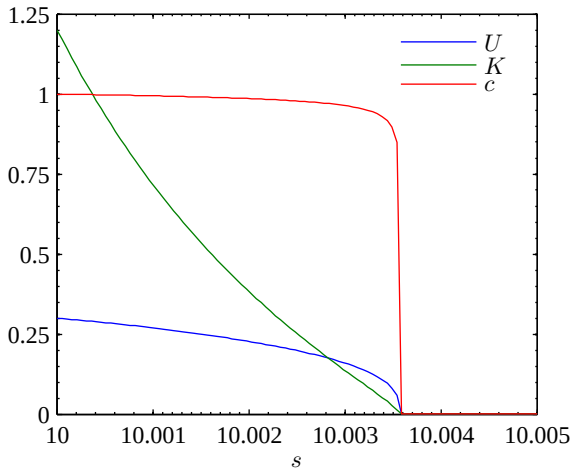

Figure 2.2: Solution of equations (2.22) – (2.23). Parameter values are given in Figure 2.1 and the initial conditions were $U = 0.3$, $K = 1.2$, $c = 1$.

We want to calculate the distance over which the current becomes extinct. To do this we use the definition of s ($s = \ln q$) and the steady state mass conservation

equation:

$$\frac{dq}{dx} = e^\star u. \tag{2.24}$$

A change of variables yields,

$$\frac{1}{s}\frac{ds}{dx} = \frac{u^4}{ce^s + \nu u^3}, \tag{2.25}$$

and upon integrating we find

$$x = \int_{s_0}^{s} \frac{ce^{s'} + \nu u^3}{s' u^4}\, ds', \tag{2.26}$$

where $s = s_0$ at $x = 0$.

From the numerical results it can be seen that c and u reach zero at a point $s = s_\infty$ downstream, which corresponds to a value $q = q_\infty$ where

$$s_\infty = \ln q_\infty. \tag{2.27}$$

As $s \to s_\infty$, the erosion has switched off, $E^\star = 0$, and thus $k = 0$. We consider the steady state conservation of sediment equation (2.7c) at this point, namely

$$\gamma q_\infty \frac{dc}{dx} = -c. \tag{2.28}$$

Hence, we find that c approaches zero like

$$c \sim A_1 \exp\left(-\frac{x}{q_\infty \gamma}\right) \quad \text{as} \quad x \to \infty, \tag{2.29}$$

for some constant, A_1.

We next consider the steady state momentum equation (2.7b):

$$\Lambda q_\infty \frac{du}{dx} = -\frac{\delta}{2} q_\infty^2 \frac{d}{dx}\left(\frac{c}{u^2}\right) + \frac{S q_\infty c}{u}. \tag{2.30}$$

As $u \to 0$ and $c \to 0$, we find that the dominant term is the term proportional to δ on the right-hand side, thus

$$\frac{c}{u^2} \sim A_2, \tag{2.31}$$

for some constant, A_2, and, hence, u approaches zero like

$$u \sim A_3 \exp\left(-\frac{x}{2q_\infty \gamma}\right), \tag{2.32}$$

where $A_3 = \sqrt{A_1 A_2}$.

We now consider the steady state mass conservation equation (2.24). Using the equations (2.29) and (2.32) this becomes

$$\frac{dq}{dx} \sim \frac{u^4}{cq_\infty + \nu u^3}, \tag{**2.33a**}$$

$$\sim \frac{A_4 c}{1 + A_5 c^{1/2}} \to 0 \qquad \text{as} \qquad x \to \infty, \tag{**2.33b**}$$

for constants $A_4 = A_2^2/q_\infty$ and $A_5 = \nu A_2^{3/2}/q_\infty$. If $q_x \to 0$ as $x \to \infty$, this is consistent with our assumption that $q \to \text{constant} = q_\infty$ as $x \to \infty$.

We briefly consider $h = q/u$. Since $u \to 0$, we will clearly have $h \to \infty$ as $x \to \infty$. We can interpret this as the current layer becoming well mixed with the ocean layer above it.

From the analysis in this section, we conclude that turbidity currents in the extinctive region of the phase plane will indeed die out.

2.2.1.2 Ignition

All trajectories that begin in the ignitive region of the phase plane, below the upper separatrix of the pseudo saddle point and to the right of the ignition line, terminate at $\mathbf{\Sigma}$, the spiral sink. Properties of this steady state situation are now looked at in more detail.

At the spiral sink, U and K have reached constant values which depend on the size of the source term in equation (2.19a); however we always find that $U, K > 0$ at the spiral sink. The current is said to be igniting if a trajectory in the phase plane is approaching the spiral sink because the values of velocity and turbulent kinetic energy at $\mathbf{\Sigma}$ are constant, meaning the current will propagate forever. The source term is proportional to S and can only decrease if the downstream slope decreases, since $c = 1$. We show the dependence of the steady state values of U and K upon S in Figure 2.3.

As S is increased from one, the steady state values of U and K increase, as might be expected if the underlying slope steepens. As S is decreased from one, the values of U and K in the steady state also decrease. For the chosen parameter values there is a critical value $S = S_c \approx 0.147$. At this point the spiral sink disappears in a saddle-node bifurcation. We will see that this critical slope is greatly significant in later chapters, particularly in the unsteady solutions of the

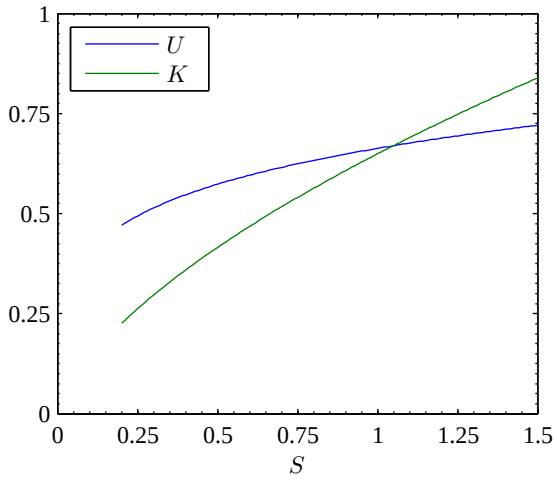

Figure 2.3: The steady state values of U and K in the ignitive region of the phase plane as a function of the bed slope S. The steady state equations are given by (2.19). Parameter values are given in Figure 2.1.

two-equation model in Chapter 3.

Figure 2.4 shows the phase portrait for the system (2.19), when $S < S_c$. There is now a single saddle point in the phase plane located at $(U, K) = (0.4, 0.14)$, (for the parameter values we have chosen). Only two types of trajectory behaviour can now be seen; extinction and termination on the ignition line. The region of ignition has been eliminated by removing the steady state from the system.

By adjusting the slope such that $S < S_c$ we have eliminated the region containing the spiral sink which corresponded to turbidity currents which would ignite. The critical value S_c corresponds to a real slope of $0.42°$. In Chapter 1 we looked at the typical geometry of the seafloor (Figure 1.2). We recall now that the continental slope, where ignition begins, has a typical slope of $1° - 10°$. The continental rise, where an ignited current runs out, has a typical slope of $0.5° - 1°$. The abyssal plain, where extinction occurs and the sediment in the current spreads out in a deposit termed a deep sea fan, has a slope of less than $0.5°$. In fact, the gradient of the abyssal plain is likely to be as low as 1:10 000; a slope of $0.005°$.

The steady state model suggests that ignition is closely linked to the slope of the sea floor; currents will only ignite under the right initial conditions and on a sufficiently steep slope. Given the assumption that the gradient of the bed decreases with distance downstream, we conclude that ignition will be eliminated as a current moves downstream.

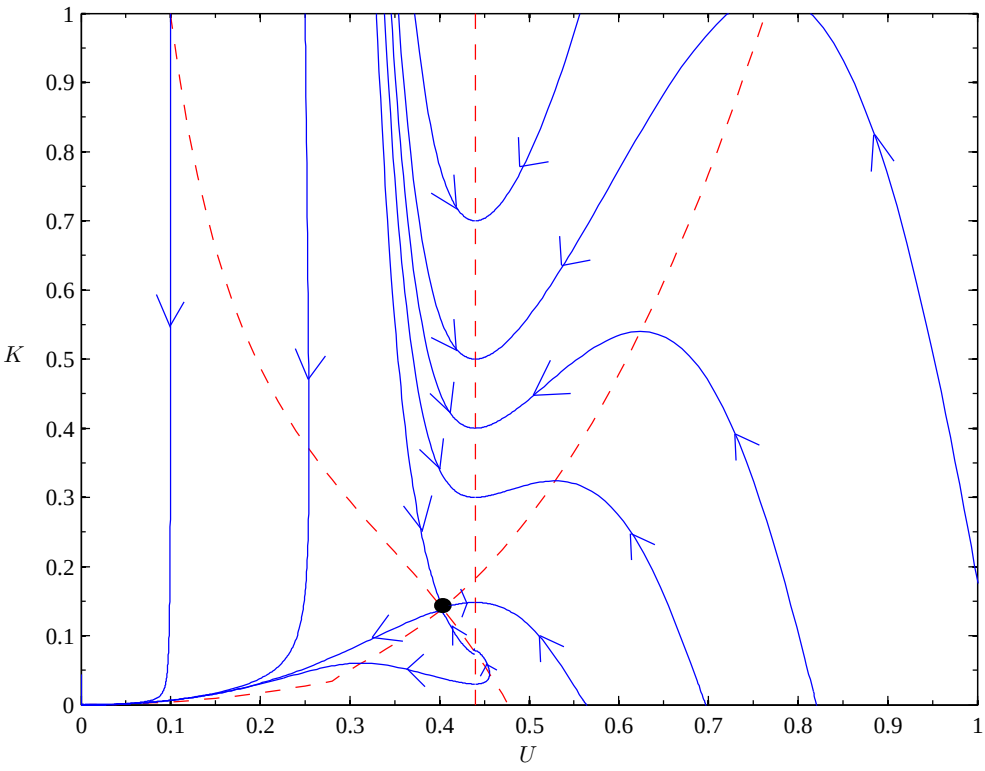

Figure 2.4: The (U, K) phase plane for equations (2.19). Here, $S < S_c$, in particular, $S = 0.1$. The vertical red dashed line marks the ignition line at $U_c = \left(\frac{\delta}{\Lambda}\right)^{1/3}$ and the curved red dashed lines mark the nullclines. Parameter values are given in Figure 2.1. The arrows indicate trajectory direction.

2.2.1.3 The ignition line

We have shown in the previous sections that the slope of the seafloor influences the process of ignition, but that we always have a region of extinction regardless of the value of the slope. That is to say that not every initial condition will ignite. We require U and K to be sufficiently large to see ignition in the system.

In addition, in each of the phase portraits plotted, there is always a region where the trajectories terminate on the ignition line. This is the case regardless of whether $S > S_c$ or $S < S_c$.

If a trajectory terminates on the ignition line, then physically it means that the current terminates in a finite distance, but has a non-zero value of velocity or turbulent kinetic energy. On the ignition line, the velocity has a value of U_c, where

$$U_c = \left(\frac{\delta}{\Lambda}\right)^{1/3}. \tag{2.34}$$

The ignition line is where the characteristic wave speed is zero. Across the ignition line there exists a reversal of trajectories; the flow is changing from supercritical to subcritical moving from right to left across this line (and vice versa). On the ignition line itself, the Richardson number is equal to one. In order to describe trajectories which cross the ignition line it would be necessary to include shocks to the model. Since the steady state momentum equation (2.19a) is degenerate on the ignition line we must reintroduce the time dependence to the model to understand what is happening here.

2.3 The time-dependent model

The non-dimensional Parker model is given by equations (2.7). In Section 2.2, the steady state version of the Parker model was considered, where it was found that the wave speed is zero on the ignition line. In this section we derive a simplified time-dependent model which we will use to understand behaviour on the ignition line more fully. This is done by considering a one-equation 'toy model' which will look only at the dynamics of the momentum equation (2.7b). This will allow us to focus solely on the behaviour of the velocity.

2.3.1 The one-equation model

In this section, we will assume that the slope is constant; however in Section 2.5.4 it will be allowed to vary slowly as a function of downstream distance. We want to consider two cases, namely depositional and erosional currents. In order to concentrate on the behaviour of u, we need to eliminate h, k and c by making suitable approximations.

First consider the sediment concentration equation (2.7c). The simplest scaling is to assume $\gamma \ll 1$ and let

$$c \sim E^\star. \tag{2.35}$$

We say that the current is depositional if $E^\star = 0$ and erosional if $E^\star = 1$. Whilst this is a crude estimation (it is not really true since the advective term in equation (2.7c) is large; $\gamma \approx 1.2$), other simplifying assumptions will be made anyway, so it makes sense to pursue the simplest case. We rewrite equation (2.7b) assuming that c is a constant equal to zero or one. We make use of the mass conservation equation (2.7a) to rewrite the left hand side of equation (2.7b) and also eliminate k by making use of the relations for the shear stress (1.10) and (1.12), which allows us to take $k \approx u^2$. Thus equation (2.7b) becomes

$$\Lambda(u_t + uu_x) = -\delta c h_x + Sc - \frac{u^2}{h} - \frac{\Lambda u^4}{h(ch + \nu u^2)}. \tag{2.36}$$

To eliminate h altogether, we consider the flux of the current, $q = hu$. As in Section 2.2 we assume that the flux of the current is large, $q \sim \mathcal{O}(10^5)$. We will assume quasi-steady mass conservation and use q as a surrogate space variable, noting that

$$\frac{\partial}{\partial x} = e^\star u \frac{\partial}{\partial q}. \tag{2.37}$$

We also note that we assume that the way in which q varies in time is small and thus,

$$\frac{\partial}{\partial t} = \frac{\partial}{\partial t} + \dot{q}\frac{\partial}{\partial q} \approx \frac{\partial}{\partial t}. \tag{2.38}$$

Equation (2.36) now becomes

$$\Lambda\left(\frac{\partial u}{\partial t} + \left(\frac{\Lambda u^5}{cq + \nu u^3}\right)\frac{\partial u}{\partial q}\right) = -\delta c\left(\frac{\Lambda u^4}{cq + \nu u^3}\right)\frac{\partial}{\partial q}\left(\frac{q}{u}\right) + Sc - \frac{u^3}{q} - \frac{\Lambda u^6}{q(cq + \nu u^3)}. \tag{2.39}$$

Again we make a substitution for u in terms of q

$$u = q^{1/3}U, \tag{2.40}$$

consistent with the scaling used in the phase plane analysis in Section 2.2. Equation (2.39) now becomes

$$\Lambda q^{1/3}\frac{\partial U}{\partial t} + \left(\frac{\Lambda U^5 - c\delta U^2}{c + \nu U^3}\right) q\frac{\partial U}{\partial q} = -\frac{2}{3}\left(\frac{2\Lambda U^3 + c\delta}{c + \nu U^3}\right) U^3 + Sc - U^3. \tag{2.41}$$

The last substitution to be made is,

$$s + s_i = \ln(q), \tag{2.42}$$

where $s_i = \ln(q_i)$. Here, $q_i = 10^5$ is the value of the dimensionless turbidity flux at the inlet, and hence $s_i = 11.5$.

The one-equation velocity model is then given as

$$\Lambda e^{(s+s_i)/3}\frac{\partial U}{\partial t} + \left(\frac{\Lambda U^5 - c\delta U^2}{c + \nu U^3}\right) \frac{\partial U}{\partial s} = -\frac{2}{3}\left(\frac{2\Lambda U^3 + c\delta}{c + \nu U^3}\right) U^3 + Sc - U^3. \tag{2.43}$$

The equation will be studied for two cases:

- Depositional currents - when erosion is switched off and $c = 0$,
- Erosional currents - when erosion is switched on and $c = 1$.

Comment on the one-equation model

The one-equation model for turbidity currents is derived by considering terms in the four- equation Parker model which are thought to be important features of the flow. To this end, some large simplifications have been made to obtain the one-equation model, and the model does not arise as an asymptotic reduction of the four-equation Parker model. However, as will be shown in this chapter, the one-equation model provides a valuable insight into some of the mathematical features of the full system and thus provides an interesting preliminary study to the four-equation model.

2.3.2 Initial and boundary conditions

The initial condition that we impose is

$$U(s,0) = U_0(s) = U^\star \left(1 + \tanh\left[a(b-s)\right]\right), \quad \text{for} \quad s > 0, \tag{2.44}$$

where a, b and $U^\star$ are constants. This represents a 'raft' of material which begins at the top of the domain and is then released downstream.

We will study two types of boundary condition in this chapter. The first is a *steady inflow* condition which constantly introduces new material into the domain at the left-hand boundary. This boundary condition represents turbidity currents that are continually fed by a fluvial system. So that the initial condition and boundary condition are continuous we take the value of U on the left-hand boundary to be

$$U(0,t) = U_i = U^\star \left(1 + \tanh[ab]\right) \quad \text{for} \quad t > 0. \tag{2.45}$$

The alternative is a *slumping boundary condition*, which represents a turbidity current that is triggered by sediment collapse. This is a no-flow boundary condition so we have

$$U(0,t) = U_i = 0 \quad \text{for} \quad t > 0. \tag{2.46}$$

Figure 2.5 shows a schematic of the initial and boundary conditions.

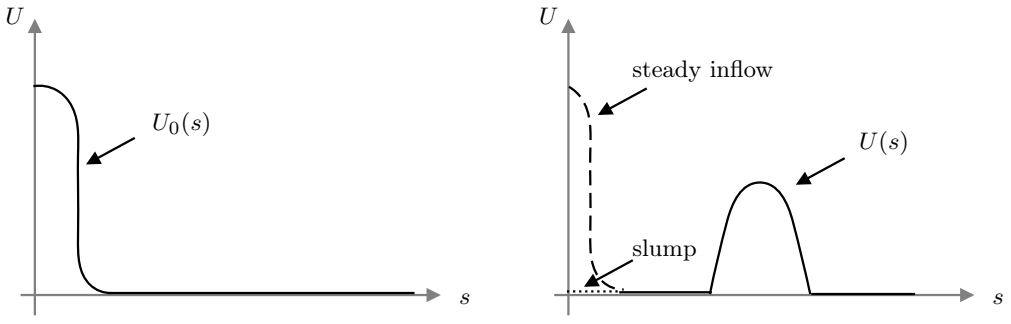

(a) Initial condition, $U_0(s)$, at $t = 0$ (b) Boundary conditions, U_i, for $t > 0$

Figure 2.5: (a) Schematic of the initial condition $U_0(s)$ at $t = 0$. This has value $U = U^\star(1 + \tanh(ab))$ at $s = 0$, and $U = 0$ for large s. The shape of the initial condition is controlled by the size of the parameters $U^\star$, a and b. (b) Schematic of the solution $U(s)$ for $t > 0$. We show the solution influenced by the steady inflow boundary condition by the black dashed line. This has value $U_i = U^\star(1 + \tanh(ab))$ at $s = 0$. We show the solution influenced by the slump boundary condition as a dotted black line. This boundary condition has value $U_i = 0$ at $s = 0$.

In Section 2.4, we begin by looking at the model for depositional currents. The depositional model will be solved parametrically and conditions under which shocks form in the equation will be considered. In order to solve the depositional model numerically, a diffusion term will be introduced. In Section 2.5, the erosional momentum equation will be considered. We will look at shock formation once more and highlight the dependence of the source term in the equation on S. Different slope values will be used when solving the model, including a slope term which is a function of distance downstream.

2.4 Depositional currents

We first look at the momentum equation for deposition currents, obtained by setting $c = 0$ in equation (2.43):

$$\Lambda e^{(s+s_i)/3}\frac{\partial U}{\partial t} + \frac{\Lambda}{\nu}U^2\frac{\partial U}{\partial s} = -U^3\left(\frac{4\Lambda}{3\nu} + 1\right). \tag{**2.47**}$$

We simplify this equation by multiplying through by ν/Λ and by defining

$$\mu = \frac{\nu}{\Lambda} + \frac{4}{3} \approx 1.387. \tag{**2.48**}$$

We also rescale t as $t = \alpha t$ where $\alpha = \nu e^{s_i/3}$. This simplifies (2.47) to

$$e^{s/3}\frac{\partial U}{\partial t} + U^2\frac{\partial U}{\partial s} = -\mu U^3. \tag{**2.49**}$$

2.4.1 Method of characteristics

The characteristic equations of (2.49) are given by

$$\dot{t} = e^{s/3}, \quad \dot{s} = U^2, \quad \dot{U} = -\mu U^3, \tag{**2.50**}$$

where the dots above the variables denote differentiation with respect to the characteristic variable. We use the method of characteristics to solve the one-equation velocity model parametrically for a range of s and t (*e.g.* Fowler (2010)). In Figure 2.6 we plot the characteristic diagram for the boundary and initial conditions given in Section 2.3.2.

There are two regions in each of the characteristic diagrams, which are as follows: in Region I the solution is determined by the initial conditions and the characteristic lines are plotted in blue. In Region II the solution is determined

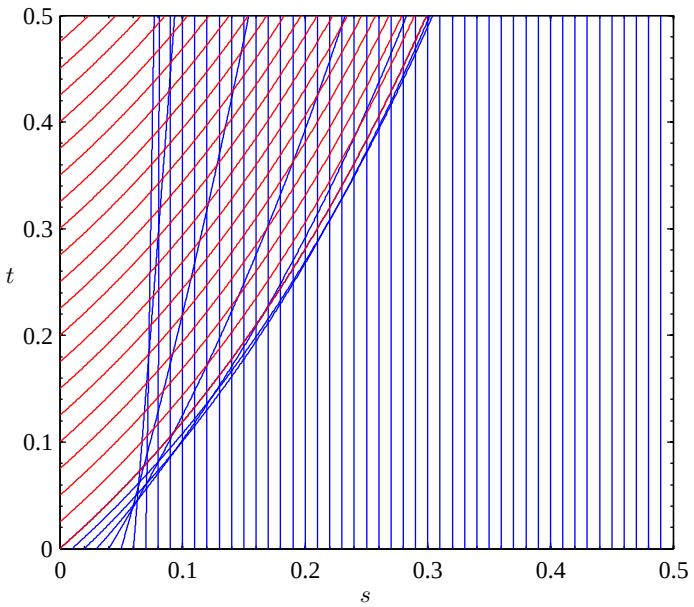

(a) Steady inflow boundary conditions, $U_i = 1$ at $s = 0$

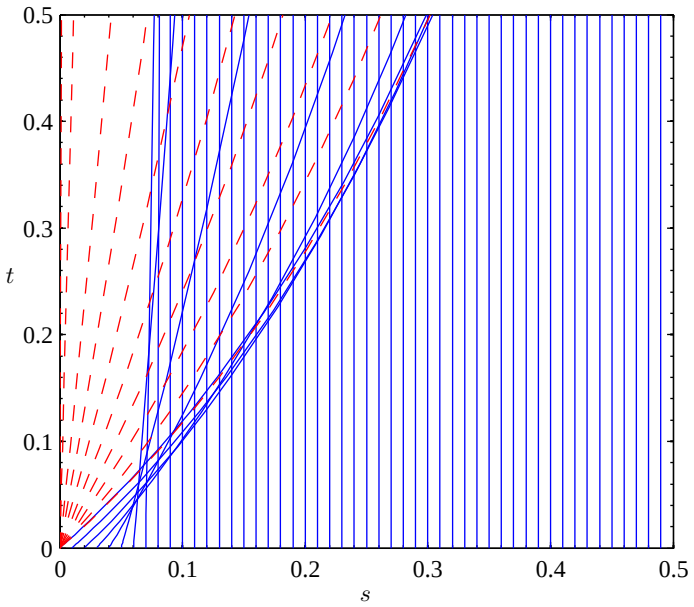

(b) Slumping boundary conditions, $U_i = 0$ at $s = 0$

Figure 2.6: Characteristic diagrams of equation (2.49). The initial condition is given by equation (2.44) and the boundary conditions are given by equations (2.45) and (2.46). The parameters values are $U^\star = 1/2$, $a = 50$, $b = 0.05$ and $\mu = 1.387$.

by the boundary conditions at $s = 0$ and the characteristic lines are plotted in red; the red dashed lines represent an expansion fan from $s = t = 0$.

Figure 2.6(a) shows the characteristic diagram for the steady inflow boundary condition. The red characteristics show information propagating from $s = 0$ for all $t > 0$. Figure 2.6(b) shows the characteristic diagram for the slump boundary condition. Here, there is a vertical solid red characteristic at $s = 0$, since the velocity is zero at the boundary. The red dashed lines coming from $s = 0$ represent the expansion fan that must occur as the characteristics fill up the $s - t$ plane.

In Region I, equations (2.50) are solved for

$$t = 0, \quad s = \eta, \quad U = U_0(\eta), \quad (\eta > 0), \tag{2.51}$$

where η is the parametric variable, and must remain positive. The solution is given by

$$s = \frac{1}{\kappa} \log \left(\kappa e^{2\mu\eta} U_0(\eta)^2 t + e^{\kappa\eta} \right), \tag{2.52a}$$

$$U = U_0(\eta) e^{\mu(\eta - s)}, \tag{2.52b}$$

where

$$\kappa = 2\mu + \frac{1}{3}, \tag{2.53}$$

and

$$U_0(\eta) = U^\star(1 + \tanh[a(b - \eta)]). \tag{2.54}$$

In Region II for the steady inflow problem, indicated by the solid red characteristic lines in Figure 2.6(a), equations (2.50) are solved according to

$$s = 0, \quad t = \tau, \quad U = U_i \quad \tau > 0, \tag{2.55}$$

where τ is defined for $0 \leq \tau \leq t$ and $U_i = U^\star(1 + \tanh[ab])$. Here the solution is given by

$$s = \frac{1}{\kappa} \log \left(\kappa (t - \tau) U_i^2 + 1 \right), \tag{2.56a}$$

$$U = U_i e^{-\mu s}. \tag{2.56b}$$

In Region II for the slump problem, indicated by the red dashed characteristic

lines in Figure 2.6(b), equations (2.50) are solved according to

$$s = 0, \quad t = 0, \quad U = v \quad \tau > 0, \tag{2.57}$$

where $0 \leq v \leq U_0(0)$. Here the solution is given by

$$s = \frac{1}{\kappa} \log\left(\kappa v^2 t + 1\right), \tag{2.58a}$$

$$U = v e^{-\mu s}. \tag{2.58b}$$

In both characteristic diagrams the blue characteristic lines begin to cross each other around $t \approx 0.04$. This is a shock forming in the solution as a result of the choice of initial condition; the solution U is becoming multi-valued at the points where the characteristic lines intersect. The shock propagates downstream in time — in Section 2.4.3 the depositional model will be solved with a diffusive term to smooth the solution at the shock and the sub-characteristics of the model will be plotted to show how the shock propagates downstream in time.

In the following section we outline how the formation of shocks in the solution to equation (2.49) is controlled by the size of the parameters used in the model and the size of the constants used in the initial and boundary conditions.

2.4.2 Shock conditions

A shock will form in the solution if

$$\left|\frac{\partial U}{\partial s}\right| \to \infty. \tag{2.59}$$

We recall equations (2.52) for U and s in the initial condition region. We let a derivative with respect to η be denoted by a prime, and so the shock condition is given by

$$\left|\frac{\partial U}{\partial s}\right| = \left|\frac{[U_0' + \mu U_0(1 - s')]e^{-\mu(s-\eta)}}{s'}\right| \to \infty. \tag{2.60}$$

Hence, equation (2.59) will be satisfied if $s' \to 0$. We calculate s' from equations (2.52):

$$s' = \frac{2U_0 e^{2\mu\eta}(U_0' + \mu U_0)t + e^{\kappa\eta}}{\kappa U_0^2 e^{2\mu\eta} t + e^{\kappa\eta}}. \tag{2.61}$$

Hence a shock will be present at time

$$t = \frac{-e^{\eta/3}}{2U_0(U_0' + \mu U_0)}, \tag{2.62}$$

for $t > t^\star$, where $t^\star$ is the minimum of equation (2.62) and is the time at which the shock first appears in the solution to the depositional model for the chosen parameter values.

We suppose that the first shock occurs at $\eta = \eta^\star$, where $\eta^\star$ is found by minimizing equation (2.62) as a function of η:

$$\eta^\star = b - \frac{1}{a}\tanh^{-1}\left\{\frac{1 + 6(2a - \mu) - \sqrt{1 + 12(2\mu - a) + 36(\mu + a)^2}}{18a}\right\}. \tag{2.63}$$

Equation (2.52a) evaluated at $\eta = \eta^\star$ determines the value in space, $s = s^\star$, at which the shock first appears. For the values that we have chosen for the initial condition (2.44) ($a = 50$, $b = 0.05$, $U^\star = 0.5$), we find that $s^\star \approx 0.0583$ and $t^\star \approx 0.0357$.

2.4.2.1 Shock formation and model parameters

Since $\eta^\star$ and $t^\star = t(\eta^\star)$ are clearly functions of the model parameters, a, b and μ, here we consider what values of these parameters will cause the formation of a shock in the solution to equation (2.49).

The time at which the first shock occurs is given by

$$t^\star = \frac{-e^{\eta^\star/3}}{2U_0(\eta^\star)(U_0'(\eta^\star) + \mu U_0(\eta^\star))}. \tag{2.64}$$

It is clear that we require $t^\star > 0$, and, since $\eta > 0$ (2.51), it must be true that $\eta^\star > 0$. The first shock will form for $t^\star > 0$ if $2U_0(U_0' + \mu U_0) < 0$. We recall the definition of U_0 from equation (2.54). The shock condition on the model parameters is thus

$$\frac{\mu}{a} < 1 - \tanh(a(b - \eta^\star)). \tag{2.65}$$

we find the maximum of the right-hand side of (2.65) (for any η) is

$$\max_{\eta > 0}\{1 - \tanh(a(b - \eta))\} = 2, \quad \forall\, a, b > 0. \tag{2.66}$$

Hence we have

$$\text{no shock if } a < \frac{\mu}{2}, \tag{2.67a}$$

$$\text{shock formation if } a > \frac{\mu}{2}. \tag{2.67b}$$

Figure 2.7 shows the time and distance downstream at which the first shock will form as a function of a and b. It is clear that $t^\star, \eta^\star \to \infty$ as $a \to \mu/2$.

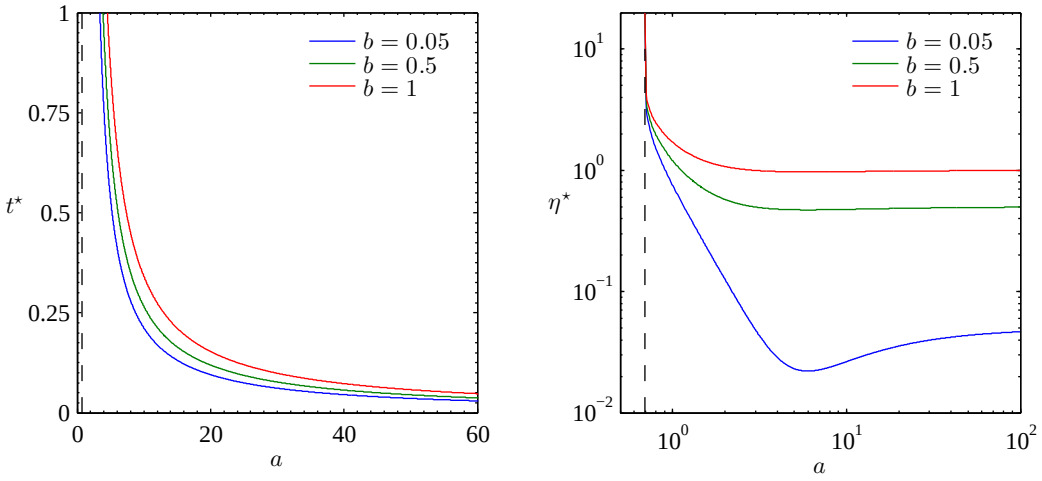

(a) Plot of $t^\star$

(b) Log-log plot of $\eta^\star$

Figure 2.7: The time and location of the first shock as functions of a and b. We plot using equations (2.62) and (2.63) for a range of a and specific values of b. The dotted line in both figures is present at $a = \mu/2$, and $\mu = 1.387$.

From equation (2.63), we see that a condition is put on b because we require $\eta^\star > 0$. In Figure 2.8 we plot the minimum value, $b = b_{min}$, obtained by solving equation (2.63) for b when $\eta^\star = 0$, as a function of a. From Figure 2.8 we can see that for $a = 50$, the minimum value b can take to return $\eta^\star > 0$ is $b_{min} \approx 0.00657$.

The limiting values of a and b at which shocks will form have a dependence on the parameter μ. We recall the definition of μ from equation (2.48), which is a function of the parameters Λ and ν, themselves given by (2.8) and (2.14), respectively. Hence, we find

$$\mu = \frac{4}{3}\left(10 c_{D0} + 1\right). \tag{2.68}$$

In Tables 2.2 we took $c_{D0} = 0.004$ after Parker et al. (1986). We now review the literature again, to see what assumptions lead to the definition of these value.

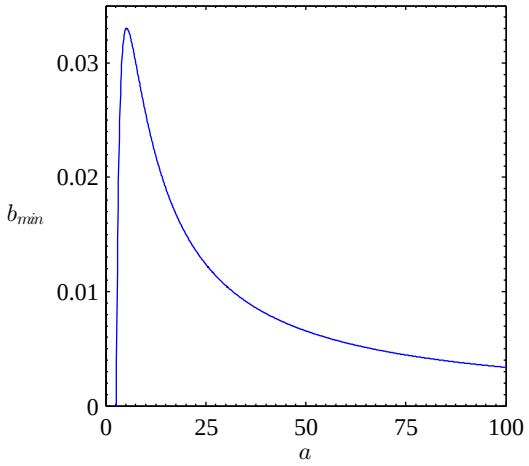

Figure 2.8: A plot defining the smallest possible value $b = b_{min}$ can take in the initial condition (2.44) for a given value of a to ensure $\eta^\star > 0$.

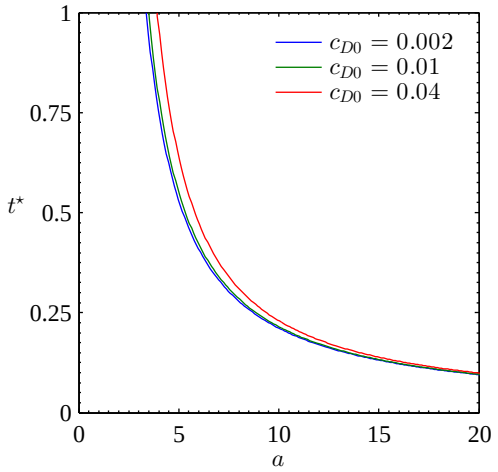

Figure 2.9: A plot of equation (2.62) showing how the time of the initial shock, $t^\star$, varies with the size of as a function of a for values of $c_{D0} \in [0.002, 0.04]$. We find only a small variation in the onset of the first shock for a difference of order 10 in c_{D0}. The initial condition was given by (2.44) and the parameters are $b = 0.05$, $U^\star = 1/2$ and $\mu = 4/3(10c_{D0} + 1)$.

Parker et al. (1986) investigate the effect of varying c_{D0} in the range 0.002 to 0.04, which is found to have little effect on the overall predictions of the model. In Figure 2.9 we look at how $t^\star(a)$ varies for values of $c_{D0} \in [0.002, 0.04]$.

We find that there is a small variation in the time of the initial shock, especially between $c_{D0} = 0.002$ and $c_{D0} = 0.01$, which is the range of c_{D0} most commonly found in the literature. From equation (2.68) we see that, since these values of c_{D0} are small, at leading order $\mu \sim 4/3$. Provided $c_{D0} \lesssim 0.1$ we expect shocks to form for $a > 2/3$ and $b > b_{min}$ where

$$b_{min} \approx \frac{1}{a} \tanh^{-1}\left(\frac{12a - 9 - \sqrt{36a^2 + 156a + 97}}{18a}\right). \tag{2.69}$$

For the remaining calculations in this chapter, we choose $a = 50$ and $b = 0.05$ as the parameter values for the initial condition (2.44). We do this in the knowledge that shocks will form in the solution to equation (2.49).

2.4.3 Depositional currents with viscous dissipation

The analysis in Section 2.4.2 show that, for the parameter values we have chosen, the one-equation velocity model will admit shocks. To solve equation (2.49) for U numerically we add in an artificial diffusion term to the model in order to smooth the solution at the shock. The most simple way in which we can add in diffusion to the model is to include an additional term as follows

$$e^{s/3}\frac{\partial U}{\partial t} + U^2\frac{\partial U}{\partial s} = -\mu U^3 + \epsilon U_{ss}, \tag{2.70}$$

where $\epsilon \ll 1$ is a diffusion coefficient. It should be noted, however, that the diffusion term used in equation (2.70) is an approximation to the correct diffusion term, which should be added to the original momentum equation and transformed into the new variables accordingly. This term would take the form

$$\epsilon(hu_x)_x, \tag{2.71}$$

when added to the equation (2.7b) and in the scaled variables U and s it would become

$$\frac{\epsilon}{9\nu\Lambda}e^{-(s+s_i)}U^2\left(U + 6U_s + 9U_{ss}\right). \tag{2.72}$$

Due to the assumption of a large flux, we find that this term is very small; in particular,

$$e^{-s_i} \sim \mathcal{O}(10^{-5}). \tag{2.73}$$

This makes the diffusion term (2.72) very difficult to deal with numerically, and hence the approximation given in equation (2.70) is used instead. In Appendix A we solve the depositional model for the diffusion term (2.72) to provide a comparison with the diffusion term used in this chapter.

In order to solve the depositional model with diffusion, we must introduce a further boundary condition. We will use a 'no flux' condition at the right hand boundary,

$$U_s = 0 \quad \text{at} \quad s = s_R, \tag{2.74}$$

where $s_R > 1$.

Solution We first look at solutions to equation (2.70) for $\epsilon \ll 1$. We compute the solution using the MATLAB inbuilt pde solver '*pdepe*' and show the solution in Figure 2.10 for the steady inflow and slumping boundary conditions.

In Figure 2.10 we can see that there is a shock which has been regularised by the inclusion of diffusion. In Figure 2.10(a) we show the steady inflow case. Here U decreases with distance downstream, and in time a steady profile is reached where U decreases to zero across the domain. The shock produces a sharp front in the solution which can be seen advancing downstream in time. This front will eventually decelerate and come to rest. Behind the shock (upstream) the current is fast flowing, and ahead of the shock (downstream) the current is slowing down.

In Figure 2.10(b) we show the slumping case. Here the maximum value of the velocity, U, is much lower than in the steady inflow problem, even after a few time steps. The shock decelerates much faster and the current quickly dies out; $U \to 0$ for all s as $t \to \infty$.

By using the solution to the diffusion equation (2.70), we can calculate the sub- characteristics of the model and show the propagation of the shock in the $s - t$ plane. The characteristics are given by equations (2.50), and the sub-characteristics are plotted in Figure 2.11. The sub-characteristics show the shock structure of the solution using the artificial diffusion term. The shock forms at the point at which the characteristic curves meet, and the diffusion term in the solution causes the curves to bend towards the shock over a thin region. In both the steady inflow case and the slumping case, the shock can

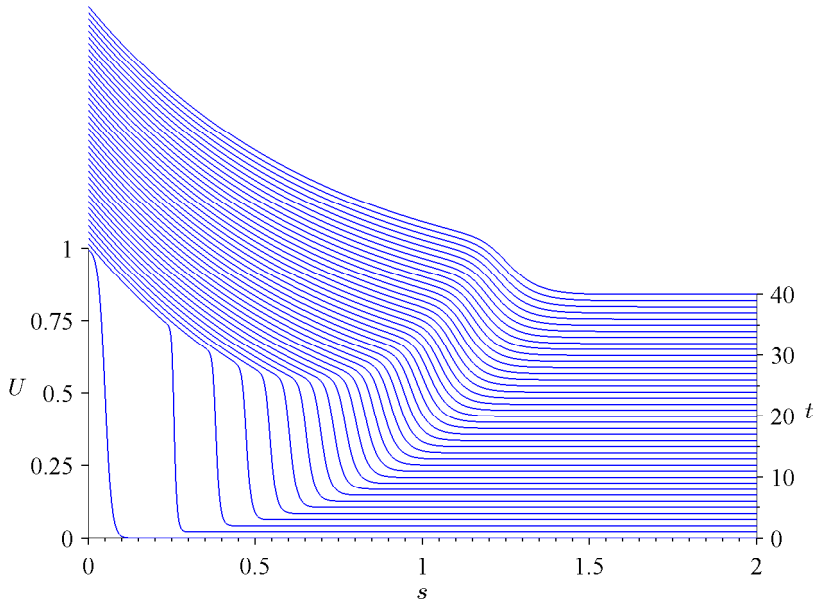

(a) Steady inflow boundary conditions, $U_i = 1$ at $s = 0$

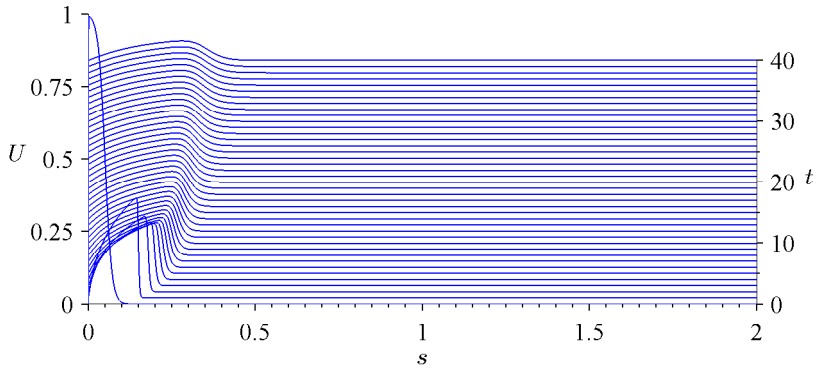

(b) Slumping boundary conditions, $U_i = 0$ at $s = 0$

Figure 2.10: Numerical solution to equation (2.70). The initial condition is given by equation (2.44). In (a) the boundary condition is given by equation (2.45) and in (b) the boundary condition is given by equation (2.46). We have used parameter values of $U^\star = 0.5$, $a = 50$, $b = 0.05$ and $\mu = 1.387$. In (a) $\epsilon = 10^{-3}$ and in (b) $\epsilon = 10^{-4}$. For both plots time intervals of $t = 2$ were used for $t \in [0, 40]$.

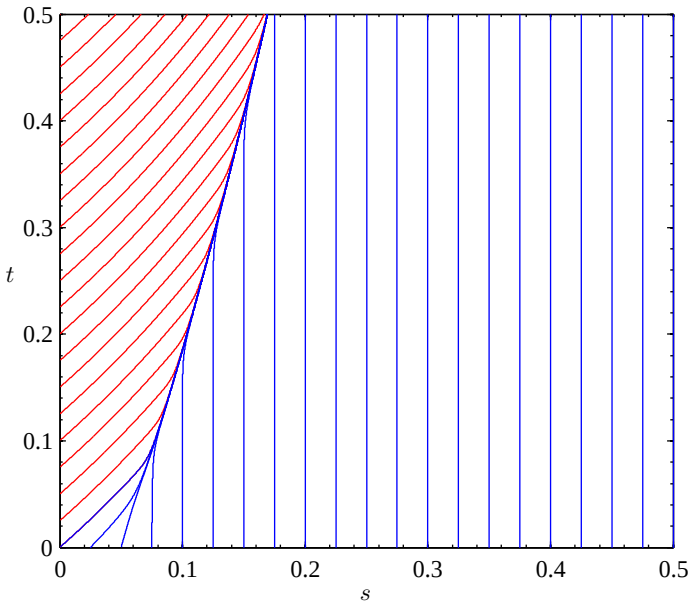

(a) Sub-characteristics for the steady inflow boundary conditions when $\epsilon = 0.001$

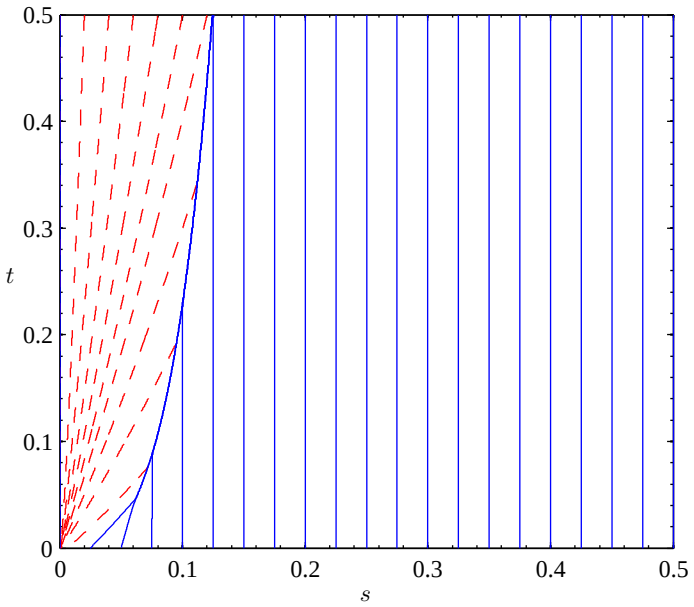

(b) Sub-characteristics for the slumping boundary conditions when $\epsilon = 0.0001$

Figure 2.11: Sub-characteristic curves of equations (2.70) when $\epsilon \ll 1$. The blue characteristics are given by the initial condition (2.44) and the red characteristics are given by the boundary condition (a) $U_i = 1$ at $s = 0$ and (b) $U_i = 0$ at $s = 0$. The parameter values are given in Figure 2.10.

be seen propagating downstream in time. It should be noted that since the diffusion term in equation (2.70) is an approximation to the correct form of the diffusion term (2.72), the location of the shock in the solution is also an approximation.

In Figure 2.12, the parametric solution for the wave is calculated using equations (2.50) and compared with the solution of the model with a basic diffusion term (2.70) and with the solution of the model using the correct form of diffusion given in Appendix A. It can be seen that the diffusion terms regularise the solution to prevent it from becoming multivalued at the shock and away from the shock the solution of both the diffusion models matches the parametric solution given by equations (2.52)–(2.58). We see that the two diffusion terms predict the location of the shock quite differently, however, as is noted in Appendix A, the basic diffusion term provides sufficient accuracy for the one-equation model, since many other simplifying assumptions are used in the derivation of equation (2.43).

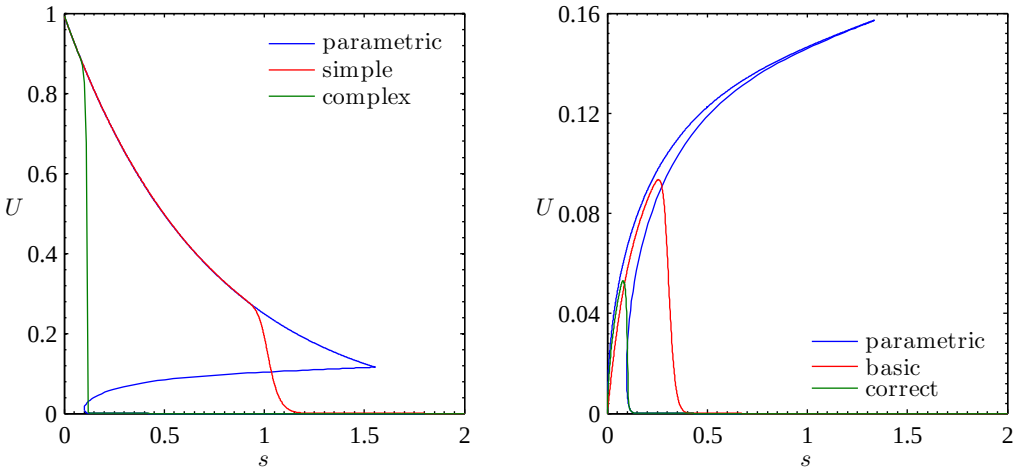

(a) Steady inflow boundary condition, $U_i = 1$

(b) Slump boundary condition, $U_i = 0$.

Figure 2.12: The solution profiles of the depositional model (2.49) at $t = 20$. In blue we plot the parametric solution, equations (2.52)–(2.58). In red we plot the solution to equation (2.70); the depositional model with 'basic' diffusion. In green we plot the solution to equation (A.1); the depositional model with 'correct' diffusion. Parameter values are $U^\star = 0.5$, $a = 50$, $b = 0.05$, $\nu = 0.25$, $\Lambda = 4.7$, $\mu = 1.387$, $s_i = 11.5$. Solutions have used the following diffusion coefficients (a) in equation (2.70) $\epsilon = 0.001$, in equation (2.72) $\epsilon = 5000$; (b) in equation (2.70) $\epsilon = 0.0001$, in equation (2.72) $\epsilon = 5000$.

2.5 Erosional currents

We now return to consider equation (2.43) for erosional currents with $c = 1$. As in the previous section we will rescale time; $t = \alpha t$, where $\alpha = \Lambda e^{s_i/3}$. Hence, the one-equation velocity model for erosional currents is

$$e^{s/3}\frac{\partial U}{\partial t} + \left(\frac{\Lambda U^5 - \delta U^2}{1 + \nu U^3}\right)\frac{\partial U}{\partial s} = -\frac{2}{3}\left(\frac{2\Lambda U^3 + \delta}{1 + \nu U^3}\right)U^3 + S - U^3. \qquad \textbf{(2.75)}$$

We recall that the aim in this section is to understand the transition that occurs as S decreases towards zero. As we saw in the phase plane analysis of Section 2.2.1, the behaviour of the steady state model is fundamentally different depending on the size of S relative to a critical value S_c. At the point when $S = S_c$ we saw that the steady state model undergoes a bifurcation, and the stability of the model changes. This corresponds to the wave speed of the momentum equation being zero, and it is this that we will examine first in this section.

2.5.1 Steady state analysis of the erosional model

We begin by considering turbidity currents where the slope, S, is constant, taking values in the range $0 < S < 1$, corresponding to real slope values between $0°$ and $3°$. We write equation (2.75) as

$$e^{s/3}\frac{\partial U}{\partial t} + V(U)\frac{\partial U}{\partial s} = R(U, S), \qquad \textbf{(2.76)}$$

where

$$V(U) = \frac{\Lambda U^5 - \delta U^2}{1 + \nu U^3}, \qquad \textbf{(2.77a)}$$

$$R(U, S) = -\frac{2}{3}\left(\frac{2\Lambda U^3 + \delta}{1 + \nu U^3}\right)U^3 + S - U^3. \qquad \textbf{(2.77b)}$$

We plot V and R as functions of U in Figure 2.13.

We see that $V(U)$ has a unique, non-zero, positive, real root which is given by

$$U_c = \left(\frac{\delta}{\Lambda}\right)^{1/3}. \qquad \textbf{(2.78)}$$

This is the value of U on the ignition line, as shown in the phase plane (*cf.* Section 2.2.1, Figure 2.1) and it is the value of U for which the wave speed in equation (2.76) is zero. Similarly, R has a single non-zero, positive, real root

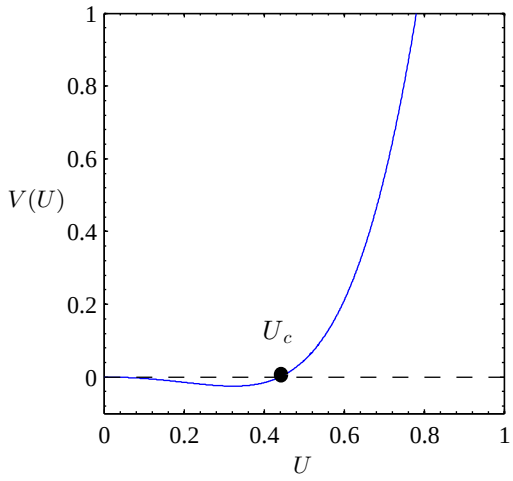

(a) Plot of $V(U)$, equation (2.77a).

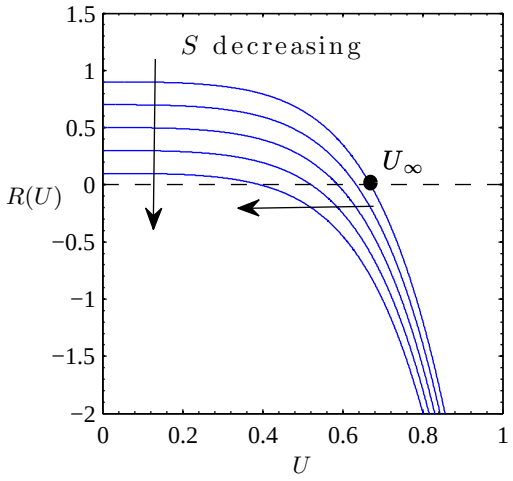

(b) Plot of $R(U, S)$, equation (2.77b).

Figure 2.13: We mark the roots of equations (2.77) as U_c and U_∞, noting that $V(U_c) = 0$ and $R(U_\infty) = 0$. In (b) we have taken values of S in the range $0 < S < 1$ and we highlight how U_∞ decreases as we decrease the slope. Parameter values are $\Lambda = 4.7$, $\delta = 0.4$, $\nu = 0.25$.

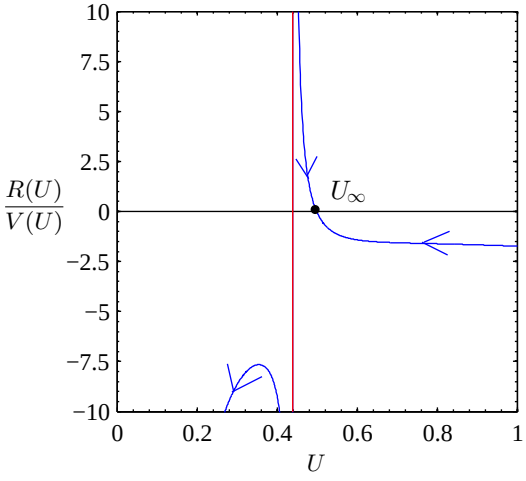

(a) Case I: $U_\infty > U_c$

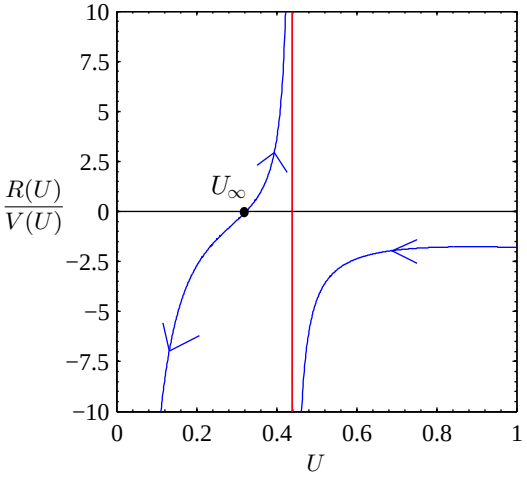

(b) Case II: $U_\infty < U_c$

Figure 2.14: Steady state phase plane of equation (2.79) shown for different sizes of U_∞ relative to U_c. The slope, S takes the values (a) $S = 0.25$ and (b) $S = 0.05$. The red line indicates the value of U_c and U_∞ is marked by a black circle in each plot. Parameter values are given in Figure 2.13.

for each value of S. We denote this U_∞. The size of U_∞ is determined by the value of the slope and U_∞ decreases as S decreases.

At $U_c = U_\infty$ we determine a unique value of the slope, $S = S_c$. We find that for $S > S_c$ (or $U_\infty > U_c$) and $S < S_c$ (or $U_\infty < U_c$) we have qualitatively different types of behaviour. This is as a result of the wave speed in equation (2.76) changing sign. We can highlight the difference in this behaviour by considering the steady state model,

$$\frac{dU}{ds} = \frac{R(U,S)}{V(U)}, \tag{**2.79**}$$

for the two cases; Case I: $U_\infty > U_c$ and Case II: $U_\infty < U_c$ in Figure 2.14. These cases are produced by choosing $S > S_c$ and $S < S_c$ respectively, in equation (2.79).

For $S > S_c$, $U \to U_\infty > U_c$, and for $S < S_c$, $U \to 0$ or $U \to U_c$. We will examine the effects of these different equilibria on the solution to equation (2.75) in Section 2.5.2 using the method of characteristics.

2.5.2 Method of characteristics

The characteristics of equation (2.76) are given by

$$\dot{t} = e^{s/3}, \tag{**2.80a**}$$

$$\dot{s} = V(U), \tag{**2.80b**}$$

$$\dot{U} = R(U,S). \tag{**2.80c**}$$

We want to plot characteristic diagrams for the erosional one-equation velocity model as we did for the depositional model. However, we must be careful here to consider the characteristic lines of the boundary condition emanating from $s = 0$. The value of U on the left hand boundary is U_i and we need to consider the size of U_i relative to U_c and U_∞. We will have six possibilities in total, or three cases each for the two phase planes in Figure 2.14:

$$\begin{array}{llll} \text{Case I} & \text{A} & U_i < U_c < U_\infty, & \text{Case II} \quad \text{A} \quad U_i < U_\infty < U_c, \\ & \text{B} & U_c < U_i < U_\infty, & \qquad\quad\ \ \text{B} \quad U_\infty < U_i < U_c, \\ & \text{C} & U_c < U_\infty < U_i, & \qquad\quad\ \ \text{C} \quad U_\infty < U_c < U_i. \end{array} \tag{**2.81**}$$

We also have to take into account the characteristic lines of the initial condition, emanating from $t = 0$. These have slope

$$\frac{ds}{dt} = \frac{V(U)}{e^{s/3}}. \tag{**2.82**}$$

At $t = 0$ the velocity is given by the initial condition (2.44) in s. In each of the Cases IA–C and IIA–C the characteristic lines of the initial condition will have positive slope for $s < b$ and infinite slope (straight lines) for $s > b$ for small values of t. For larger values of t, the solution is influenced by the boundary condition, which is why the value of U_i at $s = 0$ is important.

In Figure 2.15 the characteristics of the erosional model are plotted. These are found using the solution to the erosional model with a viscous term, given in the following section by equation (2.83), and then by solving the differential equation (2.82). The blue curves are determined by the initial condition and the red curves are determined by the boundary conditions; the red dashed curves highlight an expansion fan.

We can see clearly that there are differences between Cases I A–C (where $S = 1$) and II A–C (where $S = 0.1$). When $S = 1$, (the left-hand column of Figure 2.15, Case I), the characteristics have, broadly, a positive slope, so information is being propagated downstream; $U_\infty > U_c$ and $U \to U_\infty \approx 0.68$. The wave speed of equation (2.75) is positive. When $S = 0.01$, (the right-hand column of Figure 2.15, Case II), the characteristics have, broadly, a negative slope, so information is being propagated upstream; $U_\infty < U_c$ and $U \to U_\infty \approx 0.39$. The wave speed of equation (2.75) is negative.

In the left-hand column of Figure 2.15, Case I, we plot the characteristics of the $S = 1$ solution. The blue characteristic curves all have positive slope; these are the characteristics formed by the initial condition. The red characteristic curves are formed by the boundary condition, and so they are different in each plot, I A–C, depending on the size of U_i, as we detail below:

- Figure 2.15 IA: the characteristics emanating from $s = 0$ are negative and an expansion fan emanates from $s = 0$.
- Figure 2.15 IB: the boundary characteristics are positive for $s > 0$ and for $t \gtrsim 0.1$. An expansion fan emanates from $s = 0$ for $t \in (0, 0.2)$.
- Figure 2.15 IC: all the boundary condition characteristics are positive at $s = 0$, solid blue and red characteristic curves fill up the $s - t$ plane.

In the right-hand column of Figure 2.15, Case II, we have the characteristic

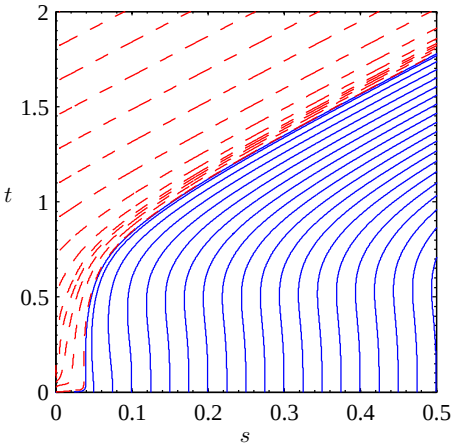

(IA): $S = 1$, $U_i = 0.3$

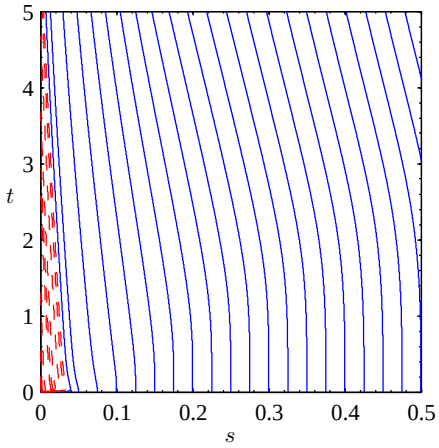

(IIA): $S = 0.1$, $U_i = 0.1$

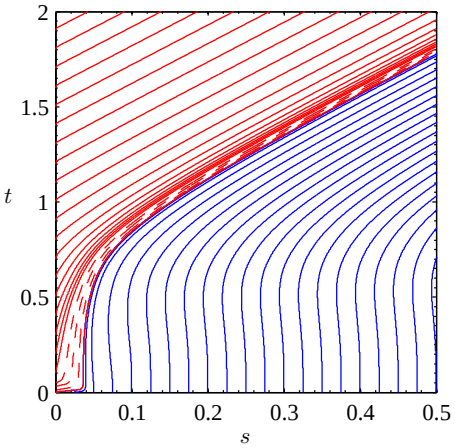

(IB): $S = 1$, $U_i = 0.5$

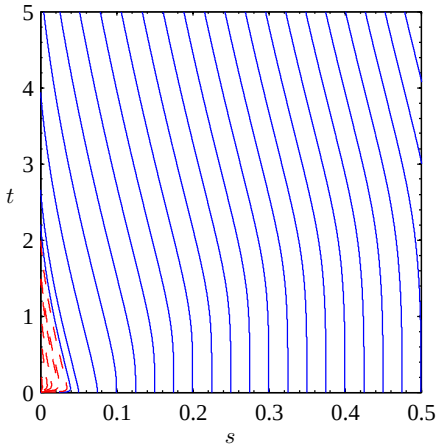

(IIB): $S = 0.1$, $U_i = 0.42$

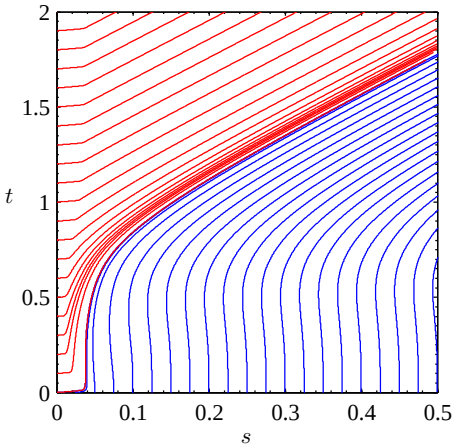

(IC): $S = 1$, $U_i = 1$

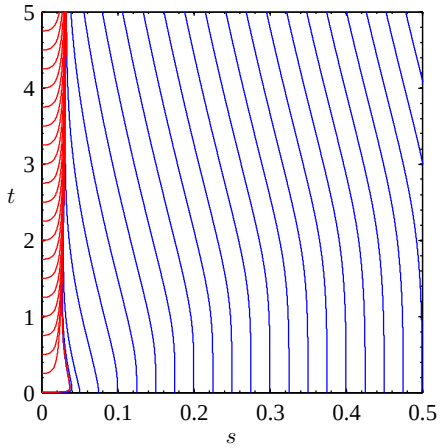

(IIC): $S = 0.1$, $U_i = 1$

Figure 2.15: The sub-characteristics of equation (2.83) when $\epsilon = 0.005$. The characteristics curves are defined by equation (2.82). The initial condition is given by equation (2.44) and the boundary conditions are listed in each subfigure. The parameter values are $\Lambda = 4.7$, $\delta = 0.4$, $\nu = 0.25$, $U^\star = 0.5$, $a = 50$ and $b = 0.05$.

diagrams of the $S = 0.1$ solution. Close to $t = 0$, the blue characteristics from the initial condition are all positive, with characteristics near $s = 0$ having pronounced positive slope. This causes a shock to form at $t \approx 0.01$. Later in time, as we see in Figure 2.15, Case II, that the blue characteristics bend and have a negative slope. This tells us that the wave speed is negative and information is being propagated upstream.

The value of U on the boundary, $s = 0$, is different for each of the plots in Figure 2.15, Case II. In both cases shown in Figure 2.15 IIA and IIB, there is an expansion fan for early times from $s = 0$. In time, it can be seen that the shock moves upstream, but at different speeds; in Figure 2.15 IIB, the shock reaches $s = 0$ more quickly than in Figure 2.15 IIA. In Figure 2.15 IIC, the shock moves upstream initially, and then a steady state is reached. The shock position remains fixed at $s \approx 0.02$.

We recall equation (2.81) where we outline the possible combinations of U_i, U_c and U_∞. By comparing this table with the characteristic diagrams plotted in Figure 2.15 we see that when $U_i < U_c$ (Figures 2.15 IA, IIA and IIB) the characteristics have negative slope at $s = 0$. Since the wave speed on the boundary is negative for these boundary conditions, in Section 2.5.3 we will only consider numerical solutions to equation (2.75) for the boundary conditions IB, IC and IIC.

2.5.3 Erosional currents with viscous dissipation

We want to solve the erosional model for U, to consider how the solution behaves for large values of t. The subcharacteristic diagrams are shown in Figure 2.15 since shocks will form in the solution to equation (2.76). These have been calculated using solutions to the erosional model with a viscous dissipation term. This model is given below:

$$e^{s/3}\frac{\partial U}{\partial t} + V(U)\frac{\partial U}{\partial s} = R(U,S) + \epsilon\frac{\partial^2 U}{\partial s^2}, \qquad \textbf{(2.83)}$$

where $\epsilon \ll 1$ is the diffusion coefficient and $V(U)$ and $R(U,S)$ are given by equations (2.77).

Solutions to (2.83) are plotted to show how U approaches its steady state value, U_∞, which is determined by the value of the slope, S. The initial condition is still given by equation (2.44) and the boundary condition is chosen such that the wave speed is positive at $s = 0$. This means we are considering Cases IB, IC

and IIC as shown in Figure 2.15. This is only the steady inflow problem, with values of $U_i > U_c$ at $s = 0$.

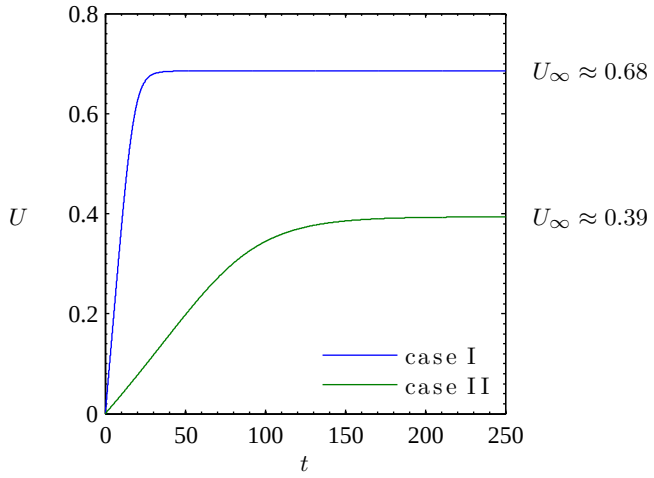

Figure 2.16: The solution U as a function of t at a point $s = 10$ downstream. The steady state values of U_∞ are reached as $t \to \infty$. The slope, S takes the values (I) $S = 1$ and (II) $S = 0.1$. The initial condition is given by equation (2.44) and the boundary condition U_i is constant; $U_i = 1$. Parameter values are given in Figure 2.15 and the diffusion coefficient is $\epsilon = 0.005$.

In Figure 2.16 we plot Cases IC and IIC only[2]. Initially $U = 0$ at $s = 10$, according to the initial condition for both cases. As the solution evolves the value of U at $s = 10$ increases from zero until we reach a steady state. For Case I the steady state value of $U_\infty \approx 0.68$ is reached at $t \approx 25$. For Case II, the steady state is reached more slowly; we see $U \to U_\infty \approx 0.39$ at $t \approx 150$.

The solution to the erosional model (2.83) shows that $U \to U_\infty$ in finite time. We interpret this behaviour as ignition, since an erosional front propagates downstream in time resulting in a high value of the velocity across the domain. Once the erosional front has propagated past a point s in the domain, the current attains the steady state value U_∞ and remains fixed at this value for all time. This means that the turbidity current will propagate forever, a situation which is not physically realistic; in real-world situations we would see a turbidity current experience ignition for some time, but ultimately die out.

Through the analysis provided in this and the previous section, we have shown that the erosional model predicts ignitive currents for both $S > S_c$ and $S < S_c$ when the slope is constant. In the next section we will let the slope be a mono-

[2]Case IB gives a very similar solution to IC, with the only difference noticeable close to $s = 0$ where the boundary condition is influencing the solution. Away from the boundary, at $s = 10$, the solution appears identical to that of Case IC.

tonically decreasing function of s, the downstream distance, with the expectation that this will allow us to eliminate the ignition line and result in extinction of erosive turbidity currents downstream.

2.5.4 Varying the slope with downstream distance

In Section 2.2.1, we looked at the steady state turbidity model and hypothesised that ignition could be controlled if the underlying slope is decreased beyond the constant value S_c. This resulted in the spiral sink being removed from the phase plane but resulted in the trajectories in the phase plane terminating on the ignition line.

To better understand the dynamics of equation (2.75) as S decreases downstream, we model the slope S as a function of downstream distance. We choose the following monotonically decreasing function,

$$S(s) = \frac{\exp(-s)}{1+\exp(-s)}, \tag{2.84}$$

after Zammett (2008). The erosional model is now given by equations (2.76) with $S = S(s)$. With the slope modelled in this way, U_∞ is now decreasing with distance downstream, and $U_\infty \to 0$ as $s \to \infty$. We show the phase plane of equations (2.80b) and (2.80c) for $S = S(s)$ in Figure 2.17, marking the fixed point, $\mathbf{\Psi}$, by a red star.

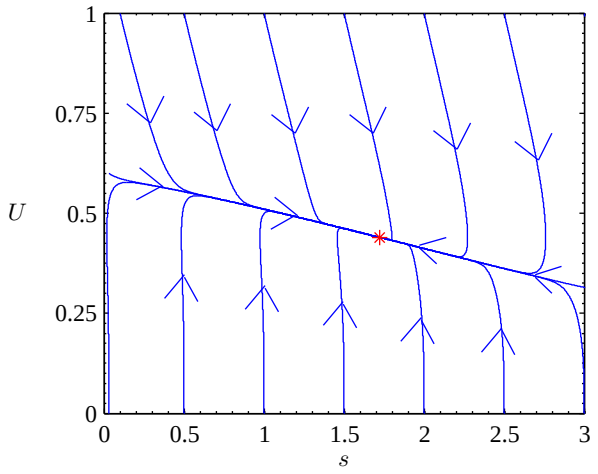

Figure 2.17: Phase plane diagram of equations (2.80b) and (2.80c) with the slope given by equation (2.84). There is a single fixed point marked by a red star at $\mathbf{\Psi} = (s_\star, U_c) = (1.72, 0.44)$. Parameter values are given in Figure 2.13.

We suppose that $U_\infty = U_c$ at $s = s_\star$. We can consider the stability of the point U_c, which is now a unique fixed point at $\mathbf{\Psi} = (s_\star, U_c)$. We calculate the Jacobian matrix $\mathbf{A}$ of equations (2.80b) and (2.80c) at the unique fixed point:

$$\mathbf{A} = \begin{pmatrix} V_s & V_U \\ R_s & R_U \end{pmatrix}_{(s_\star, U_c)} \tag{2.85a}$$

$$= \begin{pmatrix} 0 & \dfrac{U_c^2(3U_c^2\Lambda - \delta)}{1 + \nu U_c^3} \\ S'(s_\star) & -\dfrac{U_c^2((3+2\delta) + U_c^3(4\Lambda + 3\nu)(2 + \nu U_c^2))}{(1 + \nu U_c^3)^2} \end{pmatrix} \tag{2.85b}$$

We find

$$\text{tr } \mathbf{A} < 0, \tag{2.86a}$$

$$\det \mathbf{A} = -S'(s_\star)\frac{U_c^2(3U_c^2\Lambda - \delta)}{1 + \nu U_c^3}. \tag{2.86b}$$

We recall that $U_c = (\delta/\Lambda)^{1/3}$ and note the values of the parameters from Table 2.1. We find that $U_c^2(3U_c^2\Lambda - \delta) > 0$ (provided $\Lambda > \delta/27$, which is true for the values of the parameters listed in Table 2.1) and we know that $S'(s_\star) < 0$, since $S'(s) < 0$, by assumption for all s. Hence, $\det \mathbf{A} > 0$. On calculating the eigenvalues, $\lambda_{1,2}$ of the fixed point we find $\lambda_1, \lambda_2 < 0$, hence $\mathbf{\Psi}$ is a stable node.

In the phase plane all trajectories terminate at the point $\mathbf{\Psi}$, the stable node in the phase plane. Along the trajectories, $U \to U_\infty$, and $U_\infty \to U_c$ as s increases (or decreases, depending on whether we started upstream or downstream of the fixed point). In terms of the solution to equation (2.76), this means that, as the parametric variable, τ, increases, the characteristics both upstream and downstream of $s_\star$ approach the fixed point, at which $S = S_c$ and $U_\infty = U_c$. We plot the characteristic diagrams for the erosional model with a varying downstream slope in Figure 2.18. The characteristic curves are plotted by solving equations (2.80) explicitly. We mark by a dashed black line the point $s = s_\star$. The parametric variable τ is given by

$$\tau = \int e^{-s/3}\,\mathrm{d}t, \tag{2.87}$$

and thus as all characteristics tend towards the point $s = s_\star$ as $t \to \infty$.

In Figure 2.18 we see that for $s < s_\star$ the characteristics have a positive slope towards $s = s_\star$ and for $s < s_\star$ the characteristics have a negative slope towards $s = s_\star$ (ignoring early time behaviour). We might suspect a shock at $s = s_\star$,

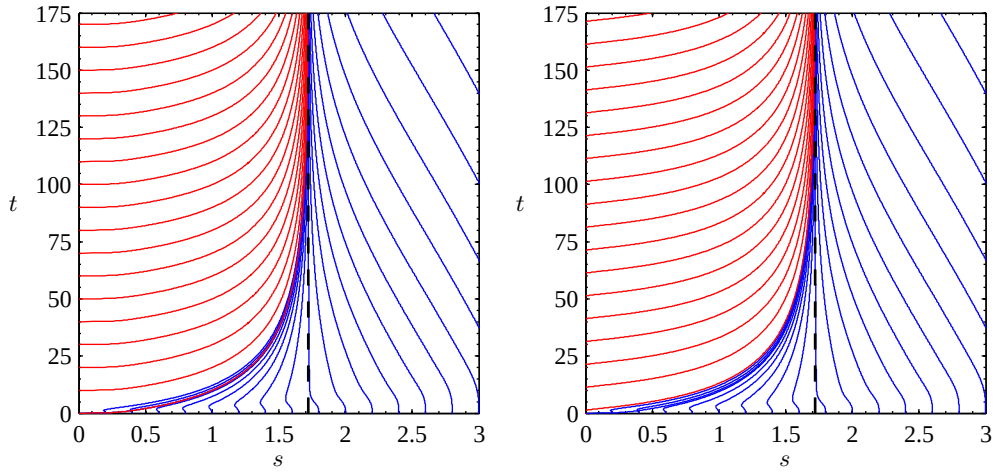

(a) $U_i = 1$ (b) $U_i = 0$

Figure 2.18: Method of characteristics for equation (2.80). The slope function, $S(s)$ is given in equation (2.84). The initial condition is given by (2.44) and the boundary conditions are (a) $U_i = 1$ at $s = 0$ and (b) $U_i = 0$ at $s = 0$. We mark by a black dashed line the point $s = s_\star$. Parameter values are given in Figure 2.15.

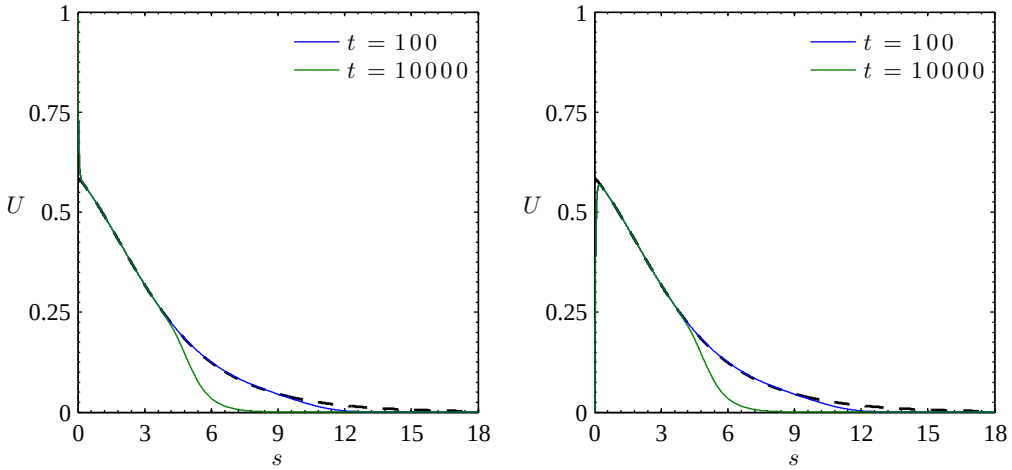

(a) $U_i = 1$ (b) $U_i = 0$

Figure 2.19: Solution to equation (2.88) where the slope is given by equation (2.84) and we take $\epsilon = 0.005$. We show the solution at $t = 100$ and $t = 10000$. The black dashed line shows the limiting steady state solution $U_\infty(s)$. The initial condition was given by equation (2.44) and the boundary conditions are listed in the subcaptions. Parameter values are given in Figure 2.15.

but in fact the characteristics tend towards this point as $t \to \infty$ and they do not intersect in finite time. From Figure 2.18 we expect a steady state profile to develop for large values of t. This steady profile is given by $U = U_\infty(s)$; the s-dependent steady state solution of the equation $R(U_\infty, S(s)) = 0$.

Whilst no shock is formed in the erosional model at $s = s_\star$, there is a shock in the solution close to $s = 0$. To see this we solve equation (2.76) with added numerical diffusion,

$$e^{s/3}\frac{\partial U}{\partial t} + V(U)\frac{\partial U}{\partial s} = R(U, S(s)) + \epsilon\frac{\partial^2 U}{\partial s^2}, \qquad (\mathbf{2.88})$$

where $\epsilon \ll 1$ is a diffusion coefficient. In Figure 2.19 we show that the numerical solution to equation (2.88) and the steady state profile, $U_\infty(s)$.

In Figure 2.19, we see that $U \to U_\infty(s)$ as $t \to \infty$, except near $s = 0$ where a shock persists. Looking ahead to Chapter 3, this is a feature of the numerical solutions for different slope profiles that we will continue to see; a boundary layer close to $x = 0$ will be associated with the flow moving from a supercritical to subcritical regime (or vice versa) caused because the solution must match the boundary conditions at $x = 0$ to the behaviour of the solution for the slope profile imposed.

The steady state profile $U_\infty(s)$ shows that $U_\infty(s) \to 0$ as $s \to \infty$. Since s is a function of q, then in the limit $q \to \infty$, (and thus, $h \to \infty$) we can say that $U_\infty \to 0$. The flux q is known to be an increasing function of x, see equation (2.24), and thus we can say that the current will become extinct with distance downstream; $U_\infty \to 0$ as $x \to \infty$.

By modelling the slope as a decreasing function of s we have eliminated the advancing front from the solution. This advancing front resulted in currents which ignited for constant S in both the cases $S > S_c$ and $S < S_c$.

2.6 Discussion

We began this chapter by nondimensionalising the Parker model to derive a dimensionless system where we balance the processes of erosion and deposition. With this model we examined the steady state solutions of the momentum and turbulent kinetic energy equations in terms of two scaled quantities, U and K. We discussed the processes of erosion and ignition using phase plane analysis, which are shown by trajectories that terminate at $(U, K) = (0, 0)$ and at $\mathbf{\Sigma}$, the

spiral sink, respectively. We determined a critical value of the slope, $S = S_c$, at which the steady state model undergoes a bifurcation and the stability of the equations changes. We found that at $S = S_c$, $U = U_c$ and the wave speed of the momentum equation is zero. The importance of this critical point can only be understood fully by looking at the time dependent model.

In Section 2.3.1 we derived a one-equation velocity model from the momentum equation. We split this model into two forms, corresponding to a depositional and an erosional model, by taking $c = 0$ and $c = 1$, respectively. The depositional model was investigated using the method of characteristics, and we found that shocks form in the solution. We investigated the parameter space of the depositional model, and solved the equation with an added viscous term to smooth out shocks in the solution. We found that for both 'slump' and 'steady inflow' boundary conditions, $U \to 0$ as $s \to \infty$.

In Section 2.5 we discussed the erosional model, which has zero wave speed at the critical slope value $S = S_c$. We found that erosional currents undergo ignition, whereby the velocity tends to a constant (non-zero) value at every point away from the inlet. This ignition state corresponds to a turbidity current which does not die out. We found that when we model the slope by a constant, we can not prevent ignition from occurring, regardless of whether $S > S_c$ or $S < S_c$. An advancing front is always present in the solution and, as this front moves downstream, the velocity remains constant and non-zero.

In Section 2.5.4 we considered modelling the slope as a decreasing function of downstream distance. We found that in this case the value of U at the fixed point decreases with distance downstream. This means that the current approaches a steady profile and becomes extinct as $t \to \infty$ and $s \to \infty$.

A particular failing in the one-equation model is that the surrogate space variable used, $s = \ln(q)$, is discontinuous. This variable was introduced so that the one-equation model could be derived in the simplest form possible however, in real space q is varying with distance downstream and since the solution to both the depositional model and the erosional model is discontinuous, the space variable s is discontinuous also. This simplification means that the one- equation model loses credibility when it encounters a shock. In the following chapter, we will relax some of the assumptions that we have used in this chapter in order to derive a more realistic model that will consider the interaction of conservation of mass and momentum. However, we will find that the behaviour of the simple model presented here persists. In particular, we will see that the critical value of the slope $S = S_c$ will be important throughout this thesis in determining

the ignitive and extinctive dynamics of the model. Moreover, the 'ignition line' found in the phase plane analysis of Section 2.2.1 can be interpreted in terms of a transition between supercritical and subcritical flow. Finally, the numerical features found in the solution to the one-equation model will also reoccur in the following chapters; we will find that shocks are predicted in the solutions to each of the models we will study and in the next chapter we will highlight that the boundary layer behaviour found in the solutions to equation (2.76) will also be a feature of the two-equation model and is again associated with a transition between supercritical and subcritical flow regimes.

Chapter 3

A two-equation shallow-water model for turbidity currents

In this chapter we investigate a reduced form of the Parker model for turbidity currents. We begin by rescaling the Parker model with respect to a large downstream length scale before reducing it to a system of two equations. We will focus on the conservation equations for mass and momentum, eliminating the equations for sediment concentration (by assuming it to be constant) and the turbulent kinetic energy (by writing it as a function of the other variables). The reduced model will allow us to investigate how the flow regime is influenced by changes in the slope of the sea bed, and how the system behaves as the current moves from being supercritical to subcritical. This chapter will act as a stand-alone description of a shallow- water type set of equations but will also lead into our investigation of the full four-equation model in the next chapter.

3.1 The Parker model with a large downstream length scale

We recall the full Parker model in dimensional form from Chapter 1, given by equations (1.3), (1.4), (1.7) and (1.8). The erosion rate and entrainment rate are given, respectively, by equations (1.14) and (1.18). Once again, the quantities v_s, r_0, R and g are assumed to be constant. Typical values of all constants used in this nondimensionalisation are given in Table 2.2 of Chapter 2.

We begin by prescribing the horizontal length scale for x, and the slope scale

for S,

$$x = lx^\star, \qquad\qquad S = S_0 S^\star. \tag{3.1}$$

This is done so that the model is scaled with respect to the continental slope, which has a typical length $l \sim 60$ km and gradient $\theta = 3°$. The slope scale is thus $S_0 = 0.05$ ($S = \sin\theta$).

The remaining variables are nondimensionalised as follows:

$$h = h_0 h^\star, \qquad u = u_0 u^\star, \qquad t = \left(\frac{l}{u_0}\right) t^\star, \qquad c = c_0 c^\star, \qquad k = k_0 k^\star, \tag{3.2}$$

where the zero subscript represents the scale, and the star denotes the dimensionless variable. The scalings are chosen to balance (*i*) the left- and right-hand sides of (1.3); (*ii*) the left-hand side of (1.4) with the forcing term proportional to S; (*iii*) the left-hand side of (1.7) with the forcing term proportional to E_s; (*iv*) the second two terms on the right-hand side of (1.8). These lead to the following scales,

$$h_0 = \sqrt{pS_0}\,l \approx 520\,\mathrm{m}, \qquad\qquad u_0 = \left(\frac{RgE_0 v_s \sqrt{S_0}\,l}{\sqrt{p}}\right)^{1/3} \approx 25\,\mathrm{m\,s^{-1}}, \tag{3.3a}$$

$$c_0 = \left(\frac{E_0^2 v_s^2}{pRgS_0^2 l}\right)^{1/3} \approx 0.0125, \qquad t_0 = \left(\frac{l^2\sqrt{p}}{RgE_0 v_s \sqrt{S_0}}\right)^{1/3} \approx 40\,\mathrm{mins}, \tag{3.3b}$$

$$k_0 = \left(\frac{RgE_0 v_s S_0 l}{\beta}\right)^{2/3} \approx 41.8\,\mathrm{m^2\,s^{-2}}. \tag{3.3c}$$

Dropping the stars on the dimensionless variables, $h^\star$, $u^\star$, $c^\star$, $k^\star$, the Parker model becomes:

$$\frac{\partial h}{\partial t} + \frac{\partial (hu)}{\partial x} = e^\star u, \tag{3.4a}$$

$$\frac{\partial (hu)}{\partial t} + \frac{\partial (hu^2)}{\partial x} = -\frac{1}{2}\delta \frac{\partial (h^2 c)}{\partial x} + Shc - \gamma k, \tag{3.4b}$$

$$\frac{\partial (hc)}{\partial t} + \frac{\partial (hcu)}{\partial x} = E^\star - \chi c, \tag{3.4c}$$

$$\Gamma\left[\frac{\partial (hk)}{\partial t} + \frac{\partial (hku)}{\partial x}\right] = \gamma k u - k^{3/2} + \frac{1}{2}u^3 e^\star - \frac{\delta h}{2}\left(\frac{2\chi c}{r_0} + cue^\star + E^\star - \chi c\right). \tag{3.4d}$$

The dimensionless erosion rate is given by

$$E^\star = H(k-P) = \begin{cases} 1 & \text{if } k > P, \\ 0 & \text{if } k \leq P, \end{cases} \tag{3.5}$$

where $H(\cdot)$ denotes the Heaviside function, and the dimensionless entrainment rate is given by

$$e^\star = \frac{u^2}{ch + \nu u^2}. \tag{3.6}$$

The model parameters are

$$\nu = \sqrt{\frac{m^2 S_0}{p}} \approx 0.12, \qquad \delta = \sqrt{\frac{p}{S_0}} \approx 0.17, \tag{3.7a}$$

$$\gamma = \left(\frac{c_D}{\sqrt{pS_0}}\right)^{1/3} \approx 0.77, \qquad \chi = \frac{r_0 v_s^{2/3}}{(S_0^2 E_0 pRgl)^{1/3}} \approx 0.067, \tag{3.7b}$$

$$P = \frac{Z_m^2 \sqrt{pS_0}\chi^2}{R_p r_0^2 \gamma} \approx 8.4 \times 10^{-4}, \qquad \Gamma = \frac{\sqrt{pS_0}\gamma}{\alpha} \approx 0.067. \tag{3.7c}$$

The Froude number of the flow is

$$Fr = \frac{u_0}{\sqrt{Rgh_0}} = \frac{1}{\sqrt{\delta}}. \tag{3.8}$$

3.2 Derivation of the shallow-water model

In this chapter we will reduce the Parker model (3.4) to a system of two pdes and one algebraic expression. We do this by making use of small parameters and by using a simplified description of the variables k and c.

As the flow moves down the slope, we assume that the current has evolved such that the sediment concentration has reached equilibrium with a balance between erosion and deposition, so that

$$c \approx \frac{E^\star}{\chi} = \text{ constant}. \tag{3.9}$$

This basic simplification allows us to focus on the behaviour of the other variables, but it does restrict our discussion of extinction, since we require $c \to 0$ for the current to become extinct. Extinction will be discussed in terms of the shallow-water model for turbidity currents further, in Section 3.7.2.

Assuming that c is constant in equations (3.4), we are now left with three equations for mass, momentum and turbulent kinetic energy,

$$h_t + (hu)_x = \frac{u^3}{ch}, \tag{3.10a}$$

$$(hu)_t + (hu^2)_x = -\delta chh_x + Shc - \gamma k, \tag{3.10b}$$

$$0 = \gamma ku - k^{3/2} + \frac{u^5}{2ch}, \tag{3.10c}$$

where we have neglected the small parameters Γ and P in equation (3.4d), along with the parameter ν which is only relevant when c is very small. We have retained the δ term in equation (3.10b) as it represents buoyancy, which is an important effect in the momentum equation. However, we neglect the δ term from equation (3.4d) which gives a simpler algebraic equation (3.10c) for k. Our aim is to obtain the simplest model that retains the important qualitative features of the full system. We will consider the effect of including the δ term in (3.10c) later, in Section 3.7.1.

We present a particular normalisation of the model where we scale the variables h, u, S, k and t with respect to c;

$$h \sim \tilde{h}c^{-1/4}, \quad u \sim \tilde{u}c^{1/4}, \quad k \sim \tilde{k}c^{1/3}, \quad t \sim \tilde{t}c^{-1/4}, \quad S \sim \tilde{S}c^{1/2}, \tag{3.11}$$

and so the parameters in the model become

$$\delta = \tilde{\delta}c^{1/4}, \qquad \gamma = \tilde{\gamma}c^{-1/12}. \tag{3.12}$$

This normalisation is equivalent to choosing $c = 1$ in equations (3.10), and so we will assume c takes the constant value $c = 1$ for the rest of this chapter.

We have now derived the simplified shallow-water model for turbidity currents. It consists of two pdes for h and u and an algebraic equation for k:

$$h_t + (hu)_x = \frac{u^3}{h}, \tag{3.13a}$$

$$(hu)_t + (hu^2)_x = -\delta hh_x + Sh - \gamma k, \tag{3.13b}$$

$$0 = \gamma ku - k^{3/2} + \frac{u^5}{2h}. \tag{3.13c}$$

The solution to (3.13c) for k is given by

$$k = \left(\frac{u^5}{2h}\right)^{2/3} \Phi(\xi), \quad \text{where} \quad \xi = \gamma \left(\frac{2h}{u^2}\right)^{1/3}, \tag{3.14}$$

and

$$\Phi(\xi) = \frac{\xi^2}{3} + \left(\frac{1}{2} + \frac{\xi^3}{3} + \frac{\xi^6}{27} + \sqrt{\frac{1}{4} + \frac{\xi^3}{27}}\right)^{1/3} + \left(\frac{1}{2} + \frac{\xi^3}{3} + \frac{\xi^6}{27} - \sqrt{\frac{1}{4} + \frac{\xi^3}{27}}\right)^{1/3}. \tag{3.15}$$

Thus equation (3.13c) can be rewritten as

$$0 = \xi\Phi - \Phi^{3/2} + 1. \tag{3.16}$$

and we note that ξ is a function of $u/\sqrt{h}$. Equation (3.15) is plotted in Figure 3.1. We find that

$$\Phi \to \xi^2 \quad \text{as} \quad \xi \to \infty, \tag{3.17}$$

and thus

$$k = \frac{\gamma^2 u^2}{\xi^2}\Phi(\xi) \to \gamma^2 u^2 \quad \text{as} \quad \frac{u}{\sqrt{h}} \to 0. \tag{3.18}$$

In addition, $\Phi(0) = 1$ and

$$\Phi \to 1 + \frac{2}{3}\xi \quad \text{as} \quad \xi \to 0. \tag{3.19}$$

Hence, to leading order,

$$k \sim \left(\frac{u^5}{2h}\right)^{2/3} \quad \text{as} \quad \frac{u}{\sqrt{h}} \to \infty. \tag{3.20}$$

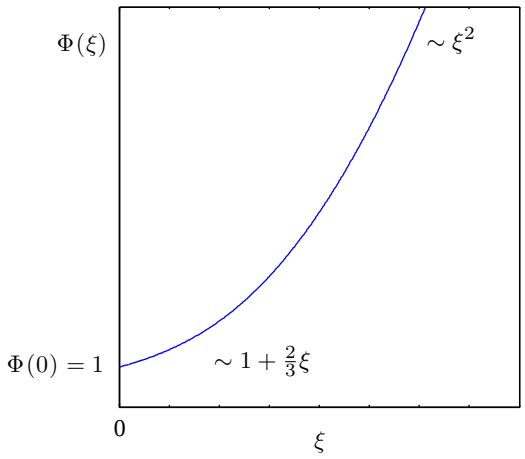

Figure 3.1: A plot of the function $\Phi(\xi)$, equation (3.15), for $\xi > 0$.

Comment on the two-equation model

As was noted during the discussion of the one-equation model, similarly, the two-equation model is not an asymptotic reduction of the full system, but, rather, is a shallow-water model derived by considering terms of importance in the four-equation Parker model. Once again, this system can provide insight into the four-equation model through the mathematical features it displays for different slope profiles and it is also an interesting system to study in its own right.

3.3 The steady state model

We begin by studying the steady state version of the shallow-water model (3.13). This is given by equations

$$\frac{d(hu)}{dx} = \frac{u^3}{h}, \tag{3.21a}$$

$$\frac{d(hu^2)}{dx} = -\delta h \frac{dh}{dx} + Sh - \gamma k, \tag{3.21b}$$

which, upon rearranging, determine two odes for h and u, namely

$$\frac{dh}{dx} = \frac{Sh - \gamma k - \frac{2u^4}{h}}{(\delta h - u^2)}, \tag{3.22a}$$

$$\frac{du}{dx} = -\frac{u(Sh - \gamma k - \frac{u^4}{h} - \delta u^2)}{h(\delta h - u^2)}. \tag{3.22b}$$

By allowing the slope S to vary, we change the magnitude of the forcing term in equations (3.22). In Figure 3.2, we plot the phase plane for the system (3.22) showing how the behaviour of the equations changes for different constant values of S.

In Figure 3.2, the nullclines of equations (3.22) are plotted as red dashed lines. These nullclines are functions of the slope, S, and so their positions in the phase plane change for different values of S. In Figure 3.2 we have also plotted, in black, the singularity line given by

$$\delta h - u^2 = 0, \qquad \text{or when} \qquad F = 1, \tag{3.23}$$

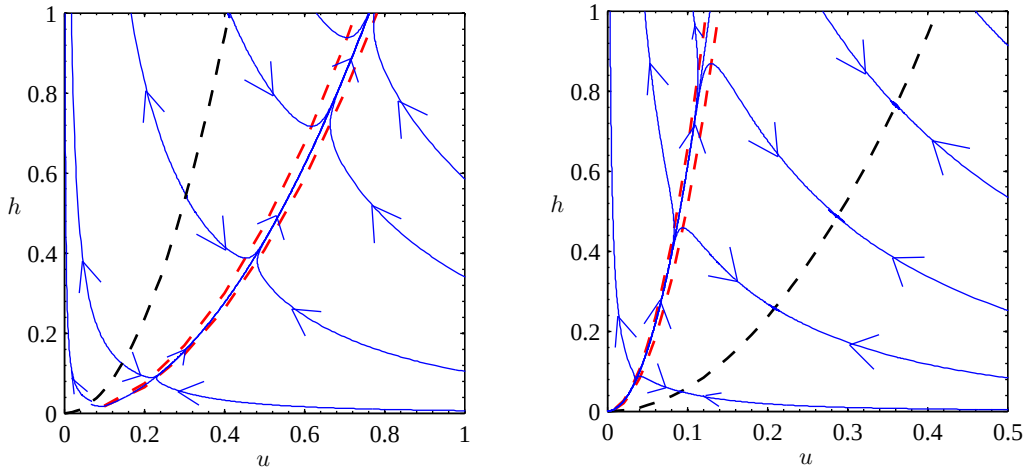

(a) Constant slope; $S = 1$

(b) Constant slope; $S = 0.01$

Figure 3.2: The phase portrait of the steady state equations (3.22). The nullclines are plotted as red dashed lines. The black dashed line is a singularity line for both equations. The blue lines show the trajectories and the arrows indicate the direction of flow. Parameter values are $\delta = 0.17, \gamma = 0.77$.

where we define the *local Froude number* as

$$F = \frac{u}{\sqrt{\delta h}} = \frac{u}{\sqrt{h}} Fr. \tag{3.24}$$

The local Froude number will help us understand the flow regime we are in. The phase planes shown in Figure 3.2 are each separated into two regions by the line $F = 1$. To the right of this line $F > 1$ and the flow is in a high velocity regime — we say the current is locally supercritical. To the left of this line, $F < 1$ and the flow is in a low velocity regime — we say the current is locally subcritical. The line $F = 1$ is fixed in the phase plane and the direction of the trajectories is reversed as we cross it.

In Figure 3.2(a), the slope is given by $S = 1$. Trajectories which begin in the supercritical region of the phase plane correspond to currents which have supercritical initial conditions. These currents have increasing values of h and u as they propagate downstream. Trajectories which begin in the subcritical region of the phase plane correspond to currents with subcritical initial conditions. These currents have increasing values of h as they propagate downstream, and values of the velocity, u, which are tending to zero.

In Figure 3.2(b), the slope is given by $S = 0.01$. Currents with initial conditions in the supercritical region of the phase plane correspond to trajectories which

terminate on the line $F = 1$. Currents with initial conditions in the subcritical region of the phase plane correspond to trajectories which either terminate on the line $F = 1$, or have increasing values of h as they propagate downstream and values of u which are tending to zero.

There is a unique value of the slope, given by $S = S_c$, where the nullclines and singularity line are identically equal and coincide in the phase plane. We illustrate this situation in Figure 3.3. We can see in Figure 3.3 that all trajectories will eventually tend towards $u = 0$ but have non-zero values of the depth, h.

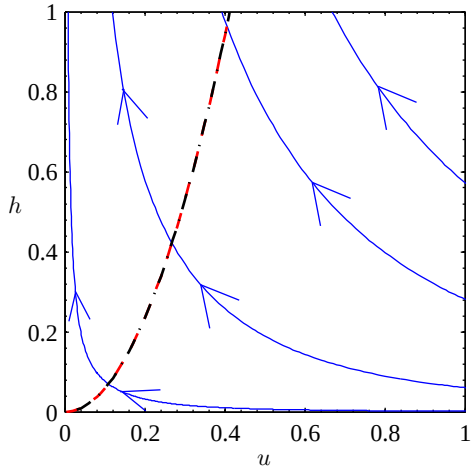

Figure 3.3: The phase portrait of the steady state equations (3.22) with $S = S_c$. The nullclines are plotted as red dashed lines. The nullclines lie on the singularity line, indicated by the black dashed curve. The blue lines show the trajectories and the arrows indicate the direction of flow. The parameter values are $\delta = 0.17, \gamma = 0.77$.

We can calculate the critical value of the slope, $S = S_c$, by setting the numerators in equations (3.22) to be equal to zero and solving for S. We find,

$$Sh - \gamma k = \frac{2u^4}{h} = \frac{u^4}{h} + \delta u^2 \qquad \Rightarrow \qquad Sh = 2\delta u^2 + \gamma k, \tag{3.25}$$

and since $\delta h = u^2$ on the singularity line,

$$S_c = 2\delta^2 + \gamma \frac{\delta^{5/3}}{2^{2/3}} \Phi \left(\gamma \left(\frac{2}{\delta} \right)^{1/3} \right). \tag{3.26}$$

With $\delta = 0.17$ and $\gamma = 0.77$ we calculate

$$S_c = 0.159. \tag{3.27}$$

At $S = S_c$ a bifurcation occurs and changes the stability of the phase plane. Regardless of whether $S > S_c$ or $S < S_c$, there are always trajectories in the phase plane of equations (3.22) which terminate at $F = 1$, except in the special case, $S = S_c$, as illustrated in Figure 3.3. When trajectories terminate on the line $F = 1$, there is a singularity in equations (3.22) and the steady state model breaks down unless we allow discontinuous solutions (shocks). The nature of the flow changes dramatically as we move across the singularity line; it corresponds to a transition between supercritical and subcritical flow (or vice versa).

Our understanding of the shallow-water model is limited by the existence of the singularity line in the steady state equations. We will therefore move on to examine solutions to the time-dependent equations.

3.4 The time dependent model with viscous dissipation

The time-dependent model with turbulent viscous dissipation is

$$h_t + (hu)_x = \frac{u^3}{h}, \tag{3.28a}$$

$$(hu)_t + (hu^2)_x = -\delta h h_x + Sh - \gamma k + \epsilon (hu_x)_x, \tag{3.28b}$$

$$0 = \gamma k u - k^{3/2} + \frac{u^5}{2h} \tag{3.28c}$$

where $\epsilon \approx 10^{-5}$ is a dimensionless eddy viscosity and k is given by the solution to equation (3.28c), or, algebraically, by equations (3.14) and (3.15). We have included a diffusive term in equations (3.28c) to smooth any shocks and to make the numerical solution easier to compute.

We solve for $x \in [0, x_R]$, where $x_R > 0$, and for $0 < t < T$ for some large time T. We specify a fine mesh in x which allows for optimal computation time without loss of accuracy. We solve the pdes using the inbuilt pde solver *pdepe* in MATLAB.

3.4.1 Initial and boundary conditions

The initial conditions are given as functions of x by

$$h(x,0) = h_0(x) = h^\star\left(1 + \tanh[a(b-x)]\right), \tag{3.29a}$$

$$u(x,0) = u_0(x) = u^\star\left(1 + \tanh[a(b-x)]\right), \tag{3.29b}$$

for $x > 0$ and constants $h^\star, u^\star, a, b$. These initial conditions are intended to reflect a 'raft' of material at the left of the domain which has a given height and velocity at $t = 0$.

The boundary conditions at $x = 0$ will be constant (*i.e.* not time dependent) and we will focus on the 'steady inflow' problem (as described in Chapter 2), representing a continuously-fed fluvial system. At the right hand boundary ($x = x_R > 0$) we specify a condition on u only, specifically, for all $t > 0$, we let

$$h = h_i = h^\star\left(1 + \tanh[ab]\right), \quad u = u_i = u^\star\left(1 + \tanh[ab]\right) \qquad \text{at } x = 0, \tag{3.30a}$$

$$\frac{\partial u}{\partial x} = 0 \qquad \text{at } x = x_R. \tag{3.30b}$$

3.5 Solution of the shallow-water model for constant downstream slope

In this section we model the slope as a constant. We let S take values in the range $0 < S < 1$ and study the two cases $S > S_c$ and $S < S_c$. We will use the method of characteristics to determine the characteristic wave speeds of equations (3.28) when $\epsilon = 0$, and we will solve the pde model numerically when $0 < \epsilon \ll 1$.

3.5.1 Method of characteristics

We consider equations (3.28) in matrix form with $\epsilon = 0$:

$$\frac{\partial}{\partial t}\begin{pmatrix} h \\ u \end{pmatrix} + \begin{pmatrix} u & h \\ \delta & u \end{pmatrix}\frac{\partial}{\partial x}\begin{pmatrix} h \\ u \end{pmatrix} = \begin{pmatrix} \frac{u^3}{h} \\ S - \gamma\frac{k}{h} - \frac{u^4}{h} \end{pmatrix}. \tag{3.31}$$

This allows us to determine the characteristic wave speeds, $\lambda_\pm$, namely the eigenvalues of the 2×2 matrix above (Fowler, 1997). The characteristic wave

speeds are

$$\lambda_{\pm} = \frac{dx}{dt} = u \pm \sqrt{\delta h} = \sqrt{\delta h}(F \pm 1). \tag{3.32}$$

If $F > 1$, then $\lambda_{\pm} > 0$, and nonlinear waves will all propagate downstream. However, if $F < 1$ then $\lambda_{+} > 0$ but $\lambda_{-} < 0$, hence nonlinear waves will propagate both upstream and downstream.

Method for plotting the characteristic curves As we will see in the following sections, the two-equation model admits shocks when the slope takes a value $S < S_c$. This is because the flow is forced to move into a subcritical regime from the supercritical inlet conditions posed at $x = 0$. Since solving the hyperbolic model (3.31) for the characteristics and the shock structure is difficult, the characteristics of the model will be calculated using the system of equations with diffusion (3.28). This will produce the shock structure automatically, and the sub- characteristics shown will still be given by $\lambda = u \pm \sqrt{\delta h}$. As the subcharacteristics approach the shock, they will bend upwards to follow the shock over a small region, since they are prevented from intersecting by the presence of the diffusive term ϵ, which acts to smooth the solution of the model. Away from the shock the subcharacteristics of the diffusion model (3.28) agree with the characteristics of the hyperbolic system (3.31).

We will plot the characteristic curves of the system in Section 3.5.2 for $S > S_c$ and in Section 3.5.3 for $S < S_c$.

3.5.2 Numerical solution for currents on a steep slope

Equations (3.28) are solved for the case $S = 1 > S_c$ and the solutions for h and u are shown in Figure 3.4. As can be seen in Figure 3.4, h and u are increasing in time and space. There is a disturbance in the solution related to the particular initial condition that was imposed at $t = 0$. In addition, h and u are attaining high values across the domain. This is a result of the constant inflow boundary condition that has been specified at $x = 0$.

The characteristics of the two-equation model are given by equations (3.32). The sub-characteristics are plotted in Figure 3.5; these are the curves defined by the characteristic equations (3.32), but plotted using the solutions to the shallow-water model with diffusion (3.28). All the characteristic curves shown in Figure 3.5 have positive slope which confirms that nonlinear waves are propagating downstream and that the current remains in a supercritical regime for

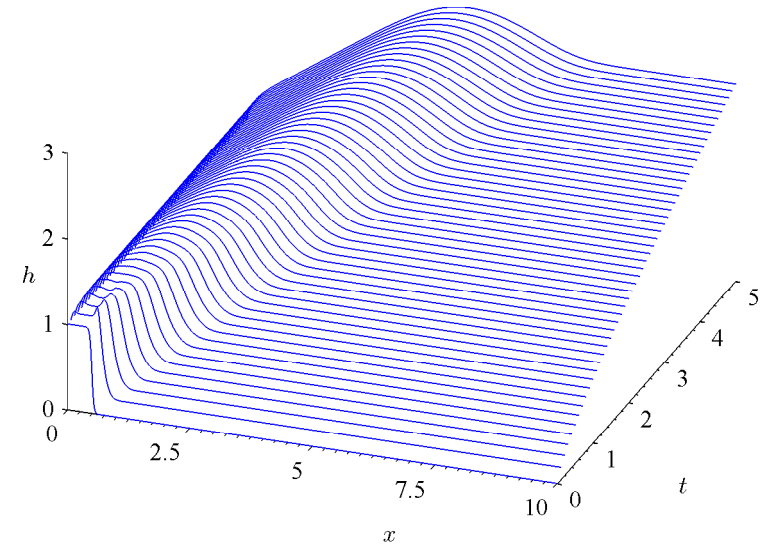

(a) Solution for h

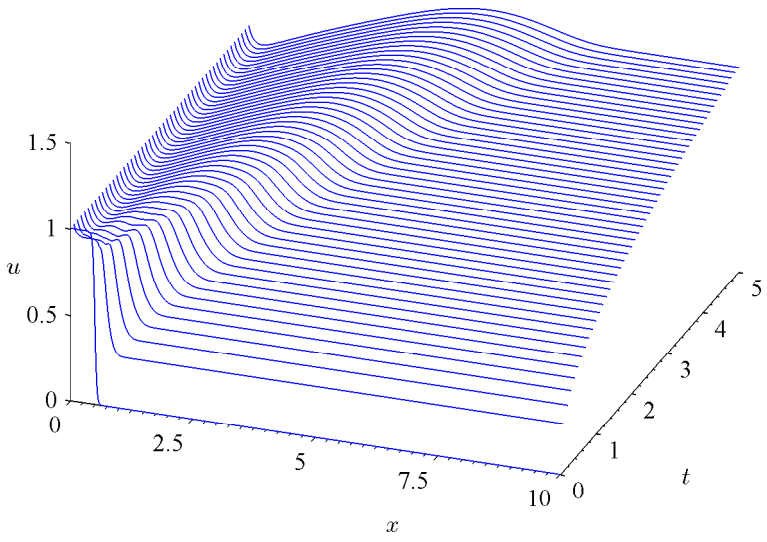

(b) Solution for u

Figure 3.4: Solution to equations (3.28) for $S = 1$ and $x \in (0, 10)$, $t \in (0, 5)$. The initial conditions are given by (3.29) and the boundary conditions by (3.30). The parameter values are $\gamma = 0.77$, $\delta = 0.17$, $h^\star = 0.5$, $u^\star = 0.5$, $a = 25$, $b = 0.5$. The diffusion coefficient is $\epsilon = 0.01$.

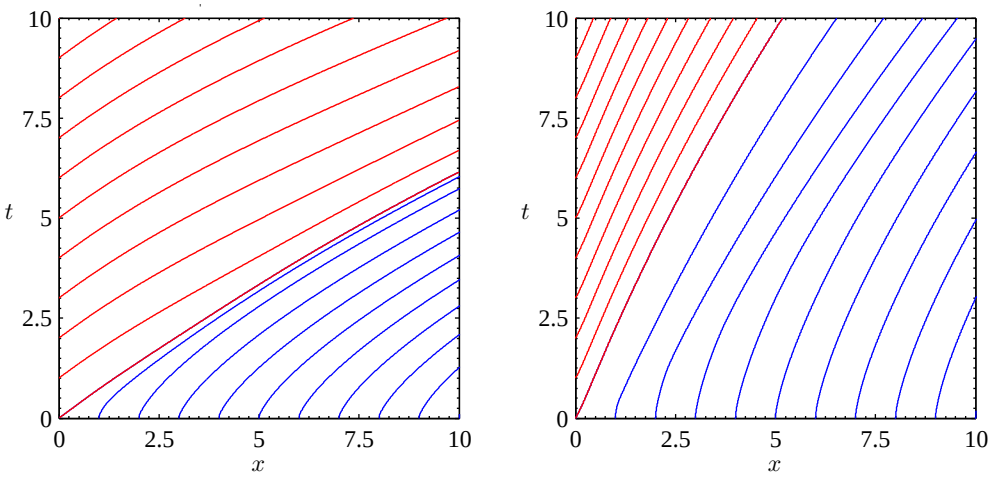

(a) $\lambda_+ = u + \sqrt{\delta h}$ (b) $\lambda_- = u - \sqrt{\delta h}$

Figure 3.5: Sub-characteristics (3.32) of equations (3.28) when $S = 1$ and $\epsilon = 0.01$. The blue characteristic curves are given by the initial conditions (3.29) and the red characteristic curves are given by the boundary conditions (3.30). The parameter values are given in Figure 3.4.

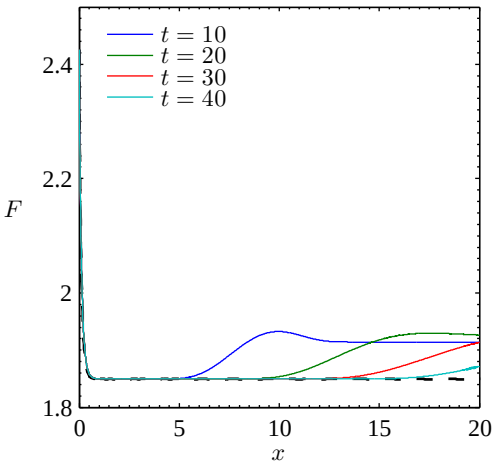

Figure 3.6: The Froude number, $F = u/\sqrt{\delta h}$, when $S = 1$. The steady state is plotted as the black dashed line, this is calculated from equations (3.22). The numerical solutions to equations (3.28) are plotted as solid lines. The parameter values are given in Figure 3.4.

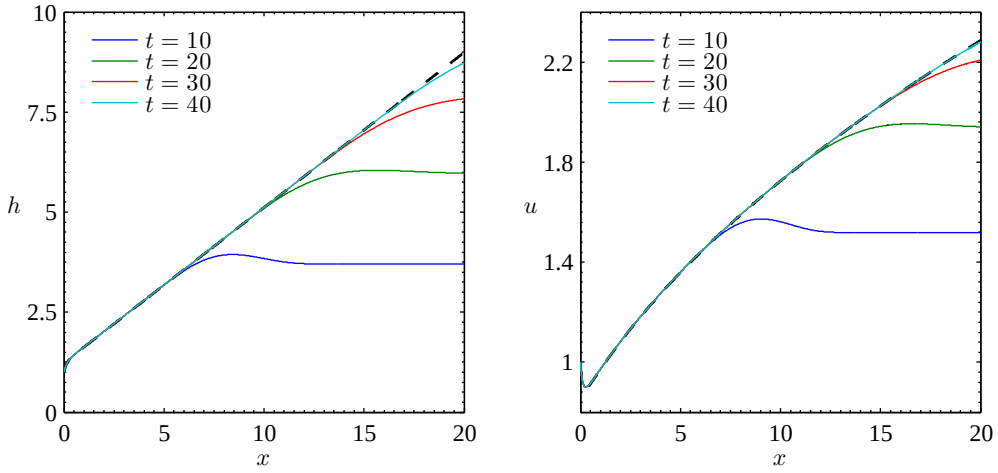

(a) h approaching the steady state

(b) u approaching the steady state

Figure 3.7: The steady state solutions of h and u calculated for equations (3.22) when $S = 1$. We show the steady state solution in black, and the numerical solutions to equations (3.28) as solid lines. The parameter values are given in Figure 3.4.

all time. This is verified by plotting the Froude number of the flow in Figure 3.6; we see that $F > 1$ for all t.

We calculate the steady state values of h and u using the steady state equations (3.22) with $S = 1$. This solution is plotted in Figure 3.7, and for the Froude number in Figure 3.6. As t increases, we will see that h and u approach the steady state values at every point downstream. As we can see in Figure 3.7, the steady state of h and u are increasing functions of downstream distance; $h, u \to \infty$ as $x \to \infty$. We interpret this as a current which is igniting.

3.5.3 Numerical solution for currents on a shallow slope

In this section we will determine numerical solutions to the shallow-water model (3.13) for the case $S = 0.1 < S_c$. In Figure 3.8 we plot the solution to equations (3.28); the shallow-water model with viscous dissipation. Once again, we see that the solutions h and u are increasing in time and we can see a disturbance in the solution associated with the initial condition imposed at $t = 0$. By comparing the solutions for $S = 0.1$ in Figure 3.8 with the solutions for $S = 1$ in Figure 3.4, we can see that when $S < S_c$ the solutions h and u evolve more slowly towards lower values downstream.

The boundary condition at $x = 0$ is still given by $h_i = u_i = \frac{1}{2}(1+\tanh(ab)) \approx 1$, and so h and u take relatively large values on the boundary. Because the current

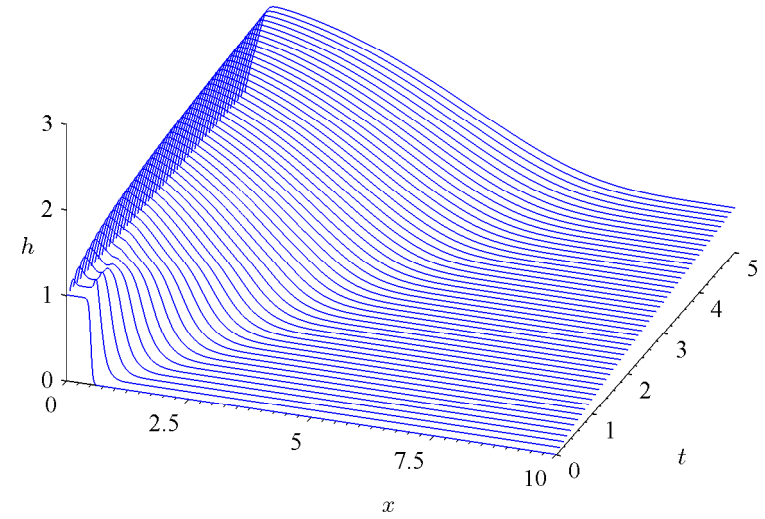

(a) Solution for h

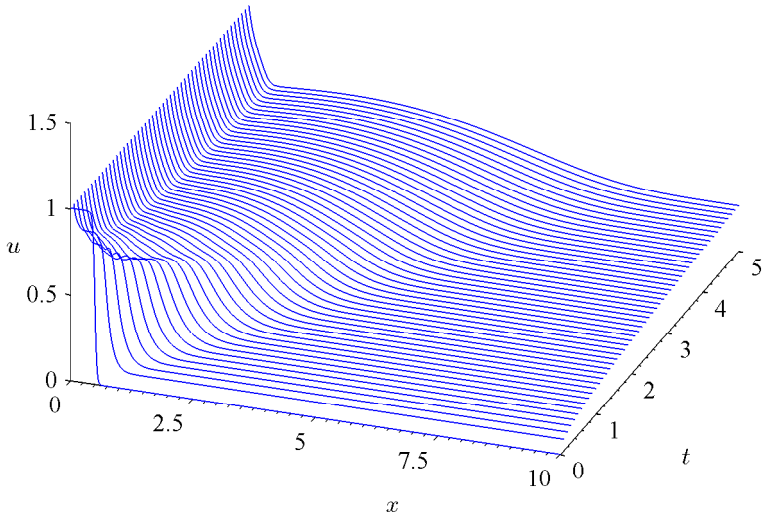

(b) Solution for u

Figure 3.8: Solution to equations (3.28) for $S = 0.1$ and $x \in (0, 10)$, $t \in (0, 5)$. The initial conditions are given by (3.29) and the boundary conditions by (3.30). The parameter values are given in Figure 3.4.

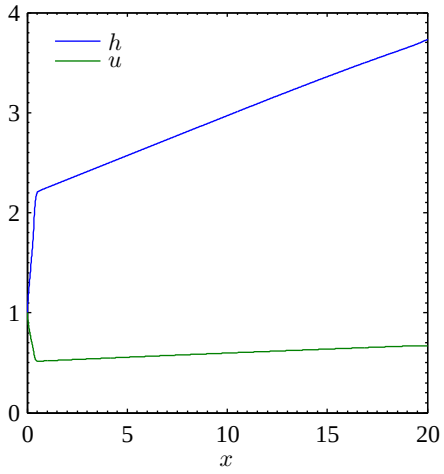

Figure 3.9: The solution to equations (3.22) at $t = 100$ when $S = 0.1$. The parameter values are given in Figure 3.4.

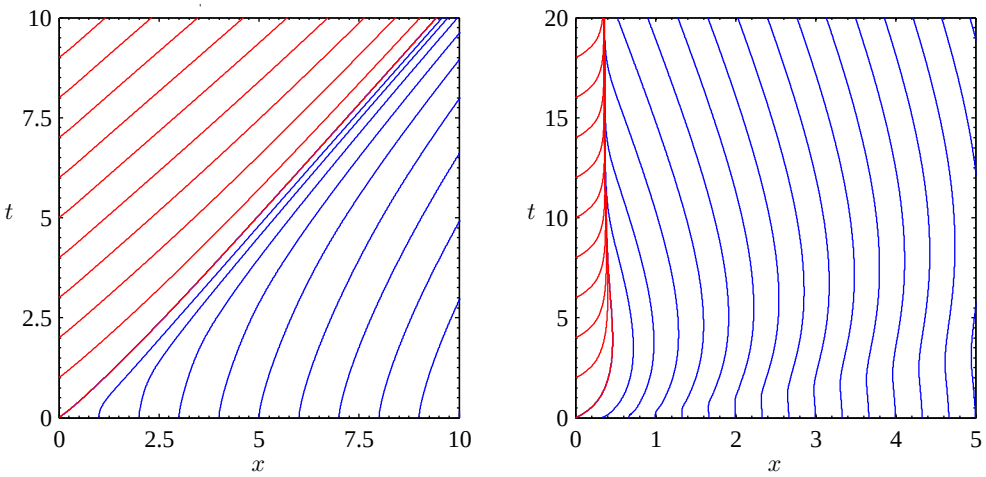

(a) $\lambda_+ = u + \sqrt{\delta h}$ (b) $\lambda_- = u - \sqrt{\delta h}$

Figure 3.10: Sub-characteristics (3.32) of equations (3.28) for $S = 0.1$ and $\epsilon = 0.01$. The blue characteristic curves are given by the initial conditions (3.29) and the red characteristic curves are given by the boundary conditions (3.30). The parameter values are given in Figure 3.4.

is unable to maintain these high values, there is a region close to $x = 0$ where u rapidly decreases and h rapidly increases. This is a boundary layer associated with the transition of the current from a supercritical to a subcritical regime. The boundary layer is highlighted in Figure 3.9 in the solutions to equations (3.28) for h and u at $t = 100$.

In Figure 3.10 we plot the sub-characteristics of the model (3.32). These curves are given by the equations (3.32), but are plotted using the solutions of equations (3.28) which contains a diffusion term, ϵ. The characteristic curves in Figure 3.10(a) have positive slope for all $x > 0$, $t > 0$; this wave is travelling downstream. However, the characteristic curves of Figure 3.10(b) are only positive close to $x = 0$ and $t = 0$. For $x > 0.5$ and $t > 2.5$ the slope of the blue characteristic lines becomes negative; this wave is now travelling upstream.

A shock can be seen in Figure 3.10(b) at $x \approx 0.3$ where the red and the blue characteristic curves meet. The characteristic curves bend towards the shock as they approach $x \approx 0.3$ as the diffusion term, ϵ, in the model prevents the characteristic lines from intersecting. The shock seen in Figure 3.10(b) is caused by a boundary layer associated with a transition through the point $F = 1$, as the values of h and u imposed at $x = 0$ adjust to their steady state values. As was discussed in Section 3.5.1, the existence of one positive characteristic wave speed, $\lambda_+ > 0$, and one negative characteristic wave speed, $\lambda_- < 0$, means that current is in a subcritical regime. We confirm this, and the presence of a boundary layer close to $x = 0$, by plotting the Froude number in Figure 3.11.

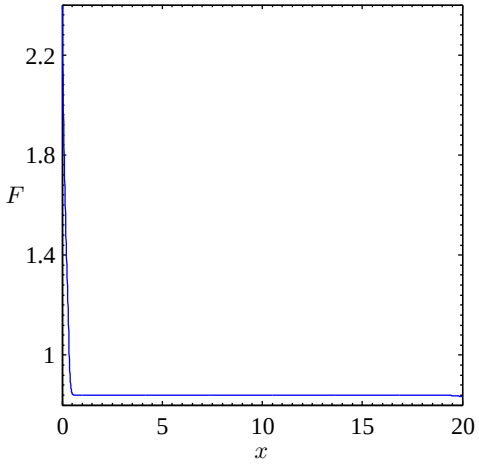

Figure 3.11: The local Froude number, (3.24), for the solution to equations (3.22). The solution is given at $t = 100$ when $S = 0.1$. Parameter values are given in Figure 3.4.

In the following section we will deduce the values that h and u are approaching

in the boundary layer, as well as finding the steady state solution to equations (3.22) for $S < S_c$.

3.5.4 Boundary layer near $x = 0$ when $S < S_c$

As discussed above, when $S < S_c$ the solutions to equations (3.28) exhibit a region of rapidly changing behaviour close to $x = 0$ as the solution adjusts from the imposed boundary conditions. This region is associated with a transition from supercritical to subcritical flow because the sub-characteristics of equations (3.28) have one wave propagating downstream, and one propagating upstream. In this section we calculate the inner solution for $x \ll 1$ and the outer solution for $x > 1$. The matching of these two solutions determines the values that h and u are approaching in the boundary layer (Hinch, 1991).

3.5.4.1 The inner solution

We assume the solution is in a steady state and consider the time-independent equations with turbulent dissipation

$$(hu)_x = \frac{u^3}{h}, \tag{3.33a}$$

$$(hu^2)_x = -\delta h h_x + Sh - \gamma k + \epsilon (hu_x)_x. \tag{3.33b}$$

To examine the small region near $x = 0$ we rescale x with respect to the parameter $\epsilon \ll 1$:

$$x = \epsilon X. \tag{3.34}$$

Equations (3.33) at leading order become

$$(hu)_X = 0, \tag{3.35a}$$

$$(hu^2)_X = -\delta h h_X + (hu_X)_X, \tag{3.35b}$$

which we can integrate once to give

$$hu = c_1, \tag{3.36a}$$

$$u_X = \left(\frac{hu^2 + \frac{\delta}{2} h^2}{h} \right) + c_2, \tag{3.36b}$$

for constants c_1, c_2. We eliminate the constants by imposing the far field boundary conditions

$$h \to h_\infty, \qquad u \to u_\infty \qquad \text{as} \qquad X \to \infty. \tag{3.37}$$

Hence, equations (3.36) become

$$hu = h_\infty u_\infty, \tag{3.38a}$$

$$u_X = \left(\frac{hu^2 - h_\infty u_\infty^2}{h} + \frac{\delta}{2} \frac{h^2 - h_\infty^2}{h} \right). \tag{3.38b}$$

Rescaling h, u and X in the following way

$$h = h_\infty H, \quad u = u_\infty U, \quad X = \frac{\zeta}{u_\infty}, \tag{3.39}$$

we obtain the set of autonomous equations in H and U,

$$U = \frac{1}{H}, \tag{3.40a}$$

$$U_\zeta = \frac{HU^2 - 1}{H} + \frac{H^2 - 1}{2{F_\infty}^2 H}, \tag{3.40b}$$

where we have defined the far field Froude number, F_∞, to be

$$F_\infty = \frac{u_\infty}{\sqrt{\delta h_\infty}}. \tag{3.41}$$

By substituting (3.40a) into equation (3.40b) we obtain a single equation for $H(\zeta)$,

$$H_\zeta = (H - 1) \left(1 - \frac{H(H+1)}{2F_\infty^2} \right). \tag{3.42}$$

In Figure 3.12 we plot the phase plane for the case $F_\infty < 1$.

A single trajectory in the phase plane takes the initial data to the stable point $(H, H_\zeta) = (1, 0)$. Hence, $H \to 1$ as $\zeta \to \infty$, and from equation (3.40a), $U \to 1$ as $\zeta \to \infty$. This means that if the initial data is $h = h_i$ and $u = u_i$ at $x = 0$ and a boundary layer exists, then h and u will reach the values h_∞ and u_∞, respectively, in that boundary layer. Moreover, from equation (3.38a) we know that

$$h_i u_i = h_\infty u_\infty, \tag{3.43}$$

i.e. the flux is conserved across the boundary layer. In particular, when $h_i =$

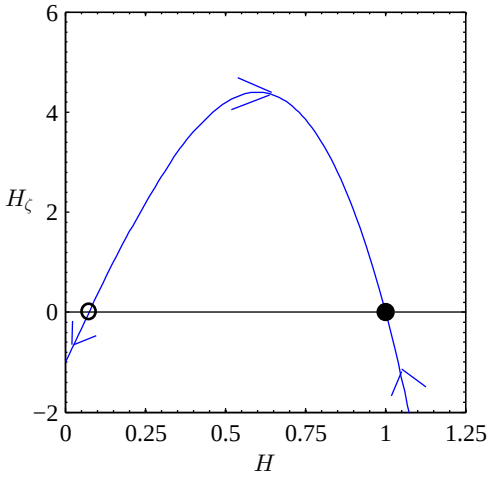

Figure 3.12: Phase portrait of equation (3.42) for $F_\infty < 1$. The arrows indicate the direction of increasing or decreasing H_ζ. The open circle marks the unstable point, and the closed circle marks the stable point.

$u_i = 1$, we find

$$h \to h_\infty, \quad u \to \frac{1}{h_\infty} \quad \text{as} \quad X \to \infty. \tag{3.44}$$

In Section 3.5.5 we determine the outer solution to the boundary layer problem by solving the steady state equations (3.22) for $S < S_c$. This solution, when matched to the inner solution will determine the value of h_∞ (Hinch, 1991), given in Section 3.5.5.3.

3.5.5 The steady state solution when $S < S_c$

In this section we solve the steady state equations (3.22) for h and u when $S = 0.1$. In this case, the equations cannot be solved by an initial value problem at $x = 0$ (two conditions imposed at $x = 0$) as the flow is subcritical. Instead, a boundary value problem is specified with one condition imposed at $x = 0$ and one at $x = x_R$. This problem is given by equations (3.22) with the boundary conditions

$$hu = 1 \quad \text{at} \quad x = 0, \quad \text{and} \quad \frac{du}{dx} = 0 \quad \text{at} \quad x = x_R. \tag{3.45}$$

In order to solve this boundary value problem, we will convert it to an initial value problem specified at $x = x_R$, and we will shoot backwards from this point towards $x = 0$ to obtain the solution for h and u across the domain.

3.5.5.1 Determining the flux at $x = x_R$ numerically

We begin by rewriting equations (3.22) in terms of the variables q and F:

$$q = hu, \qquad F = \frac{u}{\sqrt{\delta h}}. \tag{3.46}$$

This gives

$$\frac{dq}{dx} = \delta F^{8/3} q^{1/3}, \tag{3.47a}$$

$$\frac{dF}{dx} = \frac{\delta^{4/3} F^{5/3} \left[3\Sigma - F^2(2 + 4F^2 + 3\beta\Psi(F))\right]}{2q^{2/3}(F^2 - 1)}, \tag{3.47b}$$

where

$$\Sigma = \frac{S}{\delta^2}, \qquad \beta = \frac{\gamma^3}{\delta}, \tag{3.48}$$

and k has been eliminated from the equations by writing it as a function of F:

$$k = \gamma^2 u^2 \Psi(F), \tag{3.49}$$

where $\Psi(F)$ is given by

$$\Psi(F) = \left(\frac{F^2}{2\beta}\right)^{2/3} \Phi\left(\left(\frac{2\beta}{F^2}\right)^{1/3}\right). \tag{3.50}$$

The function Φ is defined in equation (3.15).

Equations (3.47) are subject to the boundary conditions

$$q = 1 \quad \text{at} \quad x = 0, \tag{3.51a}$$

$$F^2(1 + F^2 + \beta\Psi(F)) = \Sigma \quad \text{at} \quad x = x_R. \tag{3.51b}$$

Equation (3.51b) determines the value of F at $x = x_R$. We call this value $F = F_R$. As yet, the value of the flux, q, at $x = x_R$ is unknown. We will call this value q_R, where q_R is to be determined.

In order to solve the boundary value problem as an initial value problem, we normalise equations (3.47) by defining

$$q = q_R Q, \qquad x = x_R - \frac{q_R^{2/3}}{\delta^{4/3}} z. \tag{3.52}$$

Equations (3.47) thus become

$$\frac{dQ}{dz} = -F^{8/3}Q^{1/3}, \tag{3.53a}$$

$$\frac{dF}{dz} = -\frac{F^{5/3}\left[3\Sigma - F^2(2+4F^2+3\beta\Psi(F))\right]}{2Q^{2/3}(F^2-1)}, \tag{3.53b}$$

subject to the boundary conditions

$$Q = 1, \quad F = F_R \quad \text{at} \quad z = 0. \tag{3.54}$$

Equations (3.53) can be solved numerically for Q and F. Using these solutions and equations (3.52), noting that $q = 1$ at $x = 0$, the relationship between q_R and x_R can be determined;

$$q_R = \frac{1}{Q}, \qquad x_R = \frac{z}{\delta^{4/3}Q^{2/3}}. \tag{3.55}$$

In Figure 3.13, q_R is plotted against x_R for the numerical solutions to equations (3.53). Figure 3.13 also shows an analytical approximation to q_R, which is calculated in Section 3.5.5.4.

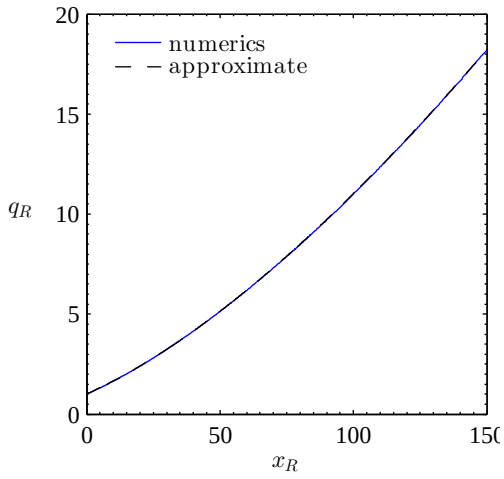

Figure 3.13: The flux, $q = q_R$, as a function of x at the right-hand boundary, $x = x_R$. The blue solid line shows the numerical solution calculated using equations (3.55) and solutions to equations (3.53). The black dashed line shows the approximate value of q_R, given in equation (3.67). The parameter values are $S = 0.1$, $\delta = 0.17$, $\gamma = 0.77$, $\Sigma = 3.46$, $\beta = 2.68$, $F_R = 0.84$.

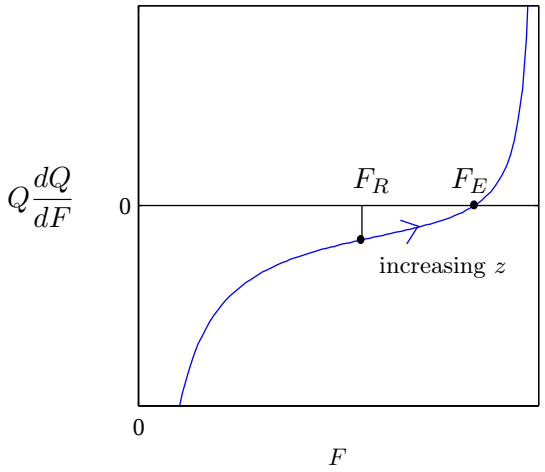

Figure 3.14: A plot of equation (3.56). The value of F at $x = x_R$, F_R, and the equilibrium value of equation (3.56), F_E, are plotted as black circles. The arrow indicates that $F_R \to F_E$ as z increases.

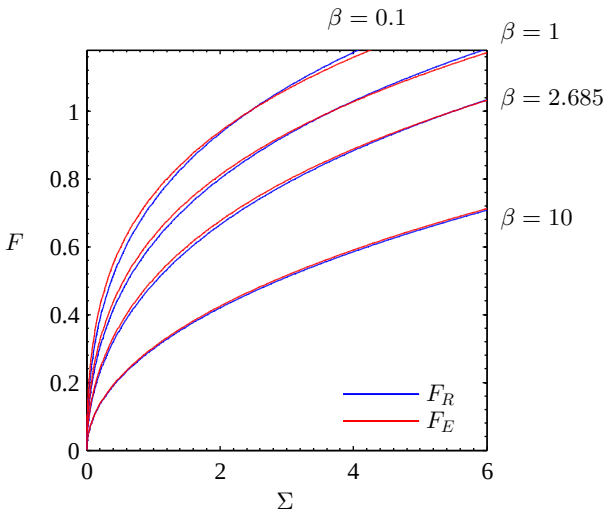

Figure 3.15: A plot of equations (3.51b) and (3.57). The value of β is varied, for $S = 0.1$, $\beta = 2.685$.

3.5.5.2 Finding the value of F at equilibrium

Equations (3.53) determine a single ode for the system,

$$Q\frac{dQ}{dF} = \frac{[F^2(2+4F^2+3\beta\Psi(F)) - 3\Sigma]}{2F(1-F^2)}. \tag{3.56}$$

Equation (3.56) is plotted in Figure 3.14. The equilibrium value, $F = F_E$, is marked and is given by the solution to the algebraic equation

$$F_E^2(2+4F_E^2+3\beta\Psi(F_E)) = 3\Sigma. \tag{3.57}$$

Since $dQ/dz < 0$, we know that F will increase from F_R, the value imposed at $z = 0$, towards its equilibrium value, F_E, as z increases. The values F_E and F_R are identically equal precisely when

$$\Sigma = \Sigma_c, \quad \text{at which point} \quad F_R = F_E = 1. \tag{3.58}$$

The critical value Σ_c is given by

$$\Sigma_c = 2 + \beta\Psi(1), \tag{3.59}$$

and agrees with the definition of S_c given in equation (3.26).

We note that as $\Sigma \to 0$, F_R, $F_E \to 0$ in the following way,

$$F_R \sim \left(\frac{\Sigma}{\beta+1}\right)^{1/2}, \qquad F_E \sim \left(\frac{\Sigma}{\beta+\frac{2}{3}}\right)^{1/2}, \tag{3.60}$$

since $\Phi(\xi) \to \xi^2$ and $\Psi(F) \to 1$ as $F \to 0$. In addition, F_R, $F_E \to 1$ as $\Sigma \to \Sigma_c$. Hence, F_R and F_E are very close for all values of $\Sigma < \Sigma_c$, and especially for relatively large values of β, as is illustrated by Figure 3.15. It thus follows that F rapidly approaches its equilibrium value F_E.

3.5.5.3 Matching the inner solution and the outer solution in the boundary layer

Since F is very close to its equilibrium value, F_E, we can now determine the values that h and u are approaching in the boundary layer close to $x = 0$. In

the boundary layer, h is given by

$$h_\infty = h|_{x=0} = \left.\frac{q^{2/3}}{\delta^{1/3}F^{2/3}}\right|_{x=0}. \tag{3.61a}$$

It is known that $q = 1$ at $x = 0$, and under the assumption that $F = F_E$ at $x = 0$ we have

$$h_\infty = \delta^{-1/3}F_E^{-2/3}. \tag{3.62}$$

This value is independent of the value of x_R. In Figure 3.16, we plot equation (3.62) alongside the numerical solution for h_∞ given by

$$h_\infty = \delta^{-1/3}F^{-2/3}, \tag{3.63}$$

where F is given by the solution to equations (3.53).

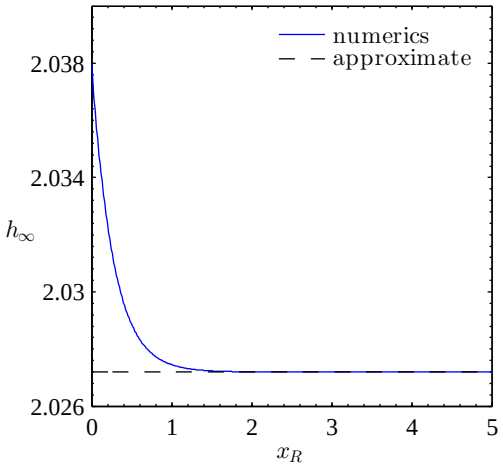

Figure 3.16: A plot of h_∞. The approximate solution is given by equation (3.62) and the numerical solution is given by equation (3.63) with F is given by the solution to equations (3.53). The parameters are $\delta = 0.17$ and $F_E = 0.8403$.

The value of u_∞ is found by solving

$$h_\infty u_\infty = 1. \tag{3.64}$$

3.5.5.4 Approximating the value of q_R

We now know that F is very close to its equilibrium value, F_E and so we can use this to approximate the value of $q_R(x_R)$. Equation (3.53a) becomes

$$\frac{dQ}{dz} \approx -F_E^{8/3}Q^{1/3}, \tag{3.65}$$

which, upon integration, determines Q:

$$Q \approx \left(1 - \frac{2}{3}F_E^{8/3} z\right)^{3/2}. \tag{3.66}$$

From equations (3.55) we can now determine q_R as a function of x_R,

$$q_R \approx \left(1 + \frac{2}{3}\delta^{4/3} F_E^{8/3} x_R\right)^{3/2}. \tag{3.67}$$

Equation (3.67) is plotted in Figure 3.13 alongside the numerical solution calculated in Section 3.5.5.1. It can be seen that the approximation to q_R obtained by assuming that $F = F_E$ at $x = x_R$ provides a very close approximation to the numerical solution.

3.5.5.5 Determining h and u in the steady state

Under the assumption that $F = F_E$, the flux, q is given by

$$\begin{aligned} q = q_R Q(z) &\approx q_R \left(1 - \frac{2}{3}F_E^{8/3} z\right)^{3/2}, \\ &= \left(q_R^{2/3} - \frac{2}{3}F_E^{8/3}\delta^{4/3}(x - x_R)\right)^{3/2}. \end{aligned} \tag{3.68}$$

Using the definition of q_R in terms of x_R from (3.67), we determine q as a function of x:

$$q \approx \left(1 + \frac{2}{3}F_E^{8/3}\delta^{4/3} x\right)^{3/2}. \tag{3.69}$$

Now, using the fact that h and u are given by

$$h = \frac{q^{2/3}}{\delta^{1/3} F^{2/3}} \quad \text{and} \quad u = \left(\delta q F^2\right)^{1/3}, \tag{3.70}$$

the approximate steady state values of h and u can be determined using equation (3.69) and the fact that $F = F_E$;

$$h \approx \delta^{-1/3} F_E^{-2/3} + \frac{2}{3}\delta F_E^2 x, \tag{3.71a}$$

$$u \approx \left(\delta F_E^2\right)^{1/3} \left(1 + \frac{2}{3}F_E^{8/3}\delta^{4/3} x\right)^{1/2}. \tag{3.71b}$$

In Figure 3.17, we plot the steady state approximations for h, u and q against the numerical solutions found by shooting backwards from $x = x_R$ to $x = 0$.

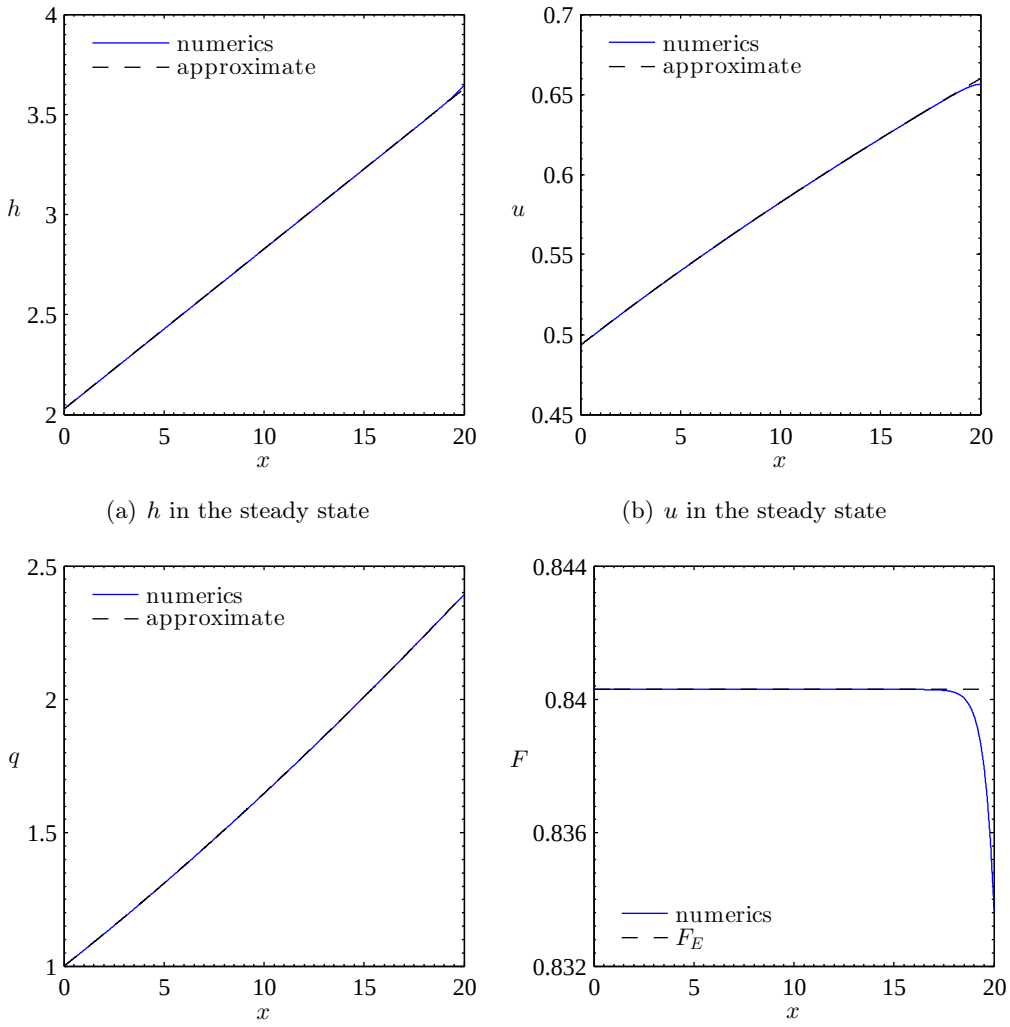

(a) h in the steady state

(b) u in the steady state

(c) q in the steady state

(d) q in the steady state

Figure 3.17: The analytical approximation to the steady state, given by equations (3.69) - (3.71), compared against the numerical solution to the initial value problem of equations (3.22) from $x = x_R$ to $x = 0$. The numerical solutions have the initial conditions $h = h_R$ and $u = u_R$, given by equations (3.72), at $x = x_R$. The parameter values are given in Figure 3.13 and $F_E = 0.8403$, $x_R = 20$.

The numerical solutions are calculated using equations (3.22), with $x_R = 20$ and $q_R = 2.39$. This gives the values $h = h_R$ and $u = u_R$ at $x = x_R$ where

$$h_R \approx \frac{q_R^{2/3}}{\delta^{1/3} F_R^{2/3}} \quad \text{and} \quad u_R \approx \left(\delta q_R F_R^2\right)^{1/3}. \tag{3.72}$$

Again, we see very close agreement between the numerical solutions calculated by shooting backwards from $x = x_R$ and the analytical approximation obtained by assuming $F = F_E$. The only region where the analytical solution varies from the numerical solution is close to $x = x_R$; this is highlighted through the plot of the Froude number, shown in Figure 3.17(d).

The fact that F_R deviates dramatically from F_E at $x = x_R$ provides the reason as to why the equations could not be solved by shooting forwards from $x = 0$; the equations would never accurately capture the behaviour of F at $x = x_R$, and thus inaccurate solutions for h and u would be predicted.

3.6 Solution of the shallow-water model for varying downstream slope

As was studied for the one-equation velocity model in Chapter 2, here we consider a slowly varying slope profile which is a function of downstream distance; $S = S(x)$. In Section 3.6.1 we look at a decreasing downstream slope, and in Section 3.6.2, we will look at a increasing downstream slope.

From the analysis carried out in Section 3.5, we expect that when the slope decreases with distance downstream that a shock will form in the solution at the point at which $S < S_c$. In addition, when the slope is increasing, we have $S < S_c$ at $x = 0$, and so we expect a boundary layer to form in the solution.

3.6.1 Slowly decreasing downstream slope

We use a monotonically decreasing exponential function of the form

$$S(x) = \frac{\exp(5 - x)}{1 + \exp(5 - x)}. \tag{3.73}$$

Equation (3.73) specifies $S \approx 1$ at $x = 0$ and $S \approx 0$ at $x = 20$. With S given in this form, we will solve the two-equation shallow water model (3.28) to examine the variation in h and u as we move downstream.

3.6.1.1 Numerical solution with viscous dissipation

Equations (3.28) are solved for the varying downstream slope, (3.73), and a fixed, small value of ϵ. The time and space dependent solutions are plotted in Figure 3.18 and profiles of the solution are shown for $t = 50$, 100, 150 in Figure 3.19.

In Figure 3.18 we can see that the initial disturbance, caused by the conditions we have specified at $t = 0$, is propagating downstream. A shock appears in the solution around $t \approx 25$ and it can be observed by the 'jump' in u from a high to a lower value of the velocity around $x \approx 7$. This decrease in velocity corresponds to an increase in the depth of the current.

In the profiles plotted in Figure 3.19, it is possible to see that the shock has clearly developed by $t > 50$ and is slowly moving upstream in time. By solving equation (3.73) for x using the critical value $S = S_c$, given in equation (3.26), we find that $x_c = 6.67$. This is the point at which the shock first appears in the solution. The solution behind the shock is in a steady state, but ahead of the shock the solution is slowly evolving to meet the boundary condition imposed at $x = 20$, equation (3.30b).

In Figure 3.20 we plot the Froude number of the flow, calculated at $t = 50$, 100, 150. This plot shows that the shock coincides with the point at which $F = 1$. It is clear that behind the shock the flow is supercritical ($F > 1$), whilst ahead of the shock the flow is subcritical ($F < 1$). As such, from equations (3.32) we expect that there will be one positive characteristic wave speed, $\lambda_+ > 0$, and one negative characteristic wave speed, $\lambda_- < 0$.

3.6.1.2 Method of characteristics

The characteristics, $\lambda_\pm$, of equations (3.28) are given by (3.32) when $\epsilon = 0$. In Figure 3.21, we plot the sub-characteristics of the model for the slope function (3.73) using the solutions to equations (3.28), where $\epsilon = 0.01$.

Figure 3.21 confirms that, for the variable downstream slope, one wave speed is always positive, $\lambda_+ > 0$, but one wave speed becomes negative, $\lambda_- < 0$, for $x > 7$, $t > 25$. Once again, the reversal of the sign of the characteristic wave speed, λ_-, is associated with the flow switching from a supercritical to a subcritical regime and, hence, the development of a shock in the solution. The shock is visible in Figure 3.21(b) where the characteristic curves meet. Behind the shock, the current is in a supercritical regime and moving in a thin layer with

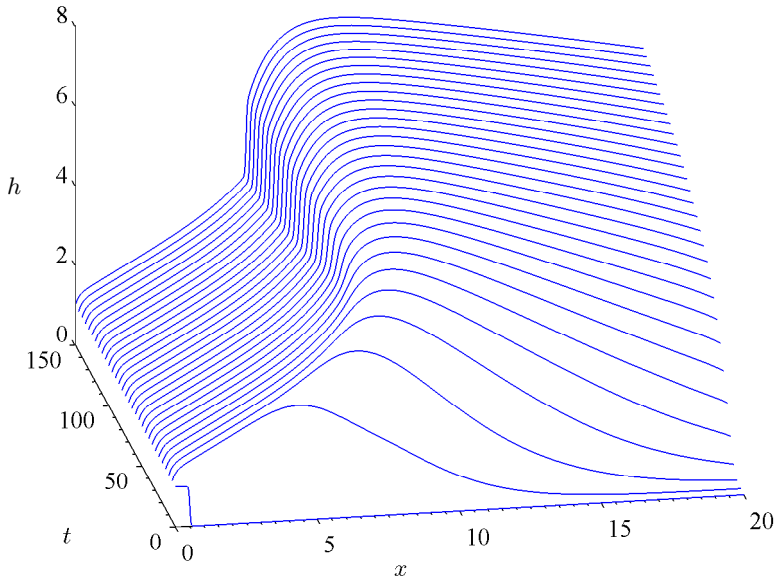

(a) Solution for h

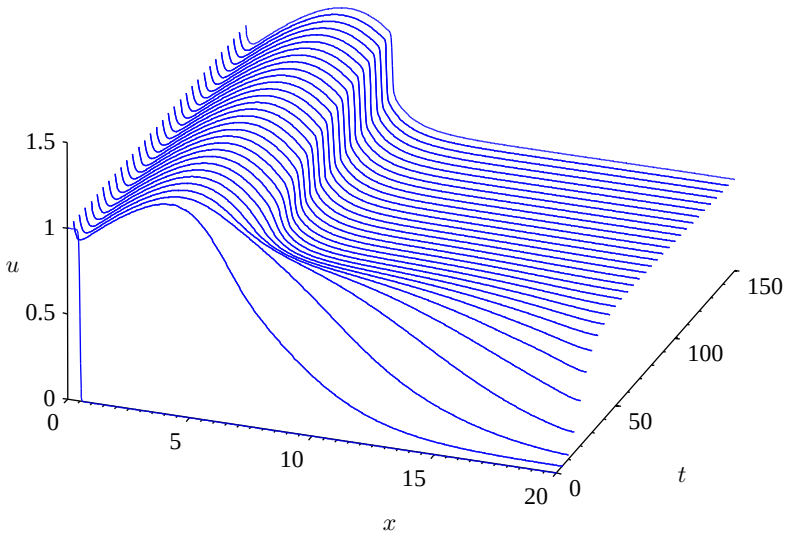

(b) Solution for u

Figure 3.18: Solution to equations (3.28) for S given by equation (3.73) and $x \in (0, 20)$, $t \in (0, 150)$. The initial conditions are given by (3.29), the boundary conditions by (3.30) and $x_R = 20$. The parameter values $\gamma = 0.77$, $\delta = 0.17$, $h^\star = 0.5$, $u^\star = 0.5$, $a = 25$, $b = 0.5$. The diffusion coefficient is $\epsilon = 0.01$.

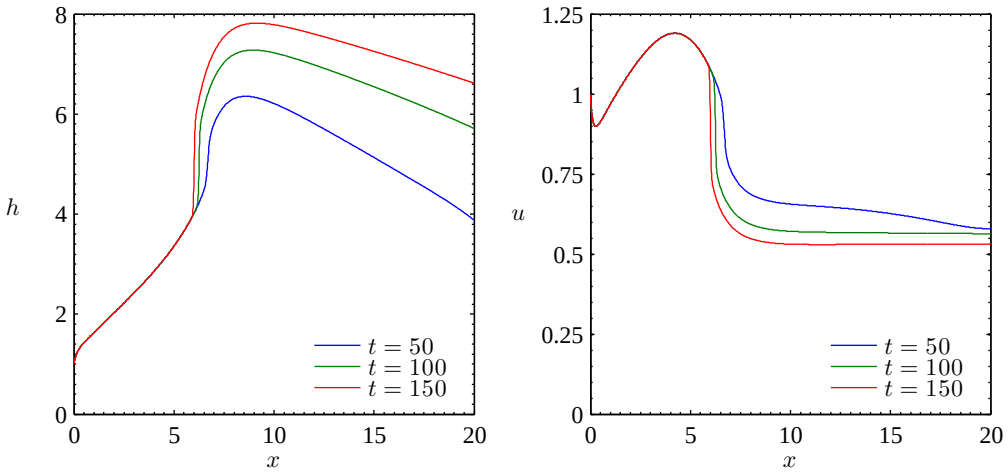

(a) Profile of the solution, h

(b) Profile of the solution, u

Figure 3.19: Solution profiles of equations (3.28) for S given by equation (3.73) at $t = 50, 100, 150$. The initial conditions are given by (3.29) and the boundary conditions by (3.30). The parameter values are given in Figure 3.18.

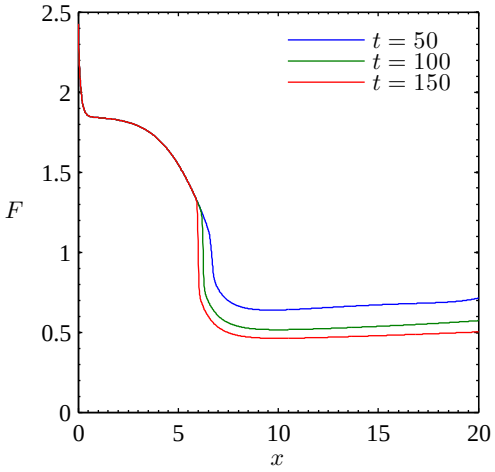

Figure 3.20: The Froude number, $F = u/\sqrt{\delta h}$, calculated using the solution to equations (3.28) for varying downstream slope, (3.73). The parameter values are given in Figure 3.18.

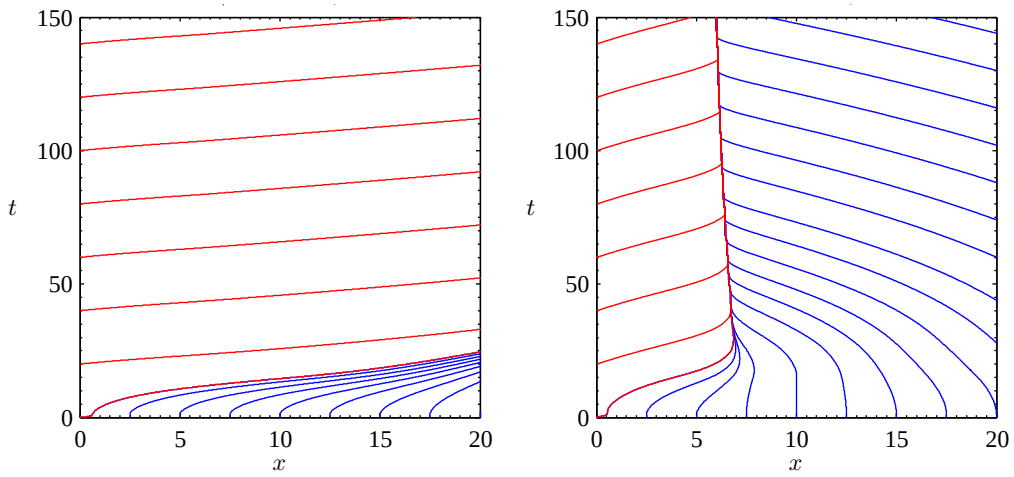

(a) $\lambda_+ = u + \sqrt{\delta h}$ (b) $\lambda_- = u - \sqrt{\delta h}$

Figure 3.21: Sub-characteristics (3.32) of equations (3.28) with S given by equation (3.73) and $\epsilon = 0.01$. The blue characteristic curves are given by the initial conditions (3.29) and the red characteristic curves are given by the boundary conditions (3.30). The parameter values are given in Figure 3.18.

a high velocity. Ahead of the shock, the current is in a subcritical regime and is moving in a thick layer at a low velocity. The shock is slowly moving upstream in time, suggesting that the solution is evolving towards a steady state.

The solutions plotted in Figures 3.18 – 3.21 continue to evolve over a long timescale, $t > 150$. In the following section, we examine the possible existence of a steady state that the solution may be approaching as $t \to \infty$.

3.6.1.3 Steady state solution with a shock

Let us suppose that the shock is located at the point x_s. The shock speed, $\dot{x}_s$, is given by the Rankine-Hugoniot conditions

$$\dot{x}_s = \frac{[hu]_-^+}{[h]_-^+} = \frac{[hu^2 + \frac{\delta}{2}h^2]_-^+}{[hu]_-^+}. \tag{3.74}$$

In the steady state, the shock is stationary, $\dot{x}_s = 0$, which implies

$$[hu]_-^+ = 0 \quad \text{and} \quad \left[hu^2 + \frac{\delta}{2}h^2\right]_-^+ = 0. \tag{3.75}$$

We recall that the solution behind the shock is in the steady state, and so h_- and u_- are known in principal as functions of the shock position x_s. Hence, we

are seeking solutions to the equations

$$h_+ u_+ = h_- u_-, \tag{3.76a}$$

$$h_+ u_+^2 + \frac{\delta}{2} h_+^2 = h_- u_-^2 + \frac{\delta}{2} h_-^2 \tag{3.76b}$$

for h_+ and u_+. By substituting (3.76a) into (3.76b) and rearranging, we obtain an equation for h_+,

$$h_+ = \frac{h_-}{2}\left(-1 + \sqrt{1 + \frac{8u_-^2}{\delta h_-}}\right). \tag{3.77}$$

Then, from equation (3.76a) and (3.77), we can find u_+.

Now that we know the values of h and u at the shock, x_s, we must try to calculate the location of the shock itself, using the remaining piece of information, namely

$$\frac{du}{dx} = 0 \quad \text{at} \quad x = x_R. \tag{3.78}$$

Given the values of h_+ and u_+ calculated from (3.76) for a given value of x_s, we solve equations (3.22) numerically subject to $h(x_s) = h_+$, $u(x_s) = u_+$ and read off the corresponding value of $du/dx(x_R)$. In principal the ultimate shock position is the value of x_s that results in $du/dx(x_R) = 0$. In Figure 3.22 we plot the value of du/dx at $x_R = 20$ for a range of x_s.

For $x_s > 5$, $du/dx(x_R)$ is becoming large, and so we concentrate on values of $x_s < 5$. Figure 3.22 shows that there is no positive value of x_s giving $du/dx(x_R) = 0$. This suggests that the shock will continue to progress towards $x_s = 0$ as t increases, eventually becoming a boundary layer at $x = 0$. In Figure 3.23, we plot solutions to equations (3.22) for three different values of x_s. Here, we confirm that as we choose smaller values of x_s, the shock moves upstream and begins to take on the appearance of a boundary layer region close to $x = 0$. The boundary layer solution is calculated in the following section.

As we have seen, there is no steady solution satisfying the boundary condition (3.78) with $x_s > 0$. However, Figure 3.22 shows that steady solutions with $x_s \in (0, 5)$ are extremely close to satisfying (3.78). This explains why the shock is observed to propagate so slowly in Figures 3.18 – 3.21. The unsteadiness is driven by the small discrepancy between the steady solution and the boundary condition (3.78), and this, in turn, drives the slow evolution of the shock position $x_s(t)$.

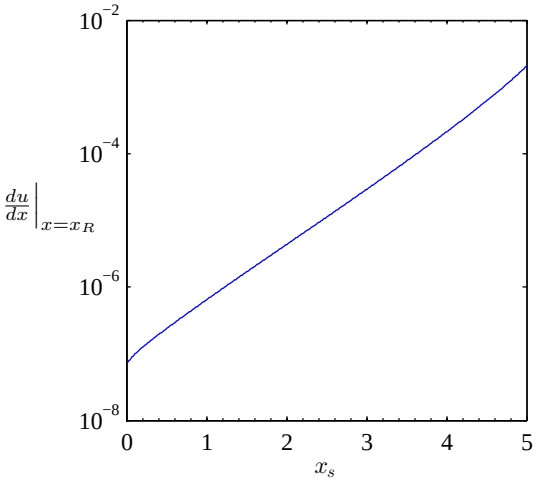

Figure 3.22: The value of du/dx, equation (3.22b), evaluated at $x_R = 20$ for a range of x_s values.

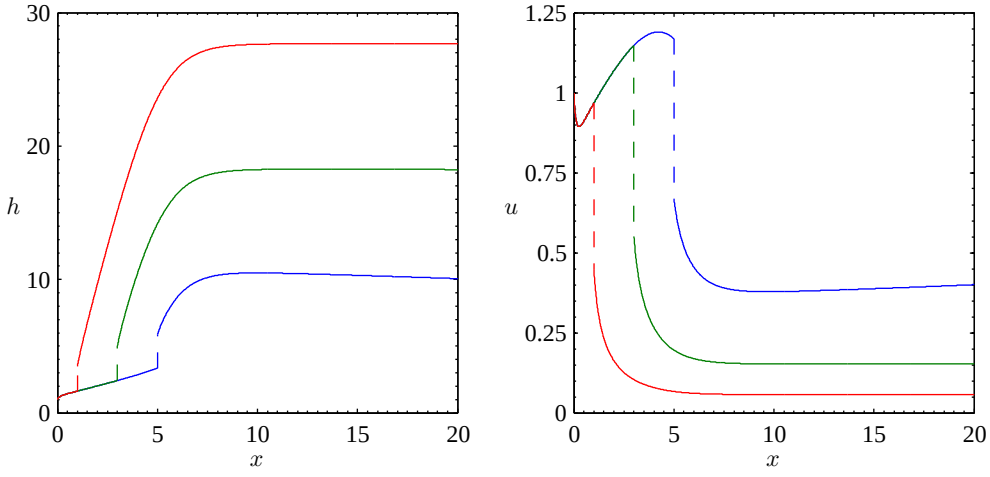

(a) Steady state solution for h

(b) Steady state solution for u

Figure 3.23: Steady state solutions calculated for different values of x_s. The plots show $x_s = 5$ in blue, $x_s = 3$ in green and $x_s = 1$ in red. The solution is made piecewise continuous by joining the top and bottom of the shock by a dashed line. We have used equations (3.22), the jump conditions, (3.76), at x_s and the boundary conditions, (3.30a), at $x = 0$.

3.6.1.4 Boundary layer solution

In order to calculate the boundary layer solution to equations (3.22) with $S(x)$ given by equation (3.73) we make use of equations (3.47) for the dependent variables F and q again, noting that $\Sigma = \Sigma(x)$.

At $x = x_R$ the value of the Froude number, $F = F_R$, is known provided we know the value of $\Sigma_R = \Sigma(x_R)$. For our problem, $x_R = 20$, thus $\Sigma_R = \Sigma(20)$ is known and from equation (3.51b) we determine F_R.

Now, given a value of q_R, the solution is completely determined. To find the value of q_R, we solve equations (3.47) from $x = x_R$ to $x = 0$, varying the value of q_R at $x = x_R$, until the condition $hu = q = 1$ at $x = 0$ is satisfied. In Figure 3.24 we plot the value of $q_0 = q(x = 0)$ versus q_R; because the values of q_R and q_0 are very close to $q = 1$, the axes show $q_0 - 1$ versus $q_R - 1$. We find that taking a value of $q_R \approx 1 + 9.24007899 \times 10^{-8}$ at $x = 20$ predicts that $q_0 = 1$.

With the value of $q = q_R$ determined, the solution for h and u can be constructed by shooting from $x = 20$ to $x = 0$. We solve equations (3.47) for q and F and recover the variables h and u from equations (3.70). The boundary layer solutions are shown in Figure 3.25. The Rankine-Hugoniot conditions can be used to match the boundary conditions imposed at $x = 0$ to the solutions h and u for $x > 0$.

3.6.2 Slowly increasing downstream slope

In this section we consider a current which is initiated on a flat slope and travels downstream over a slowly increasing slope. To model this slope, the following function is used;

$$S(x) = \frac{\exp(x-5)}{1+\exp(x-5)}. \qquad (\mathbf{3.79})$$

This function appears similar to equation (3.73), but now $S(x)$ is an increasing function with $S \approx 0$ at $x = 0$, and $S \approx 1$ at $x = 20$. Equations (3.28) are solved for this function $S(x)$, and the profiles of the solutions are plotted in Figure 3.26.

The solutions plotted in Figure 3.26 show that no shock is present in the solution. There is a boundary layer close to $x = 0$ as the current rapidly transitions from the initial supercritical regime, due to the inlet conditions imposed at $t = 0$. In Figure 3.27 the Froude number is plotted using the solutions to

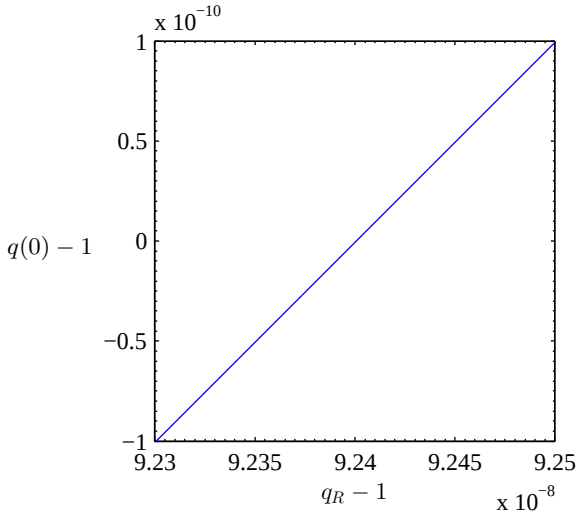

Figure 3.24: Determining $q = q(0)$ at $x = 0$ for a range of q_R values. Equations (3.47) are solved by shooting backwards from the point $x_R = 20$ subject to the initial conditions $F_R = 0.0016947$, $q = q_R$ where q_R is varied in the range $(1 + 9.23 \times 10^{-8}, 1 + 9.25 \times 10^{-8})$. The computed final value $q(0)$ is found. The slope, $S(x)$, is given by equation (3.73) and $\Sigma(x) = S(x)/\delta^2$. The parameter values are $\delta = 0.17$, $\gamma = 0.77$, $\beta = 2.68$.

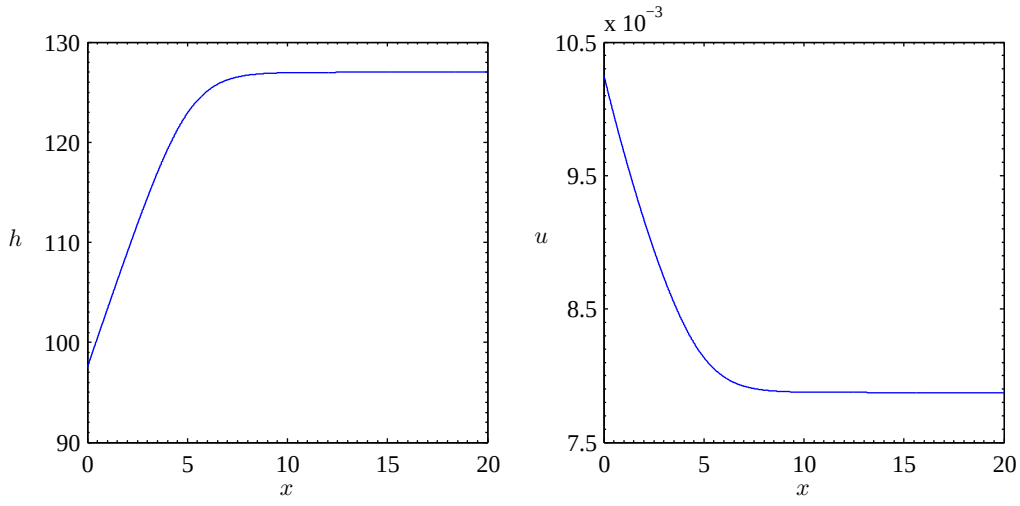

(a) h (b) u

Figure 3.25: Steady state solutions for h and u. These solutions are found from equations (3.70) using the solutions to equations (3.47) for F and q when the slope, $S(x)$, given by equation (3.73). The solution is found by shooting backwards from the point $x = x_R$ to $x = 0$ with the initial conditions $q = q_R = 1 + 9.24007899 \times 10^{-8}$, $F = F_R = 0.0016947$. The parameter values are listed in Figure 3.24.

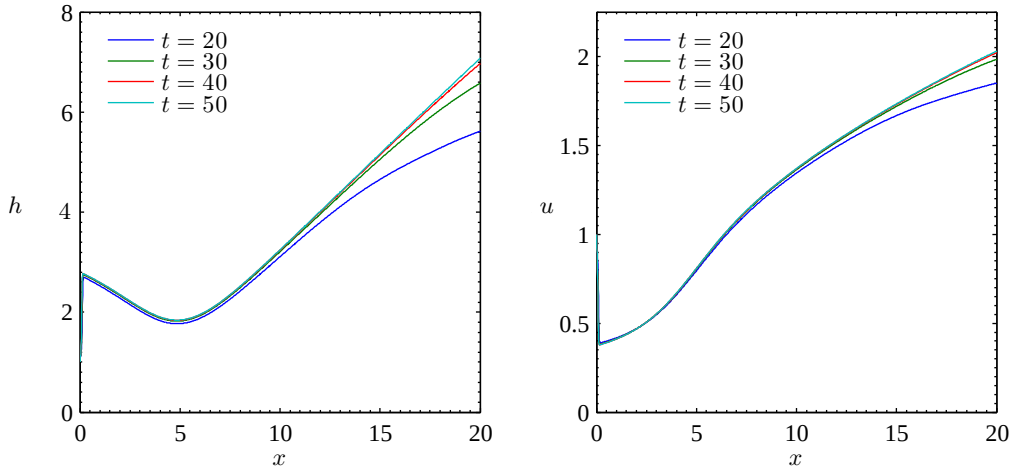

(a) h (b) u

Figure 3.26: Solution profiles of h and u calculated using equations (3.22) when $S = S(x)$, given by equation (3.79). The initial and boundary conditions are given by equations (3.29) and (3.30), respectively. The parameter values are $\gamma = 0.77$, $\delta = 0.17$, $h^\star = 1/2$, $u^\star = 1/2$, $a = 25$, $b = 0.5$, $x_R = 20$ and the diffusion coefficient is $\epsilon = 0.01$.

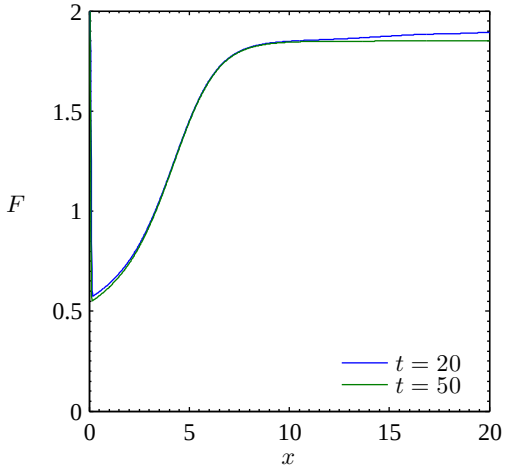

Figure 3.27: The Froude number, $F = u/\sqrt{\delta h}$, calculated using the solutions to equations (3.28) when S is given by equation (3.79). The parameter values are given in Figure 3.26.

equations (3.28). This plot shows that, outside the boundary layer at $x = 0$, the current transitions through the point $F = 1$ smoothly, as we would expect for a transition from subcritical to supercritical flow.

3.6.2.1 The steady state solution

In order to calculate the steady state solution to equations (3.22) with $S(x)$ given by equation (3.79) we make use of equations (3.47) for the dependent variables F and q again, where now $\Sigma = \Sigma(x)$. The solution transitions smoothly through the point $x = x_c$ where

$$\Sigma(x_c) = 2 + \beta\Psi(1), \tag{3.80}$$

and we suppose that at $q = q_c$ at $x = x_c$.

We expand F and q about $x = x_c$ in the following way (*e.g.* Howison (2004)),

$$\left.\begin{aligned} F &\sim 1 + f_1(x - x_c) + \dots \\ q &\sim q_c + q_1(x - x_c) + \dots \end{aligned}\right\} \quad \text{as} \quad x \to x_c. \tag{3.81}$$

We substitute these expansions into equations (3.47), and at leading order obtain

$$q_1 \sim \delta^{4/3} q_c^{1/3}, \tag{3.82}$$

and a quadratic for f_1:

$$4q_c^{2/3} f_1^2 + \delta^{4/3}\left\{20 + 3\beta[2\Psi(1) + \Psi'(1)]\right\} f_1 - 3\delta^{4/3}\Sigma'(x_c) = 0. \tag{3.83}$$

We note that $\Psi > 1$ and that $\Psi' > 0$. In addition, $\Sigma' > 0$ for S given by equation (3.79). Hence, equation (3.83) always provides one positive and one negative real root for f_1. We will take the positive root, as we want the flow to move from subcritical to supercritical (*cf.* equation (3.81); at $x < x_c$ we want $F < 1$, and at $x > x_c$ we want $F > 1$).

Now, given a value of q_c, the solution is completely determined. In order to find the value of q_c, we solve equations (3.47) from $x = x_c$ to $x = 0$, varying the value of q_c at $x = x_c$, until the condition $hu = q = 1$ at $x = 0$ is satisfied. In Figure 3.28 we plot the value of $q_0 = q(x = 0)$ versus q_c. We find that $q_c \approx 1.1423$ predicts that $q_0 = 1$.

With the value of q_c determined, we can now construct the entire solution for F and q by using the solution from x_c to $x = 0$ and by using equations (3.47) to shoot forwards from x_c to x_R. This gives solutions $F(x)$ and $q(x)$. The variables

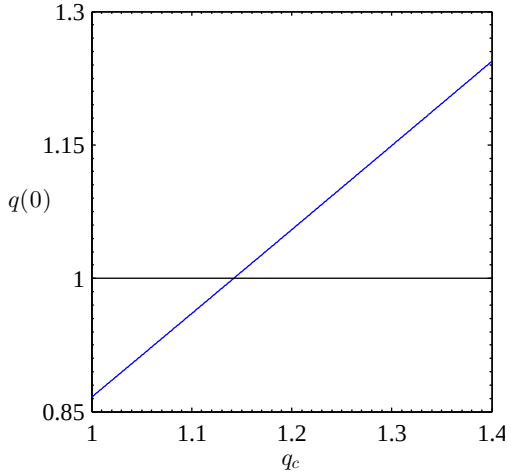

Figure 3.28: Determining $q = q(0)$ at $x = 0$ for a range of $q_c = q(x_c)$ values. Equations (3.47) are solved by shooting backwards from the point $x = x_c - \varepsilon$ subject to the initial conditions $q = q_c - \delta^{4/3} q_c^{1/3} \varepsilon$, $F = 1 - \varepsilon f_1$, for $0 < \varepsilon \ll 1$. The initial value q_c is varied, and the computed final value $q(0)$ is found. The parameter values are $\delta = 0.17$, $\gamma = 0.77$, $\beta = 2.68$, $x_c = 3.335$, $\varepsilon = 10^{-4}$.

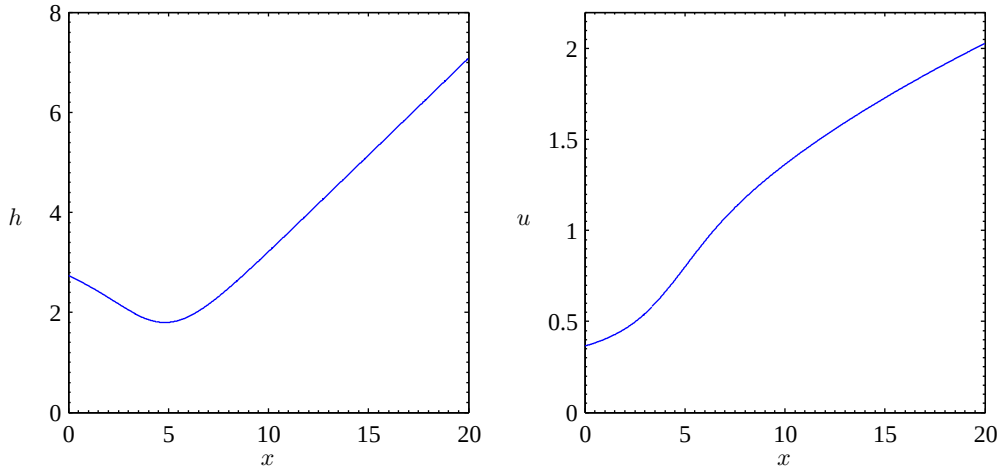

(a) h (b) u

Figure 3.29: Steady state solutions for h and u. These solutions are found from equations (3.70) using the solutions to equations (3.47) for F and q when the slope, $S(x)$, given by equation (3.79). The solution is found by shooting backwards from the point $x = x_c - \varepsilon$ to $x = 0$, and forwards from the point $x = x_c + \varepsilon$ to $x = x_R$ with the initial conditions $q = q_c \pm \delta^{4/3} q_c^{1/3} \varepsilon$, $F = 1 \pm \varepsilon f_1$, for $0 < \varepsilon \ll 1$. Values of $\varepsilon = 10^{-4}$, $q_c = 1.1423$ and $x_R = 20$ are taken. The parameter values are listed in Figure 3.28.

h and u are then recovered using equations (3.70) and plotted in Figure 3.29.

This procedure does not satisfy the boundary condition $du/dx = 0$ at $x = x_R$ which was used in the numerical solution to equations (3.28). This is because the flow is supercritical for $x > x_c$ and so there is no information propagating back from the boundary at $x = x_R$. Instead, a boundary layer at $x = x_R$ will exist in the numerical solutions plotted in Figures 3.26 and 3.27, as the solution adjusts to the condition $du/dx = 0$.

3.6.2.2 The boundary layer at $x = x_R$

In order to study the boundary layer we reconsider the viscous term in the governing steady equations, (3.33). We look for a boundary layer where h and u are constant to leading order and equal to their outer solutions, given by

$$h_\infty = h(x_R), \qquad u_\infty = u(x_R). \tag{3.84}$$

We consider an asymptotic expansion in a small region about h_∞ and u_∞:

$$\begin{aligned} h &\sim h_\infty + \varepsilon h_1 + \dots \\ u &\sim u_\infty + \varepsilon u_1 + \dots \end{aligned} \tag{3.85}$$

for $x = x_R - \varepsilon X$ (*e.g.* Howison (2004)).

To lowest order, equations (3.33) become

$$u_\infty \frac{dh_1}{dX} + h_\infty \frac{du_1}{dX} = -\frac{u_\infty^3}{h_\infty}, \tag{3.86a}$$

$$u_\infty^2 \frac{dh_1}{dX} + 2h_\infty u_\infty \frac{du_1}{dX} + \delta h_\infty \frac{dh_1}{dX} = -S_\infty h_\infty + \gamma k_\infty - h_\infty \frac{d^2 u_1}{dX^2}, \tag{3.86b}$$

where $S_\infty = S(x_R)$ and $k_\infty = k(x_R)$. We can eliminate h_1 by rearranging equation (3.86a) and substituting into (3.86b). This gives

$$\frac{du_1}{dX} + \left(\frac{u_\infty}{u_\infty^2 - \delta h_\infty}\right) \frac{d^2 u_1}{dX^2} = \frac{u_\infty}{h_\infty(u_\infty^2 - \delta h_\infty)} \left(\frac{u_\infty^4}{h_\infty} - \delta u_\infty^2 - S_\infty h_\infty + \gamma h_\infty\right). \tag{3.87}$$

Comparing the above with equation (3.22b), we find that the right hand side of equation (3.87) corresponds to (3.22b) evaluated at $x = x_R$, given by the outer solution. We call this λ, where

$$\lambda = \left.\frac{du}{dx}\right|_{x=x_R} = \frac{u_\infty}{h_\infty(u_\infty^2 - \delta h_\infty)} \left(\frac{u_\infty^4}{h_\infty} - \delta u_\infty^2 - S_\infty h_\infty + \gamma h_\infty\right). \tag{3.88}$$

In addition, we know that the outer flow is supercritical, hence

$$\frac{u_\infty}{\sqrt{\delta h_\infty}} = F_\infty > 1, \tag{3.89}$$

and so

$$\frac{u_\infty}{u_\infty^2 - \delta h_\infty} = \sigma > 0. \tag{3.90}$$

The solution of (3.87) gives

$$\frac{du_1}{dX} = \lambda \left(1 + e^{-\sigma X}\right). \tag{3.91}$$

hence,

$$\frac{du_1}{dX} = 0 \quad \text{at} \quad X = 0, \tag{3.92a}$$

$$\frac{du_1}{dX} \to \lambda \quad \text{as} \quad X \to \infty, \tag{3.92b}$$

as required.

The existence of the boundary layer at $x = x_R$ ensures that the solution adjusts to $du/dx = 0$ over a short distance, thus satisfying the right-hand boundary condition imposed in the numerical solution.

3.7 Examining assumptions made in the shallow-water model

As was stated in Section 3.2, an idealised turbulent kinetic energy function was chosen so as to make the shallow-water model (3.13) easier to solve. In this section we will consider the influence of the terms which we neglected from equation (3.4d). In addition, we will also consider what it means for a turbidity current to become extinct in the context of the shallow-water model where the sediment concentration is modelled as a constant.

3.7.1 The turbulent kinetic energy function

We reconsider the derivation of the shallow-water model, detailed in Section 3.2. Here, the sediment concentration was assumed to be constant, and under a suitable normalisation (outlined in Section 3.2) we choose $c = 1$. The small parameters Γ, P and ν were neglected but the parameters $\delta \approx 0.17$ and $\gamma \approx 0.77$

were retained in the model. However, in the turbulent energy equation (3.4d) we chose to neglect the δ term, which was assumed to have a minimal effect on the model of turbulent kinetic energy.

We restate the turbulent kinetic energy equation now, but retain the $\mathcal{O}(\delta)$ term. Since Γ is small for any reasonable slope scale (this will be shown in Chapter 4), we continue to neglect the advective term in equation (3.4d) . The turbulent kinetic energy in equilibrium is

$$0 = \gamma k u - k^{3/2} + \underbrace{\frac{u^5}{2h} - \frac{\delta h}{2}\left(\frac{2\chi}{r_0} + \frac{u^3}{h} + 1 - \chi\right)}_{f}. \tag{3.93}$$

Here, f is used to denote the terms which have no dependence on k. Previously, when the effect of the $\mathcal{O}(\delta)$ term was neglected, the turbulent kinetic energy equation always met the condition $f > 0$. However, with the $\mathcal{O}(\delta)$ terms included, it is possible that $f < 0$. Equation (3.93) does allow f to become negative; however, f must exceed a minimum real value, $f^\star = -4\gamma^3 u^3/27$, or else there will be no real-valued, positive solution for k. In the following chapter we will address this concern and show that when $f < f^\star$ the equilibrium description of turbulent kinetic energy will break down and the Parker model becomes degenerate.

3.7.2 Extinction of the turbidity current

In this section we return to the basic turbulent kinetic energy function, (3.14), used in the solutions to equations (3.22) and (3.28) throughout this chapter. We will use it to come to some conclusions about the extinction of a turbidity current.

We recall that extinction is defined as occurring when the current velocity and sediment concentration tend to zero. In this chapter we have seen that decreasing the magnitude of the downstream slope causes the velocity to decrease and the current to become subcritical. When the slope is a slowly varying, decreasing function of x, the solutions to the two- equation model show that the velocity reaches a uniform value on the flat bed which tends to zero as $t \to \infty$.

We recall that, in the full four-equation Parker model, the sediment concentration equation is given by equation (3.4c). Here, the erosion rate is $E^\star = H(k-P)$ where H is the Heaviside function and P is a small constant. Consequently erosion can be either 'switched on', when $k > P$, or 'switched off', when $k < P$.

When erosion is switched off then we expect the sediment concentration to tend to zero; there is no forcing term left in (3.4c) and the only equilibrium of the equation is at $c = 0$.

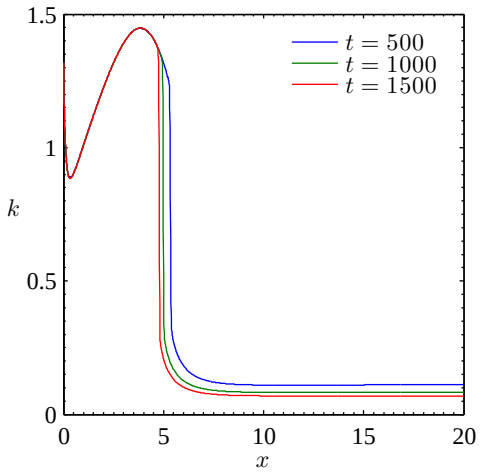

Figure 3.30: Plots of k using equations (3.14) and (3.15) with h and u given by the numerical solutions to equations (3.28). The slope is given by (3.73). Parameter values are $\gamma = 0.77$, $\delta = 0.17$ and the diffusion coefficient is $\epsilon = 0.01$.

For the erosion rate to switch off we require $k < P$. In Figure 3.30 we plot the function k for the numerically computed solutions, h and u, of the shallow water model (3.28). Since k is a decreasing function of time, we expect that if we solved the model for large enough values of t then eventually k would decrease below the threshold value P. At this point, erosion would switch off and the current would only be depositing sediment. Thus, as $t \to \infty$ we can expect that the sediment concentration will decrease to zero and, hence, that the current will eventually become extinct.

However, we have seen that this decrease in k occurs extremely slowly, implying that extinction make take a physically unreasonable length of time to occur. Again, we will see in Chapter 4 that this is an artifact of neglecting the $\mathcal{O}(\delta)$ term in equation (3.93); when this term is retained we will find that extinction occurs on a realistic time-scale and is associated with f falling below the critical value $f^\star$ identified above.

3.8 Discussion

In this chapter we have provided a new nondimensionalisation of the Parker model for a large downstream length scale, $\lambda \sim 60$ km and a bed slope, $\theta \sim 3°$.

These scales are intended to reflect the typical dimensions of the continental slope, and this scaling will prevail throughout the remainder of this thesis.

In Section 3.2, a reduced form of the Parker model was derived; the shallow-water model for turbidity currents. This model focuses on the behaviour of h and u via the conservation of mass and conservation of momentum equations. Through a suitable normalisation, we take $c = 1$, and by exploiting small parameters in the model, we find that k is given by a simple algebraic expression of h and u.

Section 3.3 considers the steady state model, and phase planes for h and u are plotted for different values of the downstream slope. There is a unique value of the slope, $S = S_c$, at which the model undergoes a bifurcation. A singularity line is present in the phase plane at the point where the local Froude number, F, is equal to one and moving from right to left across this line corresponds to a transition between supercritical and subcritical flow. When trajectories terminate on the line $F = 1$, there is a singularity in the steady state equations and so this model breaks down.

The time-dependent model was solved in Section 3.5 for a constant downstream slope. Characteristic diagrams were used to consider shock formation and the solutions h and u were plotted as they evolved in time and space. When $S > S_c$, the current reaches a steady state for the particular initial conditions we have chosen. When $S < S_c$, there is a boundary layer present close to $x = 0$ where the solution rapidly adjusts from the supercritical regime imposed by the inlet conditions, to the subcritical regime the slope is able to sustain. The boundary layer problem was considered in Section 3.5.4 and a steady state solution for h and u was constructed in Section 3.5.5.

In Section 3.6, the time-dependent model was solved for a varying downstream slope. Once again, characteristic diagrams were used to calculate the location of a shock in the solutions, and the time and space dependent solutions were plotted for h and u. The shock was found to be slowly propagating upstream as the solution evolved to meet the boundary condition imposed at $x = x_R$. In Section 3.6.2 an increasing downstream slope was briefly considered, which highlighted that the transition from subcritical to supercritical flow occurs smoothly in this case. The steady state solution was found, and a boundary layer associated with the boundary condition imposed at $x = x_R$ in the numerical solution was discussed.

The slope profiles studied in this section resulted in a number of different solu-

tion features, depending on whether the flow is supercritical or subcritical flow at the left- and right-hand boundaries. In Table 3.1 we draw up a taxonomy of the different solution features we have observed, making particular reference to examples given in this chapter.

$x = 0$	$x = x_R$	Features observed in the numerical solution
$F > 1$	$F > 1$	weak boundary layer at $x = x_R$; see Section 3.5.2
$F > 1$	$F < 1$	shock appears at $x = x_s$ where $S = S_c$, the shock moves upstream until a boundary layer solution is seen, the Rankine- Hugoniot conditions ensure the boundary conditions match to the solution for $x > 0$; see Section 3.6.1
$F < 1$	$F < 1$	boundary layer at $x = 0$; see Section 3.5.3
$F < 1$	$F > 1$	boundary layer at $x = 0$; smooth transition through $x = x_c$ where $S = S_c$, weak boundary layer at $x = x_R$, see Section 3.6.2

Table 3.1: Taxonomy of flow regimes and numerical solution features observed for the slope profiles and boundary conditions imposed on the two-equation model.

Table 3.1 indicates the boundary layers, shocks and transitions seen for each numerical example considered in this chapter. Different types of behaviour are seen, depending upon the slope profile used in the model and the boundary conditions imposed. The shallow-water model has been solved numerically in each case for the boundary conditions given by equation (3.30). We find that the supercritical boundary condition at $x = 0$ results in a strong boundary layer when the slope takes a value $S < S_c$, forcing the flow into a subcritical regime. In addition, the right-hand boundary condition (3.30b) at $x = x_R$ is not necessary when the flow is supercritical at $x = x_R$, and so there is a weak boundary layer as the current adjusts from the outer solution resulting from the direct solution, and the inner solution which takes the solution to $du/dx = 0$.

In the final section, Section 3.7, we analysed some of the assumptions made in this chapter in order to arrive at a two-equation model. The turbulent kinetic energy equation was simplified by neglecting the parameter δ, which was otherwise retained in the momentum equation. This provided a real-valued, positive solution for k, for every solution h and u as the current evolved downstream. In addition, the sediment concentration was assumed to be constant, which is a significant simplification to the model. It was found that both of these assumptions limited the discussion of extinction for the shallow-water model. However, it was illustrated that since $u \to 0$, and, hence, $k \to 0$, as $t \to \infty$, we would

expect erosion to switch off eventually. This would ensure that $c \to 0$ and, thus, that the current would become extinct.

Chapter 4

The four-equation model: the importance of turbulent kinetic energy

In this chapter we will explore the role of turbulent kinetic energy, considering why it is important to the study of density currents, how it affects the dynamics of a turbidity current and how it is included in the model. The basic model of turbulent kinetic energy, derived for the shallow-water model, will be considered once more and the interaction between the turbulent kinetic energy and the sediment concentration will be discussed. This model results in 'enforced ignition' and so the full k-equation will be considered. It will be shown that there is a catastrophic failure of the turbulent kinetic energy equation of Parker et al. (1986), as it is unable to provide a real-valued, positive solution for k at every point.

To prevent the model from breaking down, a new description of turbulent kinetic energy is proposed. This will provide two flow regimes for the current; a turbulent, erosional regime, where $k > 0$, and a stably stratified, depositional regime, where $k = 0$. A number of modelling ideas, including the formulation of a suitable description of the erosion rate as $k \to 0$, will be considered towards the end of the chapter.

4.1 What is turbulent kinetic energy?

The turbulent kinetic energy of a current is a means by which we quantify the fluctuations of the velocity of a fluid. In Chapter 1, we gave the turbulent kinetic energy equation of the Parker model in its depth averaged form and we pointed to Parker et al. (1986) where the model is derived from the Navier-Stokes equations. In this section, we highlight how k plays a role in the model and we will consider in particular the 'ignition condition' outlined by Parker et al. (1986).

4.1.1 How is fluid turbulence measured?

Obtaining a suitable mathematical description of the fluid turbulence of a turbidity current is essential in order to accurately model the evolution of the flow. As was shown in Chapter 1, the turbulent kinetic energy is closely linked to the erosion rate of the current via the friction velocity, which appears in the erosion rate relation used by Parker et al. (1986). As a result, the turbulent kinetic energy plays a large part in both increasing the erosive power of the current, and also in damping the current and thus controlling the entrainment of sediment into the flow. In effect, the turbulent kinetic energy determines the level of entrainment of sediment, and, crucially, it puts a limit on the ignition of a current as we will see in Section 4.1.2, which prevents any flow from accelerating and increasing its sediment load unboundedly.

Authors such as Hu and Cao (2009) have numerically studied the propagation of a current down a constant, steep slope using the model for fluid turbulence derived by Parker et al. (1986). The turbulent kinetic energy equation clearly caps the ignition of the current (versus an earlier version of the model (Parker, 1982) which did not contain a description of turbulent kinetic energy). The resulting height, velocity and sediment profiles calculated by Hu and Cao (2009) are shown to agree well a range of experimental data compiled by the authors. In this chapter we will focus our attention on understanding the mathematics of the turbulent kinetic energy equation of the Parker model.

4.1.2 The turbulent kinetic energy equation

The Parker model is derived from the Reynolds averaged Navier-Stokes (RANS) equations which model the turbulence in the flow by time-averaging the fluctuations in the velocity of the fluid. In a turbidity current, turbulence is prevalent

in the fast-flow phase of the current and is key to keeping sediment in suspension. Reynolds averaging is widely used in environmental fluid mechanics and we refer the reader to Parker's original derivation of the turbidity current model (Parker et al., 1986), Chapter 5 of Rubin and Atkinson (2001) or Chapter 4 of Davidson (2004) for the derivation of the RANS equations for a fluid suspension.

Parker et al. (1986) arrive at equation (1.8) for turbulent kinetic energy by integrating the model over the layer, and by making use of a series of other mathematical approximations, which are fully described in Appendix A of Parker et al. (1986). We recall the depth averaged turbulent kinetic energy equation here:

$$\frac{\partial(kh)}{\partial t} + \frac{\partial(khu)}{\partial x} = u_s^2 u - \beta k^{3/2} + \frac{1}{2}u^3 e_w - \frac{Rgh}{2}\left(2v_s c + cue_w + v_s(E_s - r_0 c)\right). \tag{4.1}$$

Parker et al. (1986) highlight that this equation is introduced as a means of quantifying the 'energy constraint' of the current. This constraint prevents the current from eroding indefinitely and ensures that the turbulence will eventually collapse and the sediment in the current will settle out, causing the current to die. This process is achieved by making use of a generalised Knapp-Bagnold constraint, which will be outlined here.

The final terms on the right-hand side of equation (4.1) are

$$\underbrace{Rghv_s c}_{\text{(a)}} \quad + \quad \underbrace{\frac{Rghcue_w}{2}}_{\text{(b)}} \quad + \quad \underbrace{\frac{Rgh}{2}v_s(E_s - r_0 c)}_{\text{(c)}}. \tag{4.2}$$

These terms represent the rate at which turbulent kinetic energy is expended by working against the density gradient, or the effect of sediment-induced stratification. Term (a) is the Knapp-Bagnold term, which represents the work that is necessary to maintain a given suspension in equilibrium and to prevent deposition of sediment from the current. Term (b) represents the thickening of the current layer due to entrainment; as water is entrained and mixed by turbulence, the centre of gravity rises. This results in an increase in the potential energy of the current, and thus term (b) represents a loss of turbulent kinetic energy through mixing. Term (c) quantifies the energy which is expended as sediment is lifted into suspension. This term will be positive (kinetic energy loss) or negative (kinetic energy gain), depending upon whether erosion exceeds entrainment, or vice-versa.

The autosuspension criterion of Bagnold (1962) is given by

$$\frac{uS}{v_s} > 1. \tag{4.3}$$

Bagnold (1962) argued that if this condition was satisfied, the entrainment of sediment from the bed would continue indefinitely, thus causing the velocity of the current to increase unboundedly. Parker (1982) argued that equation (4.3) is a necessary, but not a sufficient condition for a turbidity current which is accelerating, and instead, generalised this condition to the form

$$u_s^2 u + \frac{1}{2}u^3 e_w > \frac{Rgh}{2}\left(2v_s c + cue_w + v_s(E_s - r_0 c)\right). \tag{4.4}$$

When equation (4.4) is satisfied, ignition occurs. However, Parker et al. (1986) states that if equation (4.4) fails to be satisfied for a sufficient amount of time, the turbulence must die out. Hence, the sediment will settle from the current and the flow will become extinct; thus, the inequality (4.4) puts a limit on ignition.

We note that Parker states that the model for turbulent kinetic energy is suitable for '*supercritical disequilibrium currents* ($Ri < 1$)', and thus we might expect that in the case where the Richardson number, Ri, starts to increase, it might be necessary to reconsider the mathematics of the k-equation. We find this to be the case in Section 4.3 when the Parker model is shown to provide a valid description of turbulent kinetic energy only under certain conditions.

4.2 The basic equilibrium model of turbulent kinetic energy

In Chapter 3, a simple model of turbulent kinetic energy was derived by neglecting the small parameters, Γ, ν, $\delta \ll 1$, in equation (3.4d). Throughout Chapter 3, it was assumed that the sediment concentration of the current remains constant and that k is given by the solution to the algebraic equation

$$\gamma k u - k^{3/2} + f = 0, \quad \text{where} \quad f = \frac{u^5}{2h}. \tag{4.5}$$

This equation was used alongside two pdes for conservation of mass and momentum to give a closed 'shallow-water' model for h, u and k.

A key problem with the shallow-water model is in its capacity to model extinc-

tion, since it assumes that the sediment concentration of the current is fixed at $c = 1$, while for true extinction we require $c \to 0$ as $u \to 0$. It was shown in Section 3.7.2 that extinction cannot be accurately described by the shallow-water model, as k only approaches zero if $f \to 0$, and f typically takes positive values. However, if f did approach zero, k would decrease and erosion would be expected to 'switch off'. At this point we might take $c = 0$, and consider a depositional model, which would show the current approaching extinction.

This theoretical description of extinction illustrates that the shallow-water model is satisfactory, but overly idealised. It is only possible to discuss extinction indirectly, by considering the evolution of k in relation to u, and it should be highlighted that the expression for k, given by equation (4.5), is also idealised. In order to understand extinction fully, the first goal in this chapter is to include the equation for conservation of sediment (3.4c) into the shallow-water model of Chapter 3. This will allow us to look at the interaction of turbulent kinetic energy and the evolution of sediment in the current, directly.

The model is outlined in the following section, and will be solved with the decreasing downstream slope, $S(x)$, used in Chapter 3. It is expected that on the steep slope, where $S \approx 1$, ignition will be seen and the sediment concentration and velocity of the current will be high. However, on the flat bed, where $S \approx 0$, we expect to find that the model predicts extinction; the velocity should decrease, and this should cause the turbulent kinetic energy of the current to decrease. In turn, this should cause erosion to 'switch off' and we expect $c \to 0$.

4.2.1 Adding evolution of sediment to the shallow-water model

This model is formed using the pdes for h and u, equations (3.28) of Chapter 3 (including c as a variable), a simple description of turbulent kinetic energy, given by equation (4.5), and a pde for c, given by equation (3.4c) of Chapter 3, with an additional viscous term. These equations are restated below:

$$\frac{\partial h}{\partial t} + \frac{\partial hu}{\partial x} = \frac{u^3}{ch}, \tag{4.6a}$$

$$\frac{\partial hu}{\partial t} + \frac{\partial hu^2}{\partial x} = -\frac{\delta}{2}\frac{\partial h^2 c}{\partial x} + Shc - \gamma k + \epsilon \frac{\partial}{\partial x}\left(h\frac{\partial u}{\partial x}\right), \tag{4.6b}$$

$$\frac{\partial hc}{\partial t} + \frac{\partial huc}{\partial x} = E^*(k) - \chi c + \omega \frac{\partial}{\partial x}\left(h\frac{\partial c}{\partial x}\right), \tag{4.6c}$$

$$0 = \gamma k u - k^{3/2} + \frac{u^5}{2ch}. \tag{4.6d}$$

Here, ϵ and ω are the coefficients of eddy viscosity and eddy diffusivity respectively; these are physically realistic terms which are included here to the hyperbolic system to smooth any shocks in the numerical solutions. We have also simplified the entrainment rate function, (3.6), since we expect $ch \gg u^2$ when the current is in an erosional regime where the concentration of the flow is high.

The erosion rate The erosion rate function, $E^*(k)$, is recalled from equation (3.5) of Chapter 3;

$$E^*(k) = H(k-P) = \begin{cases} 1 & \text{if } k > P, \\ 0 & \text{if } k \leq P, \end{cases} \tag{4.7}$$

where $P \approx 8.4 \times 10^{-4}$. Since $P \ll 1$ we will take the limit $P \to 0$, which simplifies equation (4.7) to

$$E^*(k) = \begin{cases} 1 & \text{if } k > 0, \\ 0 & \text{if } k = 0, \end{cases} \tag{4.8}$$

i.e. the current is erosional whenever turbulence is present in the current. In the numerical solutions below, we will smooth out equation (4.8) by setting

$$E^\star(k) = \tanh(E_0 k), \tag{4.9}$$

for some large constant E_0. Equation (4.9) approaches equation (4.8) as $E_0 \to \infty$.

The downstream slope Once again, the slope is given by the exponentially decreasing function $S(x)$ of Chapter 3, restated here

$$S(x) = \frac{\exp(5-x)}{1+\exp(5-x)}. \tag{4.10}$$

4.2.1.1 Initial and boundary conditions

As in Chapter 3, we will be using a 'raft' initial condition at $t = 0$. Once again, 'steady inflow' boundary conditions are imposed at $x = 0$ and conditions on u and c are imposed at the right hand boundary, $x = x_R$.

The initial condition takes the form

$$h_0(x) = h^\star G(x), \quad u_0(x) = u^\star G(x), \quad c_0(x) = c^\star G(x) \quad \text{at} \quad t = 0, \quad \textbf{(4.11a)}$$

where

$$G(x) = 1 + \tanh[a(b - x)], \quad \textbf{(4.12)}$$

and $h^\star, u^\star$, $c^\star$, a, b are constants.

The boundary conditions are given as follows:

$$h_i = h^* G_0, \qquad u_i = u^* G_0, \qquad c_i = c^* G_0 \qquad \text{at} \quad x = 0, \qquad \textbf{(4.13a)}$$

$$\frac{\partial u}{\partial x} = 0, \qquad \frac{\partial c}{\partial x} = 0 \qquad \text{at} \quad x = x_R, \qquad \textbf{(4.13b)}$$

where $x_R > 0$ and $G_0 = G(0) = 1 + \tanh(ab)$.

4.2.1.2 Numerical solutions

The model (4.6) is solved numerically using the inbuilt pde solver *pdepe* in MATLAB for $x \in (0, x_R)$, $t \in (0, T)$ where $x_R = 20$ and $T = 150$. The solution profiles are plotted in Figure 4.1 for $t \in (0, 1)$ and in Figure 4.2 for $t \in (50, 150)$. The complete solutions for h and u are shown in Figure 4.3.

Initial development of the current In Figure 4.1, the early time solutions to the model are shown. Figure 4.1(c) shows that there is a rapid increase in c, the concentration of sediment, at the head of the current as the flow moves downstream. When the erosion rate of the current is plotted, in Figure 4.4, we find that this highly concentrated region corresponds to an erosional front which is rapidly propagating downstream. For $t > 4$, the current is eroding across the domain; $E^\star = 1$ for all x.

The solutions in Figure 4.1 show a small disturbance close to $x = 0$; this is associated with the imposed initial condition which causes increase in u and k and a decrease in h and c. This disturbance propagates downstream in time.

Shock development In Figure 4.2, the disturbance is located at $x \approx 14$ when $t = 50$ and it propagates out of the domain as t increases. Behind this disturbance, a shock develops in the solution at $x \approx 5$. This shock is associated with the change in the slope of the sea bed, and causes an increase in h and decrease in u and k.

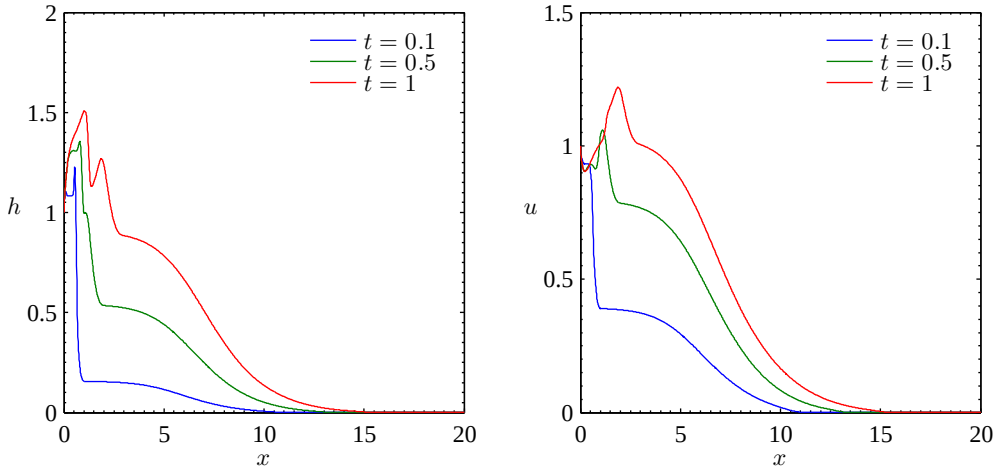

(a) Depth h

(b) Velocity u

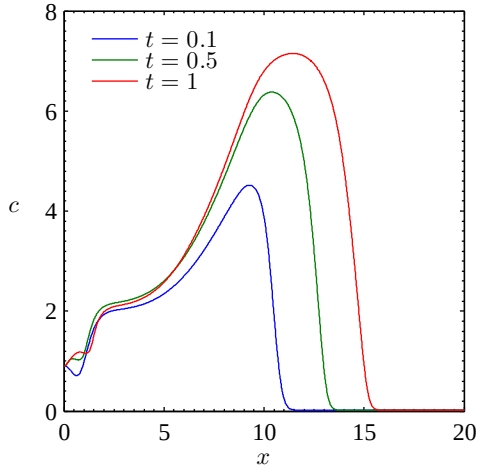

(c) Sediment concentration c

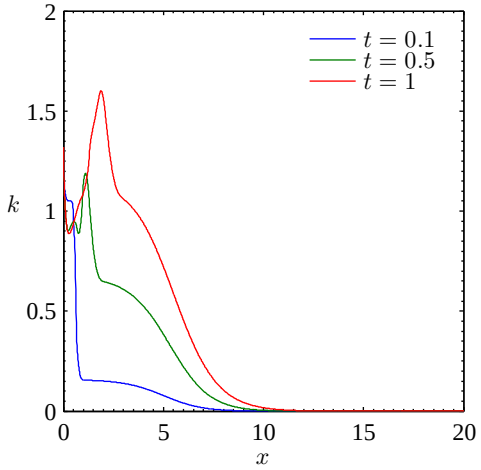

(d) Turbulent kinetic energy k

Figure 4.1: Solution profiles to equations (4.6) for S given by equation (4.10), $E^\star$ given by equation (4.9) and $x \in (0, 20)$, $t \in (0, 1)$. The initial conditions are given by (4.11) and the boundary conditions by (4.13). The parameter values are $\delta = 0.17$, $\gamma = 0.77$, $\chi = 0.067$, $E_0 = 10^4$, $h^\star = 0.5$, $u^\star = 0.5$, $c^\star = 0.5$, $a = 25$, $b = 0.5$ and the diffusion coefficients are given by $\epsilon = 0.01$, $\omega = 0.01$.

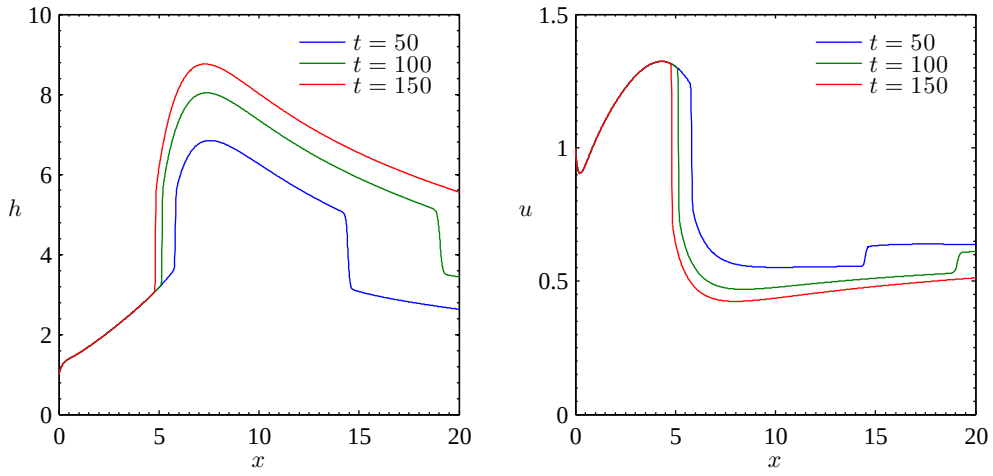

(a) Depth h

(b) Velocity u

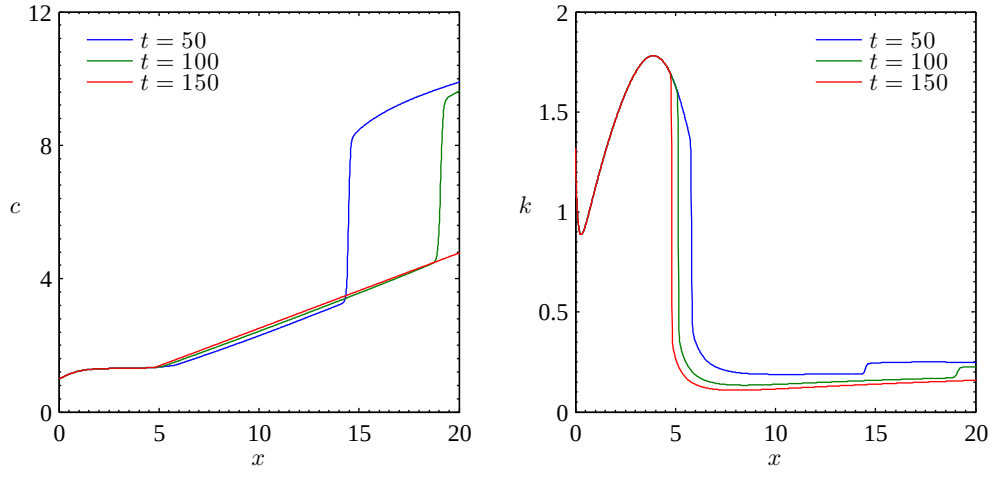

(c) Sediment concentration c

(d) Turbulent kinetic energy k

Figure 4.2: Solution profiles to equations (4.6) for S given by equation (4.10), $E^\star$ given by equation (4.9) and $x \in (0, 20)$, $t \in (50, 150)$. The initial conditions are given by (4.11) and the boundary conditions by (4.13). The parameter values are listed in Figure 4.1.

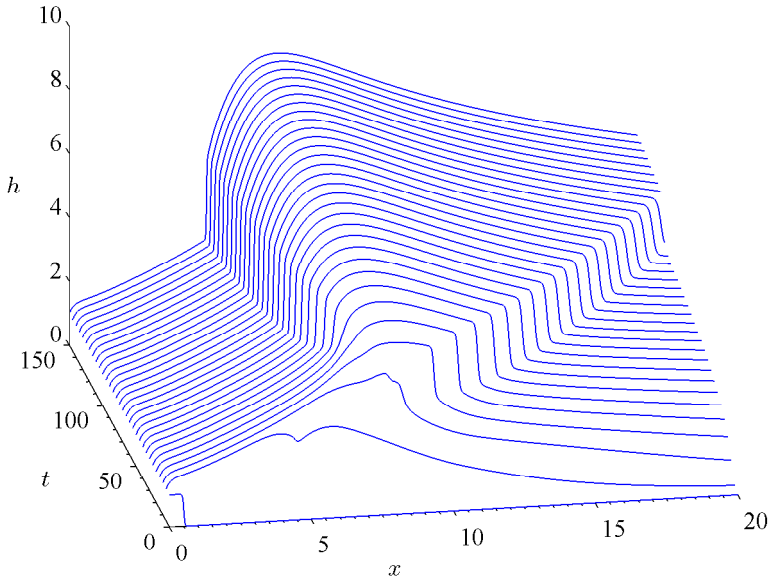

(a) Solution for h

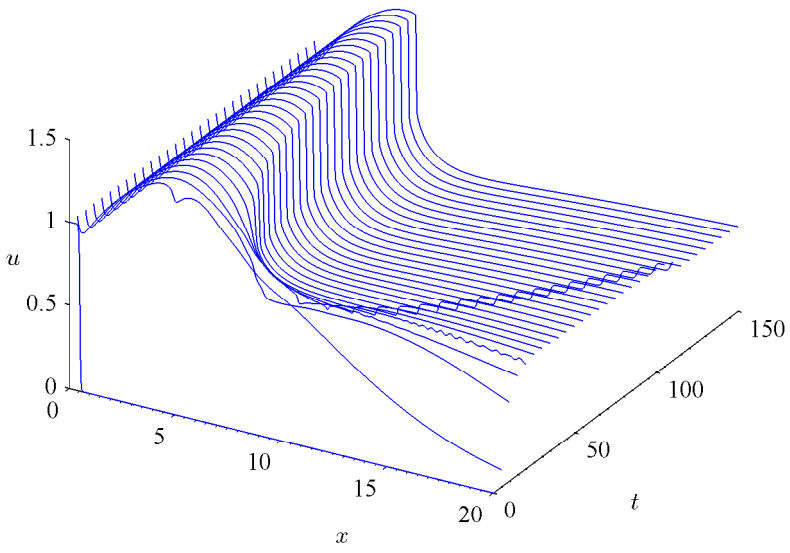

(b) Solution for u

Figure 4.3: Solution to equations (4.6) for S given by equation (4.10), $E^\star$ given by equation (4.9) and $x \in (0, 20)$, $t \in (0, 150)$. The initial conditions are given by (4.11) and the boundary conditions by (4.13). The parameter values are listed in Figure 4.1.

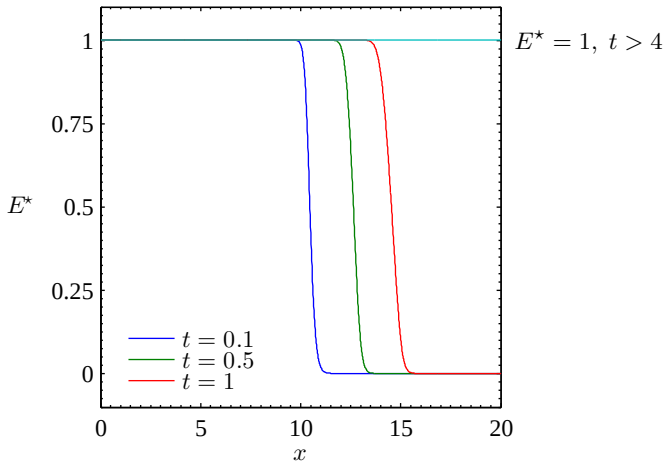

Figure 4.4: The erosion rate, (4.9), for the solutions to equations (4.6). The slope function is given by equation (4.10). The parameter values, initial and boundary conditions for the model are listed in Figure 4.1.

The location of the shock is confirmed by plotting the Froude number of the flow, shown in Figure 4.5. As expected, the shock is located at the point where $F = 1$; when $F > 1$ the flow is supercritical and when $F < 1$ the flow is subcritical. In the supercritical flow regime we have a low-concentration, high velocity, turbulent current, and in the subcritical regime we have a high-concentration, slow moving, thick current.

Comparison with shallow-water model for constant c The plots of h and u shown in Figure 4.3 allow for a comparison with the solutions to the shallow-water model of Chapter 3 shown in Figure 3.18. The qualitative behaviour is certainly the same; a shock at the change of slope is observed and the velocity is higher on the steep slope than on the flat bed, whilst the current is thicker on the flat bed than on the steep slope. These features correspond with the expected supercritical and subcritical flow regimes. A key difference between the two models is that Figure 4.3 shows a disturbance in the solution, which propagates downstream in time. This disturbance is associated with a large variation in the sediment concentration of the current downstream. In contrast, the solutions plotted in Figure 3.18 for the shallow-water model, do not show this disturbance as c is assumed to be constant across the domain.

In Figure 4.6, we plot solution profiles to the shallow-water model with varying and constant c at time $t = 75$. This plot highlights the effect of the varying sediment concentration of the current. In addition, when c is allowed to vary downstream, h and u reach lower and higher values, respectively on the steep

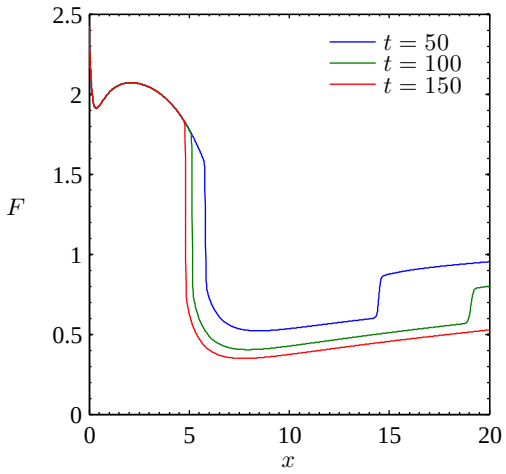

Figure 4.5: The Froude number of the flow, $F = u/\sqrt{\delta h}$, for the solutions to equations (4.6). The slope function is given by equation (4.10). The parameter values, initial and boundary conditions for the model are listed in Figure 4.1.

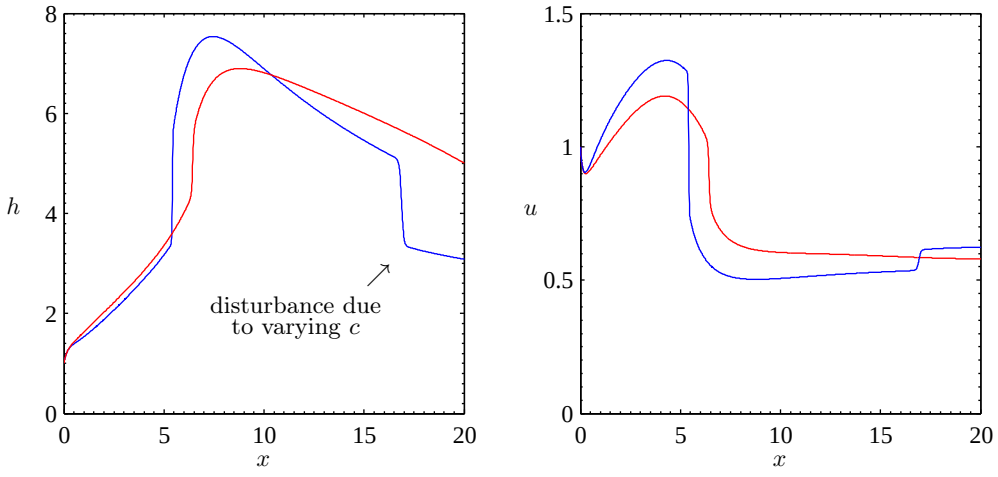

(a) Solution for h

(b) Solution for u

Figure 4.6: Comparison of solutions to the shallow-water model with fixed sediment concentration (plotted in red) and solutions to the shallow-water model with evolution of sediment (plotted in blue) at $t = 75$. The red solution profiles are calculated from equations (3.28) and the blue solution profiles are calculated from equations (4.6). The same slope profile, equation (4.10), is used for both solutions.

slope, and higher and lower values, respectively, immediately after the shock. Moreover, the shock is propagating upstream more quickly in the solutions to the shallow-water model with evolution of sediment.

A highly erosive current We would expect the sediment concentration of the current to decrease on the flat bed in the shallow-water model with evolution of sediment (4.6), however the model does not show this and the current continues to erode even when $S \approx 0$. This highlights the effect of the simplified k equation; that high values of turbulent kinetic energy are predicted on both the steep slope and flat bed. As in Chapter 3, the solution is evolving very slowly and so we will not see $k \to 0$ on any reasonable timescale. Consequently, erosion does not switch off when $S \approx 0$ and the sediment concentration of the current remains very high.

It could be supposed that since $k > 0$ on the flat bed, and erosion is occurring everywhere, that the current is igniting. However, in the next section it will be shown that the high erosion rate, and correspondingly high velocity and sediment concentration, are all artifacts of an over- simplified turbulent kinetic energy model (4.6d).The basic turbulent kinetic energy equation results in 'enforced ignition'.

4.2.2 Analysis of the basic equilibrium model of turbulent kinetic energy

The turbulent kinetic energy model (4.6d) can be rewritten as

$$\gamma k u - k^{3/2} + f = 0, \quad \text{where} \quad f = \frac{u^5}{2ch}. \tag{4.14}$$

In Figure 4.7, equation (4.14) is plotted parametrically to highlight how k approaches zero.

Clearly $f > 0$, since $u, h, c > 0$. It is therefore clear that, unless $u \to 0$, equation (4.14) ensures that $k > 0$ in every solution to the model. In particular, since $f > 0$, the solution is taken from the blue branch of the parametric plot marked in Figure 4.7. A direct consequence is that erosion will never switch off in the model after the initial erosion front has propagated downstream, the model predicts 'enforced ignition'.

The basic equilibrium model of turbulent kinetic energy captures the key supercritical and subcritical flow regimes on the steep continental slope and flat

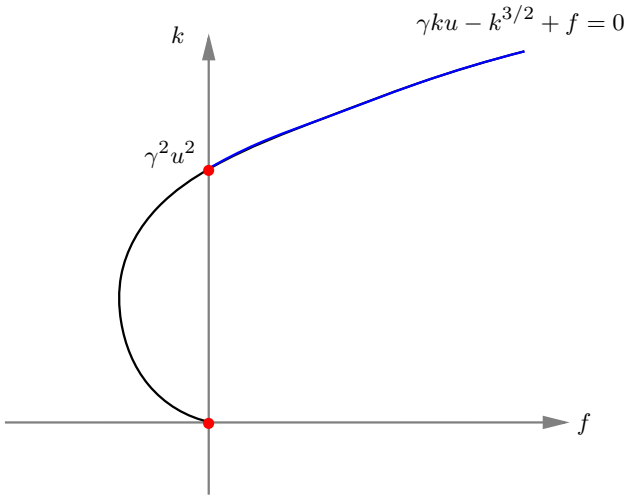

Figure 4.7: The parametric plot of equation (4.14) showing how k varies with f. We mark the roots of the equations by the red dots and the $f > 0$ solution branch in blue.

abyssal plain, respectively. These flow regimes have been observed and well documented throughout the literature; see Garcia and Parker (1989) and Kostic and Parker (2006), for example. However, as was identified above, by neglecting terms which were thought to have a minimal effect on the evolution of the turbulent kinetic energy, we have in fact oversimplified the model. This oversimplification prevents k decreasing to zero, unless $u \to 0$. The model is therefore unable to accurately predict extinction of a turbidity current.

4.3 The Parker model of turbulent kinetic energy

The full model for turbulent kinetic energy is given by equation (3.4d). When the basic equilibrium model (4.6d) was derived, it was assumed that $\delta \ll 1$ and the final four terms (inside the brackets) of equation (3.4d) were therefore neglected. These terms model the effect sediment-induced stratification on the current, which, in light of the sustained ignition observed in Section 4.2, cannot necessarily be neglected. The terms of order δ will therefore be retained in the full equilibrium model outlined below.

In addition, the parameter χ will be retained whilst the parameter Γ will be neglected. In the nondimensionalisation of Section 3.1, the slope scale is given by $S_0 = 0.05$ and both $\chi, \Gamma \sim \mathcal{O}(10^{-2})$. However, by taking $S_0 = 0.01$ in the nondimensionalisation, we find that $\chi \sim \mathcal{O}(10^{-1})$, but $\Gamma \sim \mathcal{O}(10^{-2})$. This suggests that the deposition becomes an important effect as the slope flattens out downstream, whilst the advection term is always negligible. As a result, the

parameter χ will be retained in the model of turbulent kinetic energy outlined below, however, the parameter Γ will continue to be neglected in equation (3.4d), since it is the only parameter which can be truly said to be small, relative to the other parameters in the model.

The turbulent kinetic energy is thus given by the solution to the following algebraic equation for k:

$$0 = \gamma k u - k^{3/2} + \frac{1}{2}u^3 e^\star - \frac{\delta h}{2}\left(\frac{2\chi c}{r_0} + cue^\star + E^\star(k) - \chi c\right). \qquad \textbf{(4.15)}$$

Since the erosion rate is a function of k, we will rewrite equation (4.15) as

$$\gamma k u - k^{3/2} - \frac{\delta h}{2}E^\star(k) + f = 0, \qquad \textbf{(4.16)}$$

where

$$f = \frac{u^3 e^\star}{2} - \frac{\delta h c}{2}\left(\left[\frac{2}{r_0} - 1\right]\chi + ue^\star\right). \qquad \textbf{(4.17)}$$

We recall the definition of the erosion rate (4.8), which is a Heaviside function of k. We plot equation (4.16) parametrically in Figure 4.8 for the erosive, $E^\star = 1$, and depositional, $E^\star = 0$, states.

As erosion switches off, the solution switches from being given by a point on the solution branch of Figure 4.8(a) to a point on the solution branch of Figure 4.8(b). We recall that in the numerical solutions to the Parker model, we have chosen to model the erosion rate as a tanh function, equation (4.9). This overcomes the discontinuity at $f = 0$, and erosion switches off in a smooth way. We show the parametric plot of equation (4.16) for the case when $E^\star$ is given by equation (4.9) in Figure 4.9.

Now there is a continuous transition between the erosional and the depositional regimes. By adjusting the value of E_0 in equation (4.9), the transition can be made smoother, or sharper. The sharper the transition, the closer the equation approximates the Heaviside function; however the tanh function ensures a continuous solution is provided for every $f > 0$.

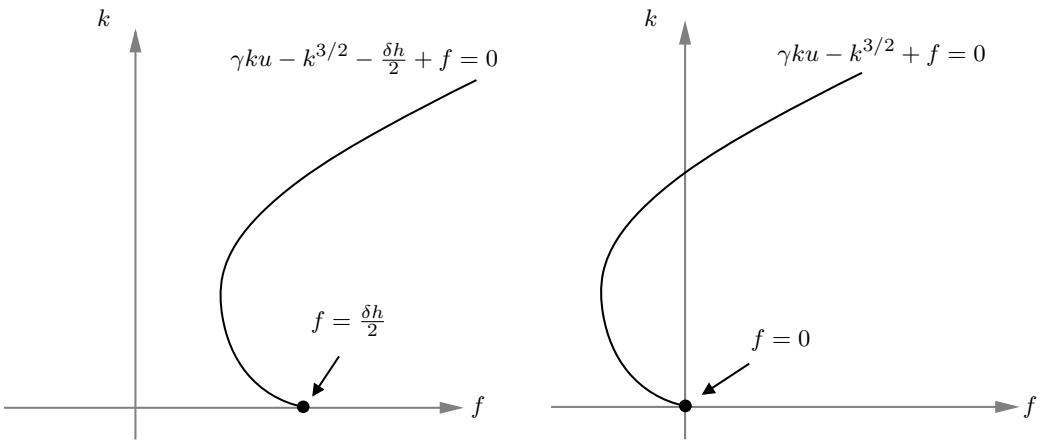

(a) Parametric plot of the erosional regime

(b) Parametric plot of the depositional regime

Figure 4.8: The parametric plot of equation (4.16) with (a) $E^\star = 1$ and (b) $E^\star = 0$.

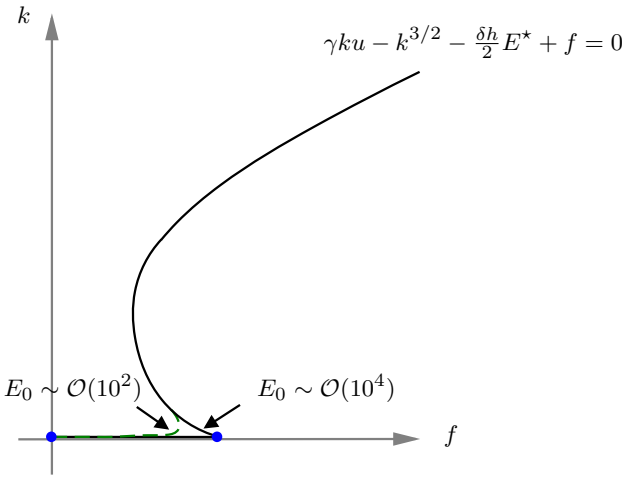

Figure 4.9: The parametric plot of equation (4.16) with the erosion rate given by equation (4.9). We highlight in green the smoother transition that occurs by letting E_0 take a smaller value. The blue circles mark the discrete points of the Heaviside function (4.8).

4.3.1 The breakdown of the equilibrium model

The global minimum in f of equation (4.16) occurs at $f = 0$, at which point $k = 0$. There is also a local minimum in f at $f = f^\star$ where

$$k^\star = \frac{4}{9}\gamma^2 u^2 \quad \text{and} \quad f^\star = -\frac{4}{27}\gamma^3 u^3 + \frac{\delta h}{2}. \tag{4.18}$$

For $f^\star < f < \frac{\delta h}{2}$, the solution, k, of equation (4.16) is multi-valued. We highlight this in the parametric plot of equation (4.16), shown in Figure 4.10.

Since equation (4.16) is multi-valued, it cannot provide a unique solution for k corresponding to every f. Without a means to calculate the correct value of k in the region $f^\star < f < \frac{\delta h}{2}$, the equilibrium equation is invalid and cannot be used to model turbulent kinetic energy.

In addition, we have, so far, only considered solutions to equation (4.16) for $f > 0$. Recalling equation (4.17), f could become negative, unlike in the basic equilibrium model of k, equation (4.6d). However, the equilibrium model cannot provide a real-valued solution for k when $f < 0$.

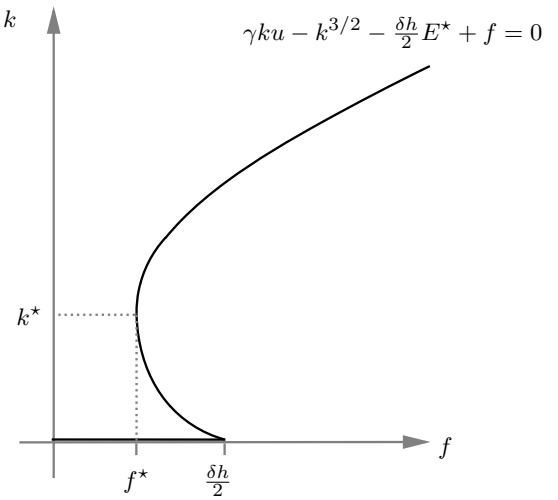

Figure 4.10: The parametric plot of equation (4.16) where the erosion rate is modelled by equation (4.9). The local minimum of the function at $f = f^\star$ is marked, and the corresponding value of k is shown at $k^\star$.

4.3.2 Breakdown of the turbulent kinetic energy equation

We return to equation (3.4d) and retain the small parameter Γ, to consider the behaviour of the time- and space-dependent equation when $f < 0$. The equation

is rearranged to the form

$$\dot{k} = \frac{1}{\Gamma h}\left(\gamma k u - k^{3/2} - \frac{\delta h}{2}E^{\star}(k) + f - \Gamma k e^{\star} u\right), \tag{4.19}$$

where f is given by equation (4.17) and we define $\dot{k}$ to be the total derivative of k. We use equation (4.19) to study the phase plane of k, shown in Figure 4.11. By varying the size of f we can see how the dynamics are expected to change.

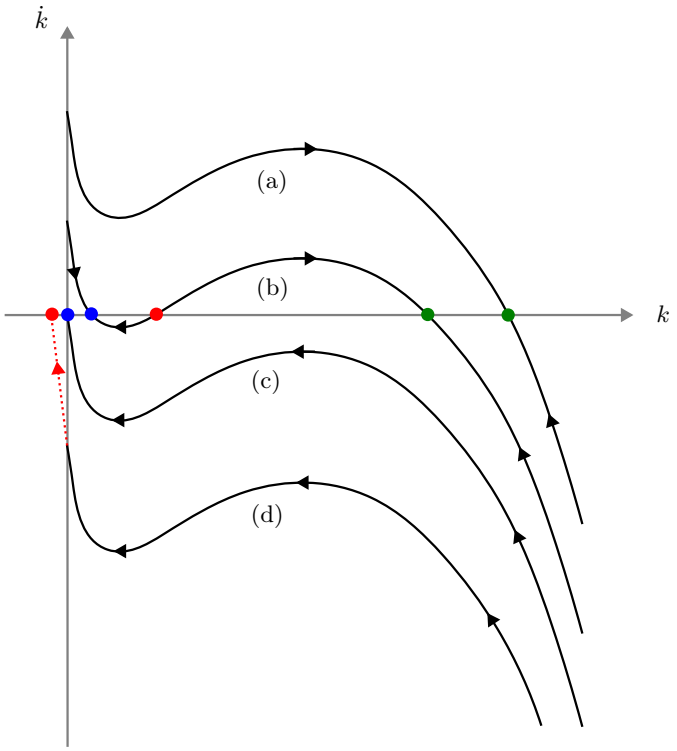

Figure 4.11: Phase plane of equation (4.19) as the size of f is varied. Curve (a) shows the case $f > \frac{\delta h}{2}$, curve (b) shows the case $f^{\star} < f < \frac{\delta h}{2}$, curve (c) shows the case $f = 0$ and curve (d) shows the case $f < 0$.

In Figure 4.11 case (a), we show that when $f > 0$, k will approach a non-zero constant, marked by a green circle. This was the only case possible in the basic equilibrium model, equation (4.6d); here, $f > 0$ when $u > 0$ and k never becomes zero. A type of enforced ignition was observed in the solutions to the model[1].

An intermediate case exits when $f^{\star} < f < \frac{\delta h}{2}$; this is illustrated in Figure 4.11 case (b). Here, there are two steady state values separated by an unstable

[1]Enforced ignition also occurs when f takes a value in the range $0 < f < f^{\star}$. Once again, k will approach a non-zero constant.

branch in the model. This case corresponds to the multivalued region of the equilibrium equation (4.16). When f takes values in this range k will, again, approach a non-zero constant, though the value of this constant will depend on the initial value of k. We label the steady state closer to $k = 0$ in blue, and the steady state for large k in green. In Section 4.5.2, we will discuss how this case could be considered as an example of hysteresis of turbulent kinetic energy and we will discuss the suitability of a hysteresis model for k.

Figure 4.11 case (c) shows the phase plane for $f = 0$. In this case, k approaches an equilibrium value of $k = 0$ in finite time. Erosion switches off and the current will become extinct.

In Figure 4.11 case (d), we show the phase plane for the model when $f < 0$. In this case, equation (4.19) predicts that k approaches zero rapidly; however, it also tells us that $\dot{k} < 0$ at this point. This means that k has not reached an equilibrium value. Instead, the equation predicts that k will want to continue to decrease beyond zero, at which point solutions to equation (4.19) cease to be real. We obviously cannot allow complex values of k to exist, and to have an equation which predicts that $k < 0$ suggests a serious flaw in the model of turbulent kinetic energy proposed by Parker et al. (1986).

4.3.3 Summary

The analysis in this section has illustrated the conditions under which the full equilibrium model is a suitable description of the flow, and when the model will fail. A decrease in the term f, equation (4.17), is key in causing the size of k to decrease; however there is a range over which equation (4.16) becomes multi-valued and returns a non-unique value of k. In addition, the equilibrium model cannot predict a real-valued solution for k when $f < 0$. As a result, the equilibrium description of the turbulent kinetic energy, as it currently stands, is not a suitable model for k.

The time- and space-dependent turbulent energy equation was considered by retaining the small parameter Γ. This model predicts real-valued solutions to k, if, and only if, the density term, f, fulfills the condition $f \geq 0$. By considering equation (4.17), it was shown there was no reason to assume that f is a strictly positive function, revealing a serious flaw in the Parker description of turbulent kinetic energy. We find that the model of Parker et al. (1986) fails catastrophically if the density term in equation (3.4d) becomes negative.

4.4 Transition model of turbulent kinetic energy

In this section, we propose a new model for turbulent kinetic energy. The main idea is to adapt the equilibrium model (4.16) such that it can provide a real-valued, unique solution k for every value of f. The model will provide continuous solutions in h, u and c and allow k to switch out of an erosional regime when f reaches $f = f^\star$.

In Section 4.4.1, the transition model is defined mathematically, with attention to certain flow parameters which must be redefined in the new flow regime. This model is then solved numerically and the solutions considered. We expect to find that the solutions to the transition model show that the current is eroding on the steep slope, when $S \approx 1$, and is depositing sediment on the flat bed, when $S \approx 0$.

We conclude this section with a discussion of transition between turbulent and laminar regimes. The transition model that we have defined ensures that when $f < f^\star$ the current rapidly approaches $k = 0$. When $k = 0$, we might suppose that the current is no longer turbulent and instead has transitioned and become 'stably stratified', which is a type of laminarisation that occurs in marine currents. We will consider the transition into a depositional regime in terms of the Reynolds number and the Richardson number, the primary dimensionless parameters used in the study of turbulent flows.

4.4.1 Derivation of the transition model

Our aim in deriving the transition model is to overcome the main fault of the original Parker equation for k, that is, we require a k to be well defined for every value of f in the model. The transition model will take the form

$$k = \begin{cases} \text{solution of (4.16)} & \text{if } f > f^\star, \\ 0 & \text{if } f \leq f^\star, \end{cases} \tag{4.20}$$

where $f^\star$ is given in equation (4.18). This model provides a piecewise-continuous, uniquely-determined solution for k as f becomes negative. We show the parametric plot of equation (4.20) in Figure 4.12.

From Figure 4.12 it is clear that k is now uniquely and piecewise- continuously defined for every value of f, both positive and negative. However, we must now think about how to model other aspects of the flow in the depositional regime.

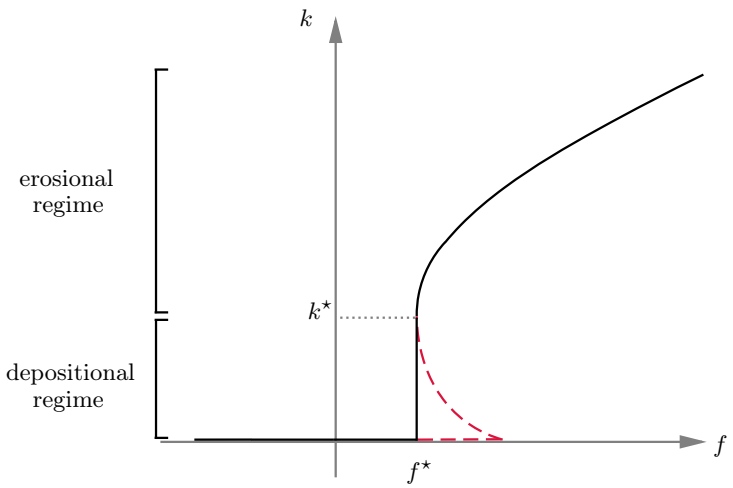

Figure 4.12: The parametric plot of the transitional turbulent kinetic energy model (4.20) showing how k approaches zero rapidly once $f < f^\star$. When $f < 0$, k remains at zero. The depositional branch and the erosional branch of the model are indicated. The point $k = k^\star$ where the erosion 'switches off' is marked. The red dashed line marks the branch of the equilibrium model which has now been disregarded.

Particularly, we need to consider the drag term in the momentum equation (4.6b) which will become zero at $k = 0$, and the erosion rate $E^\star$, which is a function of k.

4.4.1.1 Redefining the flow parameters

Drag at the base of the current The derivation of the basal drag term is recalled from Section 1.4.1 of Chapter 1. In dimensionless variables, it is given by equation

$$c_D = \frac{k}{\gamma^2 u^2}. \tag{4.21}$$

Basal drag is incorporated into the model via the friction velocity, u_s, which is parameterised by k,

$$u_s^2 = k. \tag{4.22}$$

In the transition model, outlined in equation (4.20), this parameterisation will result in the drag and the friction velocity tending to zero as $k \to 0$. Physically, however, we do not expect the drag at the base of the current to become zero when the current is depositional.

From the definition of the transition model, equation (4.20), at $f = f^\star$ the turbulent kinetic energy takes the value $k = k^\star$. For $f < f^\star$, the model imposes the condition that $k = 0$. In order for the drag on the current to be continuous,

we will model the turbulent drag in the depositional regime as a constant, given by

$$c_D = \frac{k^\star}{\gamma^2 u^2} = \frac{4}{9} \quad \text{for} \quad f \leq f^\star. \tag{4.23}$$

Hence, the drag law for the transition model takes the form

$$c_D = \begin{cases} \frac{k}{\gamma^2 u^2} & \text{if } f > f^\star, \\ \frac{4}{9} & \text{if } f \leq f^\star. \end{cases} \tag{4.24}$$

The drag law is plotted as a function of k in Figure 4.13(a).

From the definition of the basal drag term (4.24), we can derive an expression for the friction velocity in both the erosional and depositional regimes. Making use of equation (4.22), we determine the friction velocity to be

$$u_s^2 = \begin{cases} k & \text{if } f > f^\star, \\ \frac{4}{9}\gamma^2 u^2 = k^\star & \text{if } f \leq f^\star. \end{cases} \tag{4.25}$$

The friction velocity is plotted as a function of k in Figure 4.13(b).

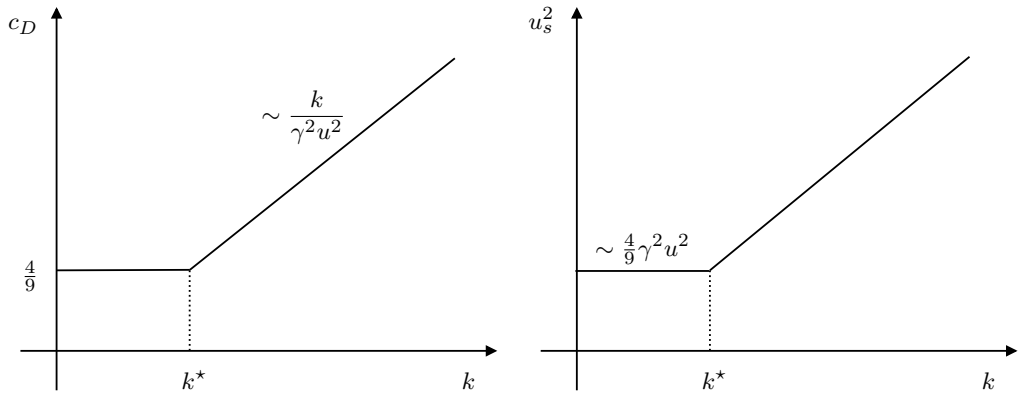

(a) Drag c_D varying with k

(b) Friction velocity $u_\star$ varying with k

Figure 4.13: (a) The drag law for the transition model, given by equation (4.24). (b) The friction velocity law for the transition model, given by equation (4.25).

The erosion rate The erosion rate appears in the Parker model as a function of k, from the parameterisation of the friction velocity provided in Chapter 1. Since the friction velocity has been redefined for the transition model, it is also necessary to consider how the erosion rate will be modelled here.

The nondimensional erosion rate is given by

$$E^\star = \begin{cases} 1 & \text{if } u_s > 0, \\ 0 & \text{if } u_s = 0. \end{cases} \tag{4.26}$$

This expression is equivalent to the expression for $E^\star(k)$, equation (4.8), when $u_s^2 = k$, but not when u_s is given by equation (4.25).

In the transition model, we want to ensure that $E^\star \to 0$ and that erosion is clearly linked to the level of turbulence in the current, rather than the shear of the bed. As such, the erosion of the current will be modelled by equation (4.26), where $u_s = k$. Modelling of the erosion rate in this manner is consistent with the literature, since Parker et al. (1986) highlights that the entrainment of bed sediment is linked to the state of the turbulence, rather than the magnitude of the velocity of the current. As such, in this section the erosion will continue to be given by the tanh function, equation (4.8); however in Section 4.5.1 we will explore alternative ways in which we could model the depositional phase of the current.

4.4.2 The turbidity current model with a transition from an erosional to a depositional regime

In summary, the transition model is given by

$$\frac{\partial h}{\partial t} + \frac{\partial hu}{\partial x} = e^\star u, \tag{4.27a}$$

$$\frac{\partial hu}{\partial t} + \frac{\partial hu^2}{\partial x} = -\frac{\delta}{2}\frac{\partial h^2 c}{\partial x} + Shc - \gamma u_s^2 + \epsilon \frac{\partial}{\partial x}\left(h\frac{\partial u}{\partial x}\right), \tag{4.27b}$$

$$\frac{\partial hc}{\partial t} + \frac{\partial huc}{\partial x} = E^*(k) - \chi c + \omega \frac{\partial}{\partial x}\left(h\frac{\partial c}{\partial x}\right), \tag{4.27c}$$

$$k = \begin{cases} \text{solution of} \quad 0 = \gamma u_s^2 u - k^{3/2} - \frac{\delta h}{2} E^\star(k) + f & \text{if } f > f^\star, \\ 0 & \text{if } f \le f^\star, \end{cases} \tag{4.27d}$$

where u_s is given by equation (4.25), f is given by equation (4.17), $f^\star$ is given by equation (4.18), $e^\star$ is given by equation (3.6), and $E^\star(k)$ is given by equation (4.9). The transition model is solved for $x \in (0, 35)$ and solution profiles for h, u, c, k are shown in Figure 4.14 for $t \in (0, 5)$ and Figure 4.15 for $t \in (50, 150)$. The solutions for h and u for $x \in (0, 20)$ and $t \in (0, 150)$ are shown in Figure 4.16.

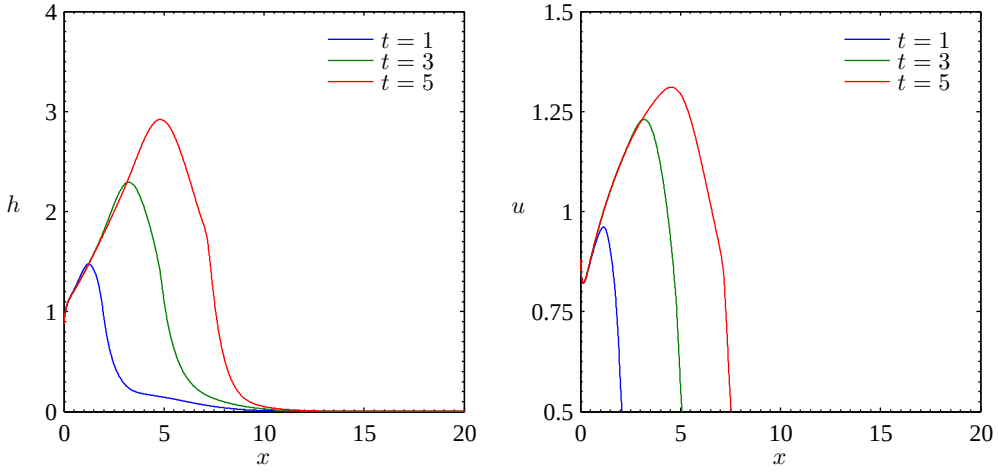

(a) Depth h

(b) Velocity u

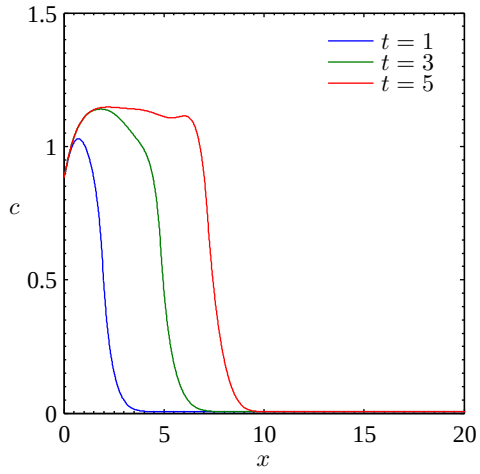

(c) Sediment concentration c

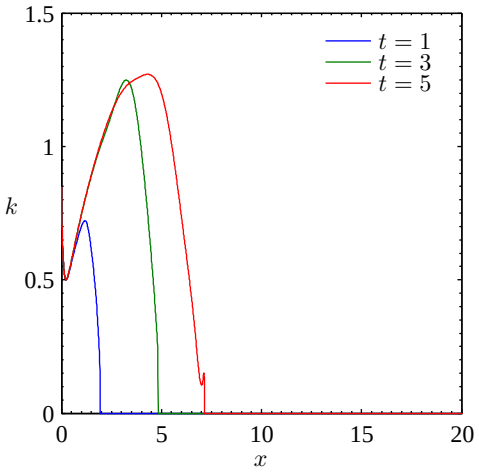

(d) Turbulent kinetic energy k

Figure 4.14: Solution profiles to the transition model of turbulent kinetic energy (4.27). The slope, S, is given by equation (4.10), $E^\star$ given by equation (4.9) and solutions are plotted for $x \in (0, 20)$, $t \in (0, 5)$. The initial conditions are given by (4.11) and the boundary conditions by (4.13). The parameter values are $\delta = 0.17$, $\gamma = 0.77$, $\chi = 0.067$, $\nu = 0.115$, $r_0 = 1.6$, $E_0 = 10^3$, $h^\star = 0.5$, $u^\star = 0.5$, $c^\star = 0.5$, $a = 2$, $b = 0.5$ and the diffusion coefficients are given by $\epsilon = 0.005$, $\omega = 0.1$.

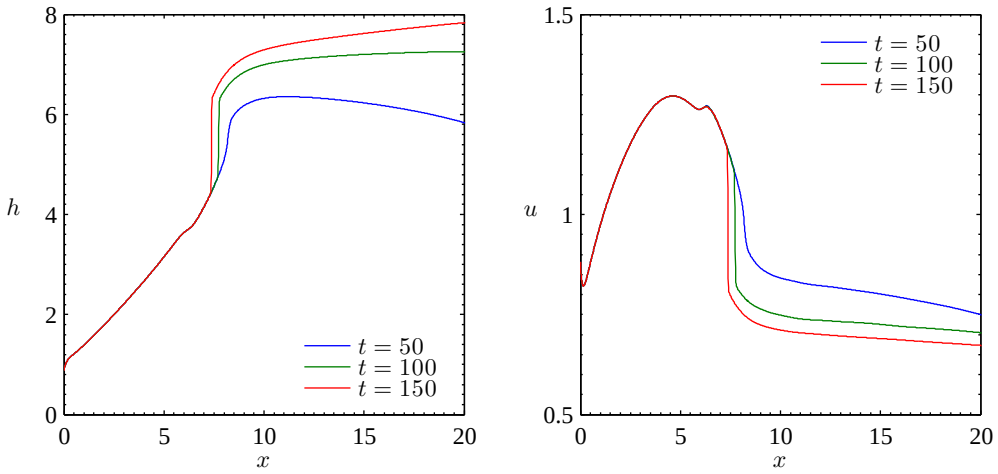

(a) Depth h

(b) Velocity u

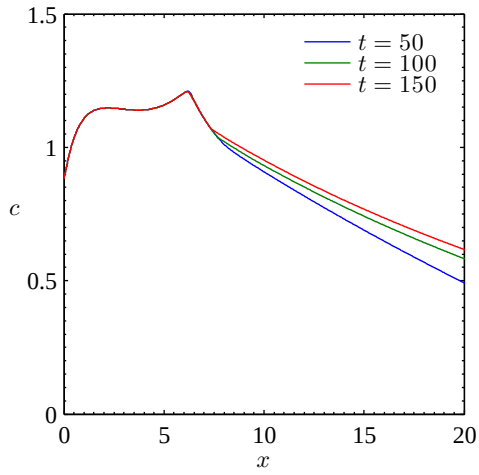

(c) Sediment concentration c

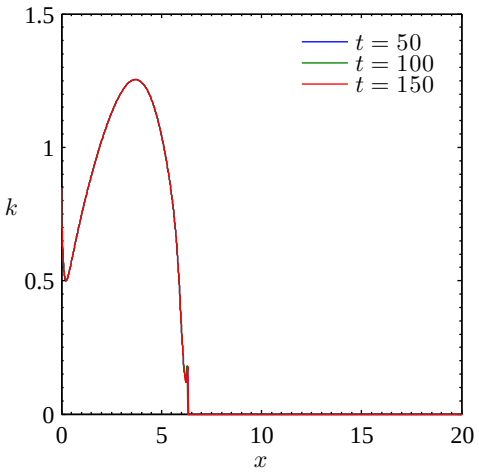

(d) Turbulent kinetic energy k

Figure 4.15: Solution profiles to the transition model of turbulent kinetic energy (4.27). The slope, S, is given by equation (4.10), $E^\star$ given by equation (4.9) and solutions are plotted for $x \in (0, 20)$, $t \in (50, 150)$. The initial conditions are given by (4.11) and the boundary conditions by (4.13). The parameter values are listed in Figure 4.14.

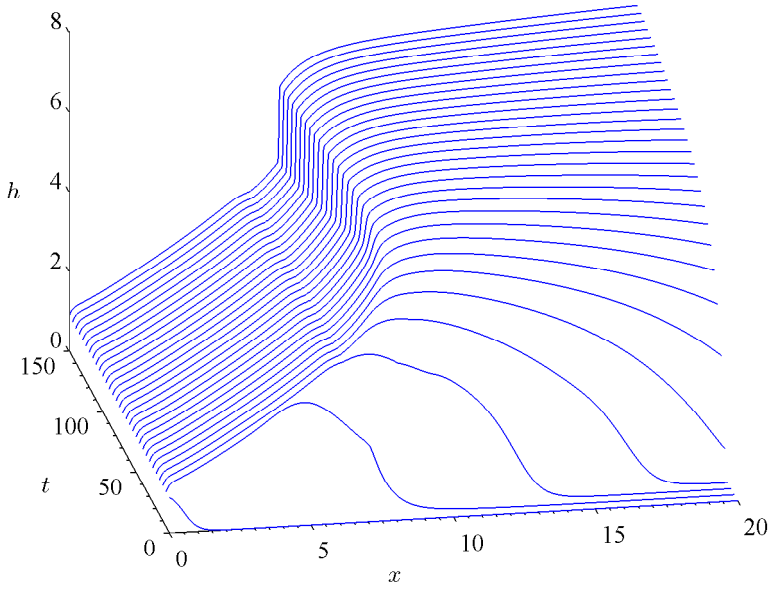

(a) Solution for h

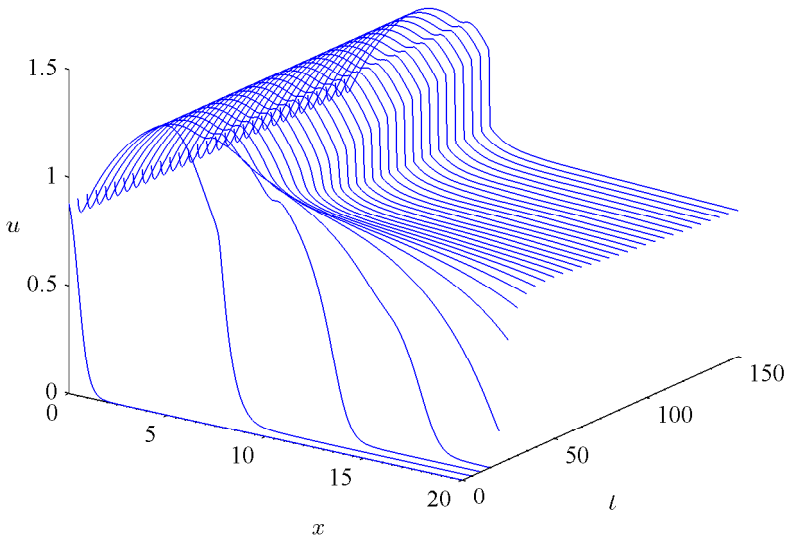

(b) Solution for u

Figure 4.16: Solution to equations (4.27). The slope, S, is given by equation (4.10), $E^\star$ given by equation (4.9) and $x \in (0, 20)$, $t \in (0, 150)$. The initial conditions are given by (4.11) and the boundary conditions by (4.13). The parameter values are listed in Figure 4.14.

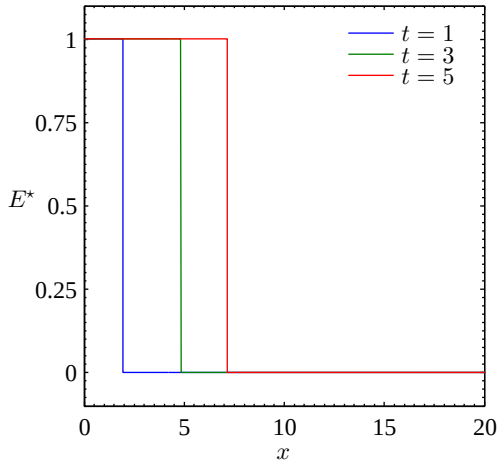

Figure 4.17: The erosion rate, (4.9), for the solutions to equations (4.27). The slope function is given by equation (4.10). The parameter values, initial conditions and boundary conditions for the model are listed in Figure 4.14.

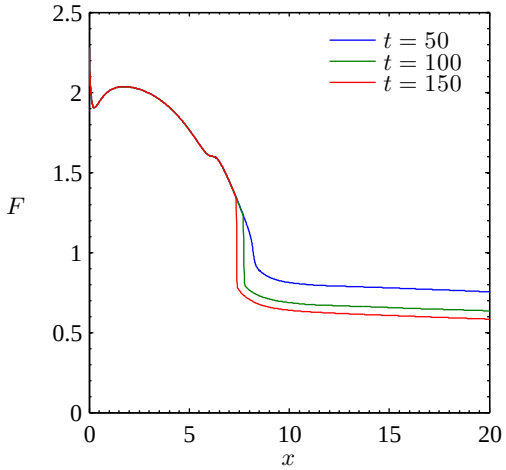

Figure 4.18: The Froude number of the flow, $F = u/\sqrt{\delta h}$, for the solutions to equations (4.27). The slope function is given by equation (4.10). The parameter values, initial and boundary conditions for the model are listed in Figure 4.14.

In the early time solutions shown in Figure 4.14, the initial flux of sediment is propagating downstream in time with a specified velocity and height. The turbulent kinetic energy is also increasing downstream, and in Figure 4.17 the erosion rate is plotted, showing the corresponding erosional front which is propagating downstream in time.

In Figure 4.15, the solution profiles are plotted for later times. A shock has developed by $t = 100$, and it can been seen in the plots of h and u in Figure 4.15 as a sharp increase in the value of h and a sharp decrease in the value of u close to $x \approx 7.5$. The shock is confirmed by plotting the Froude number, F, in Figure 4.18, which shows the flow is supercritical, $F > 1$, behind the shock and subcritical, $F < 1$, ahead of the shock.

The plot of the turbulent kinetic energy, Figure 4.15(d), shows that there is a sharp decrease in k at $x \approx 6$ and for $x > 6$, $k = 0$. This is the point at which the current switches from being in an erosional regime, where $k > 0$, to being in a depositional regime where $k = 0$. Consequently, for $x > 6$, the current is purely depositional and, as we can see in Figure 4.15(c), there is a steady decrease in the value of c for $x > 6$. As we expected, the transition model predicts erosion of sediment on the steep slope and deposition and extinction of the current on the flat bed.

4.4.3 Transition from a turbulent to a laminar regime

When $k = 0$, the fluctuations in the current have tended to zero, and so it could be supposed that the flow is now in a laminar regime. In the study of classical fluid mechanics, a transition between a turbulent and a laminar flow regime is often considered in the context of the Reynolds number, Re, a dimensionless parameter which relates the inertial and viscous forces of the flow (*e.g.* Ockendon and Ockendon (1995)). The Reynolds number is given in terms of the characteristic length scale, in this case the depth of the current, h_0, and the characteristic velocity scale u_0;

$$Re = \frac{u_0 h_0}{\nu_w}, \tag{4.28}$$

where ν_w is the kinematic viscosity of the fluid. When the viscous forces outweigh the inertial forces then the flow is laminar and Re is small. Conversely, if inertial forces outweigh the viscous forces then the flow is turbulent and Re is large. Transition between these regimes occurs at a Reynolds number of about $Re \sim \mathcal{O}(10^3)$, when we might see 'intermittency', or regions of both laminar

and turbulent flow (*e.g.* Marshall (2011)).

In a marine setting, we are dealing with very large values of the Reynolds number, compared to the usual experimental scales we would see in classical fluid mechanics textbooks. In the case of an ignitive turbidity current, the characteristic length scale is $h_0 \sim 500$ m, and the characteristic velocity scale is $u_0 \sim 25$ m s^{-1}, giving $Re \sim \mathcal{O}(10^{10})$. This is confirmed by plotting the Reynolds number of the flow in Figure 4.19(a) for the solutions calculated in Section 4.4.2.

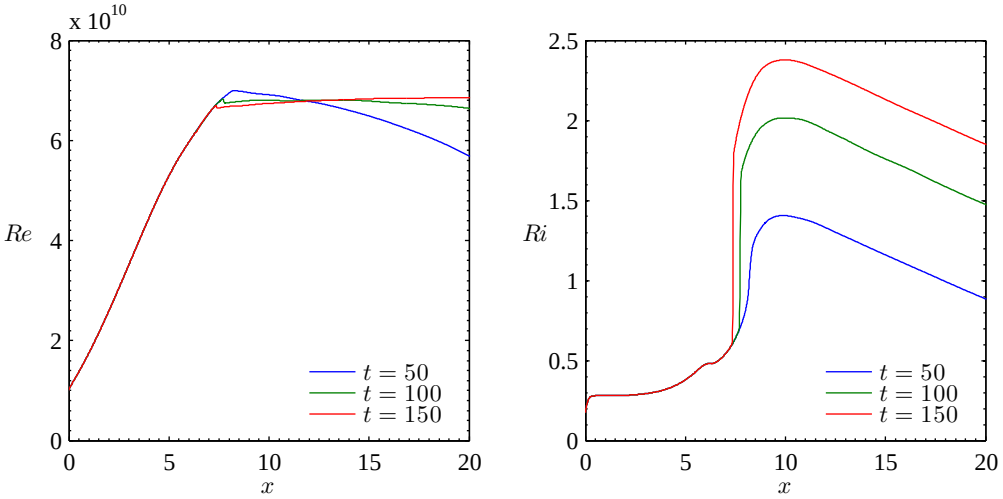

(a) Reynolds number

(b) Richardson number

Figure 4.19: The flow Reynolds number, given by equation (4.28), and the flow Richardson number, given by equation (4.29), calculated using solutions to the turbulent kinetic energy transition model, given by equations (4.27) and plotted in Figure 4.15. The parameters and constants used in the solution are listed in the caption to Figure 4.14.

Since $Re \sim \mathcal{O}(10^{10})$ for all x, it is not possible to understand the $k = 0$ regime of the transition model by looking at the Reynolds number. In fact, large-scale ocean turbulence is heavily influenced by stratification (Baumert et al., 2005) and so it is not a transition to a laminar regime we wish to describe, but, in fact, a transition from turbulent flow to stably stratified flow.

As Parker et al. (1986) highlights, the behaviour of stratified slender flows is governed by the Richardson number, Ri. This parameter relates the buoyancy forces to the inertial forces and it is given by equation (1.19) in Section 1.4.3, restated here:

$$Ri = \frac{Rgc_0h_0}{u_0^2}, \tag{4.29}$$

where the product Rg is the reduced gravity, c_0 is the sediment concentration

scale, h_0 is the depth scale and u_0 is the velocity scale of the flow we are considering. When Ri is small, typically $Ri < 1/4$, the shear of the fluid is high, the flow becomes unstable and turbulent mixing occurs. However, when $Ri > 1/4$, and certainly when $Ri > 1$, we find that the stratification stabilises the flow and turbulent mixing is suppressed (Hopfinger, 1987). In Figure 4.19(b) we plot the Richardson number of the flow for the solutions calculated in Section 4.4.2.

By plotting the Richardson number, Figure 4.19(b), it can be seen that the $k = 0$ flow regime could be explained by a transition to from turbulent to stably stratified flow (at $x \approx 6$). For $x < 6$, $Ri \approx 0.5$ and for $x > 6$, $Ri > 1$. These values are in agreement with critical values discussed above that suggest when the current moves out of a turbulent regime.

4.4.4 Summary

In this section, a turbidity current model which considers a transition from an erosional to a depositional regime is presented. This model shows that $k \to 0$ in finite time, at which point $E^\star = 0$ and the current is purely depositional. The transition model, given by equations (4.27) with associated functions listed in Section 4.4.2, is the model that will be solved numerically for the remainder of this thesis. The model provides continuous solutions for h, u and c, and k. The transition model was tested with some basic steady inflow boundary conditions in this section for a simple varying bed profile. The model shows promising results and we will make use of it in the following chapter to study more complicated initiation problems.

We present a discussion in Section 4.4.3 of a transition from a turbulent regime, where $k > 0$, to a laminar regime, where $k = 0$. Since the Reynolds number of the flow is very large, a transition from a turbulent flow to a stably stratified flow, rather than a classic transition to a laminar regime is discussed. The switch between these regimes is caused when the high sediment concentration causes significant stratification and the turbulence in the current collapses. This causes $k \to 0$ and thus $E^\star \to 0$ and the current moves into a depositional regime. It has been shown by examining the Richardson number, Ri, that $Ri \lesssim 0.5$ when the current is turbulent and takes a value greater than unity when the stratification in the current eliminates the turbulence.

In the rest of this chapter we will discuss further modelling questions that arise from the transition model of turbulent kinetic energy. This will include a dis-

cussion of the erosion rate and how it could be modelled as the current enters the depositional regime. We will also consider a 'hysteresis model', and how it might be applied to the study of turbidity currents by extending the transition model presented in this section.

4.5 Modelling questions

Here, we will attempt to address some of the modelling questions that arise from the definition of the transition model of turbulent kinetic energy. We will begin by looking at the erosion rate and studying the transition model in more depth. It will be shown that the transition model leads to a 'natural' description of $E^\star$, determined from the turbulent kinetic energy equation in the $k = 0$ regime. This description of erosion will be discussed, and other possible formulations of the erosion rate as the current moves to a depositional regime will be proposed.

A hysteresis model of turbulent kinetic energy will also be examined. This model will provide two separate solution branches for the flow. One branch will provide a solution for k when the current is moving from an erosional to a depositional flow (becoming stably stratified), and the other branch will provide a solution for k as we move from a depositional to an erosional flow (becoming turbulent).

Since we are satisfied that the turbidity current model given by equations (4.27) is accurate enough to use in case studies, the discussion in this chapter will be theoretical only, and will not feature a numerical exploration of these modelling ideas.

4.5.1 Determining the way in which erosion switches off

The transition model is derived in Section 4.4.2. As was noted in Section 4.4.1.1, when the flow parameters are reconsidered in the depositional regime, the erosion rate of the current continues to be given by the Heaviside function of equation (4.8). In the numerical model, this Heaviside function is approximated by a tanh function (4.9). Here, we outline the natural description of the erosion rate which arises from the turbulent kinetic energy equation when $k = 0$, and alternative descriptions of the erosion rate which could be considered.

4.5.1.1 The natural description of the erosion rate

The turbulent kinetic energy equation is given by equation (4.16). In the erosional regime we have $k > 0$ and the erosion rate is a constant, $E^\star = 1$. The friction velocity is a function of turbulent kinetic energy, $u_s^2 = k$, and we solve equation (4.16) for k, which provides the turbulent kinetic energy in the erosional regime.

In the depositional regime, the friction velocity is given by $u_s^2 = k^\star = \frac{4}{9}\gamma^2 u^2$, and $k = 0$. Thus equation (4.16) reduces to

$$\frac{4}{9}\gamma^3 u^3 - \frac{\delta h}{2} E^\star + f = 0. \tag{4.30}$$

In the previous section we took $E^\star = 0$, immediately, in the depositional regime, and so equation (4.30) is not necessarily satisfied, since f is given by equation (4.17). The problem is over-determined. In addition, by setting $E^\star = 1$ when $k = 0$ we are no longer conserving turbulent kinetic energy. In fact, we can use equation (4.30) to provide a definition of the erosion rate, by solving equation (4.30) for $E^\star$;

$$E^\star = \frac{2}{\delta h}\left(f + \frac{4}{9}\gamma^3 u^3\right), \quad \text{for} \quad f < f^\star. \tag{4.31}$$

Equation (4.31) is plotted as a function of f in Figure 4.20.

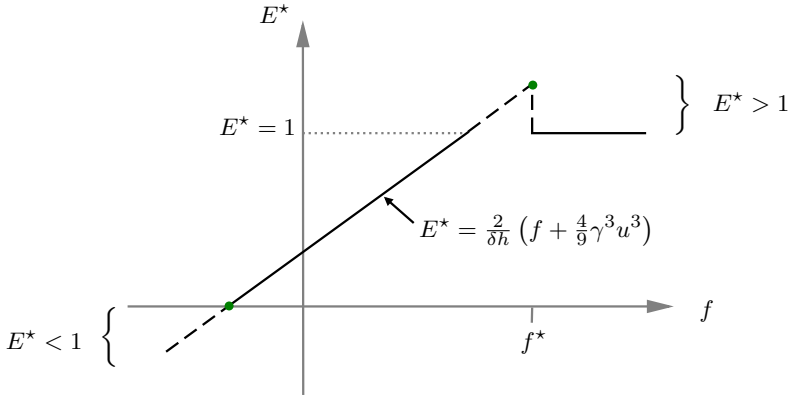

Figure 4.20: The parametric plot of equation (4.31). The maximum and minimum positive values of the erosion rate are marked by green circles. The maximum of the function occurs at $f^\star$. The dashed black lines denote the parts of the function outside of the range $E^\star \in (0, 1)$.

In Figure 4.20, it is clear that the definition of the erosion rate given by equation (4.31) allows $E^\star$ takes values outside of the range $(0, 1)$. The maximum occurs

at $f = f^\star$, where $E^\star$ takes the value

$$E^\star = 1 + \frac{16}{27}\frac{\gamma^3 u^3}{\delta h} > 1 \quad \text{since} \quad u, h > 0. \tag{4.32}$$

In addition, $E^\star$ can take on any negative value, according to equation (4.31), as f decreases. It is interesting that once $k = 0$, the turbulent kinetic energy equation leads to this 'natural' relation for erosion in terms of f, which does not constrain $E^\star \in (0, 1)$. However, as we have shown, this description is necessary for equation (4.30) to be valid and to prevent the model from becoming overdetermined.

Whilst regions of where $E^\star > 1$ or $E^\star < 1$ may just be an artefact of the transition model, we can make some attempts to explain the erosion and deposition of the current as k switches on or off by considering the Rouse number. This dimensionless quantity is given by

$$Ro = \frac{v_s}{\kappa u_s}, \tag{4.33}$$

where v_s is the settling velocity, κ is the von Kármán constant and u_s is the friction velocity (*e.g.* Fowler (2011)). As k switches on at the point $k = k^\star$ we might interpret equation (4.31) as suggesting the flow is in a near-permanent suspension regime; no deposition is taking place and the flow has a Rouse number of $Ro < 1$ (Hearn, 2008). In contrast, when $k \to 0$ and the Rouse number of the flow increases, particularly $Ro > 2.5$, we expect their to be rapid settling as the sediment in the current falls out of suspension.

4.5.1.2 Alternative descriptions of the erosion rate

It is possible to suggest other forms of the erosion rate, however it should be noted that they will not satisfy the energy equation (4.31) when $k = 0$. The most basic description we can suggest is to constrain $E^\star \in (0, 1)$ such that $E^\star$ varies in the range $f \in (0, f^\star)$ and is constant outside this range. A function describing this behaviour could be given by

$$E^\star = \begin{cases} 1 & \text{if } f > f^\star, \\ \dfrac{f}{f^\star} & \text{if } 0 < f \leq f^\star, \\ 0 & \text{if } f \leq 0. \end{cases} \tag{4.34}$$

Equation (4.34) is plotted parametrically, as a function of f, in Figure 4.21.

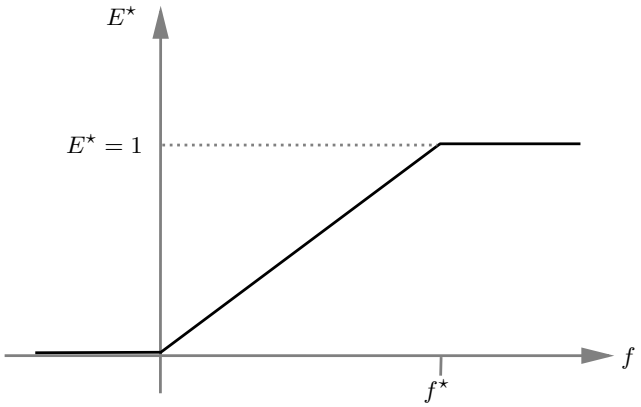

Figure 4.21: The parametric plot of equation (4.34). The erosion rate has a maximum of $E^\star = 1$ at $f = f^\star$ and a minimum of $E^\star = 0$ at $f = 0$. Between $f = 0$ and $f = f^\star$ the function varies linearly according to equation (4.34).

We can see in Figure 4.21 that the erosion rate function given by equation (4.34) defines $E^\star$ in the range $(0, 1)$ and for every value of f, including $f < 0$. The advantage of using a function of this type is that it models the erosion rate as switching off gradually, something that the 'natural' description of erosion suggests to be true.

It might be expected that $E^\star$ should exist only in the range $(0, 1)$. However, when $k = 0$, the Parker model leads to a description for $E^\star$, equation (4.31), that will cause $E^\star$ to take values outside of this range. It is possible to give a physical explanation of the erosion rate in this case, through consideration of the Rouse number, suggesting that when $k = k^\star$ we are in a regime of near-permanent suspension and when $k \to 0$ we have significant settling of sediment from the current.

The alternative description of $E^\star$ is provided by equation (4.34). Since this description does not satisfy equation (4.30), this is one of many ways in which erosion could be modelled as $k \to 0$. It is, once again, hard to suggest a particular model of $E^\star$ that is superior, without having empirical evidence to back up a particular relation.

4.5.2 A hysteresis model of turbulent kinetic energy

In the literature, a transition from a turbulent to a stably stratified regime is often mentioned alongside a discussion of hysteresis, in that the point at which a turbulent flow becomes stably stratified is different to the point at which a stably stratified flow becomes turbulent (Högström et al., 1999; Canuto, 2002; Galperin

et al., 2007). This effect is commonly considered in meteorology literature; Stull (1988) gives a good description of hysteresis in terms of the Richardson number. Stull (1988) states that there is one value of the Richardson number, Ri_T, at which the flow switches from being turbulent to being stably stratified, and another value of the Richardson number, Ri_C, at which the flow moves back from a stably stratified to a turbulent regime, with $Ri_T > Ri_C$. Authors, including Stull (1988) and Galperin et al. (2007), suggest that these critical values are given by $Ri_C = 0.25$ and $Ri_T = 1$.

There is some discussion of hysteresis being relevant for sediment currents in the ocean, however it is mostly in the context of turbulent tidal flows. Costa and Mehta (1989) and Baumert and Radach (1992) both present a study of hysteresis of turbulent kinetic energy in tidal flows. However, in each of these papers it is very clear that the hysteresis effect is caused by the differing acceleration and deceleration phases of the tide, or by the tidal flux of sediment in the estuarine environment. Due to the limited nature of the literature available, it is hard to suggest how influential a hysteresis effect would be upon the dynamics of a turbidity current. In this section we will explore, theoretically, how we could go about constructing a hysteresis model for turbidity currents. However, due to the lack of empirical data to justify such a model, we will not implement a hysteresis model numerically.

4.5.2.1 Deriving a model to describe hysteresis

The equilibrium equation for k, equation (4.16), will be used here to create the two 'branches' of a hysteresis model of turbulent kinetic energy. The model will be made up of an erosional branch which dictates the behaviour of k as the current moves from a turbulent to stably stratified flow, and a depositional branch which will dictate the behaviour of k as the current moves from being stably stratified to turbulent. The model is illustrated in Figure 4.22, and described mathematically by

$$k = \begin{cases} \text{solution of} \quad \gamma u_s^2 u - k^{3/2} - \frac{\delta h}{2} E^\star(k) + f = 0 & \text{if } f > f^\star, \\ 0 & \text{if } f < \frac{\delta h}{2}. \end{cases} \qquad \textbf{(4.35)}$$

Thus, for $f > \frac{\delta h}{2}$, the current is turbulent and erosional, and for $f < f^\star$, the current is stably stratified and depositional. We note that equation (4.35) is multivalued for $f \in (f^\star, \frac{\delta h}{2})$; both branches are locally stable and the current can be either erosional or depositional.

As can be seen in Figure 4.22, the value of f determines whether the current is turbulent or stably stratified. In practise, it is likely that the two critical values of f will be very close to each other in value. In addition, it is hard to imagine how this difference would be measured experimentally and so the description of hysteresis presented here provides a theoretical discussion only.

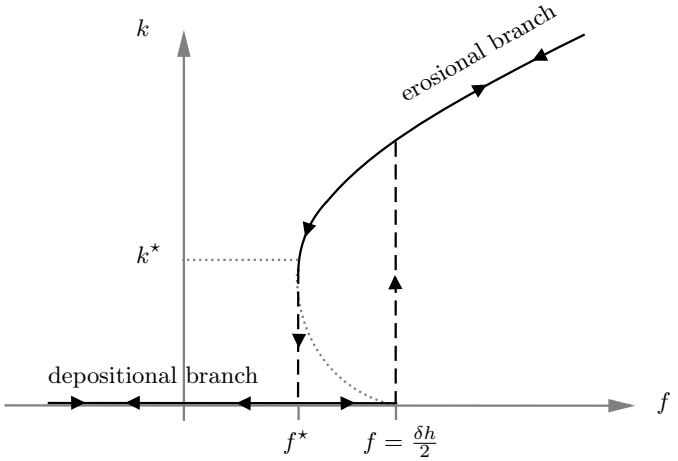

Figure 4.22: A plot of equation (4.35). The point $f^\star$, at which the current becomes stably stratified and moves into a depositional regime, is marked and the point $f = \frac{\delta h}{2}$, at which the current becomes turbulent and moves into an erosional regime, is marked. When $f^\star < f < \frac{\delta h}{2}$, both branches are locally stable and the current can be either erosional or depositional. The dashed lines indicate how the solution moves between the two branches and the dotted line marks the disregarded unstable intermediate branch of equation (4.15).

The model presented above provides an outline of how turbulent kinetic energy could be modelled, should it be found to exhibit hysteresis. It remains to be determined how the erosion rate, $E^\star$, and the friction velocity, u_s, might be determined in a hysteresis model. Further exploration of these empirical relations would have to be considered before an accurate hysteresis model could be proposed. In addition, the Richardson number could be related directly to the onset and termination of turbulent flow. This would provide further justification for a model which switches between a turbulent and stably stratified regime.

The hysteresis model of turbulent kinetic energy would change the way in which a current becomes turbulent once it has entered a depositional regime. The hysteresis model suggests that stable stratification persists longer than we expect, such that the density term in the k equation must increase more to move into a turbulent regime. The theoretical idea behind a hysteresis model has been outlined, though we did not implement a scheme numerically since there have been no direct observations of hysteresis in turbidity currents.

4.6 Discussion

In this chapter the importance of the density term in the turbulent kinetic energy equation has been highlighted. This term represents the effect of sediment-induced stratification and is key in reducing the value of k towards zero, which is required in order for erosion in the current to switch off and for the current to become extinct. It was shown in Section 4.2 that a basic equilibrium model which neglects the density term in the turbulent kinetic energy equation causes 'enforced ignition' and links the erosion rate directly to the velocity of the current, rather than the level of turbulence.

In Section 4.3, the equilibrium model of turbulent kinetic energy was considered. This was shown to be a multi-valued function, which prevents a unique value of k from being determined. In addition, the equilibrium model is not able to provide a solution for k for every possible value of the density term. Moreover, when dynamic solutions of the turbulent kinetic energy equation are considered, we showed that k may reach zero in finite time and then cease to be real. This is a catastrophic failure of the Parker model.

In Section 4.4, a new model was proposed, called the 'transition model' as it defines two regimes in the current: an erosional regime, where $k > 0$, and a depositional regime, where $k = 0$. This model was solved alongside the time- and space-dependent equations for h, u and c and the solutions show realistic results for the basic steady-inflow problem we wish to consider. The transition model was explained in the context of a turbulent to stably stratified transition; the sediment induced stratification eliminates the turbulence from the model, resulting in a depositional current.

The transition model raises several modelling questions, some of which are addressed in Section 4.5. The manner in which the erosion rate of the current 'switches off' as the flow moves becomes depositional was considered. Several descriptions of the erosion rate were proposed, but, without any experimental work describing how the erosion rate 'switches off' as the current becomes stably stratified, it remains to be determined which is the most accurate. A further modelling question was the idea of a hysteresis model of turbulent kinetic energy. An outline of such a model was proposed, which is formulated based on the ideas of hysteresis witnessed in other physical systems. The concept of a hysteresis model, in itself, creates further points for consideration, such as the nature of erosion and drag in a system which exhibits hysteresis. Once again, it remains for these points to be looked at in future work, alongside empirical

work which could provide significant insight into the ideas touched upon in this section.

Chapter 5

Case Studies

In this chapter we will use the transition model of Chapter 4 to study some realistically-scaled turbidity current events. There will be two primary areas of focus looking at two of the most common ways in which a turbidity current is initiated: through a 'slump' avalanche event, or a time-dependent 'fluvial' event. The solutions will be studied and analysed in line with previous work in this thesis, but in an attempt to answer the question: 'when does a turbidity current become extinct?'.

5.1 Triggering mechanisms

As was discussed in Chapter 1, the ways in which a turbidity current is triggered can be broadly separated into two categories: those caused by failure of existing sediment on the seabed, 'avalanche' or 'slump' events; and those caused by sediment being introduced to the ocean environment, 'fluvial' or 'steady inflow events'.

Since the 1950s, it has been known that sediment failures in the ocean can be caused by earthquakes and can trigger a turbidity current on the sea bed (Heezen and Ewing, 1952; Ryan and Heezen, 1965). It is also known that continuous deposition of sediment on a slope can lead to over-steepening and failure, initiating a turbidity current which propagates downstream on the sea floor (Girardclos et al., 2007). Both of these events are known as 'slumps', as they involve the failure of pre-existing material on a slope on the sea bed. Other slump events can be caused by human activity, such as the 1979 Nice turbidity current, which was triggered by landfilling operations during the construction of Nice Airport

(Mulder et al., 1997), or turbidity currents in the Palamós (Fonera) canyon in the Mediterranean in 2001, which were initiated when sediment was loosened by trawling nets operating in the upper regions of the canyon (Palanques et al., 2006).

Turbidity currents have also been attributed to rivers in flood when sediment concentrations are high, typically in excess of 36 kg m^{-3} (Mulder et al., 2003). Highly concentrated sediment suspension plumes, known as hyperpycnal flows, propagate into the ocean and trigger a turbidity current. These flows are negatively buoyant, with a density in excess of the surrounding water and they trigger a turbidity current as they plunge into the ocean (Mulder and Syvitski, 1995). These events may be known as 'steady inflow' currents, as typically their duration lasts several hours, days or even weeks during which they constantly introduce new sediment into the ocean environment (Mulder and Syvitski, 1995). Other events which might trigger a turbidity current by introducing material to the sea bed include jökulhlaups (flooding from a glacial lake) (Einarsson et al., 1997), lahars (highly concentrated mudflows which occur after a volcanic eruption) entering into the ocean (Mulder et al., 2003), and high rainfall events which occur after a volcanic eruption (Meiburg and Kneller, 2010).

5.1.1 The initiation problem

Until now, this thesis has considered two types of initiation conditions; 'slump' (Chapter 2) where a finite amount of material is released on a slope, and 'steady inflow' (Chapters 2-4) where material is constantly introduced at the top of the slope. In this chapter, slump initial conditions will be considered again, and steady inflow boundary conditions will be proposed, where the current is initially at rest, before material is introduced at the top of the slope.

The initial and boundary conditions considered in this chapter are intended to model realistic events. However, it should be noted that determining accurate initial conditions for turbidity currents is an open problem in the field (Meiburg and Kneller, 2010), and so here we attempt only to represent two well-known trigger mechanisms.

5.2 Slump initial conditions

A slump event is triggered when sediment located on the sea bed fails, and begins to move downstream. This is similar to the way in which a snow avalanche

might be initiated, when the cohesive properties of the material are lost, and material avalanches downstream. Due to the complexities of modelling the sediment and its internal stresses, our initial model set-up will feature a 'raft' or 'mound' of sediment on the slope with a specific depth and concentration which will be initiated by gravity acting on the material. The sediment will then evolve according to the slope conditions we have imposed for each problem. No additional sediment will be fed into the system.

5.2.1 Model set-up

The model initial and boundary conditions are given as follows: at $t = 0$, the initial conditions are

$$h_0(x) = h^\star(\tanh[a(b_1 - x) + \tanh[a(x - b_2)]), \tag{5.1a}$$

$$u_0(x) = 0, \tag{5.1b}$$

$$c_0(x) = c^\star(\tanh[a(b_1 - x) + \tanh[a(x - b_2)]), \tag{5.1c}$$

where $h^\star$, $c^\star$, a, b_1, b_2 are constants. These are 'top-hat' initial conditions, as plotted in Figure 5.1 for values of the constants we will use in this section.

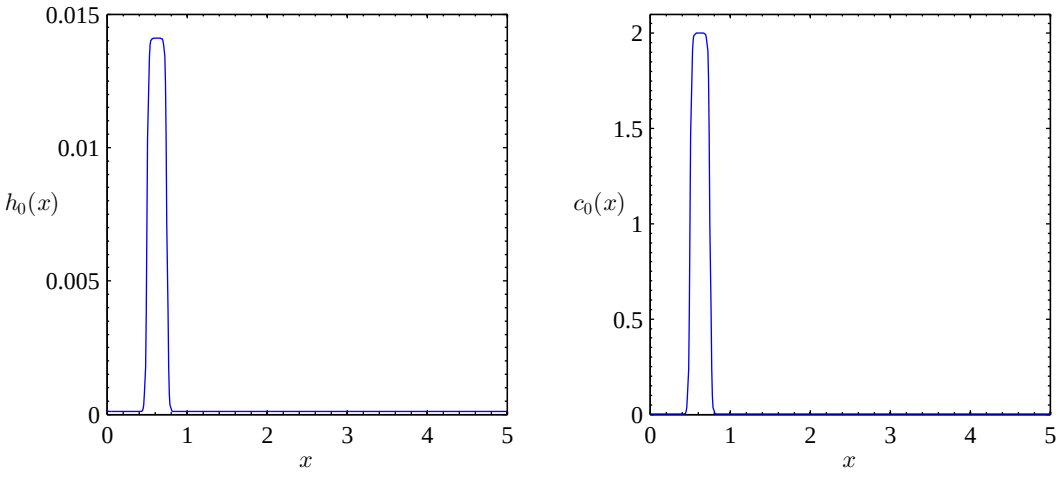

(a) Initial condition $h_0(x)$

(b) Initial condition $c_0(x)$

Figure 5.1: Slump initial conditions (5.1) for h and u. The parameter values are $h^\star = 0.007$, $c^\star = 1$, $a = 50$, $b_1 = 0.75$, $b_2 = 0.5$.

In Figure 5.1, the maximum initial values of h and c are $h \approx 0.014$ and $c \approx 2$. These correspond to a maximum initial sediment concentration of 0.025 $\mathrm{m}^3/\mathrm{m}^3$ and a maximum initial depth of 7.3 m over approximately 15 km of the upper

part of the slope. These are certainly not extreme initial conditions, and they are intended to reflect a layer of sediment at the upper part of the domain, which has perhaps built up over several decades.

The boundary conditions for $t > 0$ are given by

$$h_i = 0, \qquad u_i = 0, \qquad c_i = 0 \qquad \text{at} \quad x = 0, \tag{5.2a}$$

$$\frac{\partial u}{\partial x} = 0, \qquad \frac{\partial c}{\partial x} = 0 \qquad \text{at} \quad x = x_R, \tag{5.2b}$$

where the right-hand boundary is $x = x_R > 0$.

The model to be solved is the transition model, given by equations (4.27) and additional functions listed in Section 4.4.3. The erosion rate, $E^\star(k)$, is given by equation (4.9), the slope, S, is outlined in each subsection below and the eddy viscosity and diffusivity coefficients are ϵ, $\omega \ll 1$, respectively.

5.2.2 Slump on an almost-flat bed

This section considers the effect of a 'slump' of material on an almost-flat bed. The dimensionless slope, S, is given by $S = 0.1$, which corresponds to a real bed slope of $\theta \approx 0.3°$. The transition model (4.27) is solved for the slump initial conditions (5.1) on a domain $x \in (0, 12)$. The solutions are plotted in Figure 5.2. The flux of the current, $q = hu$, is plotted rather than the depth, h, of the current, which becomes an increasingly deep, static layer as $c \to 0$.

The surface plots in Figure 5.2 show that the 'slump' initial conditions on an almost-flat bed lead to the flux, velocity and sediment concentration dying out rapidly. Initially, the velocity increases in response to the high concentration of sediment present at $t = 0$. However, the turbulent kinetic energy, k, never increases above zero, and so the erosion, $E^\star$, never switches on. As a result, the sediment concentration of the current steadily decreases from its initial value, and, once c has reached zero, u and q rapidly follow suit.

A slump of material on an almost-flat bed appears, at least qualitatively, to represent 'column collapse', as is often studied in the theory of granular flows, when a mound of sediment is realised and spreads out on a flat bed.

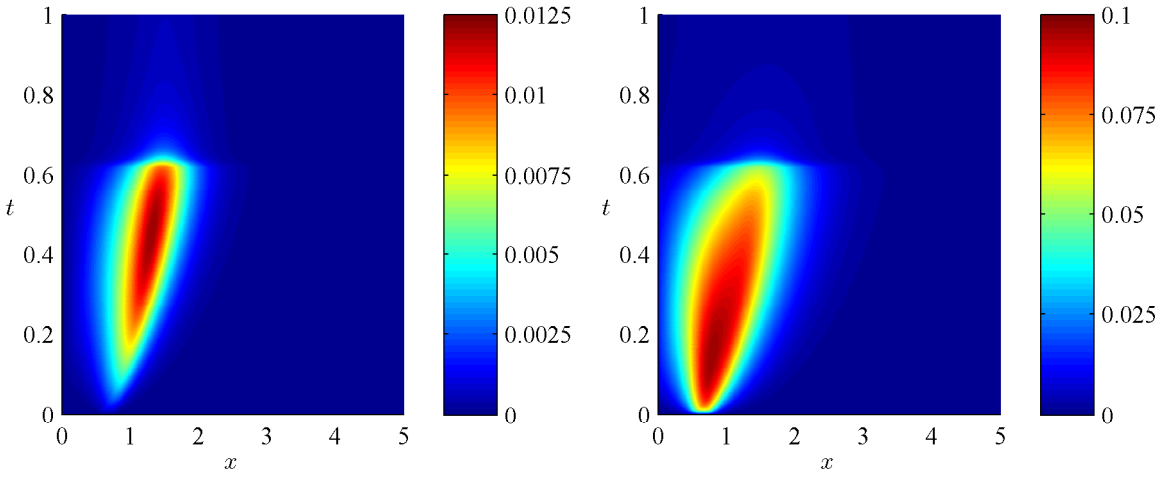

(a) Flux, q

(b) Velocity, u

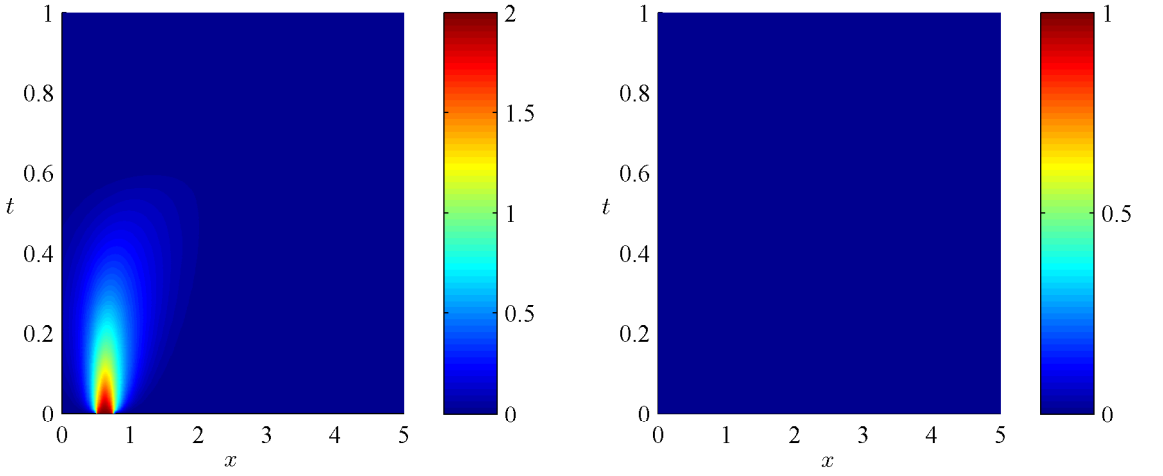

(c) Sediment concentration, c

(d) Turbulent kinetic energy, k

Figure 5.2: Surface plots of the solutions to the transition model (4.27) for an almost-flat slope, $S = 0.1$, for the slump problem. The solution is plotted for $x \in (0, 5)$, $t \in (0, 1)$. The erosion rate, $E^\star$, is given by equation (4.9), the initial conditions are given by equations (5.1) and the boundary conditions by equations (5.2). The parameter values are $\delta = 0.17$, $\gamma = 0.77$, $\chi = 0.067$, $E_0 = 10^3$, $h^\star = 0.007$, $c^\star = 1$, $a = 50$, $b_1 = 0.75$, $b_2 = 0.5$ and the diffusion coefficients are given by $\epsilon = 0.005$, $\omega = 0.1$.

5.2.3 Avalanche on a steep slope

Here, a 'slump' of material on a steep bed is considered. The slope, S, is given by $S = 1$, which corresponds to a real bed slope of $\theta \approx 3°$. The transition model (4.27) is solved for the slump initial conditions (5.1) on a domain $x \in (0, 12)$. Once again, the solutions are plotted as surface plots, shown in Figure 5.3.

Figure 5.3 shows that the initially high concentration of sediment, at $t = 0$, results in a rapid increase in the velocity of the current. In addition, the initial 'raft' of sediment begins to propagate downstream, because the material is on a steep slope. It is worth noting that the flow is fastest at the head of current, where the sediment concentration is lowest. The most concentrated part of the current is the tail, which is travelling at a lower speed.

As the material begins to move downstream, the turbulent kinetic energy, k, increases causing the erosion to switch on. The erosion rate of the current is plotted in Figure 5.4. When erosion is switched on, the sediment concentration of the current further increases, as does the velocity of the flow. In Figure 5.3 we can see that the values of q, u, c and k continue to increase with distance downstream and time; the flow has ignited on the steep slope.

Whilst ignition is seen in Figure 5.3, it does not occur across the entire domain; instead, an ignitive wave is moving downstream, taking the form of a travelling wave. Figure 5.4 highlights the propagation of the 'wave' downstream. There are two fronts visible; the erosional, ignitive front leading the current downstream, and a depositional, extinctive tail of the current. Ahead of the ignitive front and behind the extinctive front there is no erosion.

Following initial transients, it appears that the ignitive and extinctive fronts each propagate at constant speed. The extinctive tail of the current propagates more slowly than the erosional front, and so the ignitive region is growing in time. If, on the other hand, the gradient of the ignitive front were steeper than that of the extinctive tail, then the current would eventually extinguish itself.

In Figure 5.5 the Froude number of the flow is plotted. It can be seen that the erosional front and extinctive tail coincide with regions where F transitions through 1; the shock behaviour of the solutions can be examined using the characteristics of the transition model, (4.27). These are given by

$$\lambda = \frac{dx}{dt} = u, u \pm \sqrt{\delta h c}. \tag{5.3}$$

The characteristics corresponding to the solutions plotted in Figure 5.3 are

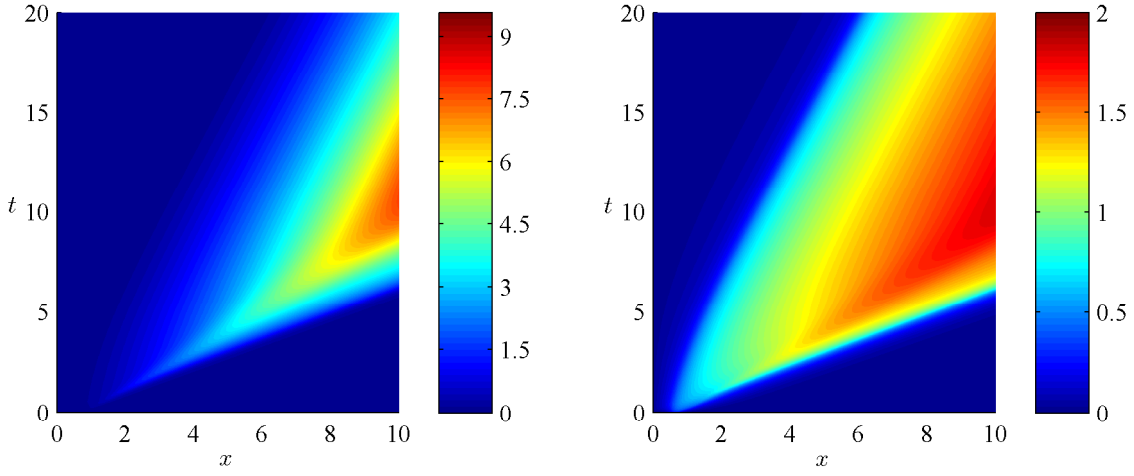

(a) Flux, q

(b) Velocity, u

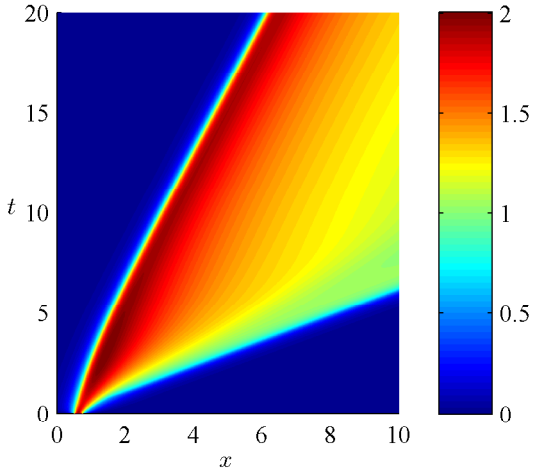

(c) Sediment concentration, c

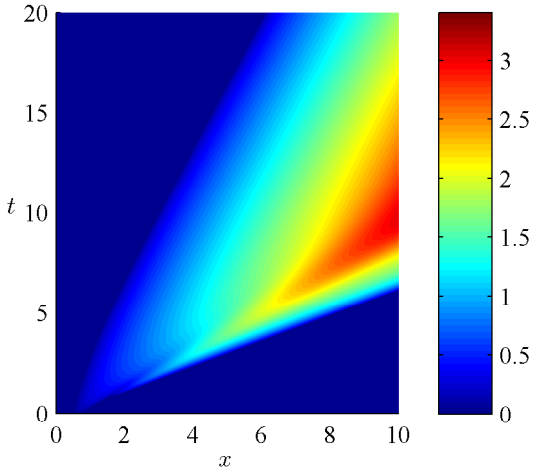

(d) Turbulent kinetic energy, k

Figure 5.3: Surface plots of the solutions to the transition model (4.27) for a steep slope, $S = 1$, for the slump problem. The solution is plotted for $x \in (0, 10)$, $t \in (0, 20)$. The erosion rate, $E^\star$, is given by equation (4.9), the initial conditions are given by equations (5.1) and the boundary conditions by equations (5.2). The parameter values are listed in Figure 5.2.

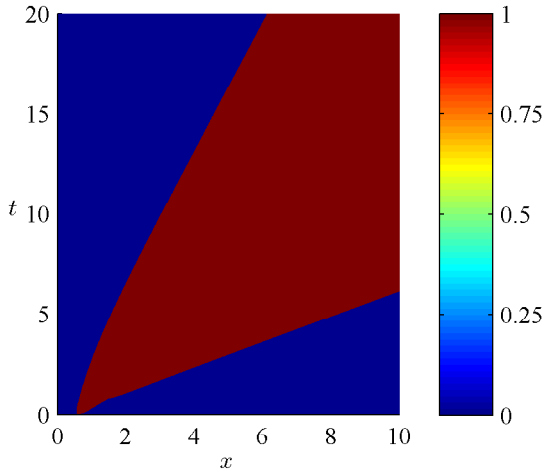

Figure 5.4: Surface plot of the erosion rate, (4.9), of the transition model (4.27) for a steep slope, $S = 1$, for the slump problem. The solution is plotted for $x \in (0, 10)$, $t \in (0, 20)$. The initial conditions are given by equations (5.1) and the boundary conditions by equations (5.2). The parameter values are listed in Figure 5.2.

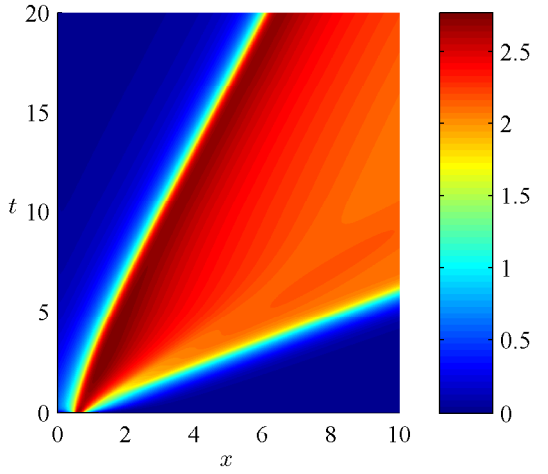

Figure 5.5: Surface plot of the Froude number, (3.24), of the transition model (4.27) for a steep slope, $S = 1$, for the slump problem. The solution is plotted for $x \in (0, 10)$, $t \in (0, 20)$. The initial conditions are given by equations (5.1) and the boundary conditions by equations (5.2). The parameter values are listed in Figure 5.2.

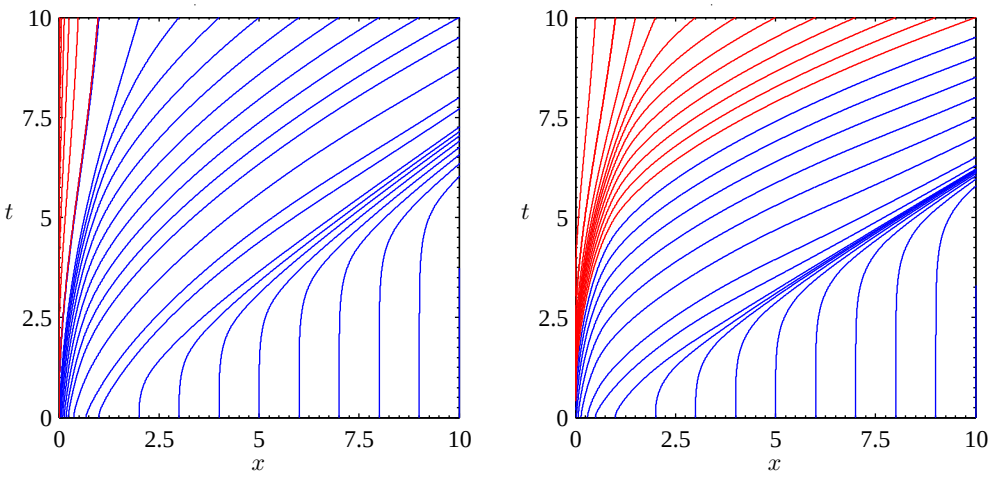

(a) $\lambda = u$

(b) $\lambda = u + \sqrt{\delta hc}$

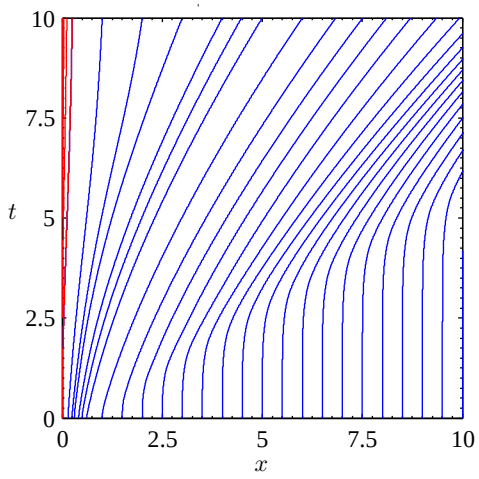

(c) $\lambda = u - \sqrt{\delta hc}$

Figure 5.6: The sub-characteristics, $dx/dt = \lambda$, of equations (4.27) for $S = 1$ and diffusion coefficients $\epsilon = 0.005$, $\omega = 0.1$. The blue characteristic curves are given by the initial conditions (5.1) and the red characteristic curves are given by the boundary conditions (5.2). The parameter values are listed in Figure 5.2.

shown in Figure 5.6. Once again, these are the sub-characteristics of the model, which show the behaviour of the system when ϵ, $\omega \ll 1$. The sub-characteristics show a shock associated with the ignitive wave front which is propagating downstream; this is clearly visible in Figure 5.6(b). The extinctive wave front, where the solution transitions smoothly through $F = 1$, appears as an expansion fan.

5.2.4 A realistic bed profile

In this section, we consider the slump initial conditions on a bed that is initially steep, but then flattens out downstream. The slope, S, is given by

$$S = \frac{1}{2}\left(1 - \tanh[10(x-3)]\right). \tag{5.4}$$

The transition model (4.27) is solved for the slump initial conditions (5.1) on a domain $x \in (0, 12)$, and the solutions are plotted in Figure 5.7.

The slope profile (5.4) has a break in slope at $x = 3$, the effect of which can be clearly seen in the solutions plotted in Figure 5.7. The slope function effectively splits the x-domain into two regions, one where ignition occurs, and one where extinction occurs. It can be seen that the high sediment concentration specified at $t = 0$ causes a rapid increase in u and k on the steep slope. This causes erosion to switch on, as is seen in Figure 5.8. With erosion switched on, the sediment concentration of the current starts to increase, leading to a further increase in u: ignition is occurring on the steep slope.

As in the previous section, there is a wave front to the ignitive region of the current and a trailing extinctive tail. It can be seen in Figure 5.8, that the ignitive front to the current is truncated by the change in slope at $x = 3$ and erosion does not carry on to the flat bed after $t \approx 2.5$. This means that the ignitive front becomes fixed at $x = 3$. The extinctive tail of the current meets the ignitive front at $x \approx 10$, and erosion is extinguished from the current altogether. The break in slope has put a limit on the ignition of the current, which is confined only to the region where erosion takes place on the steep slope. By plotting the Froude number of the flow in Figure 5.9, we see that the erosional and depositional fronts again coincide with regions where F transitions through 1, as does the break in slope at $x = 3$.

For the solutions plotted in Figure 5.7, the characteristics of the model, given by equations (5.3), are used to plot the sub-characteristics of equations (4.27) in Figure 5.10. It can be seen that there is a shock associated with the ignitive

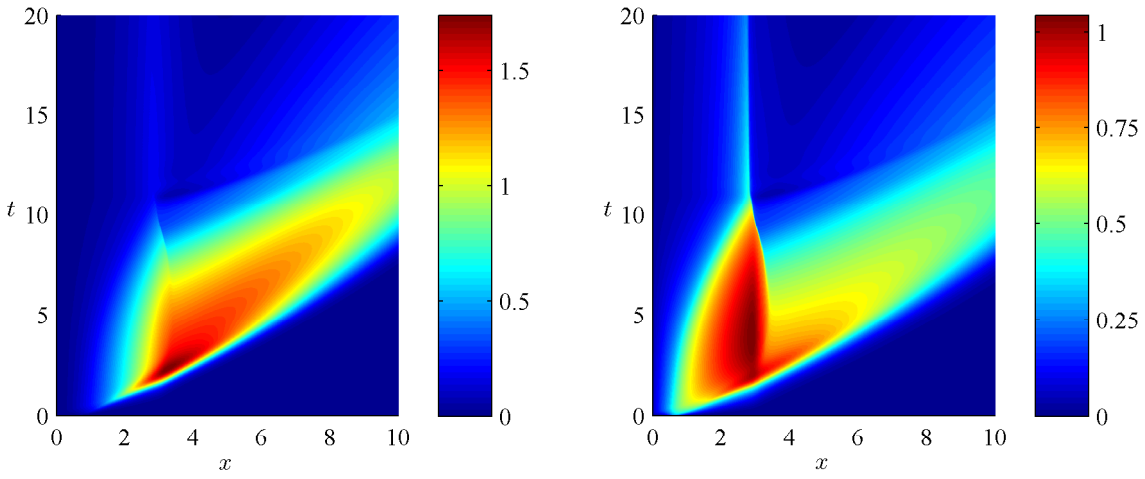

(a) Flux, q

(b) Velocity, u

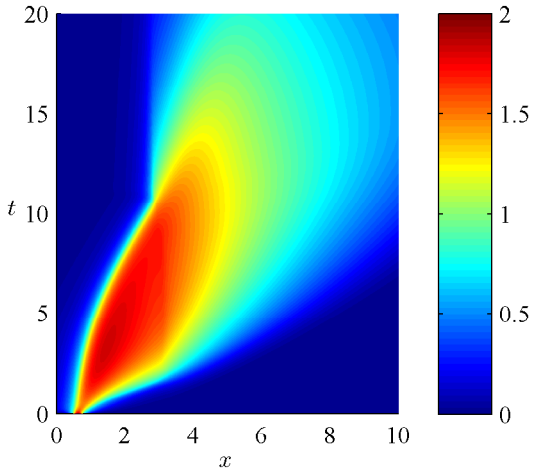

(c) Sediment concentration, c

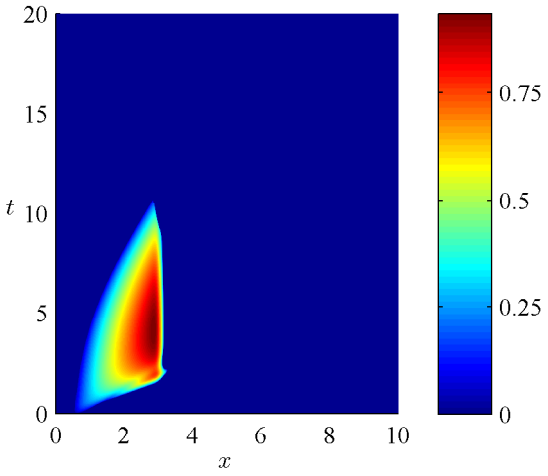

(d) Turbulent kinetic energy, k

Figure 5.7: Surface plots of the solutions to the transition model (4.27) for S given by equation (5.4), for the slump problem. The solution is plotted for $x \in (0, 10)$, $t \in (0, 20)$. The erosion rate, $E^\star$, is given by equation (4.9), the initial conditions are given by equations (5.1) and the boundary conditions by equations (5.2). The parameter values are listed in Figure 5.2.

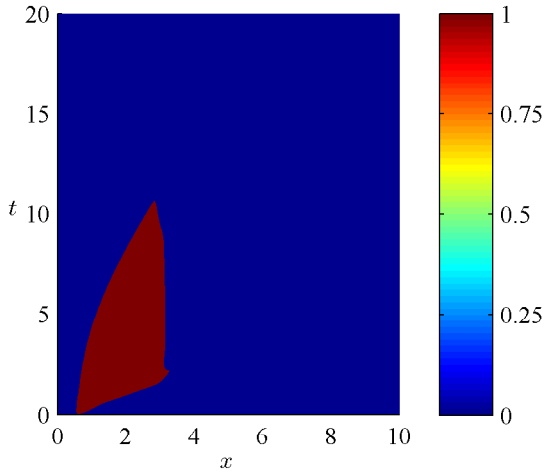

Figure 5.8: Surface plot of the erosion rate, (4.9), of the transition model (4.27) for S given by equation (5.4), for the slump problem. The solution is plotted for $x \in (0, 10)$, $t \in (0, 20)$. The initial conditions are given by equations (5.1) and the boundary conditions by equations (5.2). The parameter values are listed in Figure 5.2.

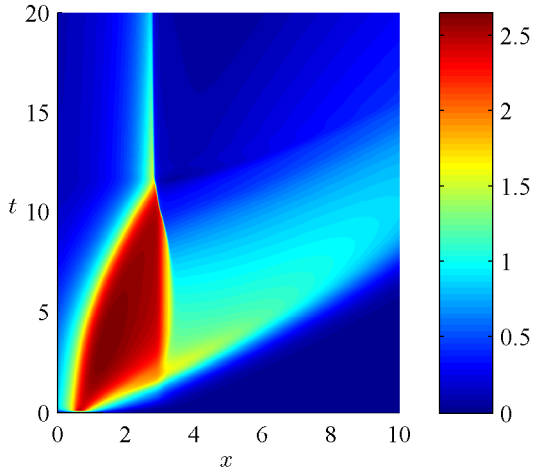

Figure 5.9: Surface plot of the Froude number, (3.24), of the transition model (4.27) for S given by equation (5.4), for the slump problem. The solution is plotted for $x \in (0, 10)$, $t \in (0, 20)$. The initial conditions are given by equations (5.1) and the boundary conditions by equations (5.2). The parameter values are listed in Figure 5.2.

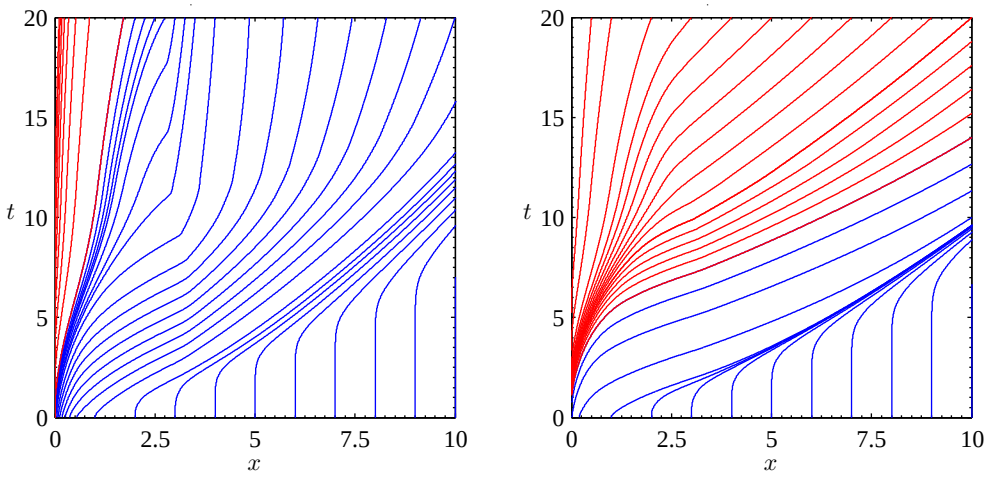

(a) $\lambda = u$

(b) $\lambda = u + \sqrt{\delta hc}$

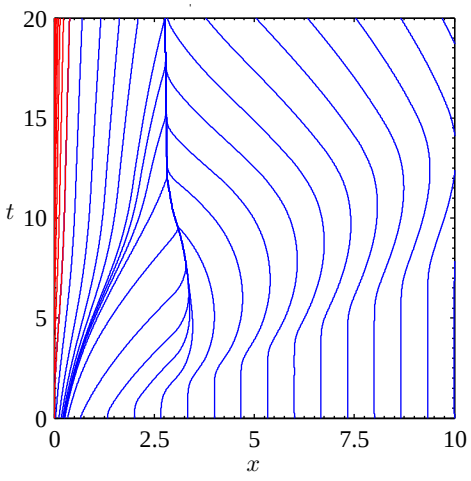

(c) $\lambda = u - \sqrt{\delta hc}$

Figure 5.10: The sub-characteristics, $dx/dt = \lambda$, of equations (4.27) for S given by equation (5.4) and diffusion coefficients $\epsilon = 0.005$, $\omega = 0.1$. The blue characteristic curves are given by the initial conditions (5.1) and the red characteristic curves are given by the boundary conditions (5.2). The parameter values are listed in Figure 5.2.

front, and an expansion fan associated with the depositional tail of the solution, as was found for the steep slope profile in Section 5.2.3. In addition, a shock is initiated in the solution at the break in slope; this is similar to the type of shock that was seen for the two-equation model (*cf.* Figure 3.21, for example). The shock is caused when the gradient of the characteristic curves, with wave speed $dx/dt = u - \sqrt{\delta hc}$, becomes negative, for $x \gtrsim 3$ and $t \gtrsim 10$, and meets the characteristic curves with positive slope at $x \approx 3$.

For $x \gtrsim 3$, and for all x when $t \gtrsim 10$, the current is purely depositional. It can be seen from Figure 5.7 that the sediment concentration is zero on the steep slope for $t \gtrsim 10$ and the velocity and flux of the current tend to zero also. On the flat bed, c decreases over time as the sediment settles out of the current. This occurs alongside a dramatic decrease in the velocity and flux of the current, and the current soon becomes extinct.

5.3 Fluvial boundary conditions

In this section, we will consider turbidity currents which are initiated when a stream of highly concentrated sediment flows out onto the continental slope. These currents will be modelled using time-dependent boundary conditions and we will refer to them as 'fluvial' events, since they are caused by a sudden, high inflow of sediment into a fluvial system at equilibrium.

5.3.1 Model set-up

The model initial conditions, at $t = 0$, are

$$h_0(x) = 0, \qquad u_0(x) = 0, \qquad c_0(x) = 0. \tag{5.5}$$

The boundary conditions for $t > 0$ are given as follows: at $x = 0$ we impose 'top-hat' functions of t, namely:

$$h_i(t) = h^\star(\tanh[a(b_1 - t)] + \tanh[a(t - b_2)]), \tag{5.6a}$$
$$u_i(t) = u^\star(\tanh[a(b_1 - t)] + \tanh[a(t - b_2)]), \tag{5.6b}$$
$$c_i(t) = c^\star(\tanh[a(b_1 - t)] + \tanh[a(t - b_2)]), \tag{5.6c}$$

where $h^\star$, $u^\star$, $c^\star$, a, b_1, b_2 are constants. The time-dependent flux, $q_i(t) = h_i(t)u_i(t)$, and sediment concentration at $x = 0$ are plotted in Figure 5.11

for the values of the constants we will use in this section. At the right-hand boundary $x = x_R > 0$, we have

$$\frac{\partial u}{\partial x} = 0, \qquad \frac{\partial c}{\partial x} = 0. \tag{5.7}$$

In Figure 5.11, the maximum values of h, u and c being introduced to the system are $h \approx 0.1$, $u \approx .06$, and $c \approx 2$; the maximum value of the flux is $q \approx 0.006$. These values correspond to a stream of sediment flowing into the domain with a depth of 52 m, a velocity of 1.5 m s^{-1}, a flux of 78 m^2 s^{-1} and a sediment concentration of 0.025 m^3/m^3. The time period over which the material flows into the domain is approximately 80 minutes.

Again, the transition model will be solved; this is outlined in equations (4.27).

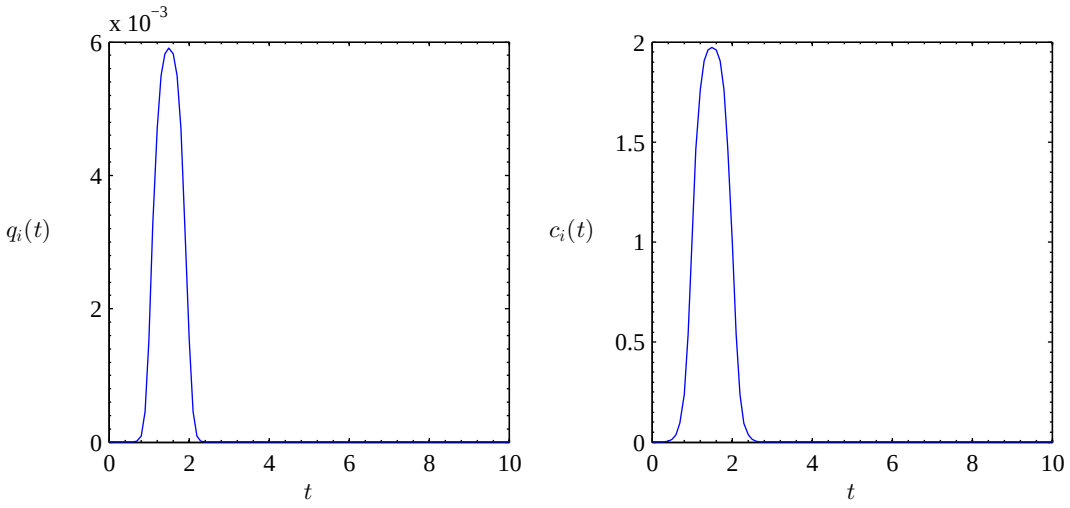

(a) Flux, $q_i(t) = h_i(t)u_i(t)$, at $x = 0$

(b) Sediment concentration, $c_i(t)$, at $x = 0$

Figure 5.11: Fluvial boundary conditions (5.6) shown for q and c. The parameter values are $h^\star = 0.05$, $u^\star = 0.03$, $c^\star = 1$, $a = 5$, $b_1 = 2$, $b_2 = 1$.

5.3.2 Collapse on a almost-flat bed

This section considers the effect of the fluvial boundary conditions on an almost-flat bed where the slope is given by $S = 0.1$. The transition model (4.27) is solved for the fluvial boundary conditions (5.6) on a domain $x \in (0, 10)$, and the solutions are plotted in Figure 5.2.

Figure 5.12 shows that $q = u = c = k = 0$ at $t = 0$. At $t = 1$ material is introduced into the system at $x = 0$, with a fixed depth, velocity and sediment

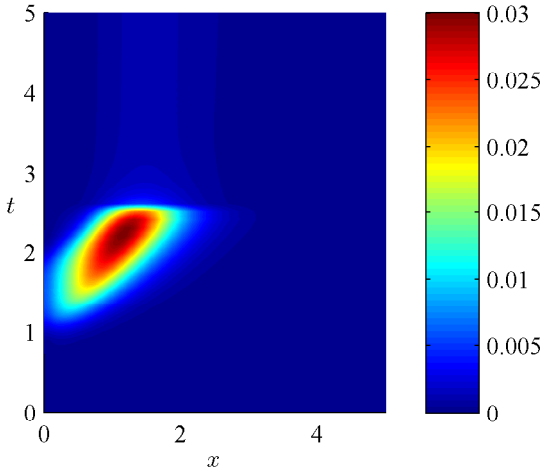

(a) Flux, q

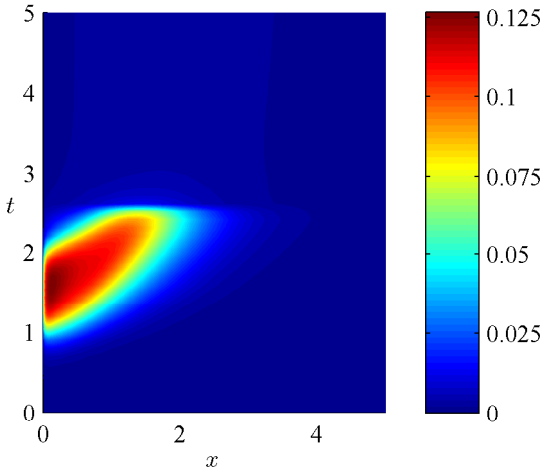

(b) Velocity, u

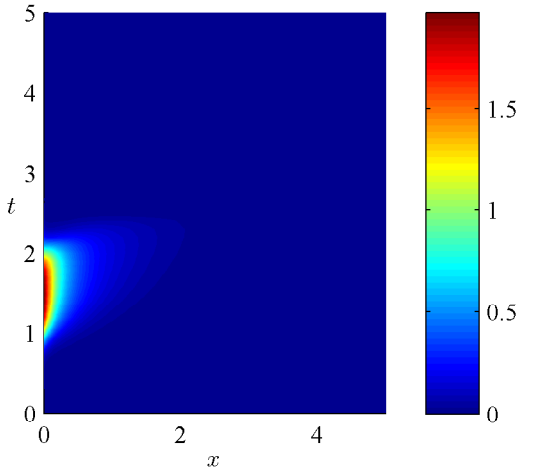

(c) Sediment concentration, c

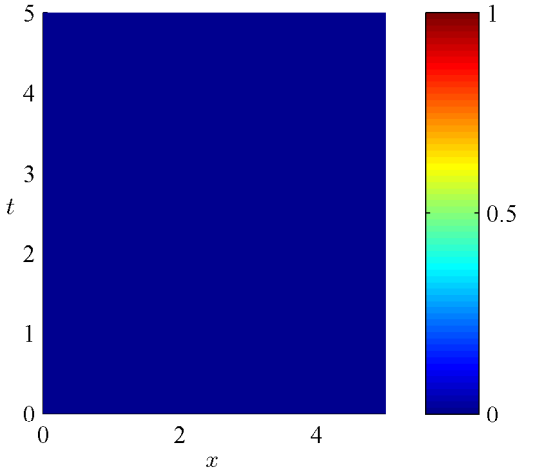

(d) Turbulent kinetic energy, k

Figure 5.12: Surface plots of the solutions to the transition model (4.27) for an almost-flat slope, $S = 0.1$, for the fluvial boundary condition problem. The solution is plotted for $x \in (0, 5)$, $t \in (0, 5)$. The erosion rate, $E^\star$, is given by equation (4.9), the initial conditions are given by equations (5.5) and the boundary conditions by equations (5.6). The parameter values are $\delta = 0.17$, $\gamma = 0.77$, $\chi = 0.067$, $E_0 = 10^3$, $h^\star = 0.05$, $u^\star = 0.03$, $c^\star = 1$, $a = 5$, $b_1 = 2$, $b_2 = 1$ and the diffusion coefficients are given by $\epsilon = 0.005$, $\omega = 0.1$.

concentration. The sediment concentration and velocity in a region close to $x = 0$ increase as sediment moves into the domain. However, the turbulent kinetic energy, k, does not increase above zero, as the threshold for the current to switch into a turbulent regime is not achieved. As a result, the current does not begin to erode. After $t = 2$ no sediment is introduced into the system and so the concentration, velocity and flux quickly die out and the current becomes extinct.

Since the slope, S, is very small in this example, we find that the sediment which is introduced at $x = 0$ merely slumps into the domain over a small distance, close to $x = 0$. As was seen in the previous section, a slump on an almost-flat bed qualitatively resembles a granular column collapse, and we see these column collapse properties again in this example.

5.3.3 Sustained ignition on a steep slope

In this section, we consider the effect of the fluvial boundary conditions on a steep bed, with slope $S = 1$. The transition model (4.27) is solved for the specified boundary conditions (5.6) on a domain $x \in (0, 10)$ and the solutions are plotted in Figure 5.13.

When sediment is introduced into the system at $t = 1$, we see in this example that the concentration increases at the top of the slope: $c \approx 3$ for $0 < x \lesssim 1$ and for $t \gtrsim 3$, see Figure 5.13(c). For $x \gtrsim 1$, the sediment concentration is decreasing with distance downstream. In contrast, the velocity and flux are increasing with distance downstream, as is the turbulent kinetic energy. This was observed in Section 5.2.3 in the travelling wave solutions for an avalanche on a steep slope; the highly concentrated part of the flow moves more slowly than the dilute part of the flow.

The erosion rate, plotted in Figure 5.14 shows that erosion switches on at $t \approx 1$ and an erosional front moves downstream in time. Unlike for the slump condition, there is no extinction tail to the solution, and the entire domain becomes erosional by $t \approx 8$. The sediment introduced at $x = 0$ causes the current to start eroding, and ignition occurs as this erosional front moves downstream. The current has been forced into a self-sustaining cycle, and maintains high concentrations and velocities across the domain.

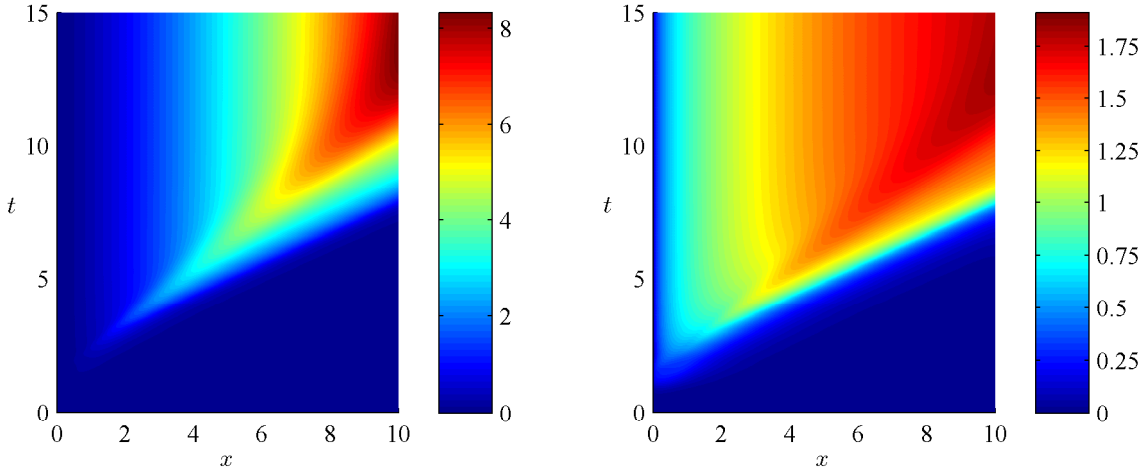

(a) Flux, q

(b) Velocity, u

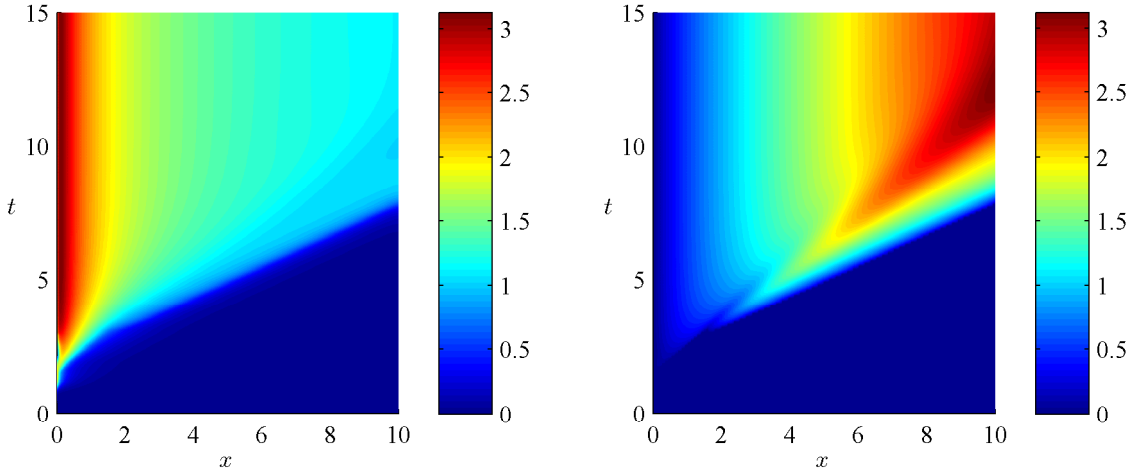

(c) Sediment concentration, c

(d) Turbulent kinetic energy, k

Figure 5.13: Surface plots of the solutions to the transition model (4.27) for a steep slope, $S = 1$, and the fluvial boundary condition problem. The solution is plotted for $x \in (0, 10)$, $t \in (0, 15)$. The erosion rate, $E^\star$, is given by equation (4.9), the initial conditions are given by equations (5.5) and the boundary conditions by equations (5.6). The parameter values are listed in Figure 5.12.

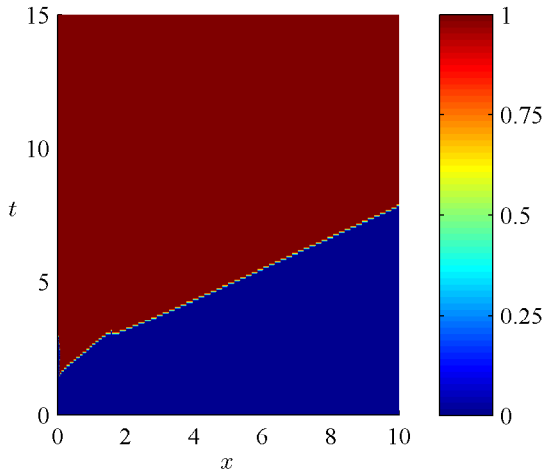

Figure 5.14: Surface plot of the erosion rate, (4.9), of the transition model (4.27) for $S = 1$ and the fluvial boundary condition problem. The solution is plotted for $x \in (0, 10)$, $t \in (0, 50)$. The initial conditions are given by equations (5.5) and the boundary conditions by equations (5.6). The parameter values are listed in Figure 5.12.

5.3.4 A realistic bed profile

Here, we consider the fluvial boundary conditions on a bed that is initially steep, but then flattens out downstream. The slope is given by

$$S = \frac{1}{2}\left(1 - \tanh[5(x-3)]\right). \tag{5.8}$$

The transition model (4.27) is solved for the fluvial boundary conditions (5.6) on a domain $x \in (0, 10)$, and the solutions are plotted in Figure 5.15.

The introduction of sediment with a fixed depth and velocity at $t = 1$ causes the turbulent kinetic energy of the current to increase. Erosion switches on almost immediately, as can be seen in Figure 5.16, and this erosional front soon propagates downstream in time. Erosion is abruptly stopped by the change in slope at $x \approx 3$; it is clear from Figure 5.15(d) that the turbulent kinetic energy drops to zero at this point. Erosion is not eliminated entirely from the system, however, as the sediment introduced for $t \in (1, 3)$ results in a persistent erosional regime for $x \in (0, 3)$. As there is no depositional tail propagating forward, erosion is maintained, indefinitely, on the steep slope.

On the flat bed, erosion is no longer occurring and so the current is purely depositional here. It can be seen from Figure 5.15(c) that the sediment concentration starts to die out with distance downstream. However, as the sediment concentration and velocity remain high on the steep slope for all time, we do

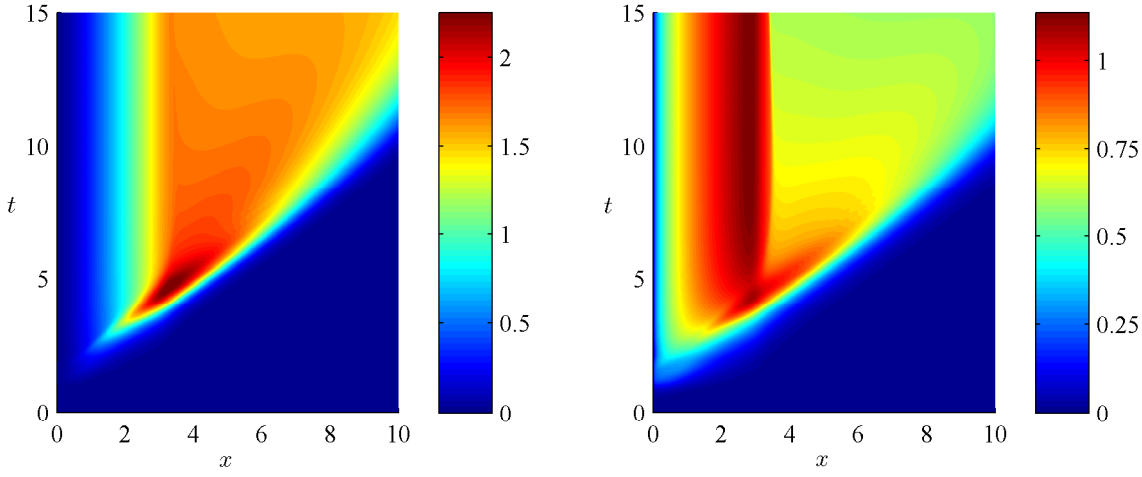

(a) Flux, q

(b) Velocity, u

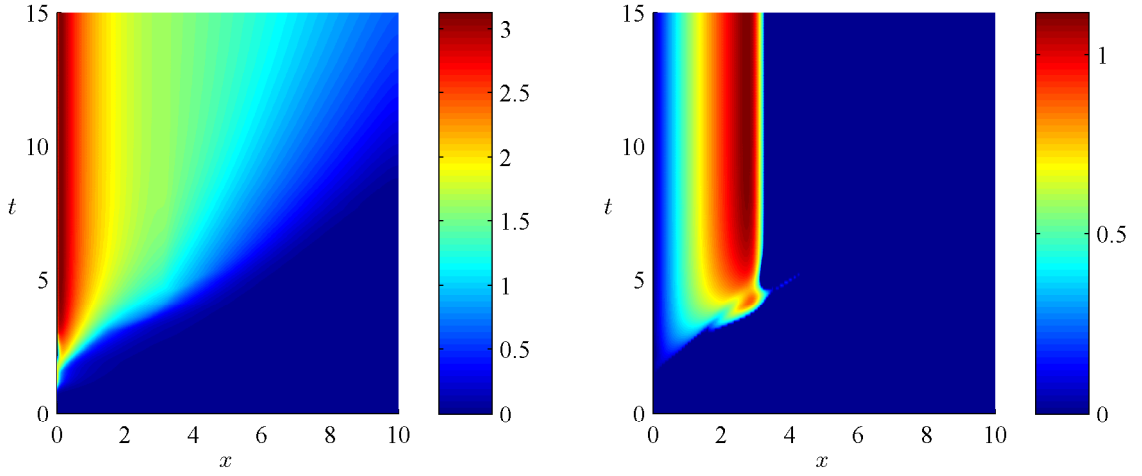

(c) Sediment concentration, c

(d) Turbulent kinetic energy, k

Figure 5.15: Surface plots of the solutions to the transition model (4.27) for S given by equation (5.8), and the fluvial boundary condition problem. The solution is plotted for $x \in (0, 10)$, $t \in (0, 15)$. The erosion rate, $E^\star$, is given by equation (4.9), the initial conditions are given by equations (5.5) and the boundary conditions by equations (5.6). The parameter values are listed in Figure 5.12 and the diffusion coefficients are given by $\epsilon = 0.01$, $\omega = 0.1$.

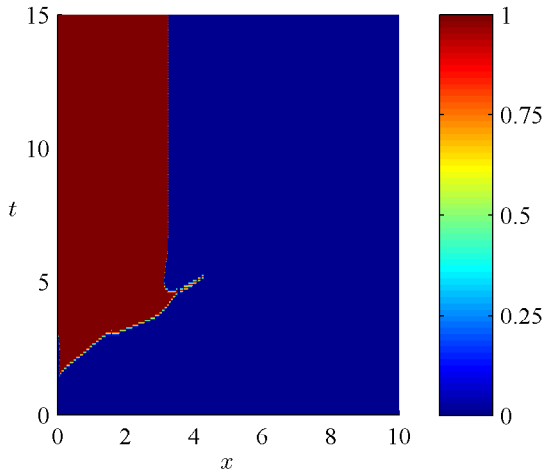

Figure 5.16: Surface plot of the erosion rate, (4.9), of the transition model (4.27) for S given by equation (5.8) and the fluvial boundary condition problem. The solution is plotted for $x \in (0, 10)$, $t \in (0, 15)$. The initial conditions are given by equations (5.5) and the boundary conditions by equations (5.6). The parameter values are listed in Figure 5.12.

not see rapid extinction of the current on the flat bed. Instead, a steady decrease in the sediment and velocity with distance downstream is observed. The fluvial boundary conditions suggest that the current will be self-sustaining on the steep slope and the current will persist over time, even after sediment is no longer being introduced at the upper boundary, by eroding material from the steep slope.

In Section 5.5, we will discuss whether the self-sustaining current of this type, which is seen for the fluvial boundary conditions, is physically realistic.

5.4 When does a turbidity current become extinct?

The case studies considered in this chapter show that a current will ignite only under certain slope profiles. This section provides a parameter study to the initial conditions listed above, showing how varying the amount of sediment introduced into the system changes the extinctive or ignitive behaviour of the current. This study is only a very tentative exploration of all the possible parameter combinations that could be considered for the case studies presented here; a more exhaustive study is beyond the scope of this thesis.

5.4.1 Numerical parameter study

In the previous two sections, slump initial conditions and fluvial boundary conditions have been considered. In the case of the slump problem, the total amount of sediment, T_S, introduced is given by

$$T_S = \int hc|_{t=0}\,\mathrm{d}x = \int h_0(x)c_0(x)\,\mathrm{d}x \approx 4h^\star c^\star(b_1 - b_2), \tag{5.9}$$

and for the fluvial problem, the total amount of sediment, T_F, introduced is given by

$$T_F = \int huc|_{x=0}\,\mathrm{d}t = \int \mathrm{d}t \approx 8c^\star h^\star u^\star(b_1 - b_2). \tag{5.10}$$

For the choice of parameters listed in Figure 5.2, $T_S = 0.0064$, and for the choice of parameters listed in Figure 5.12, $T_F = 0.0084$. These values correspond to dimensional quantities of

$$T_S = 2729\ \mathrm{m}^2, \qquad T_F = 4679\ \mathrm{m}^2. \tag{5.11}$$

Since T_S, $T_F \sim \mathcal{O}(10^3)$, the same behaviour might be expected from each case study; we have certainly shown above that column collapse is experienced for $S = 0.1$, ignition for $S = 1$ and controlled ignition for the varying slope profile in x.

We vary the amount of sediment in the initial and boundary conditions, to see how the concentration of the initial mound or stream of sediment and the gradient of the bed affects the behaviour of the current. In Table 5.1 we show the results for the slump problem, and in Table 5.2, for the fluvial problem.

Both tables show clear parameter regions where the current becomes extinct; these cases occur where the slope is too small or where the initial sediment concentration in the current is too low to result in ignition of the current. In these cases, the current rapidly becomes extinct. In both the slump and the fluvial cases, there were parameter ranges for small S or $c^\star$ that were not computed; here it is assumed the current is also depositional, based on the overall behaviour of the model.

In both the slump and the fluvial cases there are clear regions of ignition. The slump initial conditions show that an ignitive travelling wave propagates downstream, whilst the fluvial boundary conditions, show that the entire x domain becomes erosional and sustained ignition is seen. Both problems also show erosional regimes, where the current begins to erode, but ignition does not occur

		$c^\star$					
		0.75	1	1.25	1.5	2	2.5
	0.1	D	D	D	D	D	D
	0.2	D	D	D	D	D	D
	0.3	D	D	D	D	D	D
	0.4	D	D	D	D	E	W
S	0.5	D	D	D	E		
	0.6	D	D	D			
	0.7	D	D				
	0.8	D	W	W	W		
	0.9	D	W	W	W	W	
	1	D	W	W	W	W	W

Table 5.1: A numerical parameter study of $c^\star$ and S values for the slump problem. The key is; D – current dies out without ever eroding; E – erosion switches on briefly, before the current dies out; S – sustained ignition across the domain; W – ignitive travelling wave moving downstream; D – the current is assumed to be depositional. Gaps indicate a parameter regime which did not output a solution within the allowed computational time frame. The transition model, (4.27), is solved for the slump initial conditions (5.1). The parameter values are listed in Figure 5.2.

		$c^\star$							
		0.75	1	1.5	1.75	2	2.25	2.5	3
	0.1	D	D	D	D	D	D	D	D
	0.2	D	D	D	D	D	D	D	D
	0.3	D	D	D	D	D	D	D	D
	0.4	D	D	D	D	D	D	D	D
S	0.5	D	D	D	D	D	E	E	E
	0.6	D	D	D					
	0.7	D	D				S		
	0.8	D	D				S	S	
	0.9	D	D	S	S	S	S	S	S
	1	D	S		S		S	S	

Table 5.2: A numerical parameter study of $c^\star$ and S values for the fluvial problem. The key is as in Table 5.1. The transition model, (4.27), is solved for the fluvial boundary conditions (5.6). The parameter values are listed in Figure 5.12.

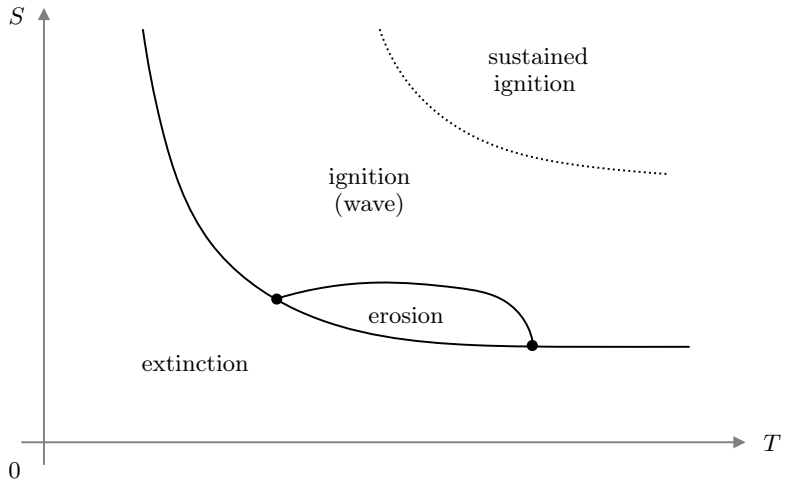

Figure 5.17: Hypothesised (T, S) parameter space showing where extinctive, erosive, and ignitive (travelling wave and sustained) regimes occur as the total introduced sediment concentration, T, and slope, S, are varied.

and erosion switches off after a short time causing the current to die out rapidly.

From these parameter studies, regions of extinction, erosion and ignition can be sketched in (T, S)-space where T is the total amount of sediment introduced, as defined in (5.9) and (5.10). This is illustrated in Figure 5.17. The parameter studies show that, in both the slump and the fluvial problems, a current can be expected to ignite only when the slope is sufficiently steep and/or the input of sediment is sufficiently high. There is a critical region where erosion switches on briefly, but ignition does not occur, and the current still dies out. A large region of extinction exists where neither the slope, nor the initial sediment concentration are sufficiently large to result in any erosion.

5.5 Discussion

The two case studies considered in depth in this chapter, and the parameter study of Section 5.4.1, provide an insight into how a turbidity current might be expected to behave for different initial and boundary conditions, sediment concentrations and slope profiles. Both slump boundary conditions and fluvial initial conditions show regions of extinction, erosion and ignition, and the parameter study provides some conclusions about the behaviour when the sediment concentration of the current is varied. However, here we have only provided a limited discussion of the factors resulting in erosion and ignition, and many other parameters have been neglected.

It is likely that the initial velocity and duration of the current, in the case of the fluvial problem, would have some effect on the erosive nature of the current. In addition, for the slump problem, the initial spread of the sediment in x is likely to effect how the current evolves. The fluvial problem can actually be considered a special case of the slump problem: if the initial 'raft' of material is located closer to $x = 0$, sustained ignition is found also for the 'slump' problem on the steep slope. This is illustrated in Figure 5.18, where it can be seen that the initial slump of sediment has resulted in a large region of sustained ignition, very similar to that seen for the fluvial problem in Figure 5.13.

It is, as yet, unclear whether sustained ignition is an artefact of the boundary conditions we have imposed on the model, rather than a physically realistic result. As has been mentioned in Section 5.1.1, the appropriate formulation of suitable initial and boundary conditions for turbidity currents, as a whole, is an area which still requires much further work.

However, despite these concerns, the case studies in this chapter have shown that there are defined ignitive, erosive and extinctive regimes of a current which are clearly dependent upon the gradient of the bed and the initial and boundary conditions prescribed for the problem. In answer to the question '*when does a turbidity current become extinct?*', it can be proposed that a turbidity current will die out, regardless of the slope profile, if the current is too low in concentration. In addition, a current will never ignite on a flat bed, regardless of the initial sediment concentration of the material introduced to the system. This parameter study has provided qualitative and quantitative predictions for the ignitive problem, and it acts as a strong motivation for an experimental study which could be compared to the predictions of the model given here.

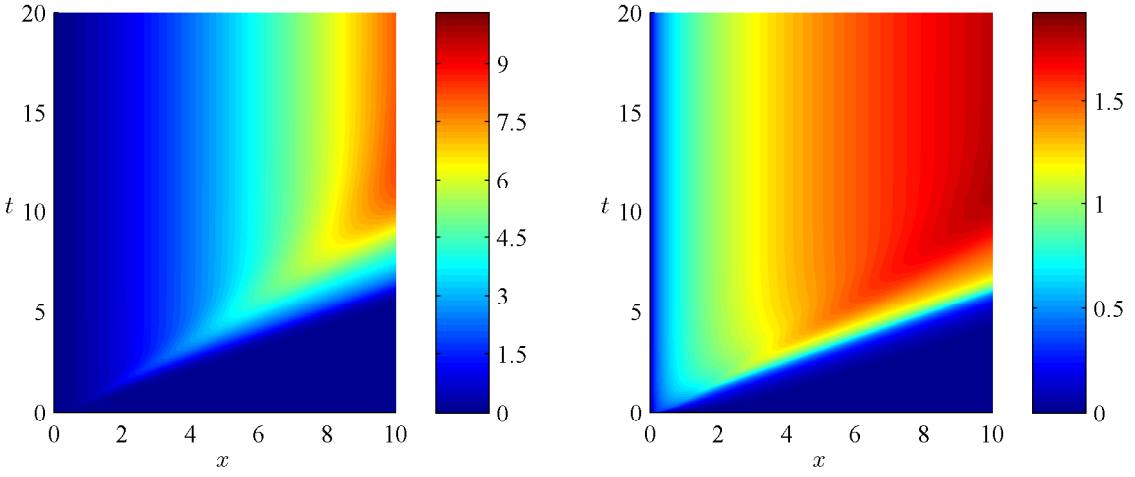

(a) Flux, q

(b) Velocity, u

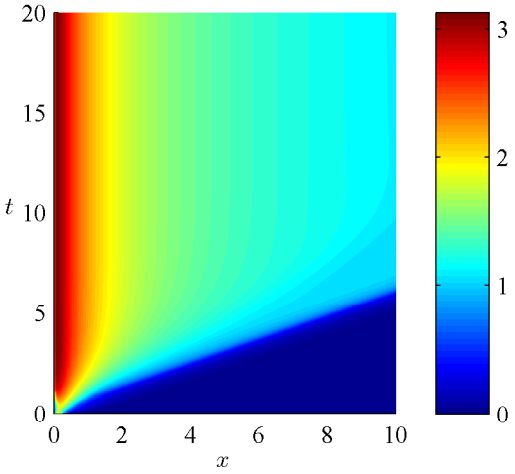

(c) Sediment concentration, c

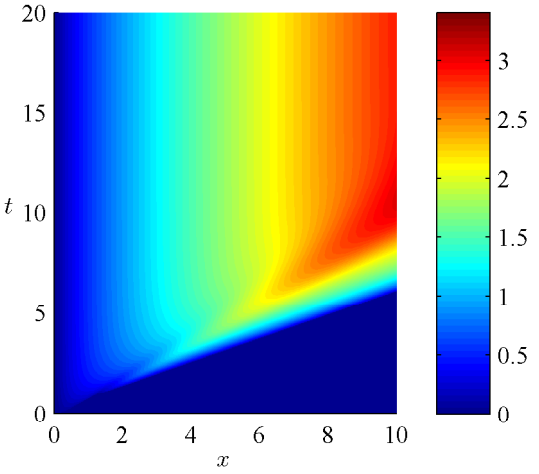

(d) Turbulent kinetic energy, k

Figure 5.18: Surface plots showing sustained ignition for the slump problem. The solutions are calculated using the transition model (4.27) for a steep slope, $S = 1$ and plotted for $x \in (0, 10)$, $t \in (0, 20)$. The erosion rate, $E^\star$, is given by equation (4.9), the initial conditions are given by equations (5.1) and the boundary conditions by equations (5.2). The parameter values are $\delta = 0.17$, $\gamma = 0.77$, $\chi = 0.067$, $E_0 = 10^3$, $h^\star = 0.007$, $c^\star = 1$, $a = 50$, $b_1 = 0.25$, $b_2 = 0$ and the diffusion coefficients are given by $\epsilon = 0.005$, $\omega = 0.1$.

Chapter 6

Discussion

6.1 Overview

In this thesis the Parker model for turbidity currents has been studied with the aim of determining when a turbidity current will become extinct.

In Chapter 2, the importance of the slope in controlling extinction and ignition of the current was highlighted using a steady state model and a one-equation velocity model. The steady state model showed that regions of extinction and ignition exist in the phase plane of velocity and turbulent kinetic energy, and it was determined how the size of these regions is governed by the value of the underlying slope. The one-equation model was split into two forms; a depositional and an erosional model. These models exhibit shocks and were solved using the method of characteristics and by adding a simple diffusion term to the equations. This chapter showed that a critical value of the slope exists, which determines the ignitive and extinctive behaviour of the flow, and that shocks are expected to form in the model. Both of these features were found to persist in more complex models studied in later chapters and so the one-equation model provided useful insight into the behaviour of the full system of equations.

The two-equation shallow-water model was derived and examined both analytically and numerically in Chapter 3. The shallow-water model allows exploration of supercritical and subcritical flow regimes, and highlights how these regimes are strongly influenced by the slope of the bed. Different slope functions were studied and solutions to the model were computed numerically and compared with asymptotic solutions. A taxonomy of the features seen in the numerical solutions was drawn up to demonstrate how the flow regimes of the current

interact with the boundary conditions imposed in the numerical model. The shallow-water model is limited in its description of ignition and extinction as the sediment concentration of the current is assumed to be constant. In addition, the simplified turbulent kinetic energy function used results in 'enforced ignition' which can only be eliminated by letting the velocity of the current tend to zero.

In Chapter 4, the full four-equation turbulent kinetic energy model was considered. Initially, a simple turbulent kinetic energy function was used while evolution of sediment was incorporated into the shallow-water model of Chapter 4. This model showed good agreement with the results of the two-equation model, but, again, enforced ignition was seen. The full turbulent kinetic energy equation was considered, but it was found that this model fails, predicting complex-valued solutions for k when the sediment-induced stratification of the current becomes significant. The catastrophic failure of the k equation shows that the Parker model, in its present form, is unsuitable in such cases.

A new 'transition' model was posed, which allows the current to move from an erosional (turbulent) regime to a depositional (stably stratified) regime as the sediment-induced stratification of the current becomes large. We believe that the numerical results of this model are promising and that a number of interesting mathematical modelling problems arise from its derivation.

Realistic initial and boundary conditions were considered as case studies to the transition model in Chapter 5. Here, it was found that a slump of material on a flat bed compares qualitatively with granular column collapse, an avalanche of material down a steep slope results in ignition of the current, and a slope which flattens out downstream puts a limit on ignition such that the current eventually dies out. A numerical parameter study was considered as part of this chapter, and provides an initial step towards determining regions of ignition and extinction for specific sediment loads and slope profiles.

6.2 Further work

There are several areas of this study suitable for further work. The transition model for turbulent kinetic energy posed in Chapter 4 raises many interesting modelling questions. Some of these were briefly addressed towards the end of Chapter 4, such as the 'natural' erosion rate determined by the transition model in the $k = 0$ regime which allowed $E^\star$ to vary outside the region $E^\star \in [0, 1]$.

This highlighted the possibility that we might want to model erosion as a function which switches off gradually once $k \to 0$. Such a model would require experimental investigation in order to validate a particular model, and the theoretical erosion rates proposed in Chapter 4 could be compared with experimental data.

Two particular areas for further thought have arisen through the case studies of Chapter 5, both regarding the suitability of the Parker model for the initiation problem. Typically, the Parker model is used to provide theoretical comparison with sustained currents in motion, rather than for the start-up of a current, as we have considered here for the slump problem. It is therefore unclear what an appropriate initial value of h would be for the slump problem, since specifying $h = 0$ when $c \neq 0$ leaves the concept of a 'mound' of sediment somewhat undefined. Further, this problem feeds into a more complex discussion regarding the suitability of the Parker model in describing the initiation problem accurately. This was highlighted through the 'sustained ignition' witnessed for the fluvial problem, and for the slump problem, at $x = 0$. It is yet to be seen whether this is an artefact of the model, or an accurate reflection of the ignition process higher up the slope. As was discussed in Chapter 1, determining accurate initial conditions is still very much an open problem in the field of turbidity current modelling.

Finally, the numerical parameter study of Chapter 5 gave some interesting results regarding the influence of the sediment load of the current and the slope of the bed upon the dynamic behaviour of the current. The study provides ample motivation for a series of experiments to validate the hypothesised regions of extinction, erosion and ignition which were found in parameter space.

6.3 Conclusions

In this thesis we have provided a mathematical study of the model of Parker et al. (1986). Models of differing complexity have been derived which have been compared and contrasted to gain a significant insight into the dynamics of the flow. It has been shown that the slope of the bed and the boundary and initial conditions play an important role in the extinctive and ignitive behaviour of the current.

A key finding of this work was to show the limitations of the turbulent kinetic energy equation of Parker et al. (1986). We find that, when the sediment-induced stratification of the flow becomes large, the turbulent kinetic energy

equation of Parker et al. (1986) predicts complex valued solutions for k, causing catastrophic failure of the model.

A new model for turbulent kinetic energy was posed which was explored using a number of cases studies and realistic initial conditions and we believe the model provides promising results. This model also raises several other modelling problems of interest which we have begun to consider theoretically and gives motivation for experimental study.

Finally, by studying a model which has been scaled in a physically realistic manner and by conducting a numerical parameter study at the end of this work, we believe we have made a first step towards understanding when a turbidity current will become extinct, showing that the input of sediment and slope profile of the bed greatly influence the extinctive and ignitive dynamics of the current.

Appendices

Appendix A

Solutions to the depositional model with 'correct' diffusion

The depositional one-equation model is given by equation (2.49). This model is solved in Section 2.4.3 with the inclusion of a 'basic' diffusion term, equation (2.70), and the solutions are plotted in Figure 2.10. In Figure 2.11 the sub-characteristics of the depositional model with basic diffusion are shown, which illustrates the shock location in space and time for the basic diffusion term.

In this Appendix we consider the solutions to the depositional model with the 'correct' diffusion term, given by (2.72). The model is thus

$$e^{s/3}\frac{\partial U}{\partial t} + U^2\frac{\partial U}{\partial s} = -\mu U^3 + \frac{\epsilon}{9\nu\Lambda}e^{-(s+s_i)}U^2\left(U + 6\frac{\partial U}{\partial s} + 9\frac{\partial^2 U}{\partial s^2}\right). \qquad \textbf{(A.1)}$$

where $\epsilon \ll 1$. As was mentioned in Section 2.4.3, the second term on the right-hand side of equation (A.1) is very small since $e^{-s_i} \sim \mathcal{O}(10^{-5})$. As such, the model is difficult to deal with numerically and must be solved for a large value of ϵ.

In Figure A.1 we plot the solutions to equation (A.1), and in Figure A.2 we plot the sub-characteristics of the model.

By comparing these plots to those for the basic diffusion term, shown in Section 2.4.3, it is clear that, by using the correct diffusion term, the location of the shock is significantly altered. Once again, the shock propagates upstream in time, but remains much closer to the boundary, $s = 0$. In Figure 2.12 we plotted the parametric solution to the depositional model, equations (2.52)–(2.58), at $t = 20$ which shows that the solution U becomes multivalued. Away from the

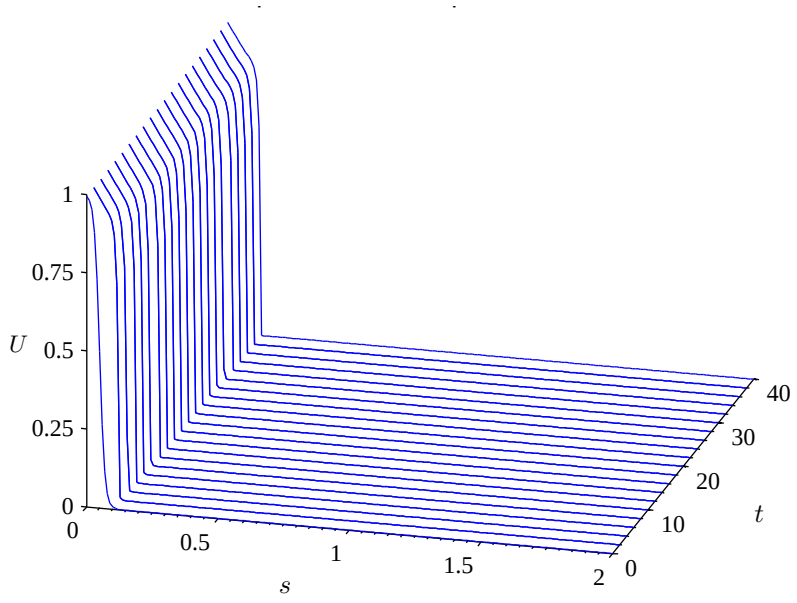

(a) Steady inflow boundary conditions, $U_i = 1$ at $s = 0$

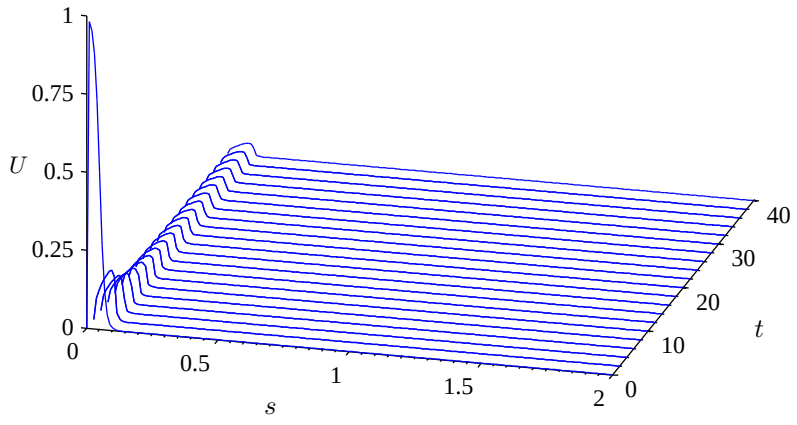

(b) Slumping boundary conditions, $U_i = 0$ at $s = 0$

Figure A.1: Numerical solution to equation (A.1). The initial condition is given by equation (2.44). In (a) the boundary condition is given by equation (2.45) and in (b) the boundary condition is given by equation (2.46). We have used parameter values of $U^\star = 0.5$, $a = 50$, $b = 0.05$, $\mu = 1.387$, $s_i = 11.5$, the diffusion coefficient is $\epsilon = 1000$.

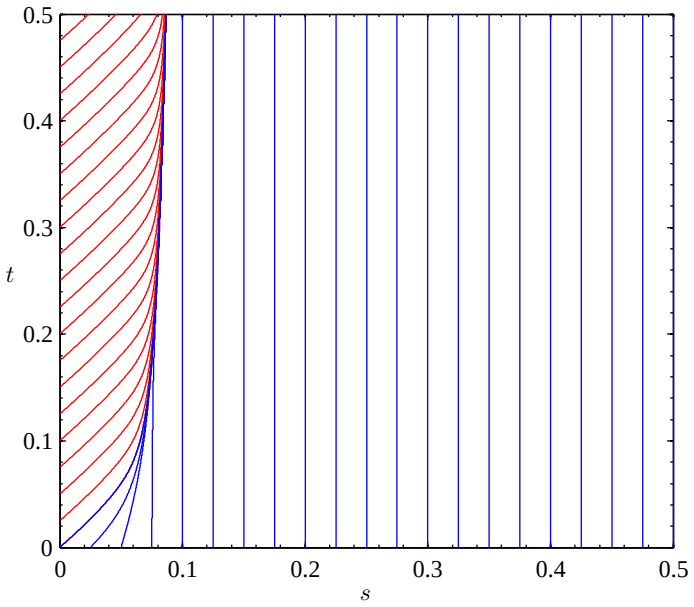

(a) Sub-characteristics for the steady inflow boundary conditions when $\epsilon = 1000$

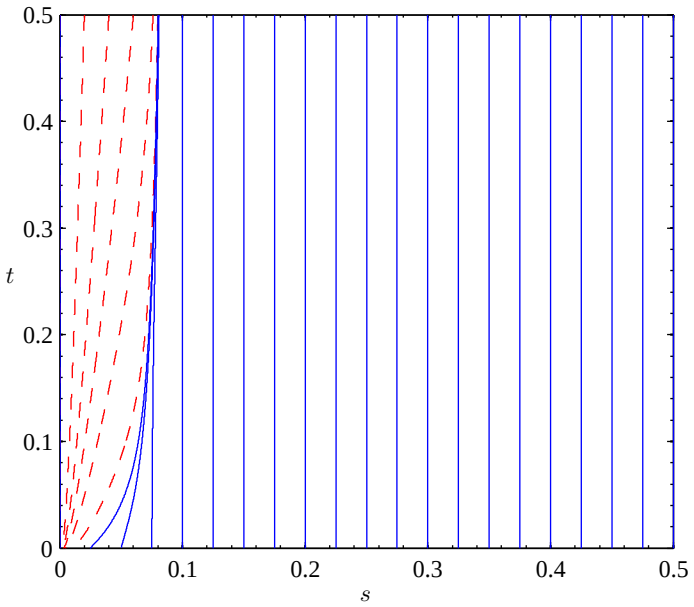

(b) Sub-characteristics for the slumping boundary conditions when $\epsilon = 1000$

Figure A.2: Sub-characteristic curves of equations (A.1) when $\epsilon = 1000$. The blue characteristics are given by the initial condition (2.44) and the red characteristics are given by the boundary condition (a) $U_i = 1$ at $s = 0$ and (b) $U_i = 0$ at $s = 0$. The parameter values are given in Figure A.1.

shock it can be seen that both diffusion models, (2.70) and (A.1), agree with the parametric solution, however the basic diffusion term 'truncates' the solution at a different point in space to the correct diffusion term.

In Figure A.3 we plot the sub-characteristics of the two diffusion models together for the steady inflow problem. This plot highlights that, away from the shock, both diffusion models agree with each other (the characteristics lie upon each other in the $s-t$ plane). In Figure A.4 we show that both sets of sub-characteristics also agree with the parametric solution. For clarity, the diffusion fronts are highlighted in these characteristic plots.

In Chapter 2 we have solved both the erosional model and the depositional model with a basic diffusion term of the form ϵU_{ss}, for $\epsilon \ll 1$. In this appendix, we have highlighted that this simple form of diffusion does not accurately predict the location of the shock in time and space. The correct form of the diffusion for the depositional model is given by the second term on the right-hand side of (A.1), however this term contains an exponentially small factor which makes the effect of the diffusion very small and the numerical solution hard to compute. Consequently, we must choose $\epsilon \gg 1$.

The correct form of diffusion will predict the location of the shock far more accurately than the basic diffusion term. However, for the one-equation model we are satisfied that the basic diffusion term is suitable, since the one-equation model has used many simplifying assumptions in its derivation. However, we note that for later chapters it is important to use the correct form of the diffusion term in the turbidity current model, in order to obtain accurate solutions to the model.

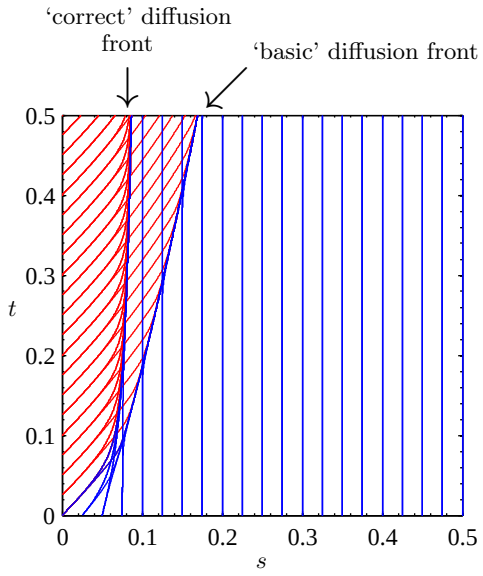

Figure A.3: Sub-characteristic curves of equations (A.1) when $\epsilon = 1000$ compared with sub-characteristic curves of equation (2.70) with $\epsilon = 0.001$. The blue characteristics are given by the initial condition (2.44) and the red characteristics are given by the boundary condition $U_i = 1$ at $s = 0$. The shock fronts are labelled at the top of the figure. The parameter values are given in Figure A.2.

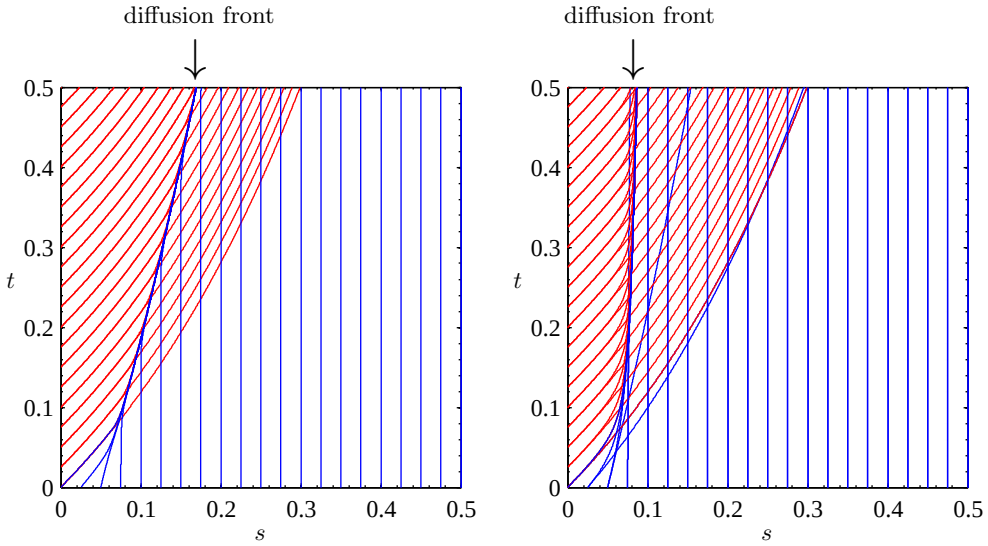

(a) Characteristics of equation (2.49) and sub-characteristics of equation (2.70)

(b) Characteristics of equation (2.49) and sub-characteristics of equation (A.1)

Figure A.4: (a) Sub-characteristic curves of equations (2.70) when $\epsilon = 0.001$ compared with the characteristic curves of equation (2.49). (b) Sub-characteristic curves of equations (A.1) when $\epsilon = 1000$ compared with the characteristic curves of equation (2.49). The blue characteristics are given by the initial condition (2.44) and the red characteristics are given by the boundary condition $U_i = 1$ at $s = 0$. The parameter values are given in Figure A.2.

Bibliography

Ancey, C. Snow avalanches. *Geomorphological Fluid Mechanics*, pages 319–338, 2001.

Bagnold, R.A. Auto-suspension of transported sediment; turbidity currents. *Proceedings of the Royal Society of London. Series A, Mathematical and Physical Sciences*, pages 315–319, 1962.

Batchelor, G.K. *An introduction to fluid dynamics*. Cambridge University Press, 1967.

Baumert, H. and Radach, G. Hysteresis of turbulent kinetic energy in nonrotational tidal flows: A model study. *Journal of Geophysical Research*, 97(C3): 3669–3677, 1992.

Baumert, H.Z., Simpson, J.H., and Sündermann, J. *Marine turbulence: theories, observations, and models*, volume 1. Cambridge University Press, 2005.

Benjamin, T.B. Gravity currents and related phenomena. *Journal of Fluid Mechanics*, 31(02):209–248, 1968.

Best, J.L., Kirkbride, A.D., and Peakall, J. Mean Flow and Turbulence Structure of Sediment-Laden Gravity Currents: New Insights using Ultrasonic Doppler Velocity Profiling. *Particulate gravity currents*, pages 157–172, 2001.

Bonnecaze, R.T., Huppert, H.E., and Lister, J.R. Particle-driven gravity currents. *Journal of Fluid Mechanics*, 250:339–339, 1993.

Bornhold, B.D., Ren, P., and Prior, D.B. High-frequency turbidity currents in British Columbia fjords. *Geo-Marine Letters*, 14(4):238–243, 1994.

Britter, R.E. and Simpson, J.E. Experiments on the dynamics of a gravity current head. *Journal of Fluid Mechanics*, 88(02):223–240, 1978.

Canuto, V.M. Critical Richardson numbers and gravity waves. *Astronomy and Astrophysics*, 384(3):1119–1123, 2002.

Costa, R.G. and Mehta, A.J. Flow-fine sediment hysteresis in sediment-stratified coastal waters. Master's thesis, University of Florida, 1989.

Dade, W.B. and Huppert, H.E. Runout and fine-sediment deposits of axisymmetric turbidity currents. *Journal of Geophysical Research*, 100:18–597, 1995.

Davidson, P.A. *Turbulence: an introduction for scientists and engineers*. Oxford University Press, USA, 2004.

Doxsee, W.W. *The Grand Banks earthquake of November 18, 1929*. Publications of the Dominion Observatory, v. 7, p. 323-335 edition, 1948.

Eidsvik, K.J. and Brørs, B. Self-accelerated turbidity current prediction based upon (k-ε) turbulence. *Cont. Shelf Res*, 9(7):617–627, 1989.

Einarsson, P., Brandsdóttir, B., Guðmundsson, M.T., Björnsson, H., Sigmundsson, F., and Grönvold, K. Center of the Iceland hotspot experiences volcanic unrest. *Eos*, 78(35):374–375, 1997.

Fowler, A.C. *Mathematical models in the applied sciences*, volume 17. Cambridge University Press, 1997.

Fowler, A.C. *Mathematics and the environment*. Lecture Notes, Mathematical Institute, University of Oxford, 2010.

Fowler, A.C. *Mathematical Geoscience*, volume 36. Springer Verlag, 2011.

Freundt, A. Entrance of hot pyroclastic flows into the sea: experimental observations. *Bulletin of Volcanology*, 65(2):144–164, 2003.

Fukushima, Y., Parker, G., and Pantin, H.M. Prediction of ignitive turbidity currents in Scripps Submarine Canyon. *Marine Geology*, 67(1-2):55–81, 1985.

Galperin, B., Sukoriansky, S., and Anderson, P.S. On the critical Richardson number in stably stratified turbulence. *Atmospheric Science Letters*, 8(3): 65–69, 2007.

Garcia, M.H. Depositional turbidity currents laden with poorly sorted sediment. *Journal of Hydraulic Engineering*, 120(11):1240–1263, 1994.

Garcia, M.H. and Parker, G. Experiments on hydraulic jumps in turbidity currents near a canyon-fan transition. *Science*, 245(4916):393, 1989.

Girardclos, S., Schmidt, O.T., Sturm, M., Ariztegui, D., Pugin, A., and Anselmetti, F.S. The 1996 AD delta collapse and large turbidite in Lake Brienz. *Marine geology*, 241(1-4):137–154, 2007.

Gould, H.R. Some quantitative aspects of Lake Mead turbidity currents. *Society of Economic Paleontologists and Mineralogists Special Publication*, 2:34–52, 1951.

Harris, T.C., Hogg, A.J., and Huppert, H.E. A mathematical framework for the analysis of particle–driven gravity currents. *Proceedings of the Royal Society of London. Series A: Mathematical, Physical and Engineering Sciences*, 457 (2009):1241–1272, 2001.

Hearn, C.J. *The dynamics of coastal models*. Cambridge University Press, 2008.

Heezen, B.C. and Ewing, W.M. Turbidity currents and submarine slumps, and the 1929 Grand Banks Newfoundland earthquake. *American Journal of Science*, 250(12):849, 1952.

Hinch, E.J. *Perturbation methods*, volume 6. Cambridge University Press, 1991.

Hogg, A.J., Ungarish, M., and Huppert, H.E. Particle-driven gravity currents: asymptotic and box model solutions. *European Journal of Mechanics Series B Fluids*, 19(1):139–156, 2000.

Högström, U., Smedman, A.S., and Bergström, H. A case study of two-dimensional stratified turbulence. *Journal of the atmospheric sciences*, 56 (7):959–976, 1999.

Hopfinger, E.J. Snow avalanche motion and related phenomena. *Annual Review of Fluid Mechanics*, 15(1):47–76, 1983.

Hopfinger, E.J. Turbulence in stratified fluids: A review. *Journal of Geophysical Research*, 92(C5):5287–5303, 1987.

Howison, S. *Practical applied mathematics: modelling, analysis, approximation*, volume 38. Cambridge University Press, 2004.

Hu, P. and Cao, Z. Fully coupled mathematical modeling of turbidity currents over erodible bed. *Advances in Water Resources*, 32(1):1–15, 2009.

Huppert, H.E. Gravity currents: a personal perspective. *Journal of Fluid Mechanics*, 554:299–322, 2006.

Huppert, H.E. and Dade, B.W. Natural disasters: explosive volcanic eruptions and gigantic landslides. *Theoretical and Computational Fluid Dynamics*, 10 (1):201–212, 1998.

Huppert, H.E. and Simpson, J.E. The slumping of gravity currents. *Journal of Fluid Mechanics*, 99(04):785–799, 1980.

Hutter, K. Geophysical granular and particle-laden flows: review of the field. *Philosophical Transactions of the Royal Society A: Mathematical, Physical and Engineering Sciences*, 363(1832):1497–1505, 2005.

Khripounoff, A., Vangriesheim, A., Babonneau, N., Crassous, P., Dennielou, B., and Savoye, B. Direct observation of intense turbidity current activity in the Zaire submarine valley at 4000 m water depth. *Marine Geology*, 194(3-4): 151–158, 2003.

Kneller, B.C. and Buckee, C. The structure and fluid mechanics of turbidity currents: a review of some recent studies and their geological implications. *Sedimentology*, 47:62–94, 2000.

Kneller, B.C., Bennett, S.J., and McCaffrey, W.D. Velocity and turbulence structure of density currents and internal solitary waves: potential sediment transport and the formation of wave ripples in deep water. *Sedimentary Geology*, 112(3-4):235–250, 1997.

Komar, P.D. The channelized flow of turbidity currents with application to Monterey deep-sea fan channel. *Journal of Geophysical Research*, 74(18): 4544–4558, 1969.

Kostic, S. and Parker, G. The response of turbidity currents to a canyon–fan transition: internal hydraulic jumps and depositional signatures. *Journal of Hydraulic Research*, 44(5):631–653, 2006.

Krause, D.C., White, W.C., Piper, D.J.W., and Heezen, B.C. Turbidity currents and cable breaks in the western New Britain Trench. *Geological Society of America Bulletin*, 81(7):2153–2160, 1970.

Kuenen, P.H. Properties of turbidity currents of high density. *Turbidity currents and the transportation of coarse sediments to deep water*, pages 14–33, 1951.

Kuenen, P.H. and Migliorini, C.I. Turbidity currents as a cause of graded bedding. *The Journal of Geology*, pages 91–127, 1950.

Kullenberg, B. Remarks on the Grand Banks turbidity current. *Deep Sea Research (1953)*, 1(4):203–210, 1954.

Marshall, D. *Flows, Fluctuations and Complexity.* Lecture Notes, Atmospheric, Oceanic and Planetary Physics, Department of Physics, University of Oxford, 2011.

Meiburg, E. and Kneller, B.C. Turbidity currents and their deposits. *Annual Review of Fluid Mechanics*, 42:135–156, 2010.

Menard, H.W. Sediment movement in relation to current velocity. *Journal of Sedimentary Research*, 20(3):148–160, 1950.

Middleton, G.V. Small-scale models of turbidity currents and the criterion for auto-suspension. *Journal of Sedimentary Research*, 36(1):202–208, 1966a.

Middleton, G.V. Experiments on density and turbidity currents: I. Motion of the head. *Canadian Journal of Earth Sciences*, 3(4):523–546, 1966b.

Middleton, G.V. Sediment deposition from turbidity currents. *Annual Review of Earth and Planetary Sciences*, 21(1):89–114, 1993.

Mosdell, H.M. *Photograph: 'Buildings in Lord's Cove tossed and smashed by the tsunami'.* From the collection of W.M. Chisholm, 1929.

Mulder, T. and Syvitski, J.P.M. Turbidity currents generated at river mouths during exceptional discharges to the world oceans. *The Journal of Geology*, pages 285–299, 1995.

Mulder, T., Savoye, B., and Syvitski, J.P.M. Numerical modelling of a mid-sized gravity flow: the 1979 Nice turbidity current (dynamics, processes, sediment budget and seafloor impact). *Sedimentology*, 44(2):305–326, 1997.

Mulder, T., Syvitski, J.P.M., Migeon, S., Faugeres, J.C., and Savoye, B. Marine hyperpycnal flows: initiation, behavior and related deposits. A review. *Marine and Petroleum Geology*, 20(6):861–882, 2003.

Naruse, H., Sequeiros, O., Garcia, M.H., Parker, G., Endo, N., Kataoka, K.S., Yokokawa, M., and Muto, T. Self-accelerating turbidity currents at laboratory scale. *River, Coastal, and Estuarine Morphodynamics*, 1:473–476, 2007.

Normark, W.R. and Dickson, F.H. Man-made turbidity currents in Lake Superior. *Sedimentology*, 23(6):815–831, 1976.

Ockendon, H. and Ockendon, J.R. *Viscous flow.* Cambridge University Press, 1995.

Palanques, A., Martín, J., Puig, P., Guillén, J., Company, J.B., and Sardà, F. Evidence of sediment gravity flows induced by trawling in the Palamós (Fonera) submarine canyon (northwestern Mediterranean). *Deep Sea Research Part I: Oceanographic Research Papers*, 53(2):201–214, 2006.

Pantin, H.M. Interaction between velocity and effective density in turbidity flow: phase-plane analysis, with criteria for autosuspension. *Marine Geology*, 31(1/2):59–100, 1979.

Pantin, H.M. and Franklin, M.C. Improved experimental evidence for autosuspension. *Sedimentary Geology*, 2011.

Parker, G. Self-formed straight rivers with equilibrium banks and mobile bed. Part 1. The sand-silt river. *Journal of Fluid Mechanics*, 89(1):109–125, 1978.

Parker, G. Conditions for the ignition of catastrophically erosive turbidity currents. *Marine Geology*, 46(3-4):307–327, 1982.

Parker, G., Fukushima, Y., and Pantin, H.M. Self-accelerating turbidity currents. *Journal of Fluid Mechanics*, 171:145–181, 1986.

Parker, G., Garcia, M.H., Fukushima, Y., and Yu, W. Experiments on turbidity currents over an erodible bed. *Journal of Hydraulic Research*, 25(1):123–147, 1987.

Parsons, J.D., Friedrichs, C.T., Traykovski, P.A., Mohrig, D., Imran, J., Syvitski, J.P.M., Parker, G., Puig, P., Buttles, J.L., and García, M.H. The mechanics of marine sediment gravity flows. *Continental Margin Sedimentation*, pages 275–337, 2007.

Peakall, J., Felix, M., McCaffrey, W.D., and Kneller, B.C. Particulate gravity currents: Perspectives. *Particulate gravity currents*, pages 1–8, 2001.

Pratson, L.F., Imran, J., Hutton, E.W.H., Parker, G., and Syvitski, J.P.M. BANG1D: a one-dimensional, Lagrangian model of subaqueous turbid surges. *Computers & geosciences*, 27(6):701–716, 2001.

Rottman, J.W. and Simpson, J.E. Gravity currents produced by instantaneous releases of a heavy fluid in a rectangular channel. *Journal of Fluid Mechanics*, 135(1):95–110, 1983.

Rubin, H. and Atkinson, J.F. *Environmental fluid mechanics*. Marcel Dekker, Inc., 2001.

Ryan, W.B.F. and Heezen, B.C. Ionian Sea submarine canyons and the 1908 Messina turbidity current. *Geological Society of America Bulletin*, 76(8):915–932, 1965.

Sequeiros, O.E., Naruse, H., Endo, N., Garcia, M.H., and Parker, G. Experimental study on self-accelerating turbidity currents. *Journal of Geophysical Research*, 114(C5):C05025, 2009.

Simpson, J.E. *Gravity currents: In the environment and the laboratory*. Cambridge University Press, 1999.

Simpson, J.E. and Britter, R.E. The dynamics of the head of a gravity current advancing over a horizontal surface. *Journal of Fluid Mechanics*, 94(3):477–495, 1979.

Stull, R.B. *An introduction to boundary layer meteorology*, volume 13. Springer, 1988.

Trofimovs, J., Sparks, R., and Talling, P.J. Anatomy of a submarine pyroclastic flow and associated turbidity current: July 2003 dome collapse, Soufrière Hills volcano, Montserrat, West Indies. *Sedimentology*, 55(3):617–634, 2008.

Trofimovs, J., Foster, C., Sparks, R.S.J., Loughlin, S., Le Friant, A., Deplus, C., Porritt, L., Christopher, T., Luckett, R., Talling, P.J., Palmer, M.R., and Le Bas, T. Submarine pyroclastic deposits formed during the 20th May 2006 dome collapse of the Soufrière Hills Volcano, Montserrat. *Bulletin of Volcanology*, pages 1–15, 2012.

Venkatasubramanian, V., Schattler, H., and Zaborsky, J. Dynamics of large constrained nonlinear systems-a taxonomy theory [power system stability]. *Proceedings of the IEEE*, 83(11):1530–1561, 1995.

Whitham, G.B. *Linear and nonlinear waves*, volume 42. Wiley-interscience, 1974.

Xu, J.P., Noble, M.A., and Rosenfeld, L.K. In-situ measurements of velocity structure within turbidity currents. *Geophysical Research Letters*, 31(9): L09311, 2004.

Zammett, R. *Gravity Currents on Earth and on Mars*. PhD thesis, University of Oxford, 2008.